Origami-based active structures for tunable Helmholtz resonators and soft robotics

Amine Benouhiba

THESE DE DOCTORAT DE L'ETABLISSEMENT UNIVERSITE BOURGOGNE FRANCHE-COMTE

PREPAREE A L'UNIVERSITE DE FRANCHE-COMTE

Ecole doctorale n° 37

SCIENCES PHYSIQUES POUR L'INGENIEUR ET MICROTECHNIQUES

Doctorat en Automatique

Par

Benouhiba Amine

Structures actives à base d'origami pour des résonateurs de Helmholtz adaptatifs et la robotique souple

Thèse présentée et soutenue à Besançon le 15 juin 2020.

Composition du Jury :

M. Manuel COLLET	Directeur de recherche CNRS, ECL, Lyon	Rapporteur
M. Frédéric LAMARQUE	Professeur des Universités, UTC, Compiègne	Rapporteur
M. Stéphane VIOLLET	Directeur de recherche CNRS, AMU, Marseille	Président
M. Patrick ROUGEOT	Ingénieur de recherche, ENSMM, Besançon	Invité
M. Kanty RABENOROSOA	Maître de Conférences, ENSMM, Besançon	Co-encadrant de thèse
M. Morvan OUISSE	Professeur des Universités, ENSMM, Besançon	Co-directeur de thèse
M. Nicolas ANDREFF	Professeur des Universités, UFC, Besançon	Directeur de thèse

À mes très chers parents
À mon frère & ma sœur
À toute ma famille

Remerciements

Au moment où on croit en avoir fini avec la rédaction de la thèse, vient la partie qui n'est pas la plus simple à écrire...

Cette thèse a été pour moi une riche expérience qui ne peut s'achever sans remercier les personnes qui m'ont encadré, aidé et soutenu durant les trois dernières années. Je tiens tout d'abord à remercier mon directeur de thèse, Nicolas ANDREFF et mon co-directeur de thèse Morvan OUISSE. Merci de m'avoir fait confiance et de m'avoir donné l'opportunité de travailler avec vous.

Je tiens aussi à remercier mon co-encadrant Kanty RABENOROSOA et Patrick ROUGEOT. Vous avez été d'une disponibilité et d'un soutien sans faille tout au long de la période de thèse. Travailler avec vous a été très motivant et surtout très formateur.

Je remercie chaleureusement les membres de mon jury, les rapporteurs Manuel COLLET et Frédéric LAMARQUE, tout comme le président de ce jury Stéphane VIOLLET, de m'avoir fait l'honneur de rapporter et d'examiner mes travaux.

Je remercie tous les personnels des départements AS2M et DMA de l'institut FEMTO-ST pour l'agréable ambiance de travail et les échanges quotidiens. Un grand merci à Cédric, Maxime, Ahmed, Mounir, Houari, Raouia, Wissem, Bassem, Vladimir, Hasnaa, Benjamin, Romain, Quentin, Jesus, Joël, Ning, Bhawnath, Benoit, Shifaa, Khaled, Safa, Fawzia, Fawzi et Abir de m'avoir offert leur amitié et pour tout que nous avons vécu ensemble.

Je voudrais finalement remercier ma famille, et y compris ma tante Zohra, pour avoir cru en moi et m'avoir toujours soutenu et encouragé tout au long de mon parcours. Je remercie tout particulièrement mes très chers parents, Ali et Zineb, pour leur irremplaçable et inconditionnel soutien. Sans eux, je n'aurais sans doute pas accompli les travaux présentés dans ce manuscrit.

Amine BENOUHIBA

Contents

List of Figures

List of Tables

Acronyms & Notations

Acronyms

SMA	*Shape Memory Alloys*
SMP	*Shape Memory Polymer*
EAP	*Electro-Active Polymer*
DE	*Dielectric Elastomer*
CP	*Conductive Polymer*
PVDF	*PolyVinylidene DiFluoride*
Py	*Pyrrole*
PPy	*PolyPyrrole*
LiTFSI	*Lithium bis (TriFluoromethylSulfonyl) Imide*
MEMS	*Micro-Electro-Mechanical System*
HR	*Helmholtz Resonator*
FE	*Finite Element*
FEA	*Finite Element Analysis*
P-TMM	*Parallel-Transfer Matrix Method*
TL	*Transmission Loss*
JCA	*Johnson-Champoux-Allard model*
PUC	*Periodic Unit Cell*
IPG	*Ionic Polymer Gel*
CNT	*Carbon NanoTubes*
LCE	*Liquid Crystal Elastomer*
PLA	*PolyLactic Acid*

Introduction

Contents

Context

Origami, from ori meaning folding and kami meaning paper, denotes the ancient oriental art of paper folding. In brief, it is the art of creating 3D models from a single sheet of paper, by successive folding. Folding, as a fabrication process, is one of the primary tools of nature. For instance, leaves of many plants and petals of various flowers are folded within the bud, insect wings often display folding inside carapaces and cocoons, and multiple proteins inherit their functions from the fashion their amino-acid chains fold. The concept of origami can also be an outstanding design and fabrication tool for engineers. From a single flat sheet of material, 3D complex structures with various properties for different purposes can be achieved. Depending on the desired functionality, origami structures can adjust their shape to meet the requirements; therefore, multi-functional devices with on-demand properties can be obtained. However, even though origami as a concept has endless potential, as a science and engineering tool, it is still a relatively new field with many open challenges that need to be addressed. A frequent predicament engineers face while using origami concepts to address highly demanding application requirements is: how to find the appropriate origami design for a given application?. Trying to answer this question can be highly challenging and extremely difficult on multiple levels. Furthermore, in order to make a complete crossover from just being an art form to becoming a fully-fledged engineering field, we need improved origami design tools as well as a better understanding of origami concepts. We can identify three main points that are holding origami from making a complete crossover:

- A better understanding of thick-origami structures: most origami algorithms and origami design software handle zero-thickness origami structures only; therefore,

a great deal of information required for the design and fabrication of origami engineering devices is not available, which can help to determine the appropriate fabrication materials, the adequate fabrication technologies, the suitable actuation system, etc.

– Performance-driven origami design: most, if not all, origami tools, as well as origami approaches and methodologies available today, can not quantify the performances of a particular origami design in a given engineering field, as they are only used for determining the crease pattern, the fold type, and the sequence of folding for the achievement of a given 3D shape.

– Origami-oriented fabrication processes and actuation systems: Traditional fabrication processes are not adaptable for origami fabrication, and new processes better suited for origami structures are required. The same applies to actuation systems and smart materials. To actuate origami devices and promote its capabilities, better actuation systems that are self-contained, lightweight, compact, and can display an extensive and reversible folding, using localized stimulus are needed.

Ultimately, this work is an attempt to address the mentioned challenges and propose better options to engineers and researchers that are interested in using origami as a solution and tool for highly demanding and complex engineering dilemmas.

Contributions

Chapter 1 introduces some of the aspects of origami engineering and origami-based active structures, and it addresses all the challenges and achievements in this relatively new engineering field, both in a global and a precise fashion. Based on the state of the art, it provides a comprehensive vision and an accurate synthesis of origami engineering. It includes definitions, axioms and theorems, mathematical tools and software, description of the used fabrication technologies and different applications, in addition to actuation systems. Lastly, it summarizes the state of the art and discusses the open challenges and obstacles concerning the development of origami-based active structures.

Chapter 2 proposes our design methodology for origami-based active structures. The main objective of this methodology is to make the process of using origami design for highly demanding engineering applications more practical and efficient. It contains several steps:

(i) identification of the application requirements;

(ii) selection of an origami base that embodies such requirements;

(iii) 2D and 3D design of the origami structure;

(iv) multi-physics modeling;

(v) selection the fabrication technologies;

(vi) integration of an actuation system;

(vii) experimental validation and control.

This methodology can help to steer and guide engineers and scientists who are interested in using origami designs to address complex engineering problems.

As one of the targeted application fields of this work, Chapter 3 discusses vibro-acoustic devices for low-frequency sound control, more precisely tunable Helmholtz resonators. It introduces Helmholtz resonators and provides their advantages and shortcomings. It also describes the working principle and the resonant frequency of such acoustic devices, including an analytical model of the frequency. Moreover, it discusses the relationship between the geometrical properties of the resonator and the resonant frequency and its sensitivity. Additionally, it presents the state of the art via some suitable examples of tunable Helmholtz resonators found in the literature. Furthermore, it also addresses the modeling of origami-based Helmholtz resonators, using to approaches: (i) analytical modeling using P-TMM model and the equivalent volume concept, and (ii) FE modeling, which includes two models, a model that describes the acoustic behavior only, and a second model for the coupling of both, the acoustic and mechanical behaviors.

Chapter 4 is a proof of concept for the origami methodology proposed in chapter 2. The targeted field is adaptative-passive noise control in the low-frequency domain for vibro-acoustic applications. The proposed solution is a tunable origami-based Helmholtz resonator. Following the proposed origami methodology:

(i) the application requirements were identified, which include a lightweight tunable acoustic device that can achieve a broad frequency shift in the low-frequency domain;

(ii) an origami base, known as waterbomb, which can provide an auxetic property (negative Poisson coefficient) for the designed structure, was picked;

(iii) the origami structure was designed in 2D and 3D, using origami dedicated software;

(iv) a set of models were developed to simulate the working behavior of the tunable origami-based Helmholtz resonator according to its flexibility (rigid, quasi-rigid, and flexible);

(v) using, 3D printing, laser machining, dipping, and rubber coating the different types of origami-based Helmholtz resonators were fabricated;

(vi) using the models developed previously (FE models) different actuation strategies for the flexible resonator were tested, and based on the results an actuation system was selected, implemented, and utilized to control the diameter of the resonator using a closed-loop control;

(vii) the three types of the fabricated origami-based Helmholtz resonators, rigid, quasi-rigid, and flexible, were experimentally tested and were able to achieve exceptional results in terms of frequency range, bandwidth, and acoustic absorption performance.

So far, we have considered origami devices as structures and mechanisms which can produce high performances in a wide range of applications. However, we did not particularly focus on actuated origami devices with self-contained actuation systems, which also known as self-folding and shape-shifting origami devices. Chapter 5 discusses the actuation of origami devices using active material, more specifically, electroactive polymers. Since origami-based structures are as capable and as competent as their actuation systems, finding the appropriate smart material for the actuation of an origami structure is crucial; therefore, we proposed to investigate the potential of polypyrrole conductive polymer for small-scale origami devices. Polypyrrole conductive polymer offers many assets that include energy efficiency, lightweight, flexibility, reversibility of the folding motion, biocompatibility, and a low activation voltage. In this chapter, a hybrid static model that describes the folding of CP-based origami devices was introduced: (i) a multi-physics model that estimates the folding of the active segments (polypyrrole tri-layer actuators) for a given voltage, and (ii) a kinematic model that reconstruct the state of folding of the full geometry (containing both active and passive segments) for a given voltage. The models were experimentally validated using different structures, including single-segment, two-segment, and three-segment active structures, as well as a more complex structure, an origami folding cube.

The last chapter provides a general conclusion of our work. Additionally, it displays different tracks for future work.

Chapter 1

State of the art

"We hear only those questions for which we are in a position to find answers."
-Friedrich Nietzsche

Contents

This chapter introduces origami-based active structures and discusses their state of the art. Furthermore, it presents their advantages, applications as well as their different methods of deployment, specifically speaking: self-folding and shape-shifting.

1.1 Introduction

By using origami, engineers have access to new and interesting ways to fabricate, assemble, store, and deploy different devices and structures. Some of the advantages, as already mentioned in the previous chapter, include the ability to compactly store auto-deployable devices (such as airbags [Hoffmann, 2001, Cromvik and Eriksson, 2006]), the ability to change shape and form also known as reconfigurability, as well as reducing the manufacturing complexity thanks to the reduction in part counts and the improvement of the assembly by utilizing collapsible/deployable part [Peraza-Hernandez et al., 2014]. Moreover, it has been demonstrated that origami can be apply across different scales and throughout a wide range of application, from DNA size application at the nano-scale [Kosinski et al., 2019, Mao et al., 2019, Engelhardt et al., 2019] to deployable outer space devices for satellites and space radars at the very large scale [Landau, 2014, Garcia, 2016, Pehrson et al., 2019] . Additionally, more current origami application also include: electronic devices with enhanced properties, such as batteries and capacitors [Miyashita et al., 2014, Gao et al., 2018, Zeng et al., 2019], numerous space devices (solar panels, solar sails, telescope lenses [Early et al., 2004]), micro-mirrors [Ocampo et al., 2004] morphing wings and foldable aircrafts [Bunget and Seelecke, 2008, Bunget and Seelecke, 2010, Pounds, 2012], Various mechanisms with enhanced mechanical properties and characteristics [Grzeschik, 2013, Gattas and You, 2013, Liu et al., 2018] , crash structures and other energy absorption devices [Zhou et al., 2017, Yang, 2018], robots [Hoover and Fearing, 2008, Rus and Tolley, 2018], shelters [Martínez-Martín and Thrall, 2014, Quagli et al., 2014], biomedical devices [Edmondson et al., 2013, du Plessis d'Argentré et al., 2018, Taylor et al., 2019], metamaterials [Fuchi et al., 2012, Schenk and Guest, 2013], microelectromechanical systems (MEMS) [Zhao et al., 2011, Goshi et al., 2018, Miskin et al., 2018], and many other applications [Debnath and Fei, 2013, Chai and Tan, 2019]. This chapter provides an introduction and synthesis of the state of the art of the relatively new fast growing field of origami engineering. It includes definitions, mathematical tools and algorithms, targeted application fields and fabrication strategies, actuation systems, and general summary and conclusion.

1.2 Origami fundamentals

This subsection defines origami structures and specifies their many advantages, which made them go from being just an ancient oriental art into becoming an interesting research field for engineers and scientists. The main advantage is their ability to produce substantial volume variation, as well as their shape-shifting capabilities, which gives them numerous different functionalities, all in one structure.

1.2.1 Definition

Origami−折り紙 is a Japanese art and historical practice of folding paper into abstract shapes that dates back to the 1600s. The word origami comes from ori, meaning "folding", and kami, meaning "paper". Traditionally, origami uses a single sheet (no cuts are

allowed) of paper in order to obtain 3D complex shapes through manual manipulation and a sequence of strategically placed folds.
Using origami-based structures offers many assets [Tolley et al., 2014, Demaine and O'Rourke, 2008]:

- reduced space requirements;
- large deformation and size variation;
- inherent compliance;
- reduced number of parts;
- reduced material consumption;
- improved energy efficiency;
- lightweight.
- possibility of having an integrated actuation and control system (smart materials).

1.2.2 Fundamentals

Origami design started as a trial-and-error art form, which allows the making of real-life like objects (animals, plants, ...) just by folding a piece of paper. Later on, several mathematical approaches were developed in order to better understand the behavior of the folded paper and also to make the design process less complex and more efficient.
There are some common notations and terms in origami that should be known and acknowledged. These terms were standardized by researchers and scientists, to name a few: Lang, Huffman, Clowes, Waltz, Takeo Kanade, and Akira Yoshizawa [Kanade, 1980] and [Lang, 2011]. All and all, the commonly used terminology in the field of origami are mountain fold (a fold that results in a Λ shape), valley fold (a fold that results in a V shape), crease (the line left behind in a flat piece paper after a fold), X-ray line (hidden fold lines and/or crease), crease pattern (all of the crease lines left on a flat piece of paper after folding), and vertex (a point where multiple crease lines meet). Furthermore, besides the terminology, there are also basic origami folding patterns, also known as origami bases, the cupboard base, windmill base, waterbomb base, and preliminary fold [Debnath and Fei, 2013].
There are a few origami mathematical approaches in the literature, such as Geometry based approaches, topology based approach (discussed by Thomas Hull [Kanade, 1980]), Robert Lang's tree theorem [Lang, 2011] and Maekawa's string-to-beads method [Lang, 2004].
The previous origami mathematical approaches are grounded on three main fundamentals: Huzita-Hatori axioms, Maekawa and Kawasaki's theorems.
Jacques Justin first introduced the Huzita-Hatori axioms in 1989; they contain seven different axioms. They were revised by Humiaki Huzita in 1991 and finalized by Koshiro Hatori, Justin and Robert Lang in 2001. The axioms [Huzita-Hatori, 2009] are:

Axiom 1.2.1 *Given two points P_1 and P_2, there is a unique fold that passes through both of them.*

Axiom 1.2.2 *Given two points P_1 and P_2, there is a unique fold that places P_1 onto P_2.*

Axiom 1.2.3 *Given two lines l_1 and l_2, there is a fold that places l_1 onto l_2.*

Axiom 1.2.4 *Given a point P_1 and a line l_1, there is a fold that places P_1 onto l_2.*

Axiom 1.2.5 *Given two points P_1 and P_2 and a line l_1, there is a fold that places P_1 onto l_1 and passes through P_2.*

Axiom 1.2.6 *Given two points P_1 and P_2, and two lines l_1 and l_2, there is a fold that places P_1 onto l_1 and P_2 onto l_2.*

Axiom 1.2.7 *Given one point P_1 and two lines l_1 and l_2, there is a fold that places P_1 onto l_1 and is perpendicular to l_2.*

Furthermore, Maekawa's theorem revolve around origami crease patterns with flat folds, in which case, for every interior vertex of a flat fold, the absolute value of difference between the number of the mountains creases (M) and the valley creases (V) must always be equal to 2:

$$|M - V| = 2. \tag{1.1}$$

As for the Kawasaki theorem, it is mainly related to the angles between the creases lines of an interior vertex. The theorem states that for a given crease pattern to be foldable, all the sequences of angles around each interior vertex must have a sum of 180°, as shown in Eqn. 1.2 and Eqn. 1.3 and represented in Fig. 1.1 [Barile, 2019].

$$\alpha_1 - \alpha_2 + \alpha_3 - \alpha_4 + ... - \alpha_{2n} = 0^\circ \tag{1.2}$$

Put differently

$$\alpha_1 + \alpha_3 ... + \alpha_{2n-1} = \alpha_2 + \alpha_4 ... + \alpha_{2n} = 180^\circ \tag{1.3}$$

These origami theorems act as a basic guideline for computational origami as well as the development of origami algorithms, which is essential in order to allow origami to cross from being just an ancient art to being a promising engineering field.

1.3 Applications and fabrication strategies

In this section, we introduce different fields of applications of origami structures as well as describe the fabrication strategies used for the different origami structures. A couple of the main application fields are space applications and biomedical applications, where size-reduction requirements are very high. However, origami structures can also be useful in a very wide range of other applications as well, such as electronics, energy, robotics, sensing, and vibro-acoustics.

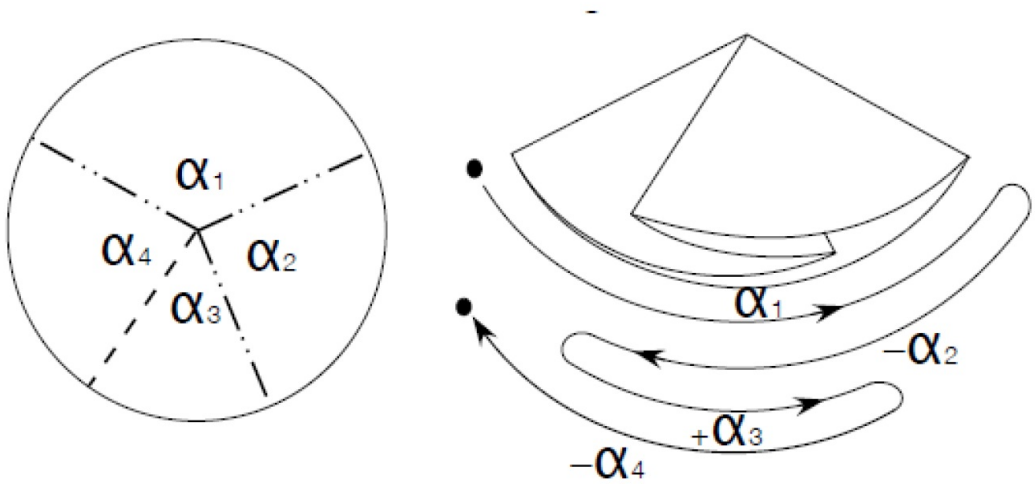

FIGURE 1.1: Kawasaki's theorem applied in the case of a foldable paper crane [Debnath and Fei, 2013].

1.3.1 Space

Large flat structures, to name some: solar arrays, solar sails, solar-powered satellites and spaces radars, are necessary for most of the outer space missions. However, sending such structures into the outer space in their functioning state can be problematic, considering the amount of energy (fuel) needed to do so. That is why adopting origami engineering for this kind of application was a game-changer. Large structures can be folded on the ground into a very compact package and, once in space, they can deploy to its fully functional size.

Miura [Miura, 1994] discussed the deployment of a solar power array (see Fig. 1.2) in a research vessal by the name of Space Flyer Unit (SFU). The origami design used for this array is called "*Miura-ori*" or "*Miura-fold*". The fold is named for its inventor Koryo Miura.

In another similar work, Lang [Lang, 2015] introduced Eyeglass, a foldable lens (see Fig. 1.3) for a space telescope which can be easily loaded into a space shuttle, in the form of a small cylinder, then once in space, the device can be deployed into a huge disc. The origami design is called "*Umbrella*", inspired by its resemblance to a collapsible umbrella, since they both have the same folding/unfolding behavior (form a cylinder to a disc and vice-versa), as well as, the fact that they are both scalable and contain mass-producible parts. In 2002, a 5-meter prototype was made. The lens contains a pattern of 72 segments, and after testing, it was able to concentrate light as expected. It was believed that a larger version, 25-meter or more, could be made in the following few years, although, the ultimate objective is making a 100-meter lens that folds into a 3-meter diameter cylinder.

NASA [Landau, 2014] also proposed a solar power array with an origami-style touch (see Fig. 1.4). Their goal is the development of an origami-based device that can be folded

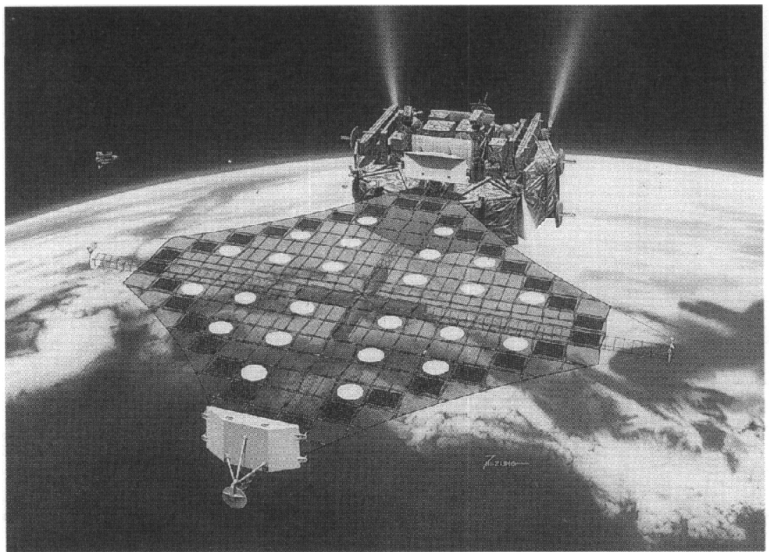

FIGURE 1.2: Deployment of an origami-based solar power array with a Miura-ori folding pattern on the Space Flyer Unit, a space satellite [Miura, 1994].

FIGURE 1.3: Prototype of the origami-based lens on its test range for the solar system's largest telescope project by the name of Eyeglass [Lang, 2015].

FIGURE 1.4: A 1/20th-scale tabletop prototype (expands to a deployed diameter of 1.25 meters) of the Origami-based solar panel array developed by NASA using the origami Patten called the "*flasher*" [Landau, 2014].

into a hexagonal tube of 2.7-meter cross-section then unfolds, when it is needed, into a membrane of a 25-meter across. Their 1/20th-scale prototype can reach an unfolded state with 1.25-meter diameter. The name of the origami pattern utilized in this project is the flasher pattern.
The three examples discussed above, even though each of them has a different origami design, they all tackle the same challenging problem, which is how to send a big as possible structures in a small as possible package toward a harsh environment like the outer space. So the search for a solution led to ancient art, enabled by mathematical tools, origami engineering.

1.3.2 Electronics and energy storage

Among other challenges, in the field of deformable electronics, the development of integrated, deformable energy storage devices is a significant one. Motivated by these reasons, Song et *al.* [Song et al., 2014] proposed an origami-based lithium-ion battery (see Fig. 1.5) that can realize a very high level of deformation, including bending, twisting and even folding. Slurry coating of electrodes onto paper current collectors was utilized in order to fabricate the origami-based batteries, as for the packaging standard materials were used. Then, they were folded using the Miura pattern. This origami battery was able to achieve high linear and surface deformations as well as large bending and twisting actions. The approach discussed here was based on the fusion of the art of origami, materials science, and practical energy storage devices. Furthermore, the former could be used as a guideline for the design and fabrication of flexible and curvilinear electronics with remarkable mechanical properties and functionalities.

Another interesting example of origami-based energy storage devices is the work of

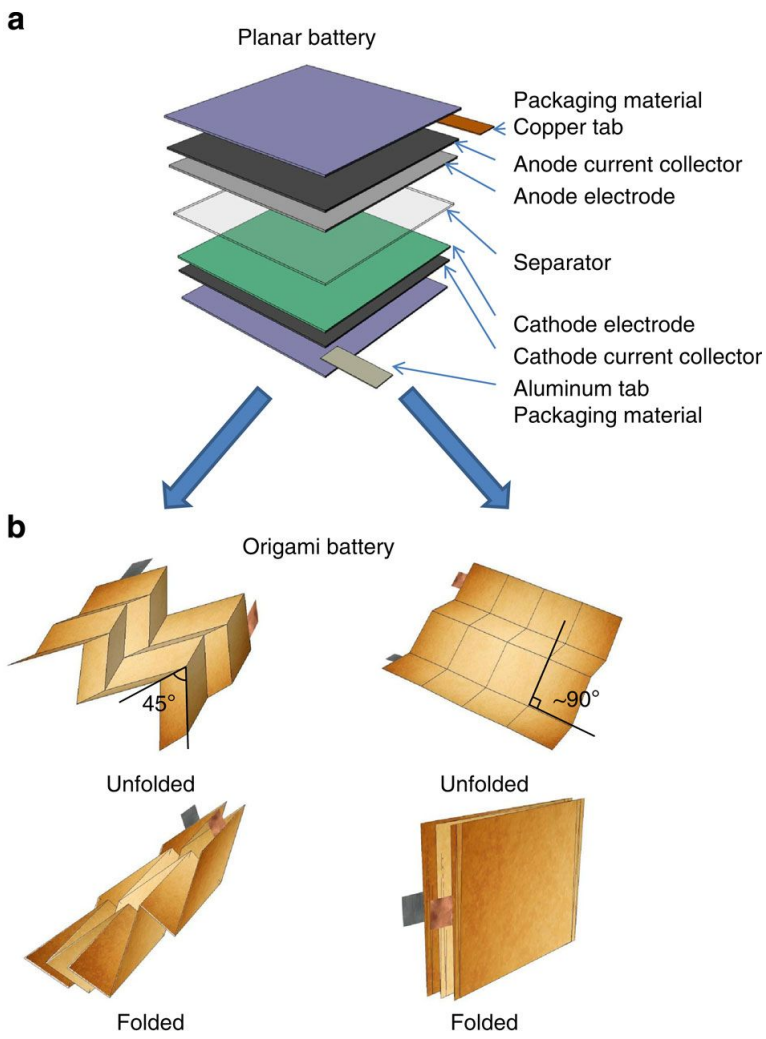

FIGURE 1.5: Illustration displaying the concept of the origami-based lithium-ion battery. (a) Schematic showing the different layers found in a traditional lithium-ion battery. (b) A couple of examples showing the design of the origami battery, in the folded and unfolded state, on the left the first example of origami battery with a 45° Miura pattern and on the right the second example of origami battery with a 90° Miura pattern. [Song et al., 2014].

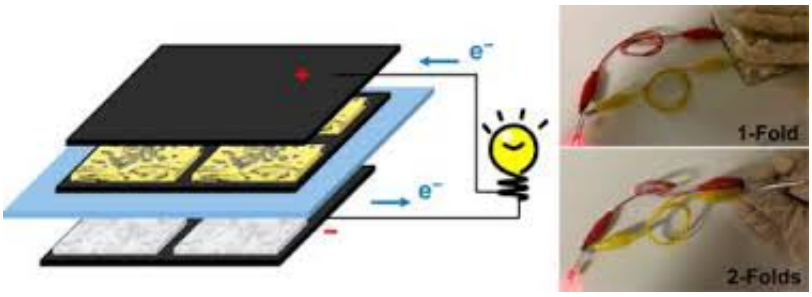

FIGURE 1.6: Demonstration of the working principle of the Foldable Lithium-Sulfur Battery [Li et al., 2015].

Lee and Choi [Lee and Choi, 2015] on paper-based bacteria-powered batteries. In their work, a stackable and integrative 3D paper-based battery was developed. The latter was able to generate power thanks to microbial metabolism. This battery has the potential to power the next generation of paper-based systems, such as low-cost and disposable diagnostic devices.
The final example in this field is the foldable lithium-sulfur battery (see Fig. 1.6) by Li et *al.* [Li et al., 2015]. This rechargeable battery has the highest areal capacity (3 mAh cm^{-2}) reported to date among all types of origami-based energy storage devices. This performance was made possible due to two reasons: (i) the use of fully foldable and superelastic carbon nanotube current-collector layers, and (ii) the impregnation of the active materials (Li and S) into layers of the desired origami pattern (in this case check-board pattern). As a result, the battery can be manually folded along two orthogonal directions. These shape-changing Li-S origami batteries that can produce significantly greater energy density than traditional lithium-ion batteries have the potential to power flexible and adaptable electronic devices of tomorrow including cell phones, laptops, tablets, surgical tools, and other biomedical devices.

1.3.3 Vibro-acoustics

One of the targeted application of origami-based devices is acoustics. For instance, sound absorption at medium and low frequencies, as it depends on the wavelength of sound, requires a significant length of an acoustic resonator, to the point where it may become unpractical for noise control applications. Therefore, compact acoustic resonators that can shift their resonance frequency while keeping a constant length are widely sought for. One example of such resonators is the work of [Cambonie and Gourdon, 2018]: a regular acoustic resonator containing a paper-based origami spiral (see Fig. 1.7) that acts as an equivalent porous medium with a dynamic tortuosity; hence, it improves the acoustic properties of the resonator. In other words, the origami spiral allows the resonator to increase its length artificially; thus, it can achieve same performance as a longer resonator. The latter was able to achieve a frequency shift of 341 Hz, from 630 to 971 Hz, and with an acoustic absorption rate varying from $\sim 100\%$ to 28.5%, respectively.

Another example of origami-based acoustic devices is the work of [Fang et al., 2018].

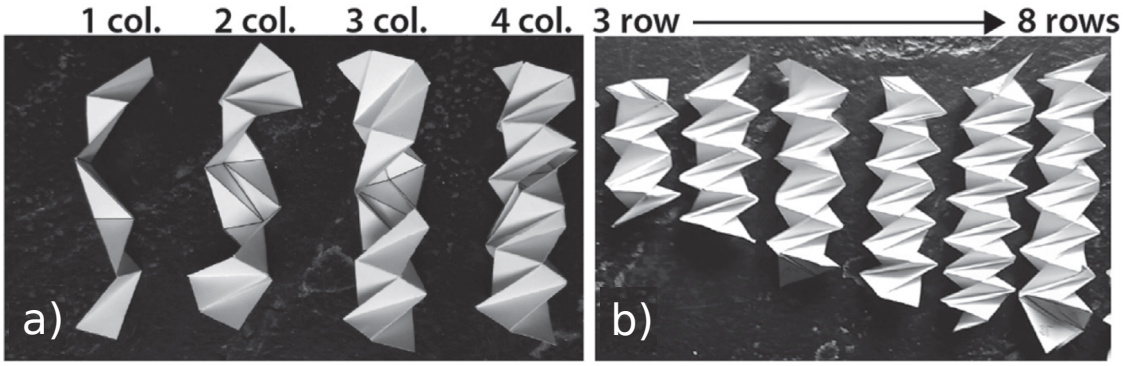

FIGURE 1.7: Photos of the origami spirals: a) 5 rows spirals, from left to right, 1 to 4 columns, b) 4 columns spiral, from left to right, 3 to 8 rows [Cambonie and Gourdon, 2018].

Similarly to the example discussed above; they revealed that a modular-origami silencer (see Fig. 1.8) could display interesting acoustic properties, through tunability and programmability. Their experimental results indicated that by reconfiguring the origami silencer via folding, efficient tuning of the device could be achieved. Moreover, their proof-of-concept study showed that by relying on origami-inspired structures, which provide great versatility in properties and functionalities, including acoustic adaptability, on-demand sound control could be performed.

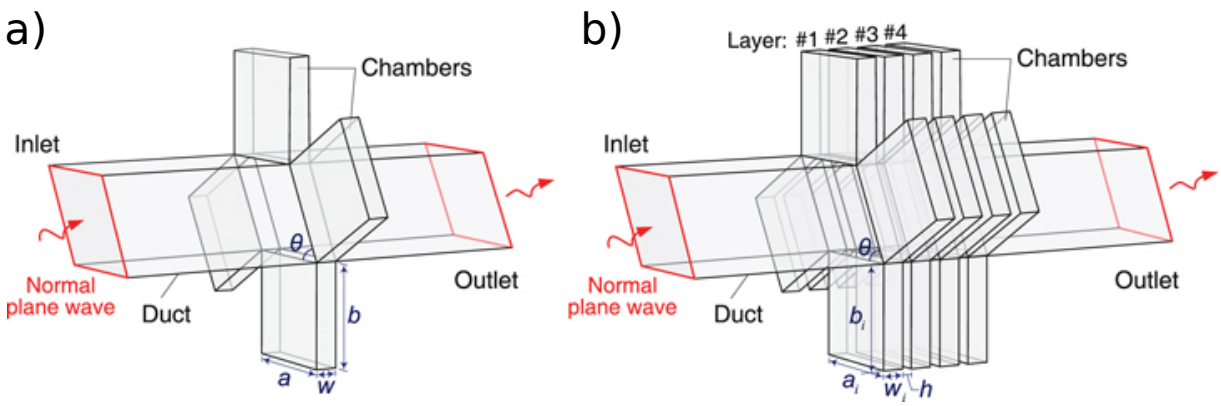

FIGURE 1.8: Conceptual designs of a) a single-layer origami silencer and b) 4-layer origami silencer, chambers within each layer share the same dimensions [Fang et al., 2018].

1.3.4 Biomedical

Biomedical researchers and engineers are becoming more and more interested in origami-based devices. When it comes to navigating in very constrained spaces, utilizing origami-

based devices can be very beneficial. The origami device can be folded into a minimal size, which will allow it to reach any targeted area of the human body, way easier than any other device. Moreover, once it is there, the device can be deployed into a bigger functioning medical device so it can accomplish its desired task. The ability of the origami device to occupy a very compact space can also be helpful during the retracting of the medical device from the human body. All and all, origami devices are a perfect choice for reaching hard-to-reach places. Furthermore, origami devices use fewer parts than regular devices which makes them somewhat more reliable.
In the literature, there are many examples of origami-based medical devices.

Kuribayashi et *al.* [Kuribayashi et al., 2006] introduced an origami-based stent-graft, as shown in Fig. 1.9. This new type of stent-graft, unlike the standard ones, are made of a single ultrafine foil of Ni-rich Ti/Ni shape memory alloy (SMA). The waterbomb pattern [Randlett, 1963] was used as a base for the origami design, and the crease pattern was produced by negative photochemical etching. The stent-graft can be deployed either by the effect of body temperature or by utilizing the superelasticity of the SMA. Rodrigues et al [Rodrigues et al., 2017] studied the kinetostatic behavior of these origami-based stent-grafts during their deployment. The origami-based stent-graft can be a good replacement to the standard stent-graft since it is made of just one layer of SMA, which makes it more reliable and durable.

[Leong et al., 2009] presented in their work origami-based tetherless microgrippers (see Fig. 1.10). Among other functionalities, these microgrippers can be used for the capture and retrieval of objects and conducting biopsies. The microgrippers were fabricated using standard cleanroom/μfabrication technology. The former was made using a silicon wafer as a support layer (a standard step in this kind of process), then by the end of the process, they were separated from the wafer, in their open state (flat) ready for grabbing. A magnetic field was utilized in order to guide in vivo the grippers to their desired

FIGURE 1.9: An origami-based stent-graft in its folded and deployed states [Kuribayashi et al., 2006].

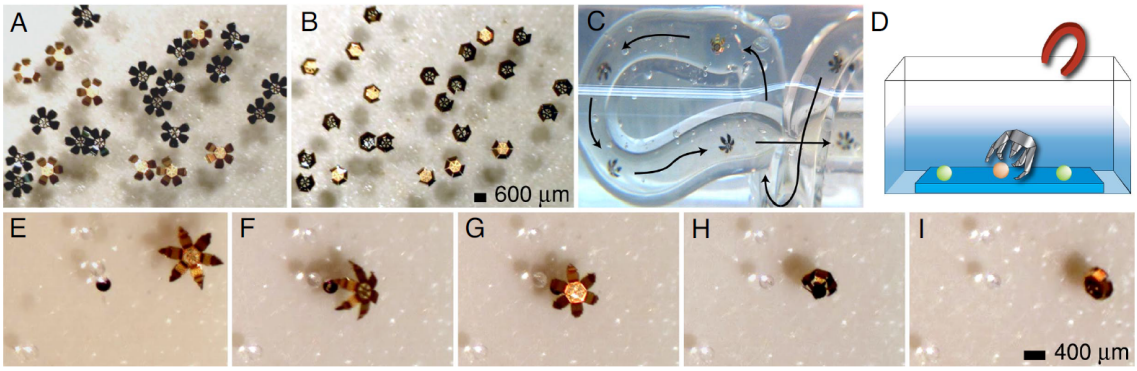

FIGURE 1.10: Thermally triggered origami-based tetherless microgripper intended for biomedical applications. (A and B) The folding action of 23 grippers simultaneously, triggered by heating, (A) open, (B) closed. (C) Overlapped image sequence displaying the tetherless control of single gripper throughout a transparent coiled tube. (D) Schematic diagram illustrating the magnetic remote-control manipulation of the microgripper during the capture of a bead. (E–I) Image sequence obtained by an optical microscope, showing the magnetically directed movements of a microgripper during the capture of a black bead (275 μm) from among several clear beads. [Leong et al., 2009].

target remotely. Also, once they reached the target, the locking mechanism can be activated either by heat ($40° - 60°$) or by using a variety of different chemicals, including organic chemicals. They start with an opening of $700\mu m$ as their initial (open) state, then when closed they are down to only $190\mu m$. These tiny tetherless grippers serve as a good example of the development of biocompatible and autonomous microdevices for minimally invasive biomedical application [Johnson et al., 2017]. Bassik et *al.* [Bassik et al., 2010] expanded on the previous work by specializing in the activation mechanism of the microgrippers. A biopolymer with a selective enzymatic degradation was utilized in the hinges of the microgrippers. The biopolymer will naturally degrade in cancerous environments, which will then trigger the closing mechanism of the microgripper. This microgripper serves as a valid example of the progress of biomedical devices with autonomous reconfiguration in response to a specific biological trigger.

Zhu et *al.* discuss in [Zhu and Li, 2014] a hydrogenation-assisted graphene origami (HAGO) approach for the nanomanufacturing of unique carbon nanostructures (see Fig. 1.11). One of the desired functionalities of the HAGO is to be able to achieve molecular mass uptake, storage, and release. In order to control the shape of the HAGO nanostructures, an electric field is applied which will render its geometry mechanically programmable. The nanoscale origami structures are made of an atomically thin layer of graphene. At first, the graphene takes the shape of a building block; then because of its chemical properties, it can be configured to several different other origami nanostructures. These origami-based graphene nanostructures have the potential to act as nano-contains for drug delivery in molecular vessels. That being said, the imperfect formation during hydrogenation of the nanostructure can be a major concern to the HAGO

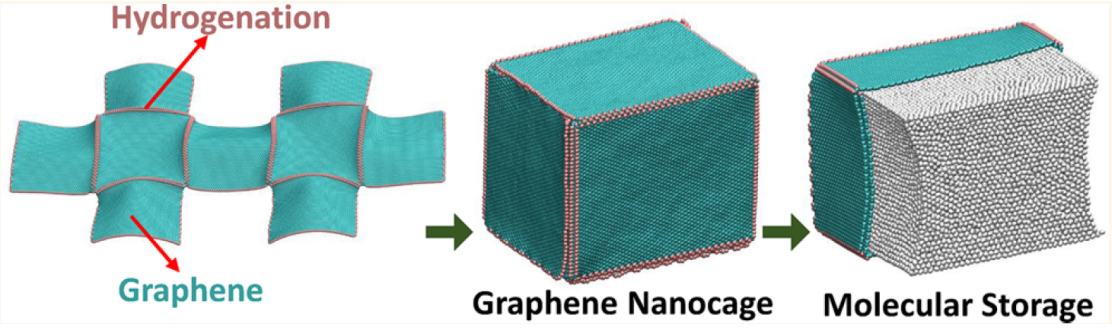

FIGURE 1.11: Nanoscale hydrogenation-assisted graphene origami device, from left to right: flat, folded and during molecular storage [Zhu and Li, 2014].

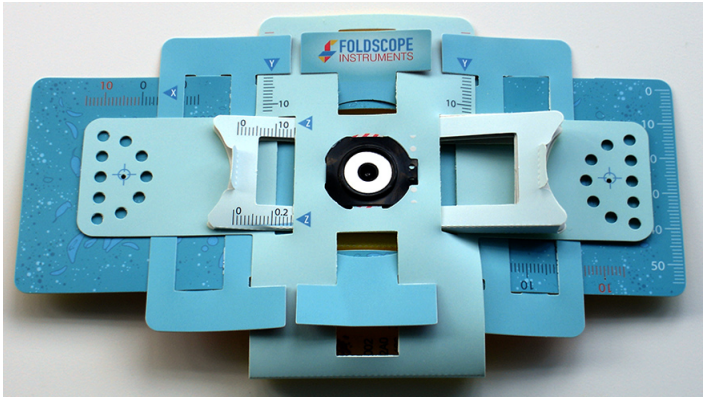

FIGURE 1.12: Assembled prototype of the ultra-low-cost, lightweight origami-based microscope [Cybulski et al., 2014].

approach, since it can lead to an inaccurate formation of nanostructures. Furthermore, the bigger the HAGO structures, the more accurate the deployment mechanism becomes. However, even so, these nanostructures have the potential to drastically improve the drug delivery, in a good way.

Cybulski et *al.* [Cybulski et al., 2014] describe a low-cost origami-based microscope (see Fig. 1.12), including brightfield, darkfield and fluorescence ones. Microscopes that start as 2D sheets of material to later becoming fully functioning devices are the result of combining the principles of origami and optical designs. A passive self-alignment of the device is ensured via kinematic constraints, provided by structural loops in the folded paper. Unlike the classic expensive microscopes, these origami-based microscopes are very light, rugged and can survive harsh outdoor conditions while offering a variety of imaging capabilities. All and all, they are cost-effective, portable devices that can provide a wide range of applications in science and education.

Schmidt et *al.* in their paper [Schmidt et al., 2011], introduced a design of a intracardiac magnetic resonance imaging (ICMRI) catheter (see Fig. 1.13). The latter is comprised of deployable imaging coils attached to the end of an electrophysiology abo-

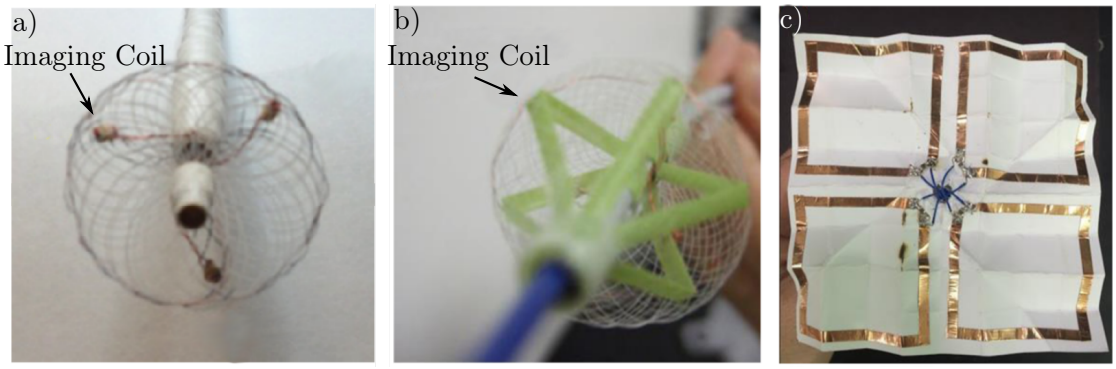

FIGURE 1.13: Expandable intra-cardiac MR imaging and MR-tracking catheter for improved MR-guided [Schmidt et al., 2011].(a) first version (b) improved version [Chen et al., 2015] and (c) origami-based version [Taylor et al., 2016].

lition catheter. Later, Chen et *al.* [Chen et al., 2015] improved the proposed design of the ICMRI catheter. For instance, they increased the diameter of the deployed device, which provided better control of the MRI-guided RadioFrequency Ablation (RFA) procedures. Finally, Taylor et *al.* [Taylor et al., 2016] proposed a completely different design of the device, an origami-based design. The new compact design provided more space for attaching electronics to the end of the catheter, which will be later on deployed inside the subject's heart. The origami structure is based on the Palmer-Shafer origami flasher. The ICMRI allows for better visualization of the RFA procedure. Furthermore, MR images obtained from ICMRI, have an increased signal-to-noise ratio (SNR) by a factor of 2-4. Moreover, 4-16 times faster imaging is achieved using the ICMRI during MR-guided RFA. In general, The ICMRI catheter allows for a safer and more reliable MRI-guided RFA procedures.

Miyashita et *al.* [Miyashita et al., 2016] present an origami robot for patching stomach wounds (see Fig. 1.14). The subject ingests the robot as an ice capsule. Then, after the melting of the ice (body heat), the robot will self deploy. A neodymium magnet attached to the robot allows for its control via an external magnetic field. The robot is made of sheets of biocompatible and biodegradable drug-including sheets, after reaching its target (stomach wound) it will finally auto-degrade, releasing the drug needed for patching the wound. Furthermore, the ice capsule itself (before the melting of the ice) can be used as a robot in order to dislocate a foreign object (button battery, for example) from its inflammation site. The ice capsule can be rolled via the external magnetic field and guided toward the intervention site. It can then attach itself to the battery using the magnet, which is followed by the removal of the battery from the injured skin. A discharge of the couple out of the body could be feasible though out the gastrointestinal tract. Despite the potential that this capsule robot has, the safety of the method is still a significant concern.

Ranzani et *al.* propose in their work [Ranzani et al., 2017] deployable origami-inspired stabilization mechanisms for endoscopic procedures (see Fig. 1.15). Even though, flexible

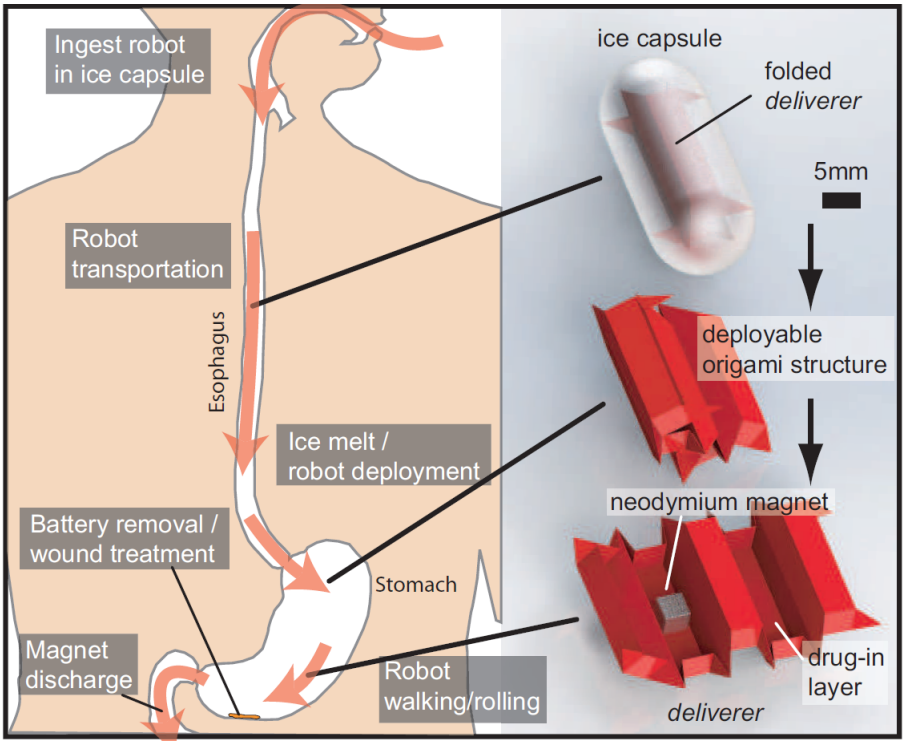

FIGURE 1.14: Schematic diagram displaying the origami robot manipulation. The subject first swallows an ice capsule containing the robot. Once the capsule reaches the stomach, it melts, as a result of body heat, which leads to the deployment of the robot. Then, the remotely controlled robot dislocates the foreign object, such as a button battery, from the damaged region and further treats the inflammation by delivering a drug [Miyashita et al., 2016].

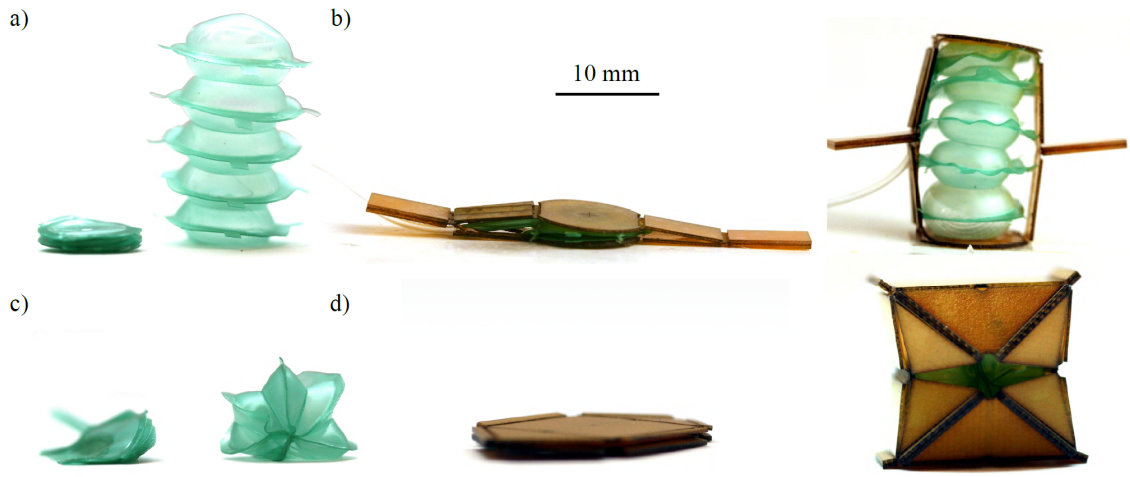

FIGURE 1.15: Fabricated prototypes of the origami-based stabilization mechanisms for endoscopic procedures. (a and c) Soft linear and rotational actuators, respectively, in the deflated and inflated states. (b and d) Soft linear and rotational actuators, respectively, integrated into origami structures during un-actuated and actuated states. [Ranzani et al., 2017].

endoscopes are still the gold standard when it comes to Natural Orifice Translumenal Endoscopic Surgery (NOTES); their flexibility, which is a crucial characteristic for them to be able to navigate the gastrointestinal system, represents a major drawback during distal manipulation. To improve the stability of flexible endoscopes, they proposed deployable endoscopic add-on in order to counteract the applied forces at their tip during the medical procedures. Three different designs were studied: a fully soft version and a couple of hybrid soft-folded ones. The fully soft version is a combination of linear soft actuators, as for the hybrid versions they are flat foldable structural shells that contain soft actuators; one of them contains linear actuators and the second one (origami magic cube) contains rotational ones. All the designs have a low footprint (a maximum of 5 mm is added to the diameter of the endoscope after reattaching the undeployed stabilization mechanism) which makes them an up-and-coming concept. However, better integration of the mechanisms in a radial arrangement is needed in order for them to be more convenient to use during a real medical procedure.

1.3.5 Robotics

The robotics field has also shown interest in origami engineering for increasing robots performances. Being able to 2D print a robot, in a fast and low-cost fashion, then build it up to a fully functioning 3D robotics system, is a game-changer. To this end, multiple works in the literature have adopted origami engineering in order to design and fabricate robotic systems. [Onal et al., 2011] discusses the possibility of passing

from a 2D fabricated structure, to a 3D functioning robot (as shown in Fig. 1.16), by using the origami-inspired planar fabrication. They started from a sheet of material (polyester, Polyether ether ketone (PEEK), polytetrafluoroethylene (PTFE)), then using a CO2 laser cutter, the design (inspired from a well-known origami base, waterbomb) was engraved in the sheet. By adjusting the power of the laser machine, engraving the folding lines instead of cutting through the sheet can be achievable. However, the engraved folding lines tended to be folded only in one direction, which means folding the sheet into the desired 3D structure is not possible. So, to fix this problem, engraving the folding lines was replaced by small stitch like holes. Moreover, holes are also taken out at the points of high mechanical stress, which occurs as multiple folds coincide. Then, the 3D structure, which has a worm-like shape, was generated, by folding the sheet manually. Furthermore, the actuation of the 3D was achieved by a shape memory alloy (SMA) coil spring, NiTi. When the current goes through the NiTi coil, the latter experiences a heat elevation (joule effect), which causes a solid-state phase transformation, leading to an expansion of the coil. The heat elevation can be problematic for a lot of foldable materials; hence, the choice of using the polyester, PPEK, and PTFE sheets that have a comfortably higher melting temperature, was made. Although the process discussed in this paper is not time-consuming and can easily be done, it still has some shortcomings, such as the limitations on the materials that can be used, and the actuation of the structure, which tends to be rather inefficient (the robot crawls about 50 mm in 3 min).

Another example of origami-based robotic systems is the "reconfigurable wheel" of Lee et al [Lee et al., 2013, Lee et al., 2014]. Their main goal is the fabrication of a robot with deformable wheels, so it can adapt to different terrains and overcome various obstacles (see Fig. 1.17). The design of the wheels was also based on the well-known origami base called waterbomb. To be precise, a variation of that pattern known as magic-ball, which has a circular shape was used here. However, the pattern was changed at the edges, because a spoke structure which connects the wheel structure with a shaft is needed.

FIGURE 1.16: A prototype of an origami-inspired mobile robotic body that can undergo earthworm-like locomotion [Onal et al., 2011].

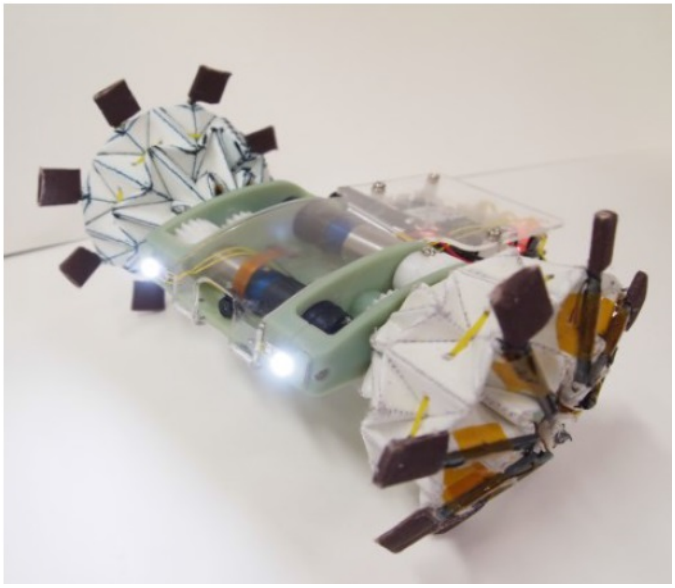

FIGURE 1.17: Adaptable origami wheel robot [Lee et al., 2014].

Paper was used as the material of choice, for the fabrication of the wheels, because it is easy to fold, and can generate very complex structures. Moreover, that is what made it a basic material for the origami art in the first place. Nonetheless, paper is very weak in shear stress, and small forces can easily tear it. So, the paper sheet was reinforced by a polyimide film, which has an adhesive layer on one side. The latter was used for joining them. For the fabrication process, a laser cutter was utilized to create the pattern on the double-layered sheet (paper and polyimide film). A stitch-like shape was cut along the folding lines, and holes were made on the vertex points where high stress is usually concentrated. The fabrication process was inspired by the work of [Onal et al., 2011] discussed above. As for the wheel deformation mechanism, a DC motor, sliding shaft and a cable were used. When the motor turns, it winds the wire, and the latter pulls the sliding shaft, making the wheel diameter larger. On the other hand, when the motor unwinds the wire, a rubber band attached around the wheel, helps it restore its original shape. In a previous version of their work, they used a complex and less effective, deformation mechanism, which was based on two types of spring, a passive spring and a shape memory alloy coil spring. However, after switching to the mechanism discussed above, generating a high wheel deformation was easily achieved (form a 55 mm diameter to 120 mm diameter).
A third example of the origami-based robots is the paper of Miyashita et al [Miyashita et al., 2015] about their an untethered Miniature Origami Robot that Self-folds, Walks, Swims, and Degrades. If it is divided into a few points, the aim of their paper is:

- Designing a 2D structure that can self fold to a 3D robot.
- Immediate actuation for untethered walking and swimming.

– Subsequent dissolving in liquid.

– Remotely controlled system by an alternating external magnetic field.

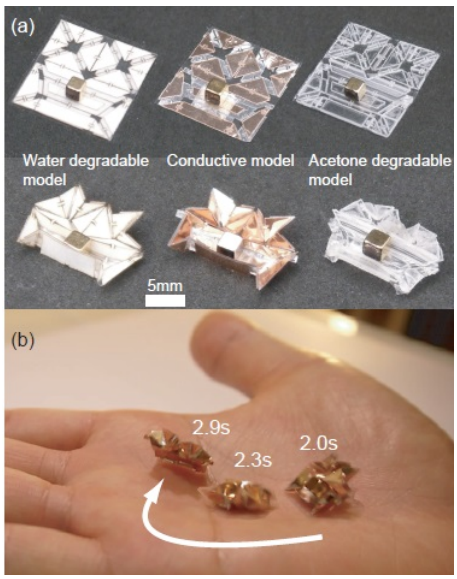

FIGURE 1.18: Remotely controlled Self-folding origami robot that walks, swims and degrades after accomplishing its task. (a) The folded and unfolded states of origami robot in its: water-degradable version, conductive version, and acetone-degradable version, from left to right, respectively. (b) Milli origami robot moving on top of a palm [Miyashita et al., 2015].

For the design and fabrication, different structural layers were used, to give different models of the final robot (a water degradable robot, a conductive robot, and acetone degradable robot, see Fig. 1.18). The structural layer was first laser cut (printing the desired design), keeping in mind that the mountain folds (folds of a 90° angle) have more significant cut gaps than the valley folds (folds of much less than 90° angle). Then, an adhesive is applied on the top side of the structural layer. Next is folding the whole layer in half, adding a polyvinyl chloride (PVC) layer between the two halves of the structural layer, before pressing everything tightly together. Also, the final product would be a PVC layer sandwiched between the two halves of the structural layer. All is left is adding the cubic neodymium magnet, which is used for controlling the robot, into its designated spot. After finishing the fabrication process, the 2D layer is heated on a paltrier element. The heat will cause the PVC layer to contract, which will trigger the self-folding process, producing a 3D robot. For controlling the robot, an electromagnetic coil system was developed. The system consists of four square electromagnetic coils inclined 45° from the horizontal plane; each was placed at a corner under the robot operating area. After the robot completes its task, the former goes into an Embedded tank for dissolving. The process discussed above produces a High speed and cost-effective robot. However, the

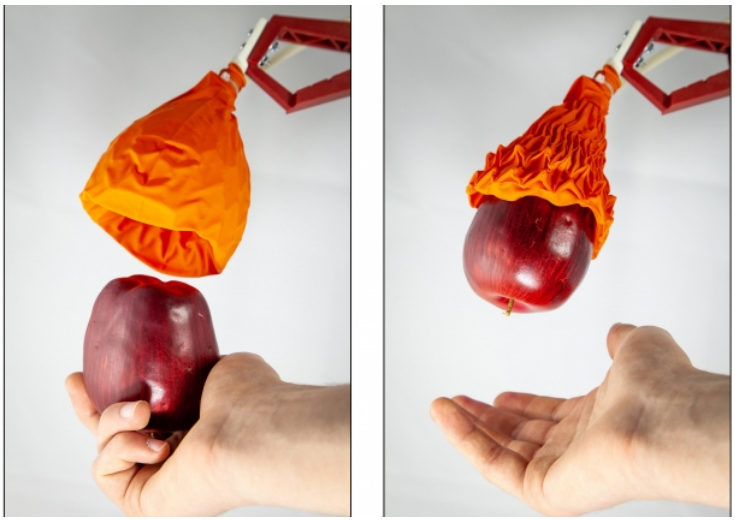

FIGURE 1.19: Demonstration of the grasping action of the origami-based soft gripper [Li et al., 2019].

produced robot also has a minimal operating area, represented by a disc with a diameter of 20 cm, located above the electromagnetic coil system.

Our final example in this subsection is the work of Li et *al.* [Li et al., 2019] on their origami-based vacuum-driven soft grippers (see Fig. 1.19). In the field of soft robotics, soft grippers have shown an impressive performance of grasping a vast range of objects simply and robustly. Nonetheless, Designing highly flexible grippers with an important grasping force while remaining gentle to delicate objects is one of the most significant challenges of this field. Following this logic, Li et *al.* proposed an origami-based vacuum-driven gripper composed of two parts: a skeleton made of an origami structure known as "magic ball" and a skin made of a thin, flexible membrane that covers the origami structure. When negative pneumatic pressure is applied (vacuum), the membrane shrinks around the origami structure leading to its folding. On its turn, the latter tightens up around the object resulting in the grasping motion. Then, when the pneumatic pressure is lifted, the stiffness of the magic ball structure helps the gripper to regain its original open state. Much like soft grippers, this gripper takes the shape of the grasped object. However, it can also apply very high grasping forces, depending on the applied negative pneumatic pressure. As a result, the origami-based gripper can grasp a wide range of objects with different shapes and sizes as well. This new gripper holds a high potential for numerous applications that require simple, secure, and strong grasping action.

1.4 Mathematical tools and algorithms

Designers and engineers need methods, tools, and software specifically tailored to origami design and its different challenges. The previous section has focused primarily on domain knowledge about origami definitions and fundamental origami theorems. Existing

computer-aided design software is not necessarily useful when it comes to origami designs and their different challenges. Such challenges, which include identifying crease patterns and fold sequencing, require unique methods and tools. This subsection introduces some of the prior work on origami engineering methods, tools and software in support of origami design activities.

The first example is Robert Lang's TreeMaker, a well-known software packages for origami fold pattern design. The tree method [Lang, 1996] describes the mathematical approach and the theoretical aspects of the TreeMaker software. This method allows for the design of an origami base by providing the crease pattern of the necessary folds. The folds are defined as non-stretching transformations of a 2D sheet into a 3D form such as all facets remain perfectly flat. The origami base is defined by certain parameters, including the crease pattern and the orientation of the folds (mountain or valley). Once the origami base is obtained, additional folding is required to achieve a specific origami model. TreeMaker determines the required crease pattern of the desired origami base via optimization methods. Fig. 1.20.a presents an application of TreeMaker's algorithm, where the tree graph of an insect is displayed together with the computed crease pattern produced by TreeMaker. Further details regarding TreeMaker are available in the literature [Lang, 2001, Lang, 2005].

A different crease pattern design approach is to directly impose the exact desired final shape, which the sheet should take after folding; therefore, no passing by an intermediate designing step (a design base) is required. Demaine et *al.* [Demaine et al., 2000] proposed a mathematical framework for folding a 2D sheet into a thin strip, which essentially can be "*wrapped*" around the desired shape or form. Moreover, in their work, they explained that a crease pattern for a specific flat silhouette or a three-dimensional polyhedral surface could be obtained. They introduced a few different algorithms for wrapping the desired shape with the 2D sheet, which includes an algorithm that utilizes any sheet with a surface area arbitrarily close to that of the desired shape, also another algorithm which maximizes the width of the sheet strip subject to certain constraints [Demaine and Demaine, 2002].

Tachi introduced an interesting algorithm for "*origamizing*" objects [Tachi, 2007, Tachi, 2010]. The algorithm is able to generate crease patterns for folding a single sheet of material into a given polyhedral surface without the need for cutting. The former is based on the concept of utilizing folds in an initially planar sheet to create flaps that are "*tucked*" (hidden). These flaps are used to reconstruct a desired three-dimensional shape. The Origamizer software solves the inverse problem of producing a crease pattern by using an arbitrary polyhedral surface as input. In his work, Tachi investigated the conditions required for creating a valid crease pattern.

Tachi has also proposed methods and algorithms for producing freeform origami structures (as shown in Fig. 1.20.b) that can approximate curved surfaces [Tachi, 2010b, Tachi, 2010a]. By using these algorithms, curved bodies such as cylinders and disks can be produced from rigid foldable origami surfaces. A free-form software based on the algorithms has been created. Besides its ability to generated crease patterns of the desired shapes, it also allows for the visualization of the folding/unfolding process of a given origami design. Moreover, Tachi proposed another method [Tachi, 2013] for constructing origami tessel-

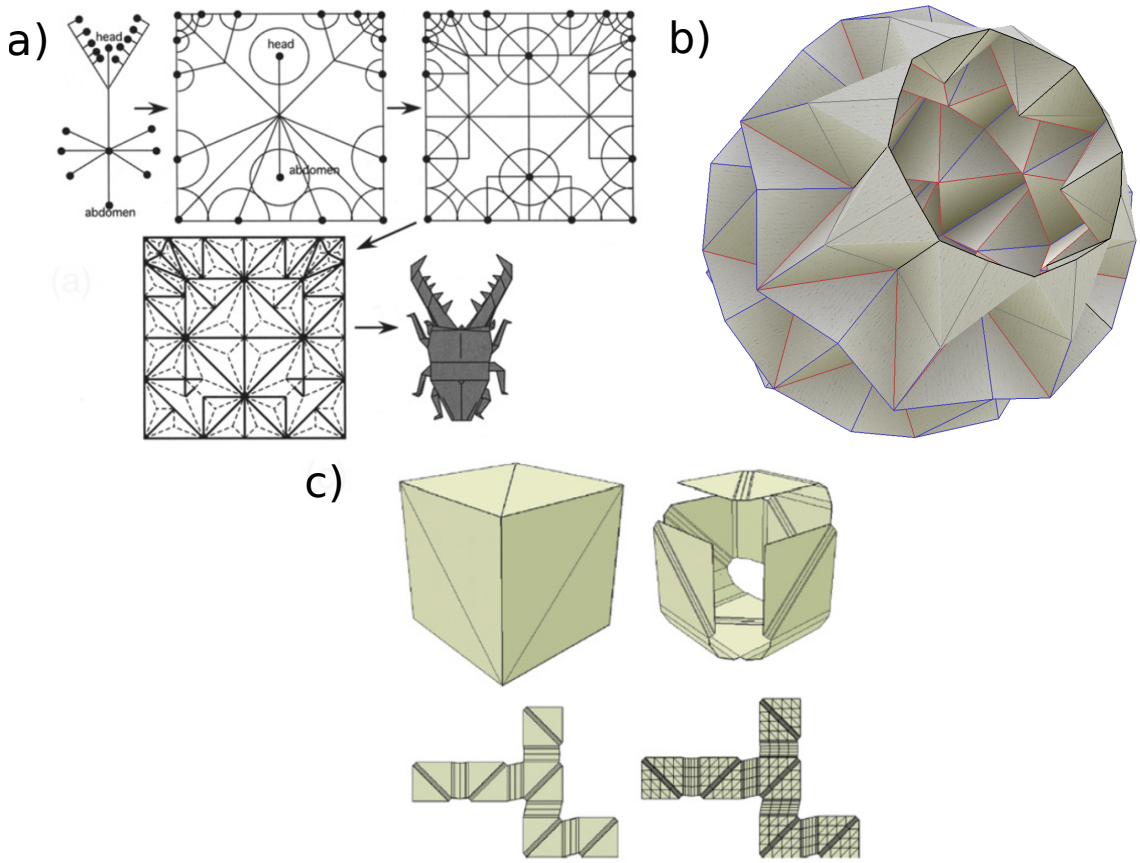

FIGURE 1.20: Examples of origami design tools: a) Illustration of the tree algorithm using one of Meguros bugs [Lang, 2001], b) Lee's origami deformable wheel [Lee et al., 2013] folded using freeform software [Tachi, 2010a], c) procedure to obtain a single-panel unfolding from a cube: initial mesh, spanning tree, unfolding, and refinement for finite element analysis [Kuribayashi et al., 2006].

lations from given polyhedral surfaces. It contains two different steps; first, the faces of the desired shape are separated, then folding patterns are inserted between them. The produced shape is then modified by satisfying geometric constraints such as developability (a surface is developable if it has zero Gaussian curvature everywhere [Mancewicz, 1992]), folding angle limitations, and self-intersections. The proposed method is applicable for paper as well as rigid foldable structures with limited foldability (folding angle less than 180°). In another work, Tachi developed an interactive simulation software for rigid origami designs [Tachi, 2009b]. The simulation program can display the gradual folding/unfolding process of an origami pattern by calculating the configuration of a given crease pattern for specific folding angles. The path of the folding is calculated by projecting the folding angles into the constrained configuration space.
Ida et *al.* introduced an origami computational interface called Eos [Ida et al., 2009,

Kasem et al., 2006, Ida et al., 2007, Kasem and Ida, 2008]. The interface allows the user to fold virtual sheets as if they were real paper. The process was enabled by the visualization and interaction with the origami models. Depending on the user's preference and his objective, Eos provides two different origami design methods: (i) the first, which is a mathematical folding method, is based on axiomatic definitions of origami folds [Ida et al., 2009, Huzita, 1989]; therefore, it requires a fair knowledge of nomenclature and coding definitions for different folding options; (ii) the second is an artistic folding method; as a result, it is more of a user-friendly method, where the user can define the folding lines, the orientation of the folds, as well as the values of the folding angles.
Akleman et *al.* proposed an origami algorithm for unfolding a given convex polygonal shape into a flat one-piece planar surface [Hernandez et al., 2013]. In order to guarantee the planarity of all the geometry's faces, the algorithm starts by triangulating (dividing the surface into triangles) the initial 3d shape. Next, a dual graph is created such that all the original faces are transformed into vertices, and all the original vertices are transformed into faces [Guibas and Stolfi, 1985]. The dual graph is a graph that consists of the edges and the vertices of the dual mesh. The spanning tree, which by definition is the tree that includes all vertices of a given graph [Weisstein, 2019], is then 2D thickened; consequently, a 3D shape that consists of a single panel is formed. The latter is then unfolded flat before conducting a re-meshing process, using a finer mesh (especially for the folding regions). Having a fine mesh is necessary to obtain more accurate results during a FE mechanical analysis of the folding motion. An example of the unfolding process of a cube using this algorithm is shown in Fig. 1.20.c.
Fuchi et *al.* [Fuchi and Diaz, 2013] proposed an origami design method based on topology optimization. In their work, the existence of a 2D origami pattern that includes folding lines as well as their type (mountain or valley) is assumed; while, folding angles are considered to be design variables. The assumed 2D pattern is known as the ground structure. Once the ground structure and the folding angles are defined, the corresponding 3D configuration can be computed using similar origami methods discussed here. Lastly, a topology optimization method is used in an iterative effort to find the optimal set of folding angles that, coupled with the ground structure, can generate the desired 3D origami shape.

1.5 Actuation systems

1.5.1 Self-folding origami devices

Self-folding is a rather significant part of origami structures; therefore, we cannot talk about origami structures without mentioning the self-folding. There are many kinds of self-folding techniques and methods, such as heat-induced, light-induced, and electric field-induced techniques. Some of them are presented in this section.

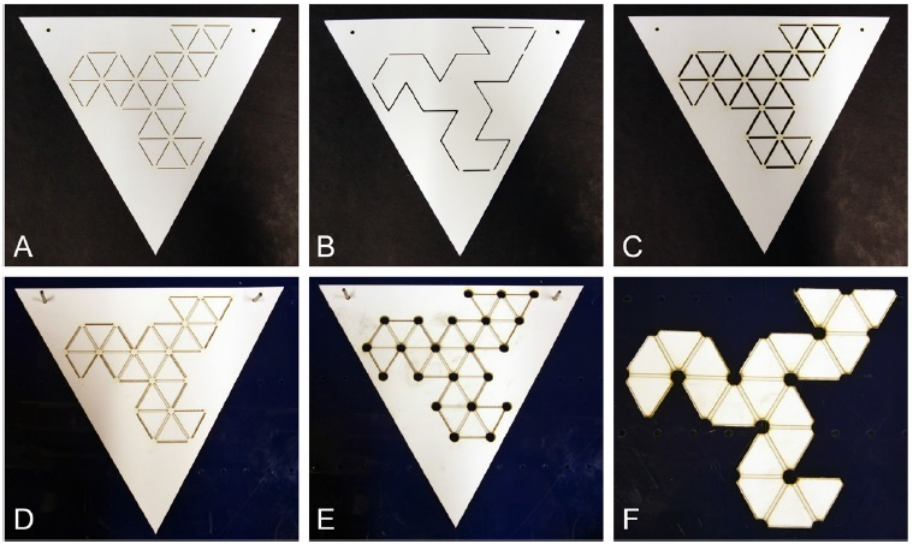

FIGURE 1.21: Fabrication process of a heat-induced self-folding composite. Three different layers were patterned using CO_2 laser machine. (A) A bottom structural layer, (B) a shape memory polymer layer, (C) a top structural layer. (D) The three layers were aligned together using pins and adhered with double-sided silicone tape. (E) The contour around the pattern was also laser cutter, leaving only (F) the final shape of the self-folding composite [Tolley et al., 2014].

1.5.1.1 Heat-induced self-folding

An authentic example of this technique is the work of [Tolley et al., 2014] regarding the development of self-folding origami, by using a shape memory composite activated by uniform heating. To meet that objective, a Shape Memory Polymer (SMP) sandwiched between two structural layers, which are made of paper, was used. The fabrication process starts by creating the pattern on each layer separately. Using a CO2 laser cutter, the whole pattern was created in the top and bottom structural layers, with just one difference, the width of the cut, in the top layer was considerably larger than the one in the bottom layer. Then, using pinholes, which were carefully made in each layer during the laser cutting, the tree layers were aligned and adhered together with double-sided silicone tape, and the result is, a three-layered laminate (a top structural layer, a bottom structural layer and in the middle the SMP layer). Finally, the laminate was cut in the appropriate shape also using the laser cutter in order to give the outer shape of the devices, and also, holes in the intersections (where more than two folding lines meet) were made, to make the folding process easier (see Fig. 1.21). After the fabrication of the laminate, uniform heating is required, to active the self-folding process. Heating the laminate in the oven, causes the SMP layer to contract, which results in the bending of the laminate towards the top side. The wide gap created in the top layer during the laser cutting is what makes the bending goes towards the top side (as shown in Fig. 1.22). Moreover, the gap acts also as a mechanical stop for the bend, when the

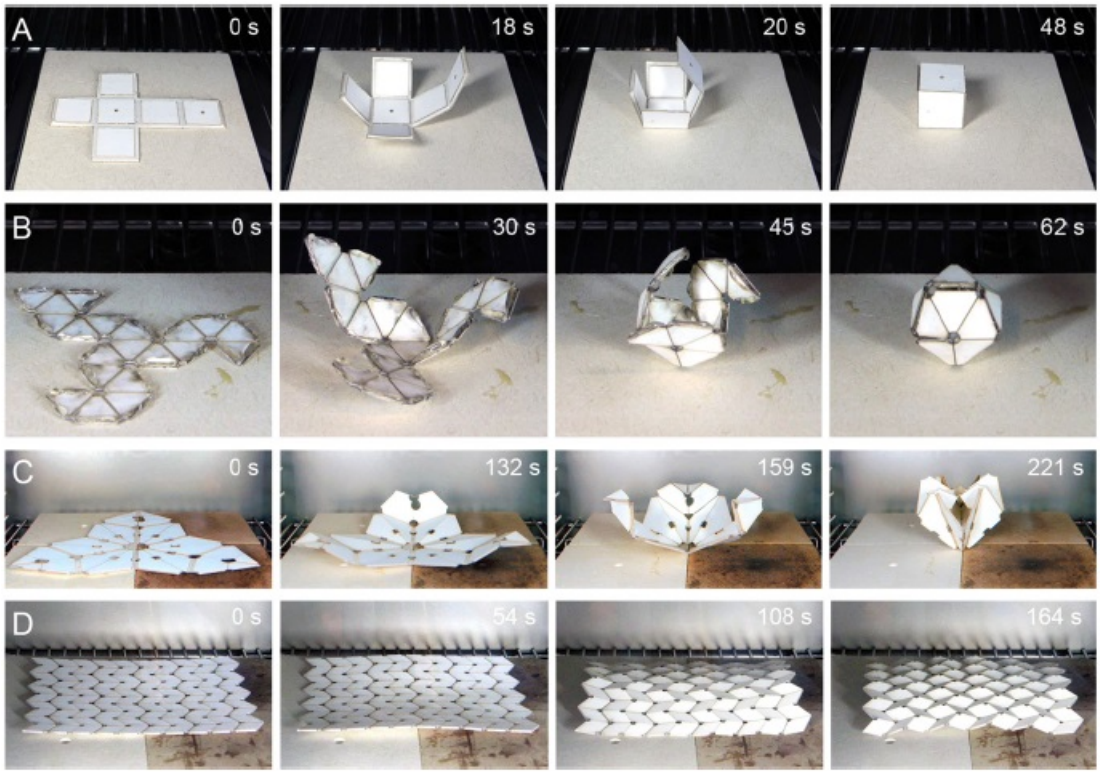

FIGURE 1.22: Experimental results of self-folding composite with different origami patterns. The image sequences represent the development during the self-folding process of (A) cube, (B) icosahdron, and (D) Miura pattern. In all the experiments, a self-folding composite with a different pattern was inserted into a preheated oven to 130 °C. The time elapsed indicating the progress of the folding since the start of the experiment is marked in the lower-right corner of each frame [Tolley et al., 2014].

two edges of the gap meet the bending stops. In other words, the direction and the angle of the bend are both controlled by the gap. There are other examples [Miyashita et al., 2014, Miyashita et al., 2013, Yasu and Inami, 2012] in the literature, which are using the same principles as the example discussed above. However, even though it is a straightforward and practical process that only needs cheap materials and equipment, it still has some limitations, such as:

- the uniform heating of an object is sometimes easier said than done, which makes triggering the folding very challenging, thus leading to an undesired outcome (undesired final shape),
- the more complicated is the final shape of the laminate, the more likely to have an incomplete fold,

FIGURE 1.23: Self-folding crane using an electric field induced technique. The device starts as a flat composite containing several layers: structural layers, shape memory polymer layer, and a copper circuit etched onto a polyimide layer. The self-folding of the device caused by joule heating requires three minutes in order to reach the fully folded state [Felton et al., 2013b].

- the maximum angle that can be reached by the self-folding process is limited to 139°. After this point, the contraction of the SMP layer is not sufficient enough to bring the two edges of the gap together,
- holes in the laminate are used to facilitate the bending process, which makes creating a closed structure infeasible (a closed cavity for example).

1.5.1.2 Electric field-induced self-folding

Now, the electric field induced technique; they generally use heat triggered smart materials, such as SMP which are stimulated via joule heating. One example of this technique is the work of Felton et al [Felton et al., 2013a, Felton et al., 2013b] on self-folding with shape memory composites (as shown in Fig. 1.23). The proposed concept here is similar to that discussed above, where several layers (structural layers and active layer SMP) are laser patterned then align glue together using pins and silicone tape, before finally laser cutting the outer shape of the full composite. However, the key difference, in this case, is the newly added layer made of copper-polyimide. The latter is a resistive circuit that provides localized stimulus via joule heating; thus, unlike uniform global heating, a local and sequential folding can be achieved. The pattern of the copper-polyimide circuit was obtained using standard lithography and etching techniques. A $0.5mm$ wide and $18\mu m$

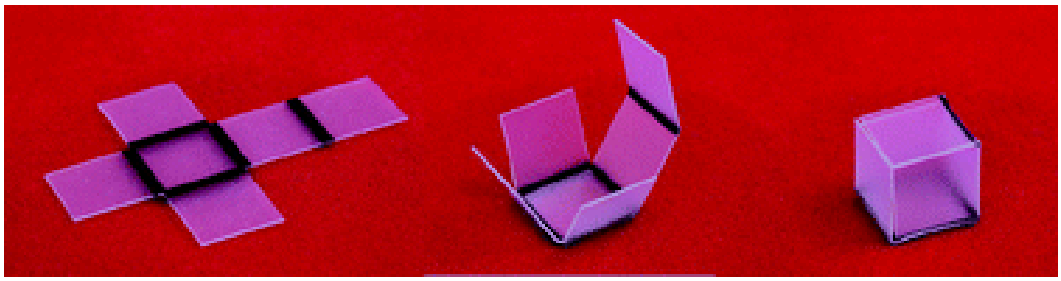

FIGURE 1.24: A depiction of the folding action of a cube using a light-induced technique. The predefined inked regions can absorb light which causes these regions to relax and shrink, thus resulting in a folding motion [Liu et al., 2012].

thick copper trace with a serpentine pattern was used, in order to maximize the joule effect. The pattern was etched onto a $12\mu m$ thick polyimide sheet.

1.5.1.3 Light-induced self-folding

Another technique to active the self-folding of origami structures consists of using light as a stimulus. Liu et *al.* discussed this technique in a couple of their works. In their first work [Liu et al., 2012] proposed a novel and simple approach based on the use of unfocused light in order to self-fold a thin sheet of polymer (as shown in Fig. 1.24). The latter is an optically transparent, pre-strained SMP that shrinks in-plane during uniform heating. A black ink pattern is printed on both sides of the sheet to provide a localized absorption of light, thus, leading to localized heating of the SMP to temperatures above its glass transition. At these temperatures, the predefined folding lines (black ink lines) shrink, and as a result, the self-folding is achieved. In other words, the black ink pattern defines the locations of the folding, and the side on which the pattern is printed determines the direction of the folding.
In a similar work [Liu et al., 2014] replaced the unfocused light source with laser light. The latter allows for localized irradiation of the SMP sheet; hence, no pre-patterning of the polymer sheet is required. Instead, the sheet is covered in black ink on both sides. The ink, as disclosed before, will allow the absorption of the light. Therefore, the photon energy is converted into thermal energy in the light targeted area; the surface of the sheet reaches the highest temperature, and it gradually decreases throughout its thickness. This temperature gradient induces a strain relaxation gradient through the depth of polymer; as a result, the folding is achieved within a few seconds of irradiation. Utilizing lasers enables precise control over the location of the folds and the angle of the folding, which depends on the power, intensity, and the pattern (width and shape) of the light. As for the direction of the folds, it only hinges on which side of the polymer sheet is under irradiation.
In more recent work [Liu et al., 2017b], following their first example, they used an ink patterned pre-strain SMP sheets, coupled with an unfocused light source, only this time they used a colored ink. By doing so, they were able to achieve a sequential self-folding

of the polymer sheet. Meaning that, depending on the color of the hinges (folding lines) and the used wavelength of the light, the order of folding can be controlled. This type of control was enabled by the fact that colors absorb light in a discriminatory fashion. Being able to not only program a polymer sheet spatially but also temporally makes the generation of complex shapes for numerous applications easily feasible.

1.5.1.4 Comparison between the different self-folding techniques

In this subsection we have presented three different techniques to accomplish self-folding for automated fabrication: heat induced technique, electric field induced technique, and light induced technique. All of these technique allow for a fast and low-cost production of self-folding devices. However, depending on the shape, size, targeted application and available infrastructure, one technique can be more suitable than the others. That is why Tolley et *al.* [Tolley et al., 2013] compared the three mentioned techniques. They fabricated a common structure (a cube) using each technique, and tested folding behavior of the structure in each case. The results of their tests are shown in Tab. 1.1.

TABLE 1.1: Comparison of the self-folding techniques [Tolley et al., 2013].

Technique	***Heat induced technique***	***Electric field induced technique***	***Light induced technique***
Infrastructure required	Oven	Power supply	Oven and IR light
Number of laminate layers	3	3[a]	2[b]
Cube assembly time	48 s	2 min 15 s	1 min 15 s
Cube completion	Very good	Good[c]	Poor
Achievable angle range	$0 - 140°$	$0 - 140°$	$0 - 40°$
Angle repeatability	Very good	Good	Poor
Sequential Folding	No	Yes	Yes
Concave Structures	Yes	Yes	No

[a]Four layers required for bidirectional folding.
[b]In general, three layers required for bidirectional folding.
[c]Some manual assistance was required.

1.5.2 Shape-shifting origami devices

Unlike the self-folding devices that go from a passive state toward an active state, shape-shifting devices are able to not only self fold but have multiple shapes with multiple functionalities as well. In other words, shape-shifting is when the folding is reversible and controllable, and depending on the desired shape the degree of folding can be changed in real time. Some of them can even change their way of being folded which makes them also reprogrammable.

One example of shape-shifting devices are the work of Hawkes et *al.* [Hawkes et al., 2010]

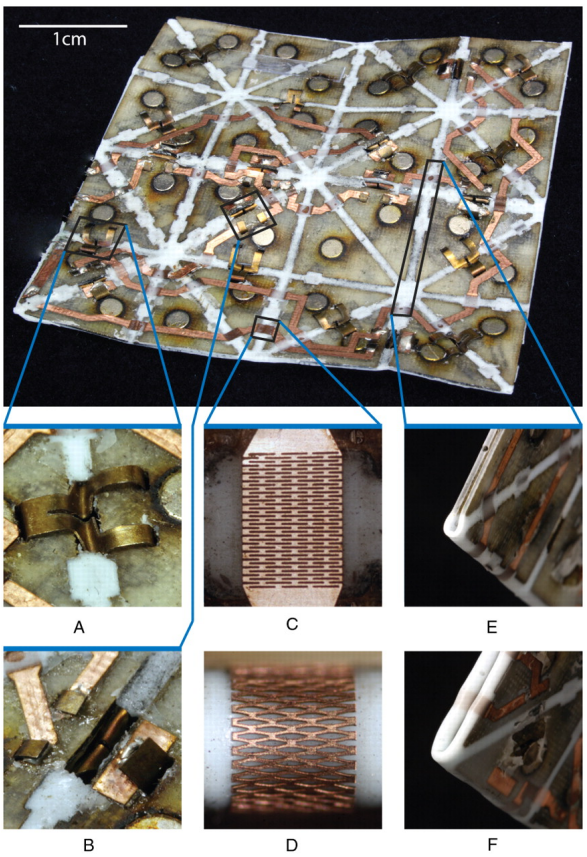

FIGURE 1.25: Shape-shifting programmable sheet that can achieve two distinct shapes: a "paper airplane" and a "boat". The folding motion is provided by shape memory alloy actuators that are stapled to the (A) top and (B) bottom of the sheet. Patterned copper traces used for electrical contact are shown cross the folding lines (C) unstretched and (D) stretched. The folding lines (E) after a single 180° fold (two layers thick) and (F) a couple of 180° folds (four layers thick) [Hawkes et al., 2010].

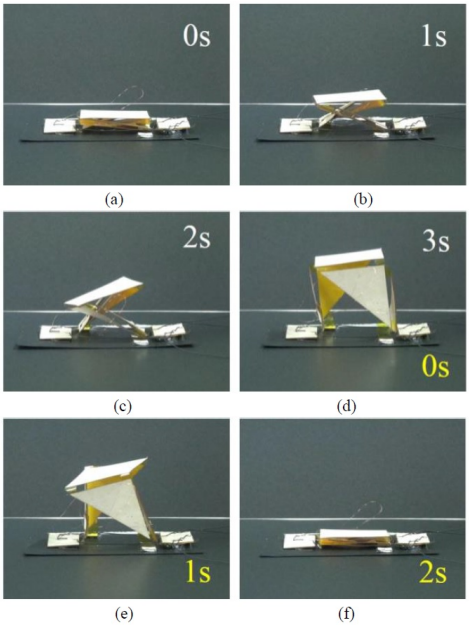

FIGURE 1.26: A depiction of the folding/unfolding action of a single module transformation. It takes three seconds to go from (a-c) flat to a cubic shape and two seconds from (d-f) a cubic shape to the flat state again [Kim et al., 2016].

entitled programmable matter by folding. Past attempts to create transforming devices were limited by size requirements (miniaturization), the high number of components, and the major complexity caused by the communication among the units. In order to avoid such limitations, they adopted origami engineering principles (as shown in Fig. 1.25). Their concept consists of a 2D sheet with a universal origami pattern; it contains 32 rigid triangular sections connected with soft material (silicone). It also has an embedded actuation system based on SMA units that can achieve folds of 180°. Traces of copper are added to the sheet in order to connect the actuation system with the power supply. The traces have a unique pattern (an origami-inspired pattern) across the folding lines (silicone) which allows them to be stretchable during the folding action. Finally, magnets are utilized in order to lock in place the device, in the folding state. Differently put, when an electric field is applied, the joule-heated SMA bending actuators will fold the activated regions, then the magnets embedded inside the sheet-like device will hold them in place. A sequential folding can be accomplished since the SMA actuators can be activated separately. Different origami structures were achieved, such as a boat and a paper airplane. However, it should be noted that after each activation; thus, folding of the device, manual unfolding is required.

The second example of shape-shifting is the work of Kim [Kim et al., 2016] regarding their fast, lightweight, and compact device composed of multiple self-folding origami modules. The proposed system can realize numerous configurations thanks to its properly arranged and identical transformable units. The latter is origami modules that can

transform their shape from a flat shape to a cubic one and vice versa, in the same manner as a three-dimensional (3D) morphing pixel (as shown in Fig. 1.26). By activating the appropriate modules, the desired shape can be obtained. The design of each module is based on a modified Kresling pattern. The latter can maintain its bi-stability during the folded and unfolded states without any help for an actuator. Furthermore, it can be deployed and reverted to its original shape in a matter of seconds thanks to a well-positioned low-profile torsional SMA wire actuators. This work is a hybrid approach that couples the modular and folding approaches in order to accomplish shape-shifting without any need for a complicated communication system between modules or bulky infrastructure. Instead, it has a compact, fast, and lightweight hardware. Moreover, as a demonstration, a 3×3 matrix system of this module was utilized (with a side length of $40mm$). This matrix can realize five different shapes. It only needs 15 seconds to transform from one shape to another. Even though the modules in the demonstrator are still relatively large, and the matrix is also relatively simple; however, this concept has much potential for various applications that require shape-shifting systems such as a morphing 3D map.

1.6 Summary of the state of the art

This section provides a summary of the state of the art of origami engineering in general and origami-based active structures in particular (see Tab. 1.2). Although origami is an ancient art, it is still a relatively new engineering field, which has yet to prove its worthiness/effectiveness before making a complete crossover from just being an art to becoming a fully-fledged engineering field. Regardless of the high potential origami holds, the limitations of such a field regarding all of its different aspects, from design and analysis tools, adaptable fabrication processes, actuation systems to performance and design selection, are all also discussed in Tab. 1.2. In an attempt to address such limitations and improve the performances and capabilities of origami-based and origami-inspired devices for engineering applications, we proposed a full-cycle multi-step origami design methodology (chapter 2). The different steps of the methodology include the identification of the application requirements, selection of the appropriate origami base, 2D and 3D design, multi-physics modeling, selection of the fabrication technologies, integration of an actuation system, and subsequently control and experimental validation. A proof of concept of our proposed origami design methodology for a vibro-acoustic application is detailed in chapter 4l. Lastly, a new method based on polypyrrole EAP, which has the potential to improve the actuation of small-scale origami devices, is also investigated and discussed in this work (chapter 5).
Notwithstanding, all the challenges, difficulties, and obstacles the field of origami engineering is facing today, it offers unconventional and far-reaching alternative solutions that reach far beyond the realm of traditional engineering approaches.

TABLE 1.2: Summary of some of the advancement made in the field of origami engineering.

		References	Comments
Modeling and design tools	TreeMaker	[Lang, 2004]	Despite the existence of numerous origami theories, algorithms, and design tools, almost all of them are only useful for kinematic studies and zero thickness analysis of foldable structures. Studying and understanding thick origami structures as well as modeling their mechanical behavior, is still a highly challenging problem, which must be addressed in order to improve the performance and to widen the spectrum of applications of such devices.
	Oripa	[Mitani, 2005]	
	Origamizer	[Tachi, 2007, Tachi, 2010]	
	Freeform	[Tachi, 2010a, Tachi, 2010b]	
	Eos	[Ida et al., 2009, Kasem et al., 2006, Ida et al., 2007, Kasem and Ida, 2008]	
Fabrication	Laser machining	[Miyashita et al., 2015, Lee et al., 2014, Ranzani et al., 2017]	Rapid prototyping and advanced manufacturing technologies have dramatically improved the design and fabrication of complex structures, including origami structures. Nevertheless, there is a real need for origami oriented fabrication technologies, which take into account all of the related technical challenges; such as fabrication of self-contained monoblock structures that can be made from a wide range of materials with integrated actuation systems, embedded electronics, and sensors; origami devices that are production-ready, able to shape-shift, communicate, sense, and act.
	μfabrication	[Leong et al., 2009, Bassik et al., 2010]	
	3D printing	[Liu et al., 2017a]	
	Molding	[Li et al., 2019]	
Actuation	SMAs	[Kuribayashi et al., 2006, Hawkes et al., 2010, Kim et al., 2016]	The compactness and inherent compliance of origami structures allow for a more natural and efficient integration of smart materials as actuation systems. That said, origami devices are as performant as their actuation systems. For instance, SMAs and SMPs (commonly used materials for origami devices) are not reversible and require the use of an external force, to regain the initial shape. Moreover, DEs are reversible, but they necessitate very high voltages which represent an unnecessarily high risk in some applications (biomedical, one of the main targeted application).
	SMPs	[Miyashita et al., 2014, Miyashita et al., 2013, Yasu and Inami, 2012]	
	DEs	[Ahmed et al., 2014]	
Applications	Acoustics	[Cambonie and Gourdon, 2018, Fang et al., 2018]	Even though there are several application examples of origami-based devices that serve a variety of purposes, the lack of proper origami approaches, which are performance-driven rather than shape-driven raises significant problems for engineers. For instance, there are many origami methodologies, approaches, and software that can determine the appropriate crease pattern and folding sequence in order to achieve a particular 3D shape; however, origami engineering applications are often more motivated by the performance of the origami device in the targeted field rather than simply by the ability of such device to achieve a specific folded shape.
	Biomedical	[Kuribayashi et al., 2006, Leong et al., 2009, Miyashita et al., 2016]	
	Electronics	[Song et al., 2014, Li et al., 2015]	
	Robotics	[Onal et al., 2011, Lee et al., 2014]	
	Space	[Miura, 1994, Lang, 2015]	

Inspired by the art and theory of origami, this field can take full advantage of active material technologies in order to produce genuine multi-functionality smart structures with on-demand properties and outstanding performance that can not be matched using traditional active structures. Origami-based active structures will allow engineers and researchers to address open issues posed and provide new technological solutions to the world at large.

1.7 Conclusion

The oriental art form, known as origami, is currently finding many engineering applications. This chapter described the fundamentals of origami, its numerous fields of applications as well as its different types of deployment. Although, applying origami mathematics in engineering is still a very limited concept at this point, the rapid expansion of the field has led to the development of various algorithms, which can be used in order to define the principles and limits of origami folding/unfolding, also serve as a guideline for all future origami approaches and applications. A vast area of applications has been explored, such as aerospace, biomedical devices, energy storage devices, electronics, packaging, manufacturing, robotics, core structures, vibro-acoustics, and architecture.

The high interest in origami research and engineering lately, was established by the fact that origami devices are easily made and affordable 3D structure that can be generated from a simple 2D design. Therefore, such a structure is very energy efficient, consumes less material than regular devices, and does not occupy as much space. Moreover, because of those reasons, these origami devices are becoming more and more desirable every day, for engineers and scientists from various scientific fields. Ongoing research and development in these engineering fields are improving the performance and characteristics of origami-based devices, such as improving the folding/unfolding efficiency. Moreover, innovation is paving the way for better origami devices with higher capabilities and usefulness.

Chapter 2

Proposed origami design methodology

"The greatest enemy of knowledge is not ignorance, it is the illusion of knowledge."
-Stephen Hawking

Contents

This chapter introduces our original methodology for the design of origami-based active structures. The methodology contains several steps: it starts by defining the application requirements, the selection of a suitable origami base, the design of the structures both in 2D and 3D, the multi-physics modeling, the selection of suitable fabrication technologies, the integration of actuator system, experimental validation, and finally control.

2.1 Introduction

The traditional Japanese art of paper folding, which is also known as origami, has long attracted the attention of various fields such as design, education, and mathematics. Many engineers today are using this oriental art to solve problems. For example, it can be an inspiration to some architectural designs, robot design, or MEMS processes. Moreover, a few researchers are analyzing their characteristics to design and utilize some patterns as mechanical components. Folding as property can be regarded as a great asset when space constraints are very high, and it also can be utilized to create compactly stowed devices that transform into 3D structures with variable functionalities. Origami mechanisms can be programmed to change shapes, functionalities, and properties (see chapter 1). Thanks to the advances in computer science and mathematics, more complex shapes and folding/unfolding algorithms can be used in order to explore a wide variety of applications in the fields of science, technology, and engineering.
Furthermore, researchers have also demonstrated self-folding and shape-shifting behaviors (see chapter 1) with different applied stimulus such as thermal, electrical, optical, chemical, and magnetic. A high number of combinations regarding the choice of geometry, material, and applied stimuli are feasible, yielding a multitude of design options. In order to narrow down the options and propose useful origami design methodologies and approaches, several considerations must be taken into account, such as whether folds should be reversible, limitations of choice of an actuation system, restrictions caused by sheet thickness, boundary conditions, and the overall shape of the origami structure. An evaluation of the origami mechanisms and devices proposed by literature for various folding concepts shows that there is no dominant actuation system or mechanism for origami applications and that design and material selection depends on the application requirements (such as the desired folding radii or angle, the size of the device, work environment). Additionally, despite the extensive research on origami principles and foldable structures, multiple challenges and unanswered questions remain. A couple of which are of high importance in the field of engineering origami:

- Performance-driven design of origami-based systems: traditionally, as an art form and as a mathematical field of study, the theme of origami has only entertained shape and form (geometric) considerations. For example, there is numerous origami software that allows the determination of the crease pattern and the folding sequence in order to generate a certain 3D shape. Nonetheless, engineering applications are more often motivated by the performance of the device in a certain field (e.g., biomedical, robotics, electronics, energy storage, optics, and vibro-acoustics) rather than only achieving a certain shape. Therefore, origami design, fabrication, and optimization need to be a performance-driven process in order to improve the properties and expand the capabilities of such devices in solving delicate as well as complex engineering problems.

- Increased understanding of the kinetostatic of folding in origami structures: despite the existence of multiple origami theories and software, only a few of them focus on the analysis and design of non-zero thickness origami structure, and even

fewer that treat the kinetostatic behavior of such structures. Needless to say that understanding the kinematics of zero thickness origami structures is important for the development and expansion of the field of origami engineering. However, the fact remains that without a higher understanding of the mechanics of non-zero thickness structures (e.g., placement and value of the applied forces in order to generate the desired fold and the possible maximum and minimum states of folds) the development of origami devices that can treat real-life engineering problems remains highly challenging if not near impossible.

In this chapter, we propose a method for designing origami-based active structures. The latter is composed of several steps (as shown in Fig. 2.1). The method, if applied correctly, ensures the determination of different parameters and design parts of the origami devices as well as achieving the performance expected from the devices and specified by the application requirements.
Generally speaking, it contains two cycles; a small cycle includes a numerical validation of the desired properties. First, by using the application requirements as a guideline, an origami base that appropriately represents the expected performance is selected. The latter is then used as a basic unit in order to generate a 2D origami design (flat passive state), followed by a 3D origami design (folded active state). Once the 3D origami design is constructed, a multi-physics FE model is used to evaluate the performance of the origami device and compared the results with the application requirements. While improving the chosen origami design, this cycle is then repeated as many times as needed until the desired performance is reached. Next, when the desired performance is reached, we move on to the bigger cycle of the method. This cycle involves the experimental validation of the origami device properties in the targeted application field (e.g., electronics, optics, vibro-acoustics, robotics, bio-medical). It starts with the fabrication of the origami device, by using one of the explored techniques: a 2D fabrication technique that utilizes the previously generated 2D design or a 3D fabrication technique enabled by the 3D design. Each technique has its advantages and limitations (see Sec. 2.6), which can be used in order to determine which one is better suited for a specific application. Then, using the results provided by the FE model of the kinetostatic behavior of the origami device such as the value and the placement of the required forces to achieve the fold/unfold motion, the integration if the actuation system is conducted. Finally, a characterization of the experimental performance of the device is conducted.
This chapter describes the proposed method and all of its steps in detail. Starting with application requirements of origami devices. It discusses the used guideline for choosing an origami base. Next, the generation of origami design is introduced in both its states, 2D and 3D. Thereafter, the 3D multi-physics FE model of origami is established. Then, both explored origami fabrication techniques are detailed. Finally, we conclude on the methodology.

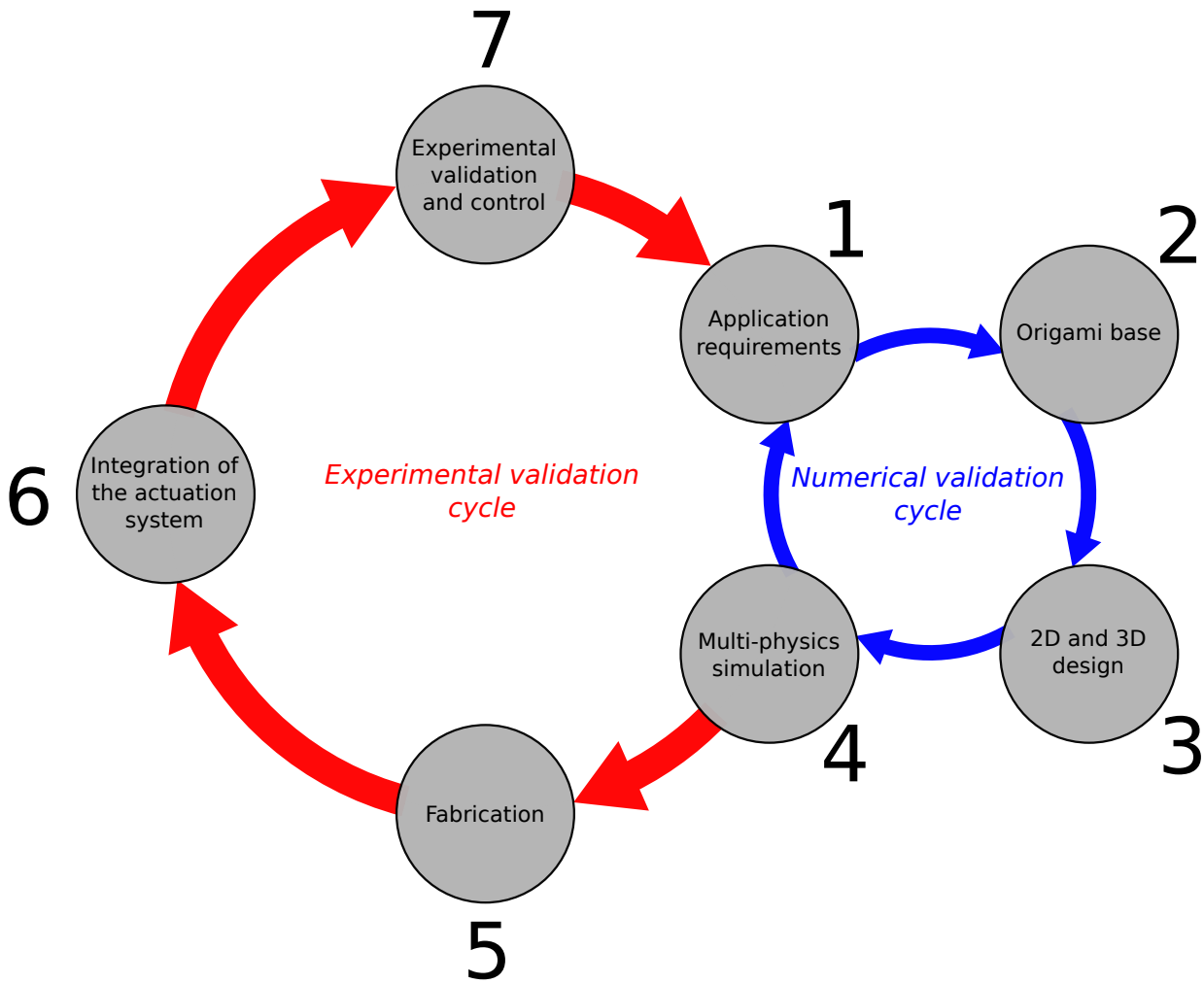

FIGURE 2.1: Diagram of the proposed origami design methodology.

2.2 Application requirements

The first step in this methodology is to define the application requirements. Depending on the application, origami structures can offer exceptional characteristics and functionalities which can not be matched by using other (traditional) structures. As an example, in the aerospace field, where fuel consumption and space requirements are crucial, sending big as possible objects in a small as possible packages is always a priority; hence, origami engineering can be very beneficial. In the biomedical field, besides the fact that origami engineering is very interesting for medical devices, for the apparent advantage of size reduction as well, which makes navigating the human body feasible, there are also other advantages. The monolithic origami design makes it easily scalable in order to accommodate a wide range of medical procedures. Furthermore, the planar nature of such design tends to make the manufacturing process inexpensive. Unlike classical medical devices, these designs drastically reduce part count, cost to produce, and could be disposable; therefore, it reduces also the operating costs, since no sterilization fees are needed. As for the robotics field, using origami engineering is a trade-off between the best characteristics of both robotics worlds, rigid (classic) robotics, and soft robotics. In other words, origami robots can be precise and support high loads like rigid robots, and at the same time, they can be as dexterous and flexible as soft robots. Moreover, origami robots have the potential to benefit from smart materials (SMA, SMP, EAP...) integration. The latter would provide a self-contained actuation system for such robots.

2.3 Origami base

The second step of the methodology is the selection of the right origami base that has the potential to accommodate all or most of the application requirements. All of the bases accomplish the primary advantage of origami engineering, which is space requirement reduction. Nonetheless, different bases have additional different advantages. For example, some origami bases allow movements in particular directions and not in others, and/or they can support high loads in one or more directions and not in others. Some bases also have the ability to create auxetic structures (structures with negative Poisson coefficient), which can be very interesting in the case of volume and size variation. Selecting the appropriate origami base is a crucial step since the performance of the full origami structure is directly linked to the performance of the origami base, in the desired field of application. A list of the commonly used origami bases/patterns is available in Tab. 2.1.

TABLE 2.1: Some of the commonly used origami bases/patterns in the literature

Origami base/-pattern	Properties	Applications	Reference
Waterbomb (see Fig. 2.2.a)	Offers the origami structure an auxetic property (structures with negative Poisson coefficient); therefore, such structures can increase their radius and length simultaneously, and vice versa	Origami stent grafts, deformable robot wheel, soft origami gripper	[Kuribayashi-Shigetomi and Takeuchi, 2011, Lee et al., 2013, Lee et al., 2014, Li et al., 2019]
Flasher (see Fig. 2.2.b)	It can transform a flat disc with a high surface area, to a relatively small cylinder with a diameter, which is only a fraction of the initial disc.	Solar array, intracardiac magnetic resonance imaging	[Landau, 2014, Taylor et al., 2016]
Accordion (see Fig. 2.2.c)	An extensive longitudinal growth, with a relatively weak resistance to normal loads, and high resistance to torsional loads	Self-folding miniature electric devices, cover of the X-ray shroud arm, deployable shelters, origami Antenna	[Miyashita et al., 2014, Varrasi, 2014, Thrall and Quaglia, 2014, Yao et al., 2014]
Kresling (see Fig. 2.2.d)	An extensive longitudinal growth, with relatively high resistance to normal loads, and weak resistance to torsional loads	Robotic wheel, 3D morphing system, robotic arm	[Miyashita et al., 2013, Kim et al., 2016, Liu et al., 2018]
Yoshimura (see Fig. 2.2.e)	An extensive longitudinal growth, with a relatively weak resistance to normal loads, and high resistance to torsional loads	Deployable shelters	[Norman and Arjomandi, 2017]
Miura (see Fig. 2.2.f)	Transform a rectangular flat surface into a small flat surface with only a fraction of the initial surface area	Solar array	[Miura, 1994]
Tachi-Miura Polyhedron (see Fig. 2.2.g)	Transform a flat surface to a metamaterial structure with different resistance to normal loads depend on their derction	Expandable habitat	[Tachi and Miura, 2012, Morgan et al., 2016]

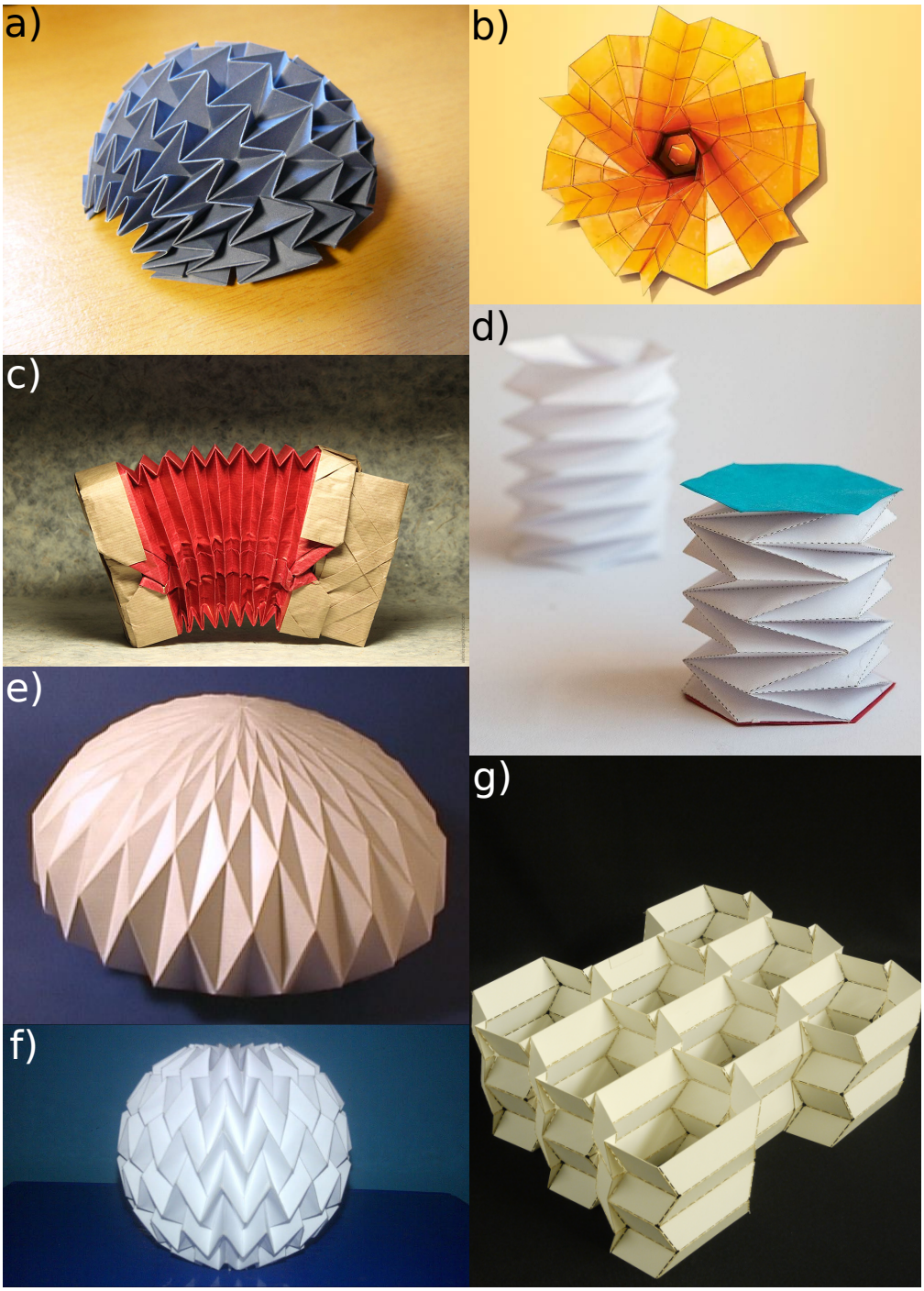

FIGURE 2.2: Some origami bases/patterns commonly used in the literature: (a) Waterbomb, (b) Flasher, (c) Accordion, (d) Kresling, (e) Yoshimura, (f) Miura, (g) Tachi-Miura Polyhedron.

2.4 Design

This section describes the different steps of the adopted origami design. Designing origami structures is quite different from designing traditional parts. The process contains a lot of steps: 2D design, 3D design, foldability testing (kinematical verification, with interaction between the facets), repairing and scaling, separation of the facets from the edges, giving the right thicknesses to both parts and finally assembly.

2.4.1 2D Design

Designing origami devices starts with defining the 2D pattern crease. The latter determines the locations of the folds and their orientation (mountain or valley folds). The 2D design could contain different parts and each part with a different objective. For example, some are used to allow the attachment of an external solid part, and others are used to allow and/or restrict movement in certain directions. There are several origami design software (see Sec. 1.4) that can be helpful during this step of the methodology; to name one, ***Oripa***[1] [Mitani, 2005], which is an open-source 2D origami design software. The latter is an intuitive drawing software dedicated for the design of origami crease patterns. With the help of a defined grid, the crease lines can be drawn, each with its appropriate color. Red and blue lines represent the mountain and valley folds, respectively. Black lines represent the edges of the paper (or the material being folded) or the cuts in the design. As for the grey lines, they are auxiliary lines, which their orientation of folding is already predetermined with the mountain and valley folds around them. After finishing the 2D design, ***Oripa*** can calculate the folded shape from the pattern. The calculation takes into account the colors of each line and considers every fold a flat fold (a 180° fold). The estimated folded shape can be displayed in many forms, such as an X-ray model, where the visible and hidden folding lines can be seen. it should be noted that any other software can be used for this step, as long as it is able the desired 2D pattern.
After designing the 2D origami pattern, the latter is exported for two reasons. First, to be utilized for the creation of a 2D origami prototype using 2D machining technologies (one option is laser machining), after some fine-tuning (appropriately scaling the design). Secondly, it is used as a starting point for the development of a 3D design of the desired origami structure. The 3D origami design is vital for our methodology since, on one hand, it is one of the improvements introduced by our methodology compared to most of the other origami methodologies, where the designing part ends with the 2D design. On the other hand, the 3D design can be helpful when it comes to better understanding the origami design, testing its foldability conducting FEM simulation, and numerically validating the application requirements (manufacturing conveniently an already folded prototypes).

[1] http://mitani.cs.tsukuba.ac.jp/oripa/

2.4.2 3D Design

As we mentioned above, one of the major and key defining parts of our methodology is designing in 3D the origami structures. In other words, designing origami structures in their fully functioning state. This will allow us to understand its behavior better, properly simulate its properties using FE modeling, numerically validate its characteristics, and even going as far as fabricating pre-folded origami devices. This part of the methodology contains several stages. The first stage is to fold the 2D design and to do so, we use other suitable origami design software, one of which is ***Freeform***[2]. The latter is free software created by Tachi from the University of Tokyo. The idea behind the software was to provide a tool that is able to create ***Freeform*** foldable structures that can imitate or rather approximate curved surfaces [Tachi, 2010b, Tachi, 2010a, Tachi, 2009a]. Differently put, a curved body such as a cylinder, for example, can be obtained from a rigid, flat, and foldable surface, just by folding. In addition to the generation of the folding pattern, the software allows the visualization of the origami model during the folding/unfolding process, which is, in this case, and unlike other origami design software, is done gradually. Moreover, this tool allows the user to vary the origami pattern in 3D in intuitive and simple manner, while respecting origami principles and other additional conditions inherent in the origami pattern and/or imposed by the user for a certain reason; for example a part of the origami pattern should not be moved because it will be attached to a rigid body. In order to realize the first stage of this designing step, the .dxf file exported from ***Oripa*** software is utilized. The file is imported to ***Freeform*** and visualized as a 2D origami pattern with different color lines: red, blue, gray and black for mountain folds, valley folds, auxiliary lines and the edges of the pattern, respectively. Next, the pattern is folded to the desired shape gradually using the red and blue lines as actuators. Afterward, the user-defined conditions are established (such as pinning in place some lines or stitching some vertex together). Once it is done, the user can examine the behavior of his design in its functioning state (3D), and test its foldability. For the next stage of this step, the folded origami pattern is exported as .obj file, then imported again into ***MeshLab***[3] software for further processing. ***MeshLab*** software is used in this case for five reasons:

- Merge close vertices (vertices that were previously stitched together in ***Freeform***), as they are redundant and serve no real purpose.
- Delete unwanted duplicated faces, as they also serve no real purpose.
- Scale the design properly to the desired size.
- Realign the design to the principal axis, so it can be easier to work with once import to a CAD software
- Convert the design file to a format that can be used by CAD software, such as .stl.

[2] http://origami.c.u-tokyo.ac.jp/~tachi/software/
[3] http://www.meshlab.net/

Furthermore, before importing the .stl file to CAD software for the finalization of the design, the file is first pretreated. Using the developed ***Matlab*** code, we first separate the edges (folding lines) from the facets. Then, we round the edges and insert opening in their intersections if we want to have a more durable design and to relieve high mechanical stress, thus, improve the folding/unfolding motion. Finally, we give our design (edges and facets) the desired thickness. This is very important for the fabrication step later on. An illustration of the rounding and thickening processes are shown in Fig. 2.3. The developed codes are:

Separation code: All the facets of the design undergo a size reduction while they maintain the same barycenter as the initial facets (they remain in the same location only with small user-defined size). Then the code produces two gemetries: (i) a geometry containing only the reduced facet as the rigid facets, and (ii) a geometry containing the difference between the initial geometry and the reduced size geometry, thus, the created geometry is the folding lines.

Thickening code: It permits the user to introduce thickness to a geometry, as shown in Fig. 2.3.(a-c).

Rounding code: It allows for replacing the sharp edges of geometries with rounded edges, also it introduce opening it the intersections of the folding lines, as shown in Fig. 2.3.(d-e).

In the CAD software, the two parts (facets and edges) are reassembled, and other parts are added if needed (as shown in the examples of Fig. 2.8). Some examples of the type of structures that can be designed using this process are presented in Fig. 2.4. Four different designs are shown: a fully closed capsule that can adapt its size (see Fig. 2.4.a), a closed cavity with an opening that can change its volume (see Fig. 2.4.b), a wheel with a varying diameter (see Fig. 2.4.c), and an origami cylinder with adaptable length, which can withstand normal loads (see Fig. 2.4.d). Each of the designs went through a separation, a rounding, and a thickening process, as discussed above.
It is worth mentioning that all the software named here are in no way relevant to the proposed origami design methodology in general nor to this step in particular. They are only named to help the reader better grasp all the aspects, features, and challenges of this step; thus, they can be replaced by any software or tools that can accomplish the same outcomes.

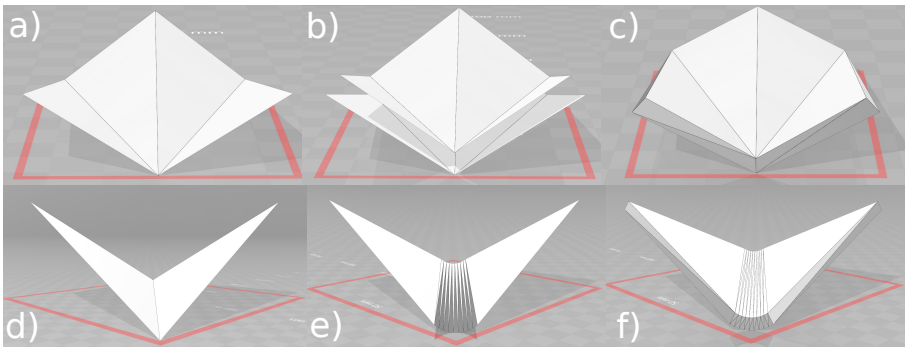

FIGURE 2.3: Illustration of the functionality of the developed origami codes. The thickening code can take (a) a folded half of a waterbomb, create (b) a similar shape at a desired distance (thickness), then (c) reconnect both shapes. The rounding code can replace (d) a folding line with (e) a rounded form, then (f) the thickening code can be utilized as well.

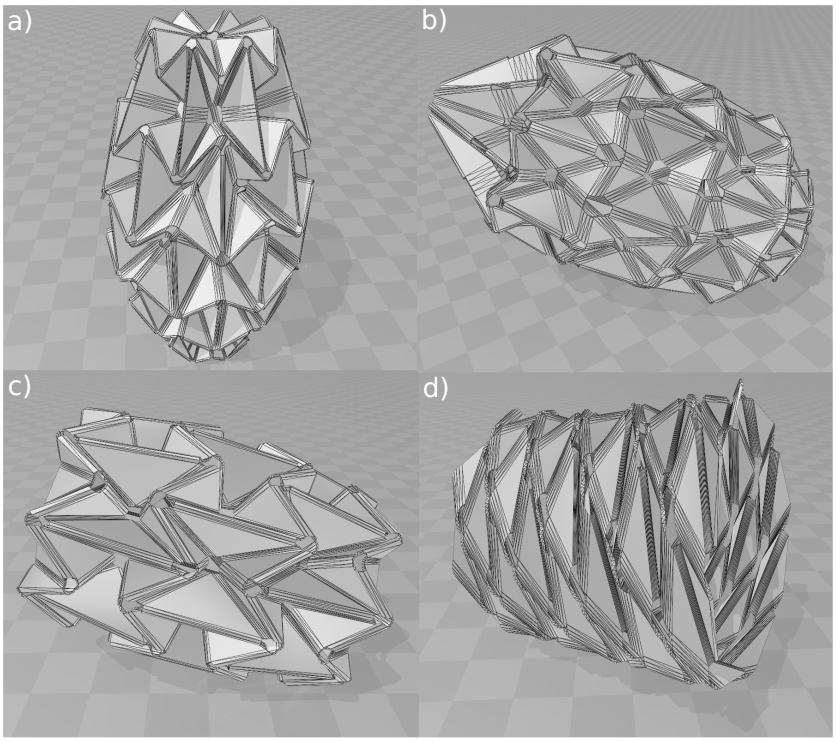

FIGURE 2.4: Few examples of the 3D designs created using our origami design methodology. (a) Adaptable capsule, (b) tunable cavity, (c) deformable wheel, and (d) adjustable cylinder. All the geometries started as 2D origami design on ***Oripa*** software; then they were folded into a 3D shape using ***Freeform*** software; next, they were adjusted using ***MeshLab*** and finally, by utilizing our origami ***Matlab*** codes the folding lines were separated from the facets and rounded, before giving thickness to the entire geometry.

2.5 Multi-physics FE modeling

In this step, the design files produced in the previous step are utilized. However, only the design as a surface (without adding thickness) is used, since 3D meshing thin thicknesses can be problematic for the FE model. Furthermore, regardless of the application (biomedical, vibro-acoustics, robotics, et cetera) we are targeting, all of them need to include kinetostatic and dynamic FE models during this step of the methodology. In the previous section, we were able to simulate the folding/unfolding behavior of the origami design using ***Freeform***. Nonetheless, as ***Freeform*** is based on a kinematic model, it is fairly limited on the amount of the information that we can extract from it (test the foldability of the design and find the maximum and minimum folding states). Therefore, kinetostatic and dynamic models are required. The models will be able to estimate the forces we need in order to actuate the origami device and where to apply those forces. Such information would provide valuable insights for the steps to come, such as the materials that should be used for the fabrication of the origami device and/or the selection of its actuation system. That said, more FE models should be created if the application requires it, as the main objective of this step is to validate the application requirements numerically. Otherwise, if the results of the FE modeling are not satisfactory, using those results as a reference, a new design should be made, by modifying different parameters, such as selecting a new origami base or changing its dimensions. This loop should be repeated until the results of the model are as expected. One advantage of using this methodology lies in the fact that changing/improving the origami design is easily feasible. Thus, after the FE model is created, finding the desired design that respects the application requirements should be attainable (iterative approach). However, this is not the case with regard to origami designs made by regular CAD software; changing/improving those designs can be extremely complicated and very time-consuming also, since they do not respect origami principles, their foldability is not guaranteed as well.

2.6 Fabrication

Now that we have the design that meets our needs, based on the results provided by the FE model, we need to fabricate the origami device. To do so, we have investigated two different techniques. Each technique has its advantages and drawbacks, and depending on the targeted application, the desired characteristics, and available equipment, one technique can be more suitable than the other. Furthermore, each technique follows a different philosophy and links to a proper strategy. The first technique can be defined as the *fabricate then fold technique* (2D fabrication technique), which has the same principles as the classic origami fabrication techniques. As for the second technique, we start with the folding then move on to the fabrication; thus, it is called the *fold then fabricate technique* (also known as 3D fabrication technique). Tab. 2.2 was created in order to compare the two techniques and understand better their advantages and limitations.

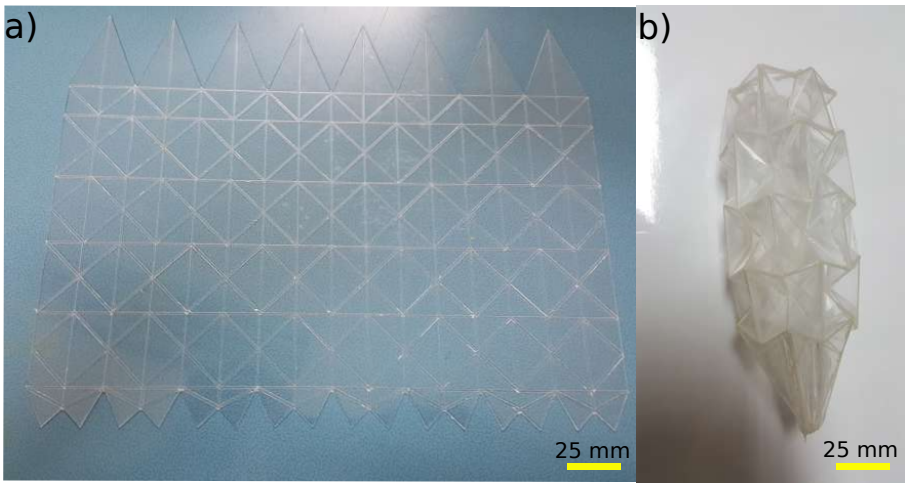

FIGURE 2.5: 2D fabrication technique using CNC machining. (a) Axpet sheet with 0.75 mm thickness patterned from both sides using a CNC machine then (b) manually folded.

2.6.1 2D fabrication technique

As mentioned in Tab. 2.2, each fabrication technique uses a different design strategy. The 2D fabrication technique needs only the 2D design, which at this point in our methodology was already generated using ***Oripa*** software and exported as .dxf file. It is essential to mention that even though we only use the 2D design in this case, designing the origami device in 3D is always required in order to build the FE model and numerically validate the application requirements. Before we settled on the laser cutter as the key equipment for the 2D fabrication step. We tried using a CNC machine as a tool to generate 2D origami designs (engrave the 2D origami design) on thin sheets of materials. An example of this process is the fabrication of an adaptable origami cavity, as shown in Fig. 2.5. However, the idea of using a CNC machine was dropped later on for several reasons. To mention some of those reasons:

- CNC machining thin sheets of material can be very challenging,
- Finding the appropriate material, that can be easily machined and have a high fatigue resistance, can be challenging as well,
- Utilizing specialized cutting tools is also required in this case,
- Aligning the two machined sides of the sheet can be fairly complicated.

Thus, among other reasons, we chose to adopt a laser cutter (a*Speedy300*[4] CO_2 laser cutter from *Trotec*), as our main tool for the 2D fabrication process. The first thing we did was to find the appropriate material for this kind of a process, and our search led us to Axpet sheets, which is the commercial name for thermoplastic polyester sheets.

[4] https://www.troteclaser.com/en/laser-machines/laser-engravers-speedy-series/

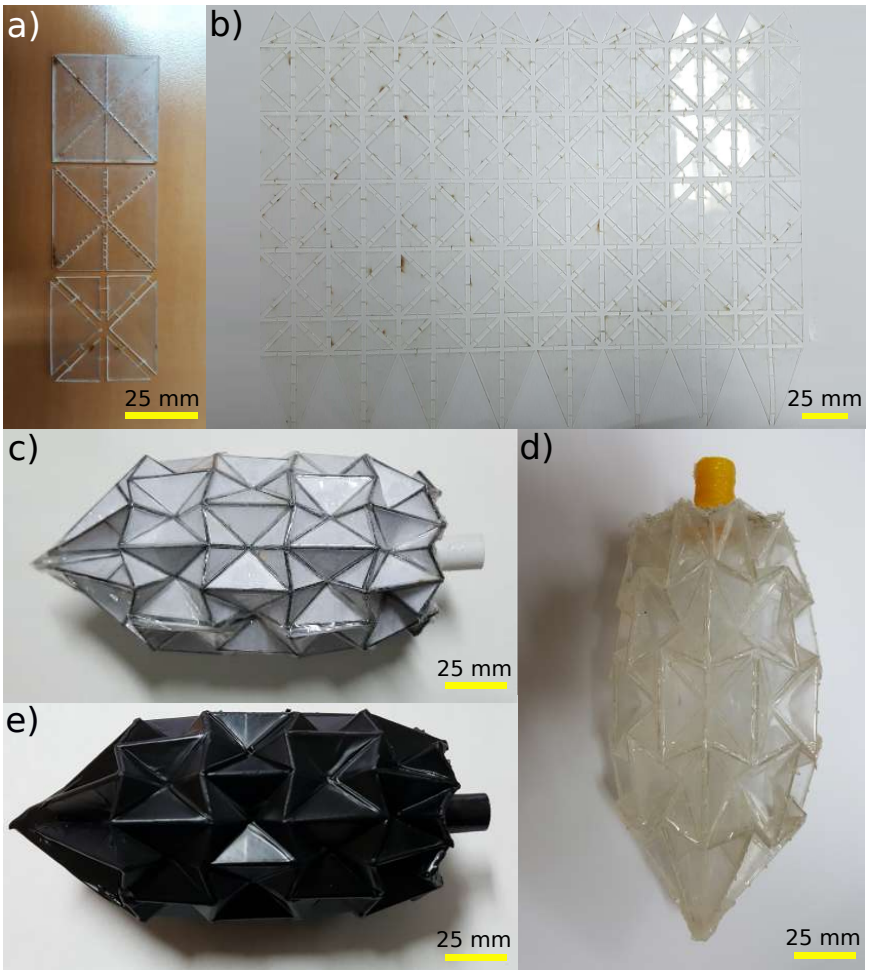

FIGURE 2.6: 2D fabrication technique using a laser cutter. An axpet sheet with 0.5 mm thickness was laser machined to (a) Waterbomb bases with different folding lines widths 0.2 mm, 0.8 mm and 2 mm form top to bottom, respectively, (b) a flat origami design with a 2 mm wide stitch-like pattern that was manually folded to 3D origami device. Several prototypes were made each with different reinforcement material (c) paper and clear thin film, (d) clear film only, and (e) clear film in addition to a rubber coating, which was added after the folding.

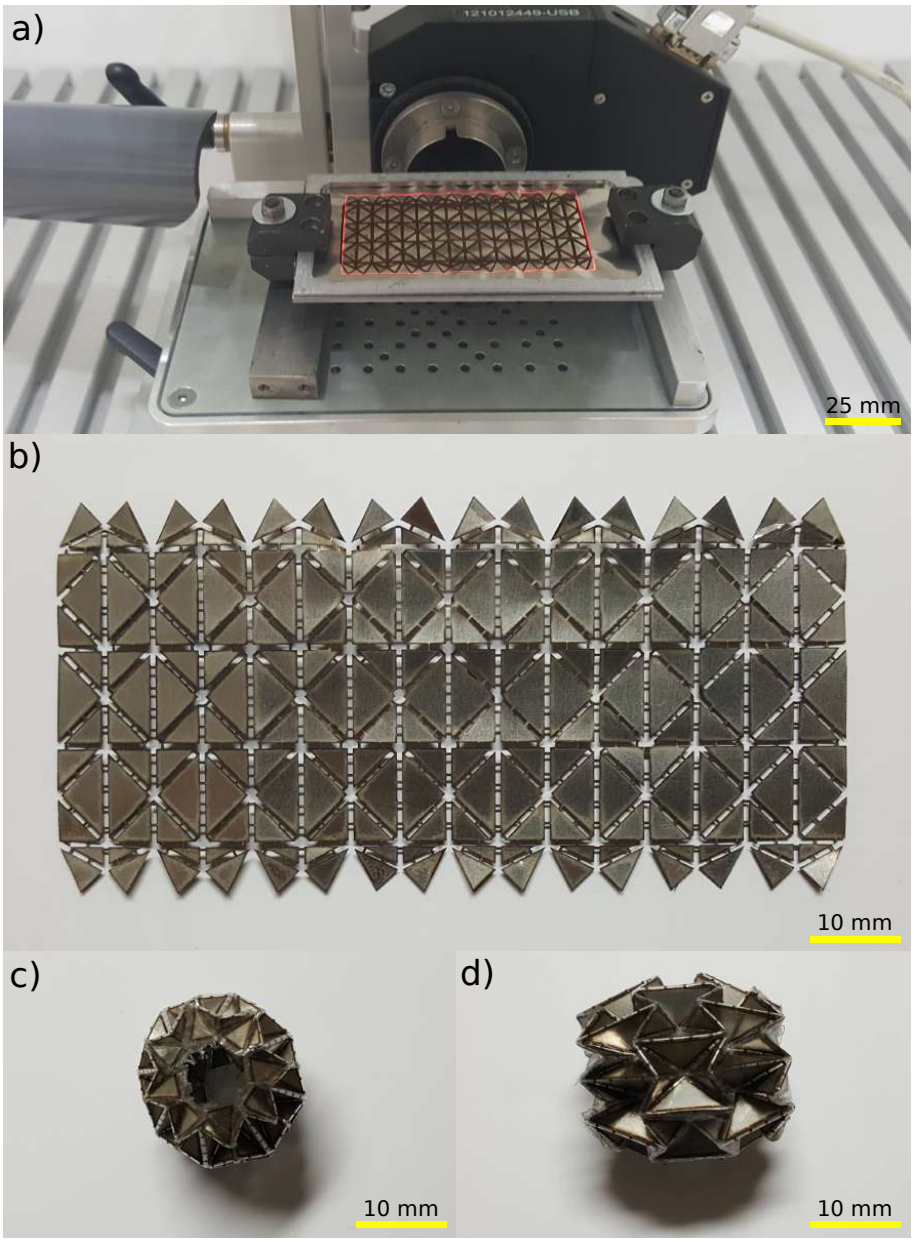

FIGURE 2.7: 2D fabrication technique using a laser cutter for milli-origami devices. a 0.6 mm wide stitch-like pattern of a magic wheel [Lee et al., 2013] was engraved on 100 μm sheet of stainless steel,(a) using a straightening support. The pattern was then cleaned (b) before being folded to a milli-magic wheel, (c) a top view and (d) a side view.

The latter are cost-effective, lightweight, have high fatigue resistance (high enough for this process), and, most importantly, can be laser machined. ***Inkscape***[5] software was used in order to fine-tune the 2D design (imported from the .dxf file generated by ***Oripa*** software) and to launch the laser machining of the sheet. Instead of engraving the sheets, we decided to cut the design in a stitch-like manner. This decision was made to avoid meeting some of the same challenges we faced while using the CNC machine. For instance, the alignment will still be very problematic in this case, as well. The stitch-like folding lines were cut with controlled thickness. In other words, instead of cutting in discontinued lines, consecutive small rectangles were cut to create a folding line (as shown in Fig. 2.6.a). The width of the rectangles (also known as the width of the folding lines) was given a value of at least twice the thickness of the sheet. The width was fixed at such values in order to make folding thick sheets of material, which completely different from paper folding, plausible. After the sheet was laser machined, the cut 2D pattern was covered from both sides with a thin layer of tape. The purpose of the thin tape is to temporarily maintain the origami pattern during the rest of the fabrication process. Then, the pattern is manually folded. Glue is used to attach external parts and/or the edges of the pattern if needed. Finally, a few layers of rubber coating spray, commercially called Plasti Dip, is utilized in order to permanently hold the rigid pattern together, also to act as actual folding lines. Furthermore, another way of conducting the 2D fabrication technique was explored. Similar to the first one, we start by printing the 2D pattern on a sheet of material. However, this time, a regular printer is used to print the pattern on a thick piece of paper. The same as always, the pattern is then manually folded, and the edges are glued together properly. Finally, the device is dipped in an elastic glue. It could also be silicone or some other glue, depending on the desired performance. The thick paper is used to better absorb the liquid during the dipping process and also to give the device its general shape. As for the glue, it was used to make the latter more stiff.
Another material for small scale origami devices was explored as well, thin stainless steel sheets. The sheets are 100 μm thick, which is ideal for milli-origami devices. Besides, stainless steel does not corrode as a result of laser machining; also, it is bio-compatible; hence, it is suitable for biomedical applications, which usually the target application of these size range devices. An example of the fabrication process is shown in Fig. 2.7.

2.6.2 3D fabrication technique

For the 3D fabrication technique, which is more of an original/unconventional technique, the same files used for the FE modeling are used here as well. As already mentioned in the previous subsection, the 2D Pattern is first folded then the edges (folding lines), and the facets are separated, using origami design software and ***Matlab*** codes. Next, thickness is given to both parts and they are assembled in CAD software. Other rigid parts are also added to the assembly if needed. Finally, the assembly was used to 3D

[5] https://inkscape.org/doc/tutorials/elements/tutorial-elements.html

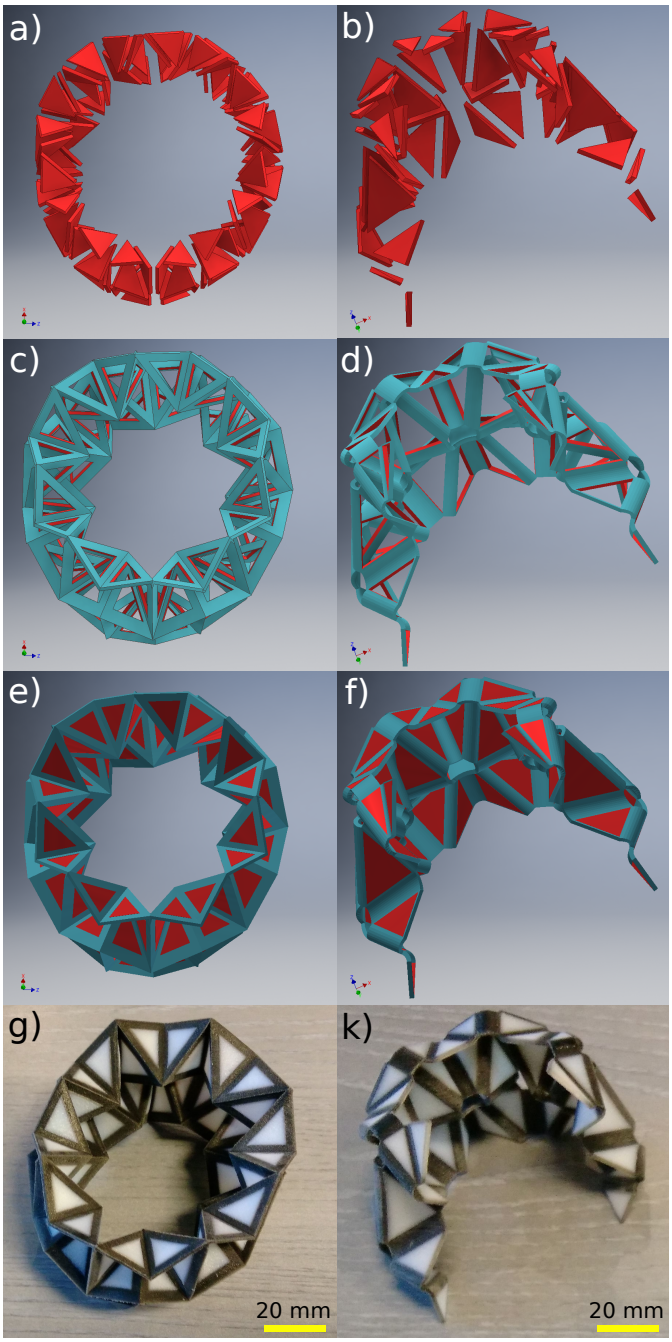

FIGURE 2.8: 3D fabrication technique using multi-materiel 3D printing. The technique was tested on two parts of the magic wheel [Lee et al., 2013]. A cylindrical slide: (a) the facets and (c) edges were separated and thickened (using our separation and thickening codes), then (e) reassembled and (g) 3D printed. A quarter of the magic wheel: (b) the facets and (d) edges were separated, rounded (only the edges) and thickened (also using our separation, rounding and thickening codes) before being reassembled and (k) 3D printed.

print the full devices with different materials, a flexible material for the edges, and a rigid material for the rest (facets and other parts). A *Connex 3 Objet350*[6] printer from *Stratasys* was used to print the fully folded origami devices (origami devices in their active state, as shown in the examples of Fig. 2.8). For the sake of convenience, the CAD software can be used to cut the assembly into two parts in order to allow for an easier integration of the actuation system. Once that is done, the two parts can be glued together using an appropriate glue. Other measures can be utilized to make the 3D printed origami devices more fatigue resistant and durable, such as adding a rubber coating by using a spray or a dipping process.

TABLE 2.2: Comparison of the proposed fabrication techniques.

Technique	***2D fabrication technique***	***3D fabrication technique***
Designing process	Simple	Complicated
Fabrication process	Complicated	Simple
Duration of the fabrication process	High	Reasonable
Repeatability of the fabrication process	Medium	High
Manual intervention	High	Limited
Mechanical properties of the device	High	Medium
Durability of the device	High	Medium
Actuation system integration	Simple	Complicated
Essential used equipment	CO_2 laser cutter	Multimaterial 3D printer
Automation and mass-production potential	Medium	High
Cost	Cheap	Expensive

2.7 Actuator selection and integration

The next step of our design method is the selection and integration of the actuation system. The latter is essential for the deployment and control of the origami-based active structure. However, before doing so, there are a few questions that need to be addressed first:

- What is the appropriate type of actuators needed for a given origami design?
- What is the value of the forces needed in order to deploy a origamiorigami device?
- Where is the appropriate location of actuators in order to generate desired the folding and unfolding motion (deployment)?

[6] https://www.stratasys.com/3d-printers/objet-350-500-connex3

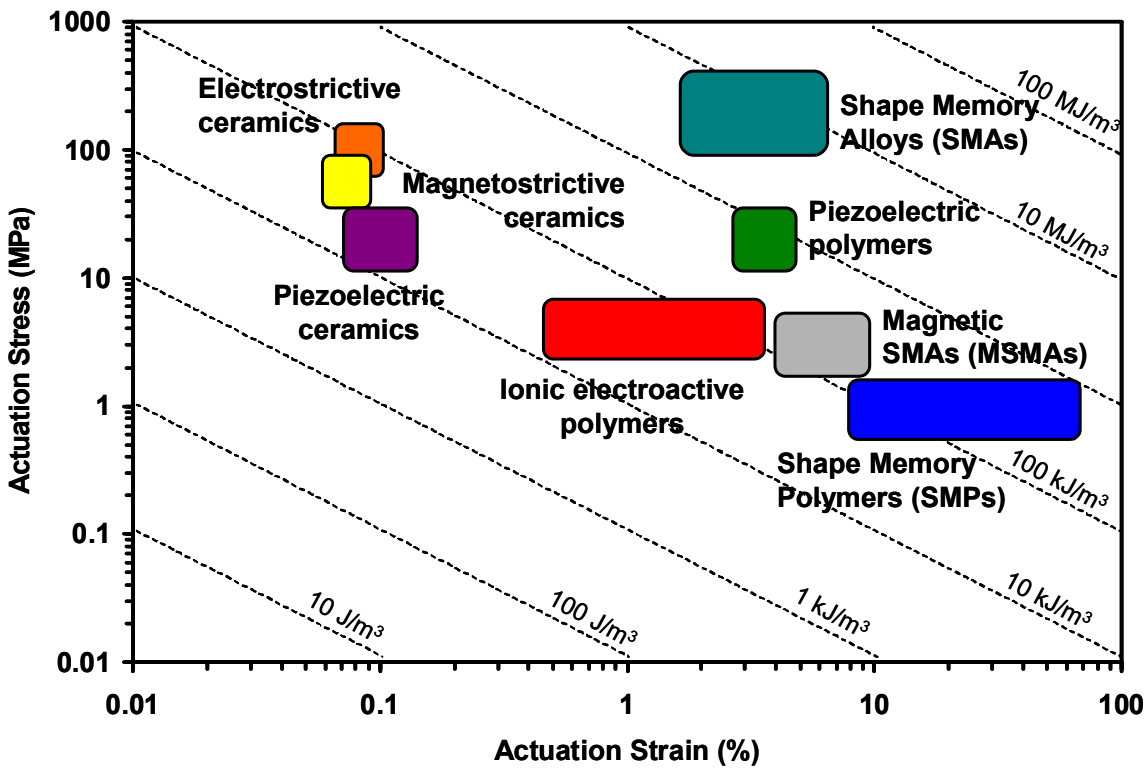

FIGURE 2.9: Typical ranges of actuation stress, actuation strain, and the actuation energy densities of different active materials that exhibit direct coupling [Lagoudas, 2008].

- What is the appropriate strategy to integrate actuators to a given origami device?

These are all valid and very challenging questions to answer, however answering these questions can be highly complex and depends on numerous parameters, such as the targeted field of application, the size of the device, the materials used for its fabrication, the folding and unfolding behavior and the overall origami design. Therefore, this step of the methodology is based on the development of a FE model of the origami device using the 3D origami design generated in the design step. The model can be crucial for understanding the kinetostatic behavior of the origami device as well as its folding and unfolding motion. This model is helpful in defining the characteristics of the actuation system. Some of the characteristics which must be taken into account during the selection of suitable actuators:

- Utilizing adequate actuators for the range of forces needed, neither less (insufficient folding and unfolding motion) nor more (running the risk of damaging the devices)
- Using the minimum number of actuators in order to generate the maximum folding and unfolding motion needed, since the higher the number of actuators used is the more complex their integration process becomes, the heavier the origami device becomes (which goes against a fundamental objective of using origami), and the more challenging controlling the devices becomes.
- Using small as possible actuators, as another fundamental objective of using origami is space reduction.
- Considering the impact of the actuators on the devices during its activation, for instance, shape memory alloys tend to heat up when activated, which can be problematic to the structural parts of the device in some cases.

Furthermore, because origami devices tend to have large deformations (folding/unfolding motion), they are fairly limited on the number of actuators and smart materials (see Fig. 2.9) that they can choose from. For instance, ceramic-type active materials (electrostrictive ceramics, magnetostrictive ceramics, and piezoelectric ceramics) may not be suitable for origami devices, as they can not provide deformations with the appropriate magnitudes for folding. On the other hand, active materials that are better suited for folding include shape memory alloys, shape memory polymers, and electroactive polymers, both dielectric polymers and conductive polymers. Finally, besides these active materials and the traditional choice of using a DC motor, which depending on the size of the origami device can be very challenging and an efficient (goes against adopting origami devices in the first place) there is also the option of using a magnetic or pneumatic actuation systems. By using precisely embedded magnetic field, an external magnetic field can be used in order to control the origami device remotely, which can be interesting for specific applications (such as biomedical applications). As for a pneumatic actuation system, depending on the active state of the origami device (if it can take the shape of a cube, a ball, or cylinder, for example), closed geometry can be added to the design in order to allow its control.

2.8 Experimental validation

The final step of the proposed methodology is the experimental validation of the performance and the aptitude of the origami device to comply with the application requirements. Apart from testing the ability of such devices to produce the desired shapes as well as the ability to control their state of folding, we need to quantify the performance of the origami device in the targeted application, then compare the results with the application requirements. For instance, we should test the ability of a foldable lens for space applications to concentrate light; the ability of a foldable battery for deformable electronics to produce energy; the ability of origami devices for sound control applications to reduce noise; also the ability of small-scale origami device for biomedical to actually hold and deliver drugs; as well as the ability of an origami arm for robotics to grasp and release objects.
If we find the results satisfactory, the origami design methodology ends here; otherwise, the cycle of the methodology is restarted once more from the beginning.

2.9 Conclusion

In this chapter, we introduced a origami-based design methodology intended for engineering fields where origami devices can be highly beneficial, such as biomedical and aerospace applications that tend to have high space reduction requirements. This original methodology is composed of several steps. The first step of the methodology, which is the application requirements and large deformations, is very application–dependent and can quite vary from one application to another thanks to the wide range of applications where applying origami engineering can be a game-changer compared to traditional methodologies. For example, in literature, origami can be found in biomedical applications, electronic and energy storage devices, aerospace, robotics, vibro-acoustics, improved mechanical parts, and architectural applications. Therefore, it is vital to fairly evaluate the application requirements in the first step of the methodology. In the second step, the origami base that best represents those application requirements is chosen. Then, when the origami base is chosen, the design for the origami design can be created. As it is usually the case with origami, the design is created in 2D. Then using the latter, a 3D design of the origami device, in its folded (functioning) state, is created as well. Next is the development of a multi-physics FE model by utilizing the 3D design generated in the previous step. The model is used as a numerical tool in order to conduct an initial validation of the application requirements. In the case where the design was not able to satisfy the application requirements, a return to the first step must be considered. However, if it is not the case, the next step, which is the fabrication and actuation system integration, can be tackled. Depending on the application requirements and the available equipment, there are two proposed fabrication techniques. The 2D fabrication technique that utilizes the 2D design generated during the designing step consists of using CO_2 laser cuter to create a flat structure, then, after covering the structure with a thin film for support the device is manually folded, before adding a layer of rubber coating. As

for the second technique, the 3D fabrication technique, the 3D design is utilized in order to 3D print the origami device in its folded state, using a multi-material 3D printer (a soft material for the folding lines and a rigid material for the facets). Afterward, the actuation system can be integrated into the device in order to make it active. The FE model can come in handy in this stage as well, where the different parameters of the actuation system can be estimated using a similar model, such as the values of forces and the appropriate locations to attach the actuators. Finally, origami-based active structures can be experimentally validated.

This proposed methodology contains two different cycles, a small cycles called the numerical validation cycle, where the chosen design is numerical tested and improved upon until it reaches the conditions of the application requirements and the bigger cycle, the experiential validation cycle, where the fabricated prototype of the devices goes through an experimental testing an optimization process. This ensures, the determination of the appropriate origami devices with a particular properties and characteristics for a specific application, thus, instead of letting the shape of the origami devices decide its application, which is the traditional way of approaching the subject, the application determines the shape and overall properties of the origami device.

Three vital points of this methodology are the creation of the 3D design, the development of the multi-physics FE model, and the 3D fabrication of origami devices. By properly mastering these key points, the potential, as well as the possibilities of the methodology, can be limitless, especially since the rapid expansion of 3D printing technology, which can one day allow for the fabrication of self-contained origami devices with already integrated circuit boards and actuation systems.

Chapter 3

Tunable Helmholtz resonator

"The most intelligent people disguise the fact that they are intelligent. Wise men do not wear name tags. The more people talk about their own skills, the more desperate they are–their work should speak for itself."
- Tsugumi Ohba

Contents

In this chapter, we discuss vibro-acoustic devices, more specifically, Helmholtz resonators, which are better known for their noise control properties in the low frequencies. They are one of the targeted applications that also play the role of proof of concept for our origami design methodology.

3.1 Introduction

In the old ages, the Greeks and Romans used several arranged cavities in their theater's walls to improve the acoustics. Later on, the same principle was applied in churches and mosques. In the 1st century BC, they were called "Vitruvian vases", named after the engineer, architect and the author of "de Architectura", which is considered to be the oldest book on acoustics in buildings [Lecocq, 2006]. However, the resonant cavity theory was introduced for the first time, by Hermann von Helmholtz (1860) then Lord Rayleigh (1870). Moreover, even though these resonators bear the name of Helmholtz, it is Rayleigh's work, presented in his book: "On the theory of resonators" [Rayleigh, 1916], which is best known and studied. If the analogy of the Vitruvian vases with the Helmholtz resonators is made, it is understood that according to the dimensions and the geometrical characteristics of the cavity and/or the neck, the role of the resonator can be very different: amplification or attenuation [Lecocq, 2006].
Helmholtz resonators are usually utilized for the control of steady, harmonic sound fields with tonal and narrowband spectrums. Thanks to their interesting vibro-acoustic properties, they have demonstrated widespread usefulness in reverberant environments such as churches [Anderson and Bratos-Anderson, 1993], mufflers in pipes, and ducts [Munjal, 1987], as well as numerous other applications. The main advantages of Helmholtz resonators are their simplicity and efficiency at low frequencies. Nonetheless, their relatively narrow bandwidth represents a significant limitation. Considering that, these resonators need to be precisely tuned to achieve significant noise attenuation. As a result, any fluctuation in the incident frequency or the environment conditions instigate a tuning for such devices, as some mistuned resonators can sometimes induce noise rather than reducing it.
Adaptive-passive devices are smart systems that can adapt their passive properties in order to preserve their high performance throughout changing work conditions. Having the ability to adjust the geometrical properties of Helmholtz resonators, such as the length of the neck or the volume, will allow for precise, real-time tuning of the devices throughout the variations of the excitation frequency. Tunable Helmholtz resonators can be very beneficial. Compared to traditional passive noise control, they guarantee high performances in the low-frequency range despite their narrow bandwidth. Moreover, compared to active noise control, they do not require complex control algorithms, and they need minimal power consumption.
This chapter introduces Helmholtz resonators and their resonant frequency model, also known as the analytical model. Additionally, it presents a state of the art of tunable Helmholtz resonators. Lastly, it discusses two different models for describing the acoustic behavior of Helmholtz resonators: a more simplified analytical model based on the concept of an equivalent volume, in addition to an FE model.

3.2 Helmholtz resonator

3.2.1 Definition

Helmholtz resonance is the name given to the resonance phenomenon occurring in a cavity linked to the surrounding atmosphere (which is usually air) via a constricted neck (as shown in Fig. 3.1). As already mentioned, Hermann L.F. von Helmholtz [Von Helmholtz, 1912] was the first scientist who established its physical and mathematical principles. The most common example of Helmholtz resonators are bottles and stringed instruments, especially bottles given the fact that they fit the description very well (small opening into a large chamber) [Webster and Davies, 2010].

FIGURE 3.1: Helmholtz resonator.

3.2.2 The resonance frequency

Depending on the dimensions of a bottle, if air is blown across the neck, the air in it resonates at a frequency proportional to the bottle dimensions. An ideal Helmholtz resonator can be compared to other oscillatory systems such as the classical mass-spring arrangement (as shown in Fig. 3.2) because at first glance such systems have a similar fundamental equation for the frequency [Webster and Davies, 2010], as shown below. Assume that the volume of the neck (SL_n , where S equals πr_n^2) is very small compared to the volume of the cavity V_c : $SL_n \ll V_c$, with L_n and r_n are the length and the radius of the neck, respectively.

Let us consider a small displacement X of the plug of fluid (usually air) into the cavity (see Fig. 3.3). The volume of the plug that enters the cavity for $X > 0$ causes the density ρ and thus the pressure to increase in the cavity. The opposite occurs for $X < 0$. Let $M = \rho_0 V_c$ be the ambient mass of the fluid in the cavity. The change in pressure in the cavity is:

$$\Delta P = c^2 \Delta\rho = c^2 \Delta \left(\frac{M}{V_c}\right) = -c^2 \frac{M}{V_c^2} \Delta V_c = -c^2 \frac{\rho_0}{V_c} \Delta V_c = c^2 \frac{\rho_0 S}{V_c} X, \tag{3.1}$$

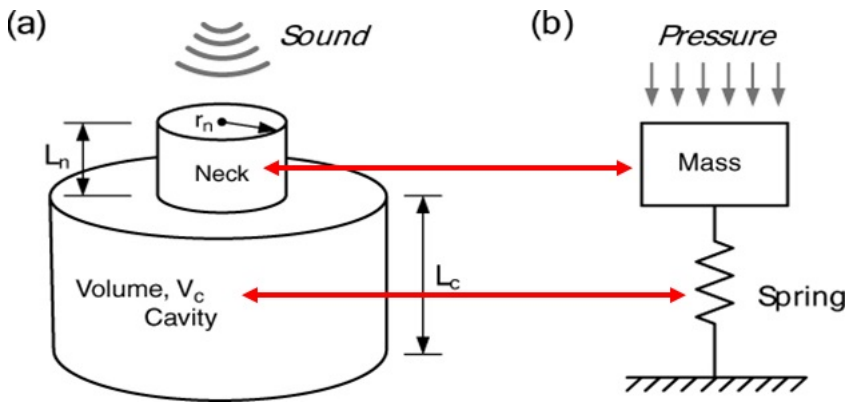

FIGURE 3.2: (a) Helmholtz resonator structure and (b) its mass-spring model [Lee and Choi, 2013].

where ρ_0 is the density of the fluid at rest, and c is the speed of sound in the fluid. The force on the plug is then: $F = -S\Delta P = -c^2 \frac{\rho_0 S^2}{V_c} X$, which is Hooke's law, where the spring constant is $k = c^2 \frac{\rho_0 S^2}{V_c}$; therefore, the cavity behaves like a spring, excited by the mass of the air plug. Finally, because the mass of the plug is $m = \rho_0 S L_n$, the natural angular frequency of the resonator is:

$$w = \sqrt{\frac{k}{m}} = \sqrt{c^2 \frac{\rho_0 S^2}{V_c} \times \frac{1}{\rho_0 S L_n}} = c\sqrt{\frac{S}{L_n V_c}} \Rightarrow f = \frac{c}{2\pi}\sqrt{\frac{S}{L_n V_c}}. \tag{3.2}$$

However, Eqn. 3.2 does not fully agree with the experiment. The measured frequency is lower than the predicted value. This was first observed by Lord Rayleigh [Rayleigh, 1945], who proposed an effective neck length, L_{eff} , in which a correction was added to the physical neck length to account for ends effect. Further refinements have been made by a number of authors, which also account for different resonator geometries; see Ingard [Ingard, 1953], Alster [Alster, 1972] and Chanaud [Chanaud, 1994]. To understand

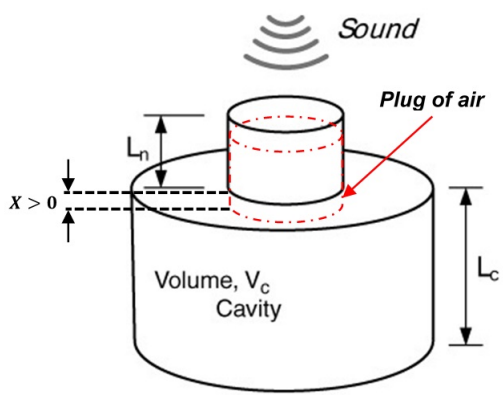

FIGURE 3.3: A Helmholtz resonator under an acoustic pressure.

this effect, we need to consider the plug of fluid in the neck. The plug does not actually rigidly oscillate. As the plug moves into the cavity or the open end, the fluid rapidly diverges. At the same time, at the opposite end, the fluid rapidly converges into the neck. The mass of the plug can then be considered as remaining constant, neglecting the fluid that converges and diverges. The above theoretical calculation is then an equivalent approach and thus yields the correct result, but only under the assumption of negligible motion of the converging and diverging fluid. However, this fluid represents an additional mass that participates in the motion. There will be thus a lowering of the frequency, which can be considered to be due to the neck being effectively longer [Webster and Davies, 2010]. The following results have been established, where r_n is the radius of the neck, λ is the sound wavelength and $\lambda \gg r_n$:

- effective increase of the neck length at the cavity $\approx \frac{8r_n}{3\pi} \approx 0.85r_n$;
- effective increase of the neck length at the open end $\approx 0.61r_n$.

This means that $L_{eff} = L_n + 1.46r_n$ and the Eqn. 3.2 rewrites:

$$f = \frac{c}{2\pi}\sqrt{\frac{S}{L_{eff}V_c}}. \tag{3.3}$$

For many years now, Helmholtz resonators have been used in adaptive-passive noise control. As mentioned above, the resonance frequency can be controlled by changing the dimensions of the Helmholtz resonator, namely those of the neck, the cavity or both. Consequently, to attenuate noise on a frequency domain of interest, it suffices to adjust the parameters of the neck and the cavity. To this end, various experiments have been conducted to determine the most effective methods of using adaptive Helmholtz resonators to control sound and, thereby, attenuation [Han, 2008].

3.2.3 Tunability of Helmholtz resonators

Although Helmholtz resonators exhibit high acoustic properties, these properties are only limited to a narrow bandwidth. Therefore, in order to improve their performance as well as increase their usefulness, tuning is required. This section discusses the possibilities and prospects of adding tunability to Helmholtz resonators. In this work, it has been chosen to tune the resonator by acting on the volume of the cavity. By considering a cylindrical from Eqn. 3.3 it is quite evident that the natural frequency is more sensitive to radius changes rather than those of the length; As, in the case of the radius r_c, the natural frequency f is a function of $\frac{1}{r_c}$, while, in the case of the length l_c, it is a function of $\frac{1}{\sqrt{l_c}}$. This sensitivity is clearly apparent in the behavior of a cylindrical Helmholtz resonator (see Fig. 3.4) with arbitrary geometrical properties (see Tab. 3.1).

TABLE 3.1: Dimensions of a cylindrical Helmholtz resonator.

Variables	Value	Unit
c_0	343	$m.s^{-1}$
r_n	6	mm
l_n	20	mm
r_c	30	mm
l_c	70	mm

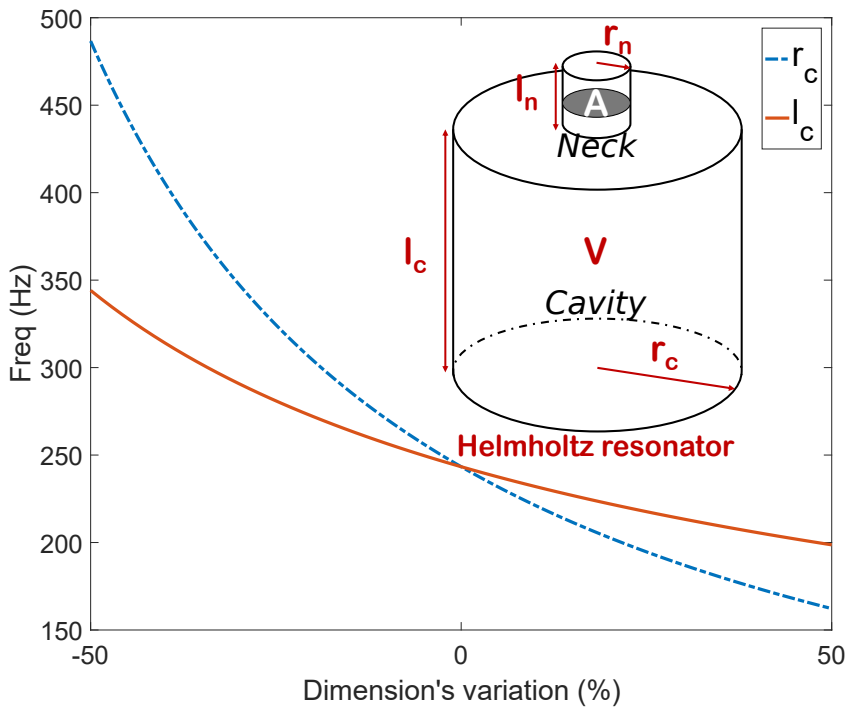

FIGURE 3.4: Comparison between the influence of the radius and the length of a cylindrical cavity of Helmholtz resonator on its theoretical natural frequency.

3.3 State of the art of tunable Helmholtz resonators

In acoustic control applications, two different methods are used: active and passive noise control techniques. Active noise control is generally achieved by introducing a canceling wave (180° out of phase "antinoise" wave) through an appropriate array of secondary sources [Kuo and Morgan, 1999]. Another strategy of active control consists in synthesizing an absorbing layer with a distributed set of sensors/actuators [Collet et al., 2014]. On the other hand, passive noise control is usually performed using two different stages

: (i) the use of porous materials, which has broadband effect, but limited in amplitude, and whose effectiveness in low frequency is directly related to the thickness of the material, and (ii) Helmholtz resonators (a cavity with an opening and a neck), which are very effective in amplitude but have a very narrow frequency bandwidth. A Helmholtz resonator is able to achieve noise reduction as a result of the high impedance produced by its cavity and neck [Allard and Atalla, 2009]; hence, this kind of resonator is widely used as passive noise control devices. One example is ventilation silencers in both air conditioning and ventilation systems [Chen et al., 1998]. Their noise reduction ability made them the subject of study of numerous researchers and scientists [Tang and Sirignano, 1973, Panton and Miller, 1975, Chanaud, 1994, Dickey and Selamet, 1996, Selamet and Lee, 2003, Tang, 2005, Abbad et al., 2019, Wang and Choy, 2019, Wu et al., 2019]. The main advantage of Helmholtz resonators is their simplicity [de Bedout et al., 1997]. Furthermore, unlike active devices, they do not require energy input; thus, they do not run the risk of generating noise rather than reducing it.
This section discusses some of the many examples found in the literature regarding tunable Helmholtz resonators. [De Bedout, 1996] introduced a self-tuning Helmholtz resonator for adaptive-passive noise control. In their paper, they discussed the realization of a Helmholtz resonator with a varying cavity volume. The volume variation was achieved by adding two rigid walls inside the cylindrical cavity of the resonator, as shown in Fig. 3.5: a fixed wall, which was glued to the cylindrical sidewall and the top plate, and a movable wall, which is glued to the bottom plate only, as a result, it can rotate freely. Both walls are linked to each other at the center of the cavity; hence, a rotational movement of the movable wall can be easily achieved. Moreover, the bottom plate is attached to a DC motor, so by rotating the bottom plate, the movable wall rotates also, changing in the process the volume of the resonator cavity.

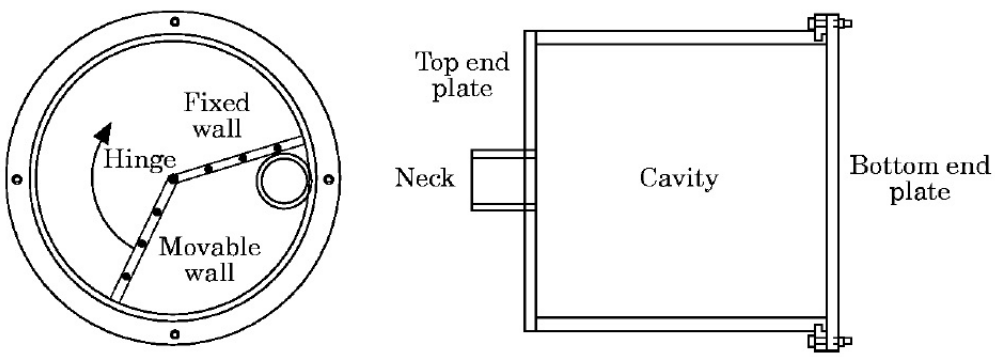

FIGURE 3.5: A variable volume Helmholtz resonator [De Bedout, 1996].

The fabricated resonator allowed optimal tuning despite changing the excitation frequency. The former was also able to achieve a tunable frequency range of 95 Hz (158% compared to the lower frequency), from 60 Hz to 180 Hz, with a maximum attenuation of 30 dB and a minimum attenuation of 15 dB, as shown in Fig. 3.6. That said, only one frequency can be treated at a time, and given the fact that the system contains differ-

ent parts linked together, there are substantial technical difficulties regarding acoustic leakage avoidance during the movable wall rotations.

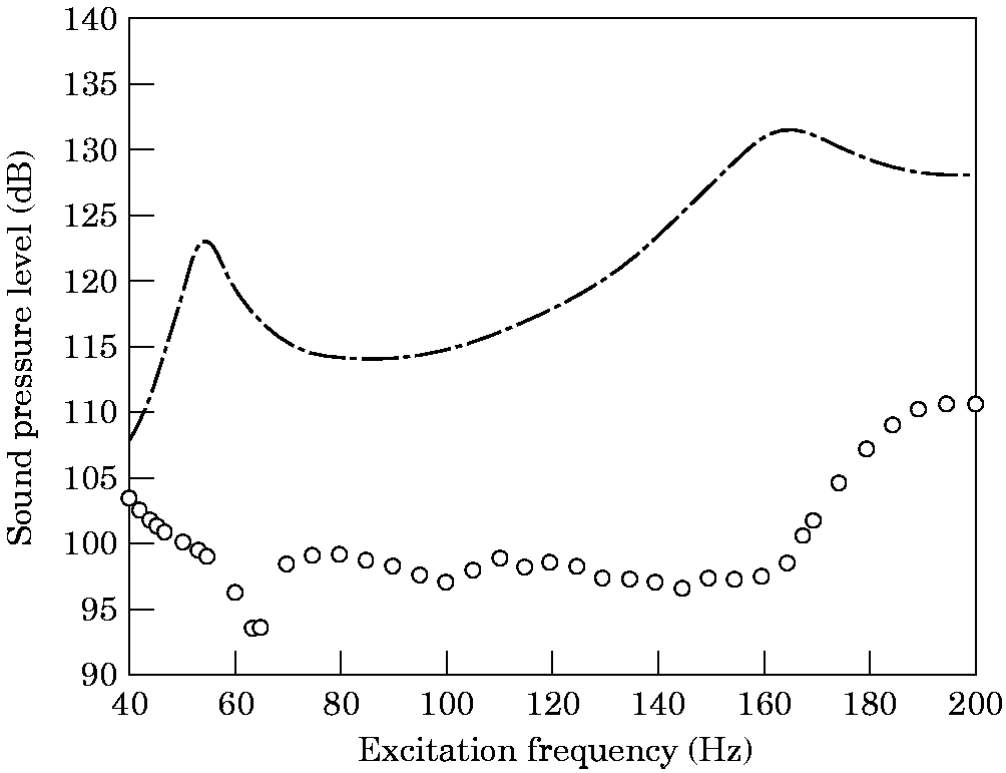

FIGURE 3.6: A comparison of the treated and untreated system sound pressure levels: · — ·— Without resonator, o with tunable resonator [De Bedout, 1996].

[Yu et al., 2017] introduced a tunable acoustic metamaterial with an array of resonators actuated by Dielectric elastomer (DE). Even though the resonators discussed in this paper are not precisely Helmholtz resonators, the fact remains that such acoustic resonators are worth mentioning here, since their overall objective goes hand in hand with those of our project (adaptive-passive systems for noise control). The problem of achieving noise reduction in this article is tackled by using two different methods. The first is based on square-shaped resonators, with one of its faces being a membrane made of a DE (see Fig. 3.7.a). Different resonators are fabricated, each one with a different pre-stretch ratio $r = A/A_0 = B/B_0$ (where A and A_0 are the dimensions of stretched and stretch-free state membrane in the x-direction, respectively, the same applies to the y-direction as well). Furthermore, Carbon grease as compliant electrodes are coated on both sides of the membrane (as shown in Fig. 3.7.b). Moreover, four DE resonators are connected in series as an array to a rigid duct (see Fig. 3.7.c), each one with a slightly different r (3.0, 3.3, 3.6 and 4.0). Different r means different mechanical proprieties of the DE membrane, which also means different resonant frequencies.

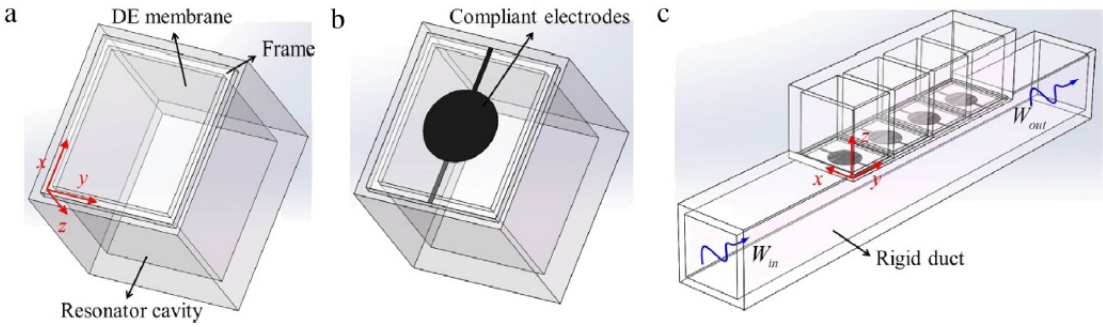

FIGURE 3.7: Schematics of: (a) DE resonator unit without electrodes; (b) DE membrane coated with compliant electrodes; (c) acoustic metamaterial comprising an array of DE resonators being attached onto a duct [Yu et al., 2017].

Based on that fact, the attenuation bands for the resonator with $r = 3.0$ are located at around 290 Hz and 310 Hz, $r = 3.3$ at 300 Hz and 335 Hz, $r = 3.6$ at 315 Hz and 355 Hz, and $r = 4.0$ at 330 Hz and 370 Hz, respectively (see Fig. 3.8). Each attenuation band has a narrow bandwidth of 10-15 Hz in the vicinity of the center frequency, which shows that each resonator alone can only cover tiny bands of frequencies. However, the four resonators combined as an array can achieve an attenuation band (transmission loss (TL) > 10 dB) from 295 to 420 Hz with a bandwidth of 125 Hz (see Fig. 3.8), which is about ten times greater than the narrow attenuation band of a single resonator.

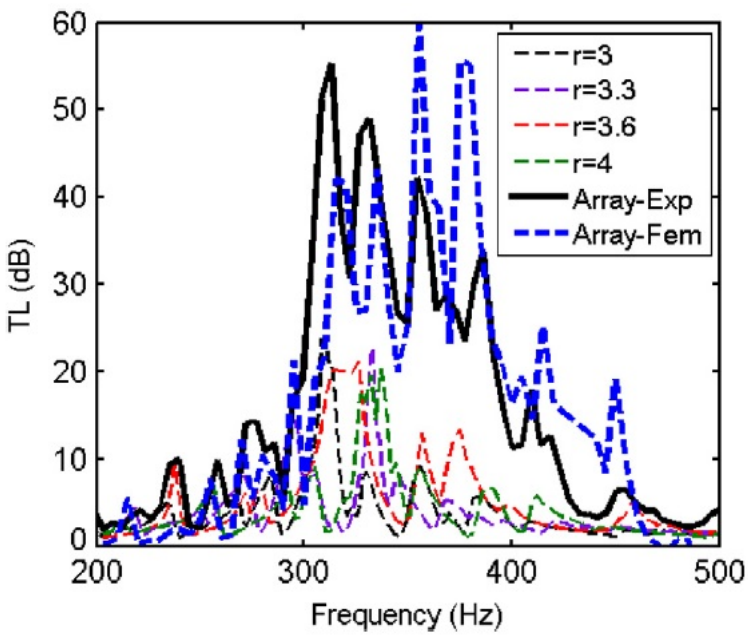

FIGURE 3.8: Connecting four DE resonators as a metamaterial array, a much broadened attenuation band can be achieved [Yu et al., 2017].

As for the second method, the tunability of the proposed device via changing control voltages was explored. An elongation in the surface area of the DE membrane can be triggered by applying voltage to the compliant electrodes, and the induced deformation can be exploited to reduce the tension force T exerted to the membrane edges by fixed frames. As voltage increases, the TL peaks and attenuation bands of the array resonator gradually shift toward lower frequencies as a result of the reduced membrane tension T. The experiments demonstrate that the proposed metamaterial has a maximum tunability (for voltages ranging from 0 to 4.6 kV) of $(295 - 255)/295 \approx 14\%$ in the frequency of the attenuation band.
Even though the proposed device has a broad frequency bandwidth, it still displays some limitations, one of which is the risks that such very high voltages can represent.

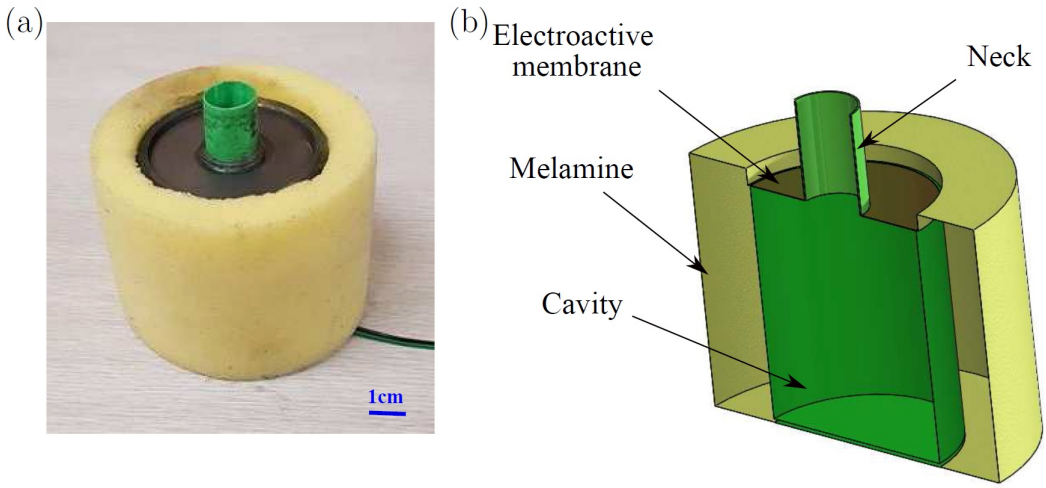

FIGURE 3.9: Helmholtz resonator with a front membrane made of electroactive polymer embedded in a melamine foam host support: (a) Real configuration, (b) 3D schematic of the HR components [Abbad et al., 2018].

Lastly, Abbad et al. [Abbad, 2016, Abbad et al., 2017, Abbad et al., 2018, Abbad et al., 2019] presented an adaptive Helmholtz resonator based on DE, embedded in a melamine foam. The designed resonator aims to improve adaptive noise control in low frequencies (<500 Hz). The proposed concept consists in replacing the top wall of a traditional cylindrical Helmholtz resonator with a dielectric membrane, as shown in Fig. 3.9. The stiffness of the membrane, which depends primarily (in the passive state) on the pre-stretch ratio, can be controlled via an applied electric field. Also, as the change in the membrane stiffness causes a frequency shift, a tunable Helmholtz resonator using an applied electric field can be achieved.
They also proposed a 2D axisymmetric numerical model based on FE method to study and investigate the acoustic performance, including both the acoustic absorption and transmission loss, of the introduced concept. The model was then experimentally val-

idated using an acoustic transmission tube. Two configurations of the resonator were tested, each with different a pre-stretch ratio of the membrane. For a pre-stretch ratio of 3, the resonator was able to achieve a frequency shift of 32 Hz (17.4% compared to the lower frequency), from 184 Hz to 152 Hz, which corresponds to an applied voltage of 0 and 5 kV, respectively, as shown in Fig. 3.10. Moreover, The second configuration that has a pre-stretch ratio of 4 was able to achieve a frequency shift of 28 Hz (15% compared to the lower frequency), from 186 Hz to 158 Hz, which corresponds to an applied voltage of 0 and 5 kV, respectively. Finally, they were also able to accurately control the resonance shift as a function of the tonal acoustic excitation variation using a neural network algorithm.

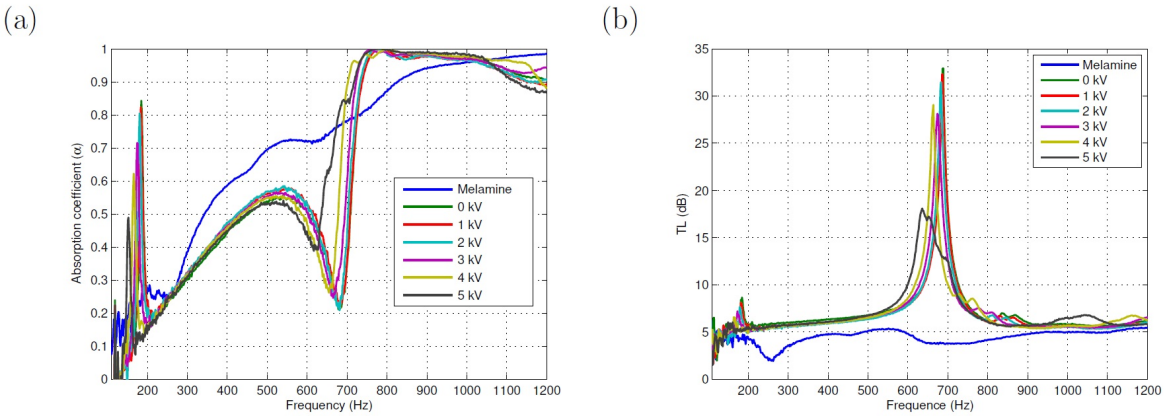

FIGURE 3.10: Experimental (a) absorption coefficient and (b) transmission loss for various voltage values and an initial membrane stretch ratio of 3, both compared to a full melamine foam. [Abbad et al., 2018].

3.4 Modeling

This section presents the models which will be used to describe the acoustic properties of the origami resonators (to be introduced in the next chapter): a simplified analytical model based on P-TMM and more precise numerical (FE model) model with various levels of complexity (in particular regarding the flexibility of the walls). All models take into account the losses in the neck by considering an equivalent fluid described by a Johnson-Champoux-Allard model.

3.4.1 Johnson-Champoux-Allard model

The Johnson-Champoux-Allard (JCA) model [Allard and Atalla, 2009, Johnson et al., 1987, Champoux and Allard, 1991] is based on a semi-phenomenological approach (from asymptotic responses at high and low frequencies) initially developed to describe describes the visco-thermal dissipative effects inside a porous media with a motionless skeleton and arbitrary pore shapes (but uniform over a short distance). It allows the

expression of the acoustic properties $K(\omega)$ representing the effective dynamic compressibility, which takes into account the thermal losses; and $\rho(\omega)$ (kg.m^{-3}) the effective density of the fluid saturating the porous media with a rigid structure which takes into account the viscous losses. the JCA model is used in equivalent fluid models, characterized by the Helmholtz equation in which the speed of sound squared c_0^2 is replaced by the term $\frac{K(\omega)}{\rho(\omega)}$. The JCA model has five intrinsic properties measurable experimentally, namely the airflow resistivity σ, the porosity ϕ, the tortuosity α_∞ and the viscous and thermal characteristic lengths Λ and Λ', respectively. The latter two parameters were introduced to take into account viscous and thermal effects at high and low frequencies. Viscous exchanges due to the movement of the fluid and thermal exchanges due to the thermal conduction are carried out in the boundary layers of the walls of these materials. Dynamic compressibility is expressed by

$$K(\omega) = \gamma P_0 \left[\gamma - \frac{\gamma - 1}{1 + \frac{8\eta}{j\omega\rho_0 \Lambda'^2 N_{pr}} \sqrt{1 + \frac{j\omega\rho_0 \Lambda'^2 N_{pr}}{16\eta}}} \right]^{-1}, \tag{3.4}$$

and the effective density by

$$\rho(\omega) = \alpha_\infty \rho_0 \left[1 - j \frac{\sigma\phi}{\rho_0 \alpha_\infty \omega} \sqrt{1 + \frac{4j\rho_0 \alpha_\infty^2 \omega\eta}{\sigma^2 \phi^2 \Lambda^2}} \right], \tag{3.5}$$

where γ is the ratio of specific heats, ρ_0 is the density of the saturating fluid ($kg.m^{-3}$), P_0 is the atmospheric pressure (Pa), η is the dynamic viscosity of air ($Pa.s$), and N_{pr} is equal to $N_{pr} = \frac{\eta C_p}{k}$, where C_p is the heat capacity of air at constant pressure ($J.K^{-1}$). Finally, this model is valid and usable for the case of pores with an arbitrary section but uniform over a short distance.

3.4.2 Equipment volume model

The Transfer Matrix Method (TMM) is a fast analytical calculation method for the prediction of acoustic performances, in particular for estimating the absorption coefficient and the transmission loss of a multilayer composed of several laterally infinite homogeneous layers assembled in series to form a stack. The method is valid under the assumption of a plane wave. This method is expressed by a matrix relation between two acoustic state variables, which are the pressure P and the acoustic velocity u (this being true for fluids, equivalent fluids, and mass walls). Equivalent fluids are described by their effective properties represented by the wavenumber k_i and the characteristic impedance Z_i (i denoting the number of the layer). They are connected to the density $\rho_i(\omega)$ and to the compressibility modulus $K_i(\omega)$. More or less complex structures (see Fig. 3.11), such as single or double walls are usually modeled by the TMM [Lauriks et al., 1992]. Recently, Verdière et al. [Verdière et al., 2013, Verdière et al., 2014] proposed an extension of the TMM called the P-TMM approach (P for parallel). The method makes possible

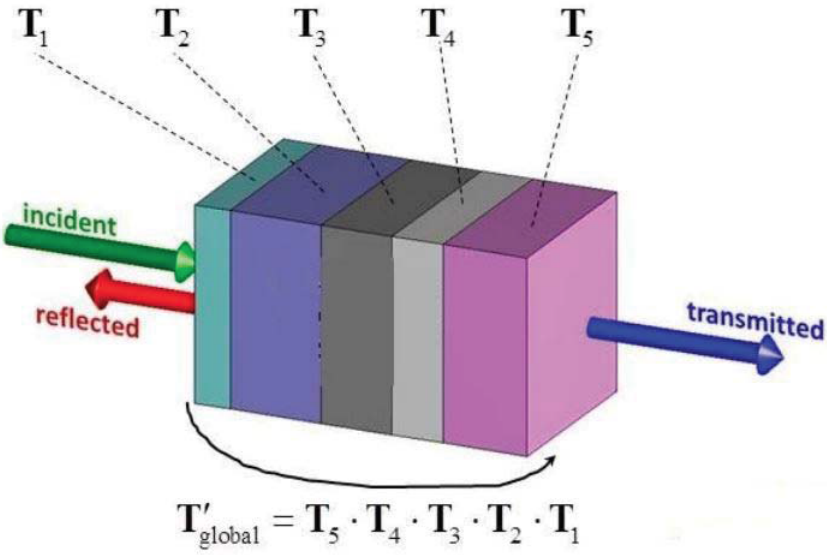

FIGURE 3.11: Diagram of a modelization by TMM (five layers): T_i represents the transfer matrix of the layer i and T'_{global} the transfer matrix of the set of all five layers [Abbad, 2017].

to take into account both materials in parallel and in series. This method, therefore, makes possible to model resonant inclusions [Doutres et al., 2015], such as Helmholtz resonators.
As a result, in this work, we decided to employ the P-TMM to model and quickly investigate the acoustic behavior of our designed origami-based acoustic devices. The studied system is an origami-based Helmholtz resonator, which, for the purpose of this model, can be replaced for each state of folding by a traditional Helmholtz resonator with a cuboid cavity that holds the same volume as the original. This assumption is only valid for Helmholtz resonator with cylindrical necks and rigid walls, as for such resonator, it is supposed that the shape of the cavity is not relevant; only the volume matters.

3.4.2.1 P-TMM model

The modeled acoustic system is Helmholtz resonators embedded in a homogeneous porous material (usually foam) in a periodic fashion, which makes for a full spectrum noise control system, foam for high and medium frequencies, and Helmholtz resonator for low frequencies. The acoustic system is defined as a 2D arrangement of cuboid periodic unit cells (PUCs), as shown in Fig. 3.12.a and Fig. 3.12.b. The P-TMM [Allard and Atalla, 2009, Pellicier and Trompette, 2007, Verdière et al., 2013, Verdière et al., 2014] is used to model its 1D acoustical behavior. In [Doutres et al., 2015], the PUC is modeled as a pile of three different layers stacked is series, with thicknesses of l_1, l_2, and l_3. The

first and last layers are made of homogeneous foam, while the second layer contains a parallel assembly of the Helmholtz resonator and foam (see Fig. 3.12.d). If needed, the three layers can be made of different porous materials. The transfer matrix of the PUC illustrated in Fig. 3.12.c is given by

$$T^{PUC} = \begin{bmatrix} T_{11}^{PUC} & T_{12}^{PUC} \\ T_{21}^{PUC} & T_{22}^{PUC} \end{bmatrix} = T^{layer,1} \times T^{layer,2} \times T^{layer,3}. \tag{3.6}$$

The acoustic behavior of the porous material is modeled using the JCA equivalent fluid model described in Sec. 3.4.1, which can be expressed by a 2×2 transfer matrix. As a result, the transfer matrices of both foam layers $T^{layer,i}$ (with i=1 and 3) are equal to

$$T^{layer,i} = \begin{bmatrix} T_{11}^{i} & T_{12}^{i} \\ T_{21}^{i} & T_{22}^{i} \end{bmatrix} = \begin{bmatrix} cos(k_{eq,i}l_i) & jZ_{eq,i}sin(k_{eq,i}l_i) \\ jsin(k_{eq,i}l_i)/Z_{eq,i} & cos(k_{eq,i}l_i) \end{bmatrix}, \tag{3.7}$$

with $j^2 = -1$, $k_{eq,i}$, and $Z_{eq,i}$ the wavenumber and characteristic impedance of the equivalent fluid, respectively. These properties are derived from the dynamic density ρ_i and dynamic bulk modulus K_i of the fluid phase such as $Z_{eq,i} = (\rho_i K_i)^{1/2}/\phi$ and $k_{eq,i} = \omega(\rho_i/K_i)^{1/2}$, with ω the angular frequency and ϕ the open porosity of the porous material.

The transfer matrix of layer 2 combines two submatrices, which are modeled using a parallel assembly as proposed by Verdière et al [Verdière et al., 2013]. In order to use P-TMM a number of conditions must be met: (1) only plane waves propagate upstream and downstream of the periodic construction; (2) only normal incidence plane waves propagate in the construction; (3) no pressure diffusion exists between adjacent parallel elements, (4) the wavelength is much larger than the PUC, and (5) each element can be represented by a 2×2 transfer matrix. Conditions (2) to (5) are satisfied here, as we consider (i) low frequencies (that is frequencies much lower than $c_0 = L$), (ii) porous substrate with intermediate airflow resistivity, (iii) equivalent fluid models for predicting their acoustic behavior and lastly, (iv) a surface impedance model to represent the HR. However, assumption (1) seems physically unrealistic around the HR resonance frequency in the vicinity of the HR neck. According to [Verdière et al., 2013], the transfer matrix of layer 2 can be formulated as follows

$$T^{layer,2} = \frac{-1}{\sum r_n Y_{21}^n} \begin{bmatrix} \sum r_n Y_{22}^n & -1 \\ \sum r_n Y_{22}^n \sum r_n Y_{11}^n - \sum r_n Y_{12}^n \sum r_n Y_{21}^n & -\sum r_n Y_{11}^n \end{bmatrix}, \tag{3.8}$$

with Y^n the components of the admittance matrix for each element; here $n = mat$ for the porous substrate and $n = HR$ for the resonator element. r_n is the surface ratio of each element and is similar to the "percentage open area" for perforated panels. Knowing the surface of the unit cell S_{PUC} (see Fig. 3.12.b) and the surface of the resonator S_i (see Fig. 3.12.d), thus $r_{HR} = r = S_i/S_{PUC}$ and $r_{mat} = 1 - r_{HR}$. The admittance matrix for each element is given by

$$Y^n = \begin{bmatrix} Y_{11}^n & Y_{12}^n \\ Y_{21}^n & Y_{22}^n \end{bmatrix} = \frac{1}{T_{12}^n} \begin{bmatrix} T_{22}^n & T_{21}^n T_{12}^n - T_{22}^n T_{11}^n \\ 1 & -T_{11}^n \end{bmatrix}, \tag{3.9}$$

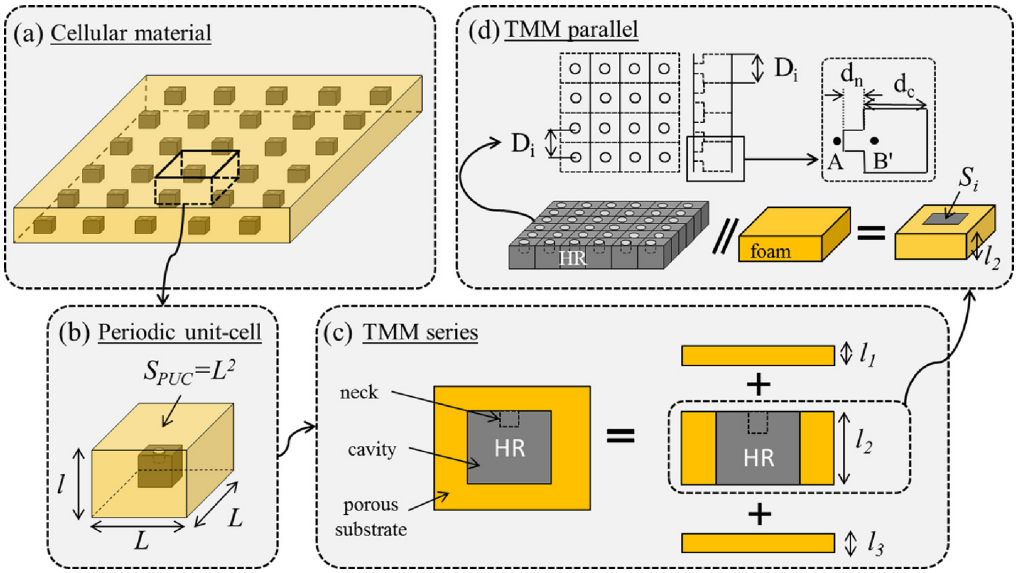

FIGURE 3.12: Scheme of the sound package and the PUC [Doutres et al., 2015].

The transfer matrix of the porous matrix T^{mat} is given by Eqn. 3.7 and the one of the resonator T^{HR} is given in Sec. 3.4.2.2.

In this work, the tunable Helmholtz resonators have an origami design. Additionally, for the purpose of this model, the resonators are inserted in square perforations of a porous layer with a l_2 thickness, as shown in Fig. 3.13.a. The mismatch between the shape of the origami-based resonators and the square perforations made to host them resulted in the creation of thin air layers within layer 2. The thin air layers occupy a significant volume; therefore, they should be included in the P-TMM model. That said, only the air layer below the resonator is considered here, as shown in Fig. 3.13.b. Consequently, layer 2 is divided into two parallel assemblies, identified as l_{2a} and l_{2HR}, and can be assembled in series by the following matrix

$$T^{layer,2} = T^{layer,2HR} \times T^{layer,2a}. \tag{3.10}$$

$T^{layer,2m}$ ($m = HR$ or a) is the matrix of the parallel elements which are open upstream and downstream. $T^{layer,2HR}$ is written exactly as Eqn. 3.8 and combines the transfer matrix of the porous layer and the one of the Helmholtz resonator. The thickness of this sublayer (i.e., l_{2HR}) is set to the length of the Helmholtz resonator cavity d_c being an equivalent cuboid with the same volume as the origami-based Helmholtz resonator and the square cross-section area of the perforation. The transfer matrix of the second parallel assembly $T^{layer,2a}$, combines the transfer matrix of the porous layer and the one of an air layer. The thickness of this sublayer is $l_{2a} = l_2 - l_{2HR}$, where l_2 is the length of the real origami-based resonator. The transfer matrix of the sublayer is also based on Eqns. 3.8 and 3.9, but the transfer matrix of the Helmholtz resonator is replaced by an

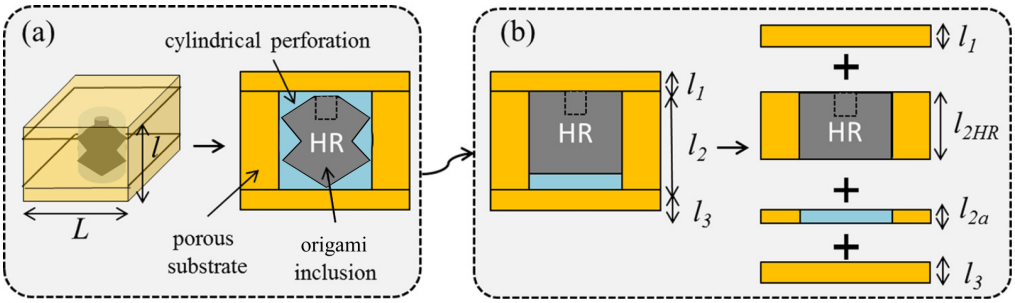

FIGURE 3.13: Scheme of the PUC with the perforation and the origami-based Helmholtz resonator adapted from [Doutres et al., 2015].

air layer matrix. The later matrix can be simply calculated from Eqn. 3.7 but $Z_{eq,i}$ has to be replaced by the characteristic impedance of air Z_0, $k_{eq,i}$ by the wavenumber in air k_0 and l_i by l_{2a}. Both parallel assemblies l_{2a} and l_{2HR} share the surface ratio of each element r_n since they occupy the same cross-section.

3.4.2.2 Helmholtz resonator model

The transfer matrix of the resonator T^{HR} required in Eqns. 3.7 and 3.8 for parallel assemblies with resonant inclusion is the one of a resonator array as described in [Allard and Atalla, 2009] and [Efimtsov and Lazarev, 2001]. It is written as a product of the inertial and acoustic components [Efimtsov and Lazarev, 2001].
The transfer matrix of a Helmholtz resonator positioned so that its neck is facing the acoustic source (this position is called AB) is written as follows

$$T^{HR,AB} = \begin{bmatrix} 1 & 0 \\ 1/Z_A & 1 \end{bmatrix} \begin{bmatrix} 1 & j\omega M_s \\ 0 & 1 \end{bmatrix}, \tag{3.11}$$

with M_s the mass per unit area of the resonator array and Z_A the acoustic input impedance. Here we limit the study to linear behavior. According to [Allard and Atalla, 2009] (see p. 203), the input total impedance of the resonator array under normal incidence plane waves, Fig. 3.12.d, is given by

$$Z_A = \frac{1}{s_e}(Z_{neck} + Z_{0,0}(B')) = \frac{1}{s_e}([(\frac{2d_n}{R_n} + 4)R_s + j\omega(\varepsilon_i + \varepsilon_e + d_n)\rho_0] - js_i Z_0 cot(k_0 d_c)), \tag{3.12}$$

with ρ_0 the air density, c_0 the speed of sound, $k_0 = /c_0$ the wavenumber, d_c the resonator cavity length, d_n the neck's depth, R_n the neck's inner radius, R_s is a surface resistance equal to $(2\eta\rho_0)^{1/2}/2$, η the dynamic fluid viscosity, and s_e and s_i the ratio of the area of the neck aperture S_n over the cross-section area of "external" elementary cell and "internal" elementary cell, respectively.
The resonator considered in the studied PUC has a negligible wall thickness. The cross-section areas of the internal and external elementary cell are thus taken equal; i.e., $s_i = s_e = Sn/D_i^2$ with D_i shown in Fig. 3.12.d. Under the large wavelength assumption

($\lambda \gg Di$ and $\lambda \gg d_c$), the normal surface impedance of the air layer at point B' is $Z_{0,0}(B') = -js_i Z_0 cot(k_0 d_c)$. Furthermore, the terms related to the modes of higher order in the resonator cavity are replaced by an added length effect (i.e., ε_i) added to the resonator neck depth. As mentioned above, the shape of the resonator cavity is thus irrelevant, and the resonator is characterized by its cavity inner volume. The length of the neck is also corrected (i.e., ε_e) to account for the mass loading associated with the sound radiation of the neck and to the distortion of the acoustic flow at the resonator surface. In the case of a circular neck aperture in contact with two air media on both ends, the two length corrections can be approximated for $s_e < 0.16$ by [Allard and Atalla, 2009]

$$\varepsilon_i = \varepsilon_e = 0.48\sqrt{S_n}(1 - 1.14\sqrt{s_e}). \tag{3.13}$$

The resistive part in Eqn. 3.12 (i.e., $(2d_n/R_n + 4)R_s$) accounts for the viscous effects occurring within the resonator's neck due to the viscous boundary layer and around its edges at the panel surface due to the distortion of the acoustic flow.

3.4.2.3 Acoustic performances of Helmholtz resonators

Various acoustic features can be determined from the transfer matrix of the PUC given by Eqn. 3.6. It is worth noting that the combination of Eqns. 3.6, 3.8, and 3.11 stands for an acoustic wave impinging on the neck side of the Helmholtz resonator (i.e., position AB). The transfer matrix of the PUC in the opposite direction BA, i.e., the PUC is inverted, and the acoustic wave now impinges on the rear side of the Helmholtz resonator, can be obtained by simply inverting the matrix of Eqn. 3.6 accounting for a change in the sign of the velocity by $-u$, [Panneton, 2009]

$$T^{PUC,BA} = \frac{1}{det(T^{PUC,AB})} \begin{bmatrix} T_{22}^{PUC,AB} & T_{12}^{PUC,AB} \\ T_{21}^{PUC,AB} & T_{11}^{PUC,AB} \end{bmatrix}. \tag{3.14}$$

The normal incidence sound transmission coefficient TL_n is ten times the common logarithm of the reciprocal of the sound transmission coefficient τ, the latter being the fraction of airborne sound power incident on a material that is transmitted by the material and radiated on the other side [E2611-09, 2009]. In the case of an anechoic-backed PUC, it is given by

$$TL_n = -20log_{10}(\frac{2}{|T_{11}^{PUC} + T_{12}^{PUC}/Z_0 + Z_0 T_{21}^{PUC} + T_{22}^{PUC}|}). \tag{3.15}$$

The sound absorption coefficient α is related to the reflection coefficient R^b defined as the ratio of the pressures created by the outgoing and ingoing waves at the surface of the layer: $\alpha = 1 - |R^b|^2$. The normal incidence reflection coefficient of the PUC backed by a rigid backing, R^b, or by an air cavity of thickness H, R^w, can be obtained, respectively, by

$$R^b = \frac{T_{11}^{PUC} - Z_0 T_{21}^{PUC}}{T_{11}^{PUC} + Z_0 T_{21}^{PUC}} \tag{3.16}$$

and

$$R^w = \frac{T_{11}^{PUC}T_{11}^a + T_{12}^{PUC}T_{21}^a - Z_0T_{21}^{PUC}T_{11}^a - Z_0T_{22}^{PUC}T_{21}^a}{T_{11}^{PUC}T_{11}^a + T_{12}^{PUC}T_{21}^a - +_{21}^{PUC}T_{11}^a + Z_0T_{22}^{PUC}T_{21}^a}, \tag{3.17}$$

with T_{ij}^a the transfer matrix coefficients of the backing cavity which can be obtained from Eqn. 3.7 by replacing $Z_{eq,i}$ by Z_0, $k_{eq,i}$ by k_0, and l_i by H.

3.4.3 Finite element model

Besides the analytical model described above, we also developed numerical models based on FE method to study, analyze, and predict the vibro-acoustic behavior of our acoustic devices. In particular, the impact of a non-cylindrical geometry for the cavity has been investigated with a rigid walls model, and the effect of the flexibility of the walls has been checked with a coupled mechanico-acoustic model.

3.4.3.1 Rigid walls model

A numerical model capable of describing the 1D acoustic behavior of Helmholtz resonators with arbitrarily complex shapes, including origami designs, was developed. The numerical model can be used to validate the equivalent volume model discussed above. The former reproduces the transmission tube tests (see Fig. 3.14). The acoustic fields inside the tube and the resonators cavities are described by Helmholtz equation:

$$\Delta p + k^2 p = 0, \qquad k^2 = \frac{\omega^2}{c_0^2}, \tag{3.18}$$

where p is the acoustic pressure, k is the wave number, and c_0 the sound speed in air.
In order to simulate the normal incidence excitation, a unit pressure is applied from one side of the tube, while the other side is considered to be acoustically rigid. Using the resulted virtual measurements of the acoustic pressure at two different locations, which serve as microphone locations, the normal acoustic absorption was deduced according to the one load, two microphone technique [E1050-10, 2012].
The modeled acoustic devices are origami-based Helmholtz resonators with circular neck aperture. The walls of the resonators are modeled as impermeable, rigid, and motionless. Moreover, The Johnson-Champoux-Allard equivalent fluid rigid model (see Sec. 3.4.1) was also used here to account for viscous and thermal dissipations caused by the resonator's neck. The effective properties of the air layer of the neck were determined by a cylindrical pore model [Allard and Atalla, 2009]. The values of the parameters of the model are provided in Tab. 3.2.
The numerical simulations will be compared to the analytical model (natural frequency equation), equivalent volume model (P-TMM model), and experimental tests conducted in a Ø100 mm cylindrical acoustic transmission tube. The simulations are carried out for Helmholtz resonators in the AB as BA positions. Furthermore, since both the acoustic transmission tube and the neck of the resonator are cylindrical, and the origami-based (introduced in the next chapter) cavity of the resonator is also symmetrical, by considering symmetry only an 8th of the acoustic device can be modeled; also, this is true for

TABLE 3.2: Parameters of the Johnson-Champoux-Allard equivalent fluid model used for the neck.

Variables	Expression [Stinson, 1991]	Value	Unit
Porosity ϕ	–	1	–
Airflow resistivity σ	$\frac{8\eta}{r_n^2}$	4	Nsm^{-4}
Tortuosity α_∞	–	1	–
Viscous characteristic length Λ	r_n	6	mm
Thermal characteristic length Λ'	r_n	6	mm
Density ρ_0	–	1.2	kgm^{-3}

normal plane waves only. This will decrease the computation time significantly, compared to the full model.
The reflection coefficient R is calculated using the transfer function method [E1050-10, 2012]. Once the reflection coefficient is determined, the surface impedance is given by:

$$Z_s = Z_0 \frac{1+R}{1-R}, \qquad Z_0 = \rho_0 c_0, \tag{3.19}$$

where ρ_0 and c_0 are the air density and sound velocity, respectively. Lastly, the absorption coefficient α can be obtained using the equation introduced previously, $\alpha = 1 - |R|^2$.

3.4.3.2 Flexible walls model

As it will be observed later, the walls of the resonators may vibrate under specific conditions. A FE model coupling the acoustics of the resonator and the vibration of the walls has been developed in order to check the impact of these vibrations on the 1D acoustic behavior of origami-based resonators. It reproduces the same acoustic tests and has the same boundary conditions as the one presented in the previous chapter. The walls are modeled as shells (thin mechanical structures). The origami design contains two different types of shells, one for the folding lines of the resonator, and a second one (more rigid) for the facets of the structure.
The transverse displacement of the plane shells $w(x,y,t)$ under a vibratory pressure load $p(x,y,t)$ is:

$$D\left(\frac{\partial^4 w(x,y,t)}{\partial x^4} + 2\frac{\partial^4 w(x,y,t)}{\partial x^2 \partial y^2} + \frac{\partial^4 w(x,y,t)}{\partial y^4}\right) + \rho h \frac{\partial^2 w(x,y,t)}{\partial t^2} = p(x,y,t), \tag{3.20}$$

in which D represents the flexural rigidity of the plate:

$$D = \frac{Eh^3}{12(1-\nu^2)} \tag{3.21}$$

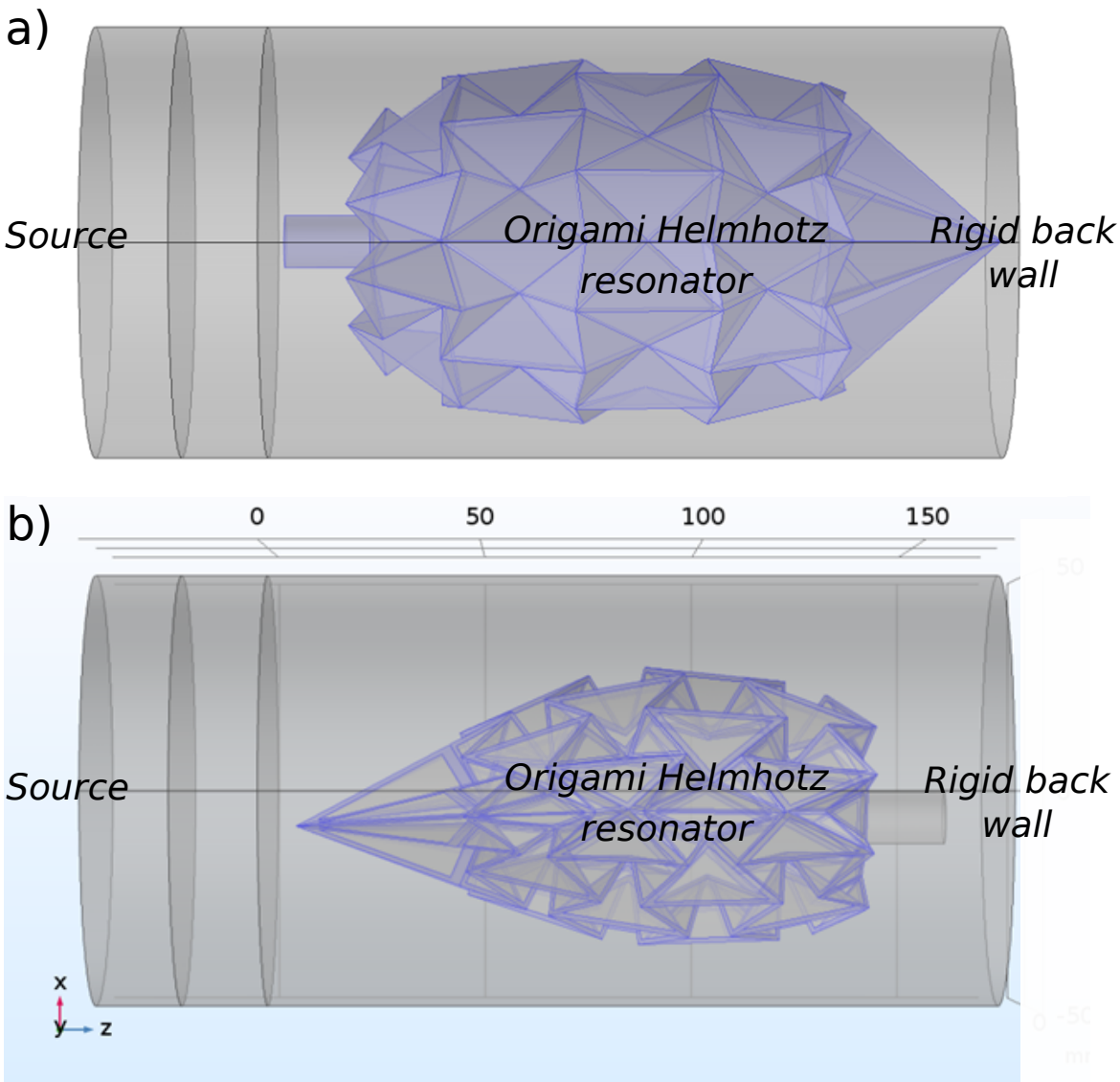

FIGURE 3.14: One load, two microphone technique [E1050-10, 2012], where (a) the origami-based Helmholtz resonator (unfolded state) is placed inside the transmission tube in AB position, and (b) the origami-based Helmholtz resonator (folded state) is placed inside the transmission tube in BA position.

and ρ is the density, h is the thickness, E is Young's modulus, and ν is Poisson's ratio of the shell. The structural damping effect is accounted for by using an isotropic damping loss factor for the shell η_s ($Cst^* = Cst(1 + i\eta_s)$). The value of η_s is identical to the value given in the data-sheet of the used materials. A constant damping loss factor of $\eta_s = 0.01$ is used for the simulations.
Furthermore, the Johnson-Champoux-Allard equivalent fluid model was also used here,

TABLE 3.3: Parameters of the The Johnson-Champoux-Allard equivalent fluid model.

Variables	Diameter of the Helmholtz resonator					Unit
	74 mm	72 mm	70 mm	68 mm	66 mm	
Porosity ϕ	1	1	1	1	1	–
Airflow resistivity σ	32000	28000	4000	3000	2000	Nsm^{-4}
Tortuosity α_∞	1.42	1.43	1.45	1.46	1.47	–
Viscous characteristic length Λ	6	6	6	6	6	mm
Thermal characteristic length Λ'	6	6	6	6	6	mm
Density ρ_0	1.2	1.2	1.2	1.2	1.2	kgm^{-3}

not to only model the viscous and thermal dissipations of the neck of the resonator, but also to model the structural loss factor for the dissipation associated with the structure. The parameters of the JCA model vary with the state of folding, which made their determination a challenging process. An optimization algorithm (genetic algorithm) coupled with the multiphysics FE model was used to identify their values. The values of the parameters of the model are provided in Tab. 3.3.

3.5 Conclusion

Helmholtz resonators are simple yet effective low-frequency sound control devices. As a result, they attracted the attention of many engineers and scientists as a promising concept for vibro-acoustic applications. In this chapter, which is considered as an introduction to tunable Helmholtz resonators, we introduced and defined Helmholtz resonators, their advantages, and their limitations. Moreover, we discussed the working principle of Helmholtz resonators and their resonance frequency, as well as their modeling. Also, we considered the tunability of these acoustic devices and its sensitivity to the geometrical properties, especially to those of the cavity. In addition, we reviewed the state of the art of tunable/adaptative Helmholtz resonators. Furthermore, we addressed the modeling of origami-based Hemlhotz resonators, using the P-TMM analytical model, based on the equivalent volume concept. Lastly, we also addressed the modeling of these origami-based devices using FE modeling, for the case of perfectly rigid walls (acoustic behavior only), as well as the case that includes walls resonance (coupling both the acoustic and mechanical behaviors).
This chapter includes the definitions, elements, and tools (from an acoustics point of view) needed for the development of origami-based Helmholtz resonators using the previously proposed origami design methodology. In other terms, it is the acoustic backbone of our chosen proof of concept, referred to as origami-based tunable Helmholtz resonators, which is the topic of the next chapter.

Chapter 4

Origami based Helmholtz resonator

"A theory is a supposition which we hope to be true, a hypothesis is a supposition which we expect to be useful; fictions belong to the realm of art; if made to intrude elsewhere, they become either make-believes or mistakes."
- George Stoney

Contents

This chapter plays the role of a proof of concept of our proposed methodology for origami-inspired structures. The designed structure is a tunable origami-based Helmholtz resonator for noise control and vibro-acoustics applications.

4.1 Introduction

In the transport industry, noise and vibration control is a major requirement in order to allow high performance, as well as to ensure customer satisfaction. From the control point of view, there are three different manners where intervening seems most interesting: the source, the element transmitting the noise or the vibration, and the recipient. In this study, we are most interested in the transmitting element. A common strategy in this field is the passive control, which does not require an energy input. The latter permits the dissipation of the undesired acoustic energy throughout the viscous and thermal losses that occur inside the materials. Porous materials, such as melamine or polyurethane foams, exhibit a very high performance (both in acoustic absorption and in transmission loss) in the medium and high-frequency domains. Nonetheless, at low frequencies [0-500 Hz], these materials display a poor efficiency, hence mastering them represents a significant challenge in order to achieve better acoustic isolation. One way to do so is by coupling the passive performance with an active control for the attenuation of low-frequency sound, where the classical intervention using foams is inefficient.
The state of the art has revealed a real need for the development, implementation, and validation of an original and consistent concept for a tunable Helmholtz resonator. Such devices offer fascinating characteristics regarding adaptive low-frequency sound control. The control is done by altering the volume of the cavity of an origami-based Helmholtz resonator. Thus, a complete study of the origami-based Helmholtz resonator volume variation is conducted and presented in this chapter. The study is based on the origami design methodology proposed in chapter 2, as shown in Fig. 4.1.
The primary motivation of this study is to propose a hybrid technological solution for a better sound control. It consists of coupling the high characteristics of passive foams at medium and high frequencies with an adaptive-passive control for low frequencies (tunable Helmholtz resonators). The intended application for this system is the aeronautic field; nonetheless, it is also suitable for ducts and ventilation systems. Following the different flying phases of an airplane (lift-off phase, flight phase, and landing phase), the fan that generates tonal and low-frequency noise, and most importantly, variable, must be controlled. The same goes for ventilation systems, where opening a ventilation traps can lead to a change in the acoustic response of the ducts. In both cases, an adaptive system must be able to follow these variations. A study in terms of acoustic absorption behavior of the tunable system is targeted. The developed principle in this study consists of using a Helmholtz resonator that has controllable acoustics characteristics (by altering its volume), in order to vary the controlled frequency range. Combining the latter strategy with a spatial distribution of the tunable resonators implanted inside a foam material, and the result is an acoustic system type intelligent meta-material (each

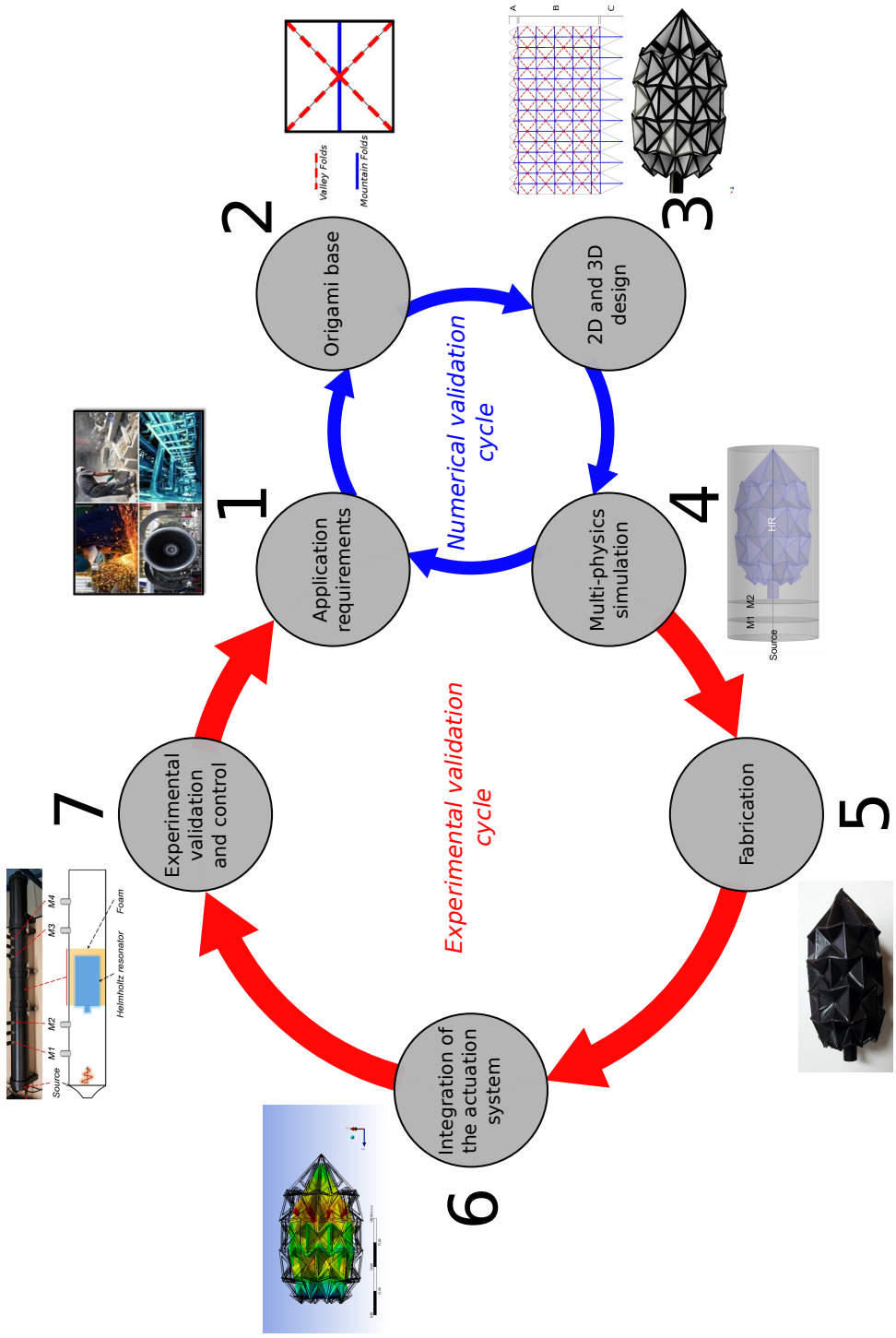

FIGURE 4.1: Diagram of the proposed origami design methodology for the origami-based Helmholtz resonator.

Helmholtz resonator is a tunable cell in this case) with reconfigurable properties that can adapt to satisfy the desired acoustic performance.
It is essential to mention that the ultimate aim of this study is to create a hybrid acoustic system, i.e. passive foams coupled with adaptive-passive Helmholtz resonators. However, since the origami-based Helmholtz resonators is an original concept with hard to predict acoustic behavior, we propose here to study the characteristics of the origami-based Helmholtz.

4.2 Application requirements

There are numerous objectives in order to be able to meet the application requirements. The main aim of this part of the doctoral project is the development of a passive-adaptive acoustic smart system with high performances that contains foam implanted by appropriately placed acoustics resonators (a tunable origami-based Helmholtz resonator that is able to adapt to a tonal type, varying acoustic excitation).
The application requirements can be defined as such:

1. Proposal of a technological solution for noise control based on origami-inspired tunable Helmholtz resonators with high characteristics, including:
   (a) Adaptive structure with high acoustic performances and maximum volume variation, which can be translated to a maximum frequency control, in the range of low-frequency domain [0-500Hz];
   (b) Lightweight concept;
   (c) Minimal number of parts in order to reduce acoustic leakage;
   (d) High potential for simple and fairly simple actuation system integration.
2. Conduct a full study of the feasibility of the proposed solution, including complete design, foldability test, fabrication strategies, modeling of the performances, experimental characterization (acoustic absorption), integration of actuation system, and control. Because of the complexity of the study and all the technical and scientific challenges that include, it seemed better to divide it into less complex, easier to tackle sub-studies:
   (a) Test the potential of the concept by characterizing the performance of 3D printed (rigid) origami-based Helmholtz resonators with different states of the folding (folded, half-folded and unfolded)
   (b) Fabricate adaptive Helmholtz resonators with different folding properties, fairly flexible (easy to fold), and fairly rigid (harder to fold), then compare their performances to fully rigid origami resonators as well as traditional Helmholtz resonators.
   (c) Conduct a study on the kinetostatic behavior of the origami-based Helmholtz resonator and depending on the results, propose a lightweight actuation system and test its performance by controlling the device

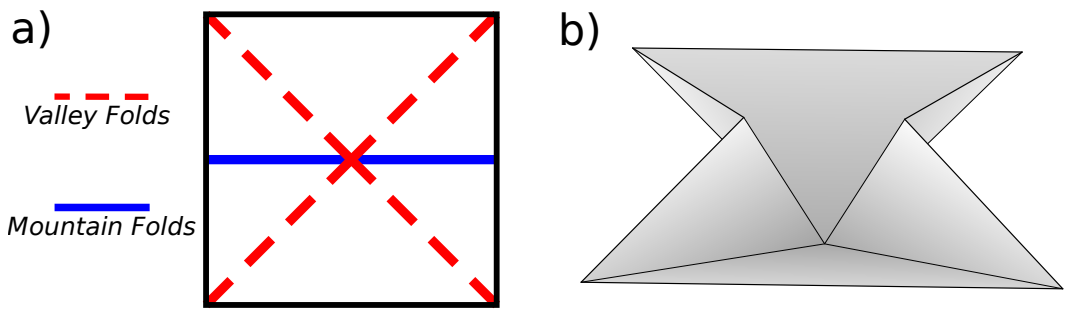

FIGURE 4.2: Waterbomb origami base: the blue lines for the mountain folds and the red lines for the valley folds, (a) flat and (b) folded configurations.

3. Proposal of several applications for industrial problems where tunable origami-based Helmholtz resonators can be highly beneficial for sound control and vibro-acoustics applications in general.

4.3 Waterbomb base

Origami designs offer extreme reconfigurability and a wide range of deployability thanks to their hinges rotation and their facets deformation. This can be exploited to create lightweight devices with controlled characteristics and tunable properties [Kamrava et al., 2018]. Much like the relationship between the microscopic and macroscopic properties of materials, each origami design inherits his properties from its origami base. In definition, the origami base is actually the crease pattern that can be duplicated in two directions, as origami designs are purely 2D designs, in order to recreate the full origami design or most of it in some cases. Therefore, designing an origami device starts by choosing the appropriate origami base. Guided by the application requirements and inspired by the state of the art [Kuribayashi et al., 2006, Lee et al., 2013, Lee et al., 2014], we decided to go with the origami base called, waterbomb (see Fig. 4.2). The origami waterbomb base is a single-vertex origami mechanism with unique characteristics that may prove advantageous in a wide range of applications, one of which is vibro-acoustics. The base shows a high potential as a testbed for smart materials and integrated actuation systems thanks to its straightforward geometry and multiple phases of folding/unfolding motion, which ranges from simple (completely flat) to more complex (3D configurations) [Hanna et al., 2014].
One of the reasons for using the waterbomb base lies in the fact that it exhibits an auxetic behavior. Mechanisms with auxetic behavior are mechanisms that have a negative Poisson coefficient. They display a counter-intuitive behavior, as under uniaxial compression (tension), these mechanisms contract (expand) transversely. A design that offers maximum volume variations is one of the critical requirement of the application requirements, hence using a design that allows for the expansion/contraction of the origami device in all direction at the same time (also known as displaying an auxetic behavior), seems to be an appropriate choice for an origami base in this case. Furthermore, the waterbomb can

be used in order to reproduce a rough example of fully closed simple geometries such as cylinders and spheres, which is another key requirement of the application requirements.

4.4 Design

4.4.1 2D design

Following the origami design methodology, we proposed in chapter 2, once the appropriate origami base (a base that has the potential to fulfills the application requirements) has been chosen, the next step is to generate the 2D design using ***Oripa*** software. The main goal of this step is to create a 2D design of a Helmholtz resonator, which is actually a cavity with an opening and a neck, that can vary its resonance acoustic frequency by altering its geometrical properties using origami principles. To that end, we need first to answer a couple of important questions:

1. Which geometrical part we need to vary in order to create our tunable origami-based resonators, the neck, the cavity, or both?

2. How can we keep the origami-based Helmholtz resonator acting like a traditional Helmholtz resonator (for example, keeping the cavity perfectly closed) while varying its geometrical properties?

As for the first question, for some reasons which will be mentioned later, we decided to go with the cavity; hence, the only part of the resonator, which will be made using origami concepts, is the cavity (that also includes the only part that is concerned by this step). A traditional rigid cylindrical neck, in this case, will be 3D printed and added to the device later on. The choice to only vary the cavity was made because of the following couple of reasons:

1. The neck is relatively much smaller than the cavity, which makes varying its geometrical properties that much more complex

2. Unlike the cavity where the only important property is its size (this is only the case for Helmholtz resonators with cylindrical rigid necks), the shape of the neck in addition to its size has a high influence on the acoustic properties of the resonator, thus trying to study the behavior of a Helmholtz resonator by altering the geometrical properties of its neck is a complex process

Now to answer the second question, the 2D origami design of the cavity was split into three different parts:

- A top-end part (see Fig. 4.3.a) that allows the attachment of the neck later on. The used concept was the same as [Lee et al., 2013] for their deformable wheels. They lacked a way to add the shaft for their wheels. Therefore, they came up with a new design for both their ends of the wheel. The design allows the addition of the shaft without compromising the fold-ability of the wheels. This part is crucial for our design since it will be utilized in order to add on the neck later on.

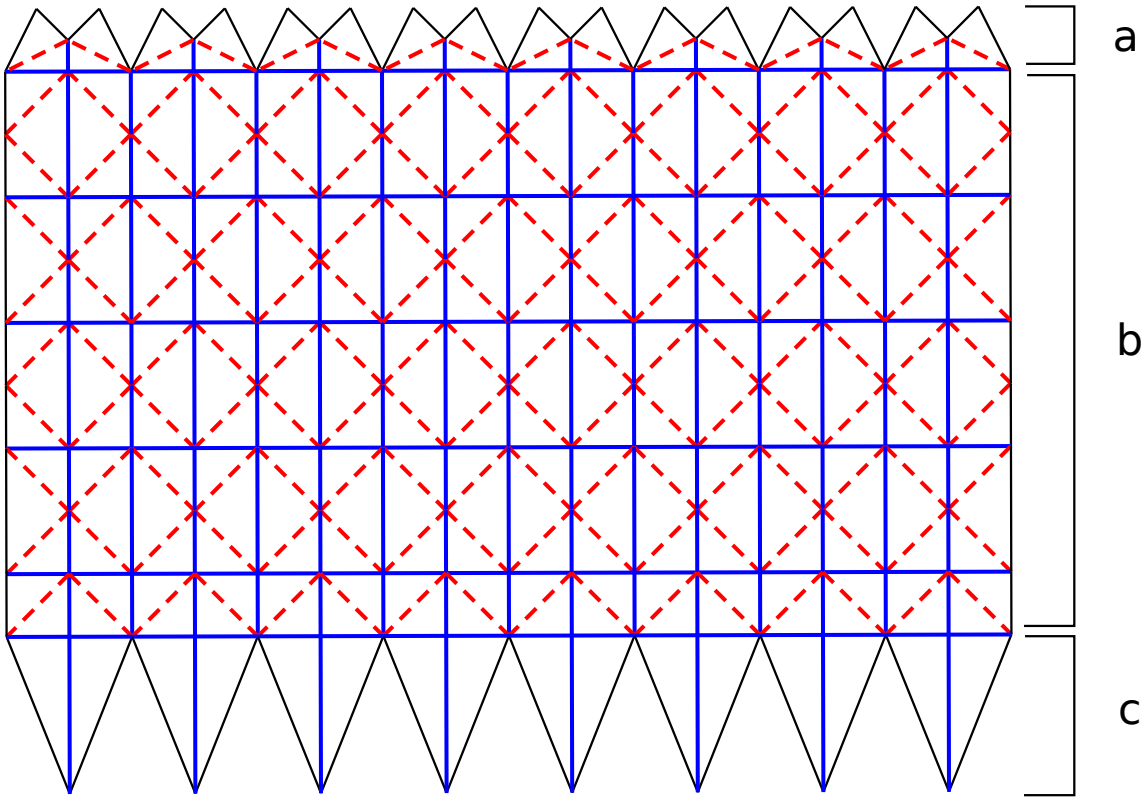

FIGURE 4.3: 2D design of the proposed origami Helmholtz resonator, made using the ***Oripa*** software, a) top end part b) cylindrical part c) bottom end part.

- Secondly, the waterbomb-based cylinder (see Fig. 4.3.b), which is an origami cavity with an auxetic behavior (negative Poisson coefficient).
- Finally, we added a bottom end part (see Fig. 4.3.c), which was inspired by the mechanism of the umbrella, as it is required for a Helmholtz resonator to have a closed cavity. This last part will keep the cavity closed during the shape-changing of the resonator.

4.4.2 3D design

The 3D design of the origami-based Helmholtz resonator is one of the key steps of our proposed methodology, for several reasons:

1. The ability to visualize the folded form (active form) of the origami device, and determine its geometrical properties in this state.
2. The possibility to test the foldability (functioning) of the origami-based Helmholtz resonator, from a purely kinematic point of view. In other words, determine if the

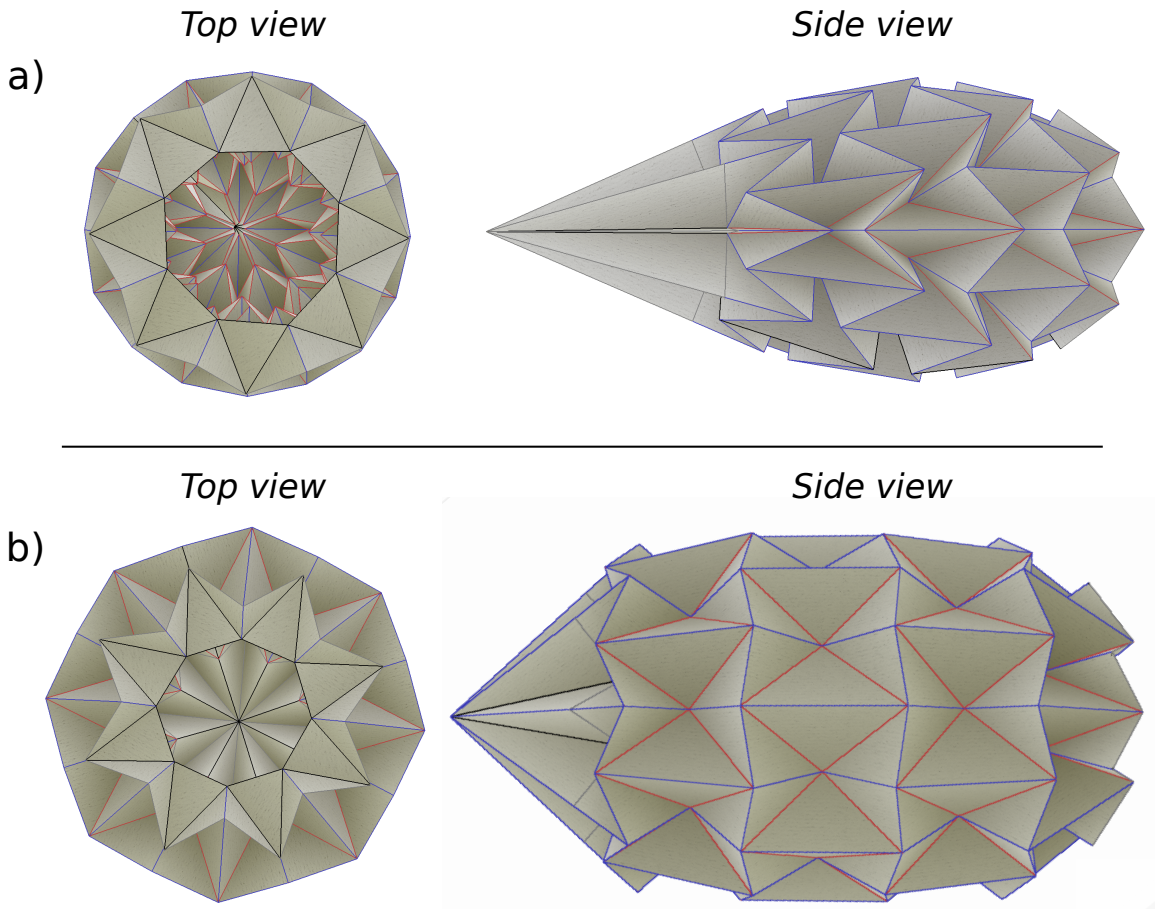

FIGURE 4.4: 3D design of the proposed origami Helmholtz resonator, made using the ***Freeform*** software, a) folded state b) unfolded state.

geometry respects the theories of origami when folded/unfolded. The device must also respect the application necessities, which are to maintain an entirely closed cavity and a rigid opening for the neck to be added later on.

3. The ability to develop a FE multi-physics model in order to numerically assess the performances of the resonator in the intended field of application (vibro-acoustics), as well as, to determine the parameters of the actuation system needed (a kinetostatic study), such as the number of actuators needed, the required forces for folding and the appropriate locations to attach the actuators.

4. The possibility to fabricate the device in its folded state (active state). One option is the utilization of multi-material 3d printing.

The starting point of the 3D designing process is the 2D design files, made using ***Oripa*** software. The flat design is first imported to ***Freeform*** as .dxf file. Then, using the predefined folding lines and with respect to their orientation (mountain and valley folds),

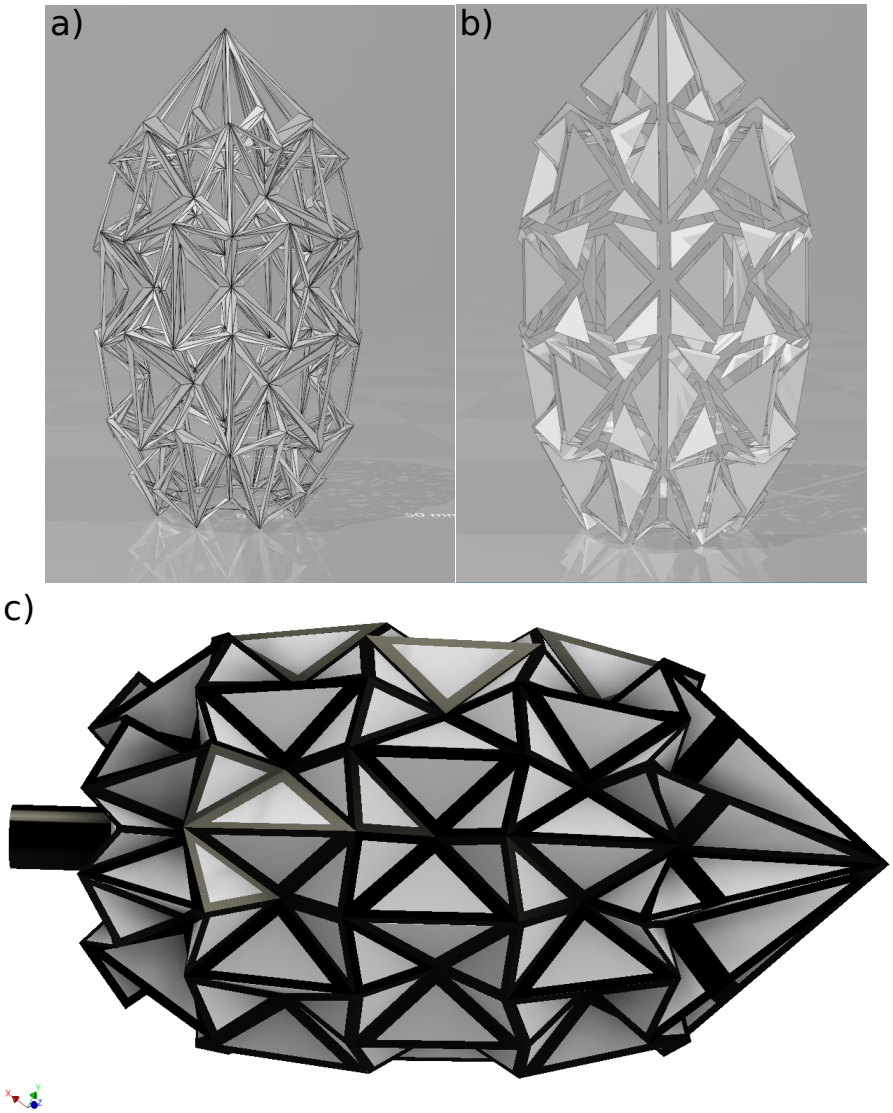

FIGURE 4.5: 3D design of the proposed origami Helmholtz resonator: first, the initial 3D design is divided into two parts a) folding lines and b) rigid facets, then using CAD software, c) the origami Helmholtz resonator is re-assembled, using both parts, as well as, a cylindrical neck.

the origami structure is folded, as shown in Fig. 4.4. Once both edges of the folded origami pattern come closer to each other, they are stitched together in order to create the resonators cavity using an available stitching tool. Finally, the foldability (functioning) of the device is tested in ***Freeform*** before exporting the design as .obj file. Next, ***MeshLab*** is used to repair the 3D design (remove duplicated vertices and facets generated from the stitching process in ***Freeform***). Using our ***Matlab*** codes, the design is then separated into two parts: soft edges (folding lines) and rigid facets, as shown in Fig. 4.5. This step will allow us to model the origami device accurately. Finally, the two parts are re-assembled using CAD software, then the rigid neck of the resonator is added. This structure is used later on for the development of the FE model.

4.5 FEA multiphysics simulations

This subsection discusses FE modeling simulation of the vibro-acoustics as well as the mechanical behavior of the proposed origami Helmholtz resonator. To that end, two different models were developed each for a different purpose. As mentioned above, one will be used in order to quantify the acoustic performances of the origami resonator, as for the second, it is for identifying the parameters of the actuation system, such as the number of actuators needed, the required forces for the folding and the appropriate integration of the actuators. Both models use the generated design files during the 3D designing step. The folding lines and the facets were each given different materials, as it is supposed to be while dealing with origami structures: a soft material for the folding lines and a rigid material for the facets.
The first model, which has been developed to describe the acoustic behavior, is a multi-physics model that couples the acoustic response and the mechanical behavior of the origami structure for a particular folding state, during a frequency analysis (low-frequency domain). The acoustic performances of the origami resonator were quantified using the acoustic absorption coefficient (α). See Sec. 3.4.3 for more details. The second developed FE model of the resonator is a kinetostatic model. It is utilized for determining the actuation system parameters. The model is first experimentally validated. Then, using the model several actuation strategies were tested and compared in order to find the appropriate actuation system, meaning the system, which optimizes the application requirements.

4.6 Fabrication

In the fabrication step of the methodology, several prototypes of the origami-based Helmholtz resonator were fabricated. Since origami-based Helmholtz resonator is a completely original concept and origami-based acoustic devices is still a relatively new field of research, trying to anticipate or foresee the properties of such devices can be very challenging and widely misleading. Therefore, in order to better understand the behavior of such devices, different prototypes with different properties and purposes were fabricated. As a result, it was possible to isolate the different properties and evaluate

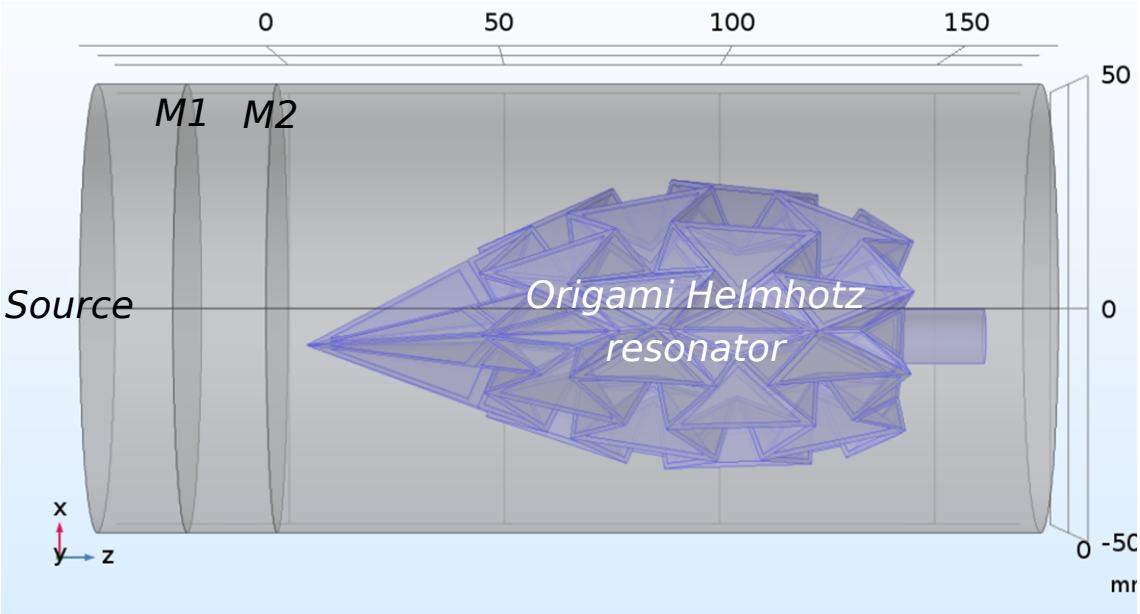

FIGURE 4.6: FE modeling of the one-load, two-microphone (M1 and M2) technique [E1050-10, 2012] for an origami Helmholtz resonator.

them separately. Three types of origami-based Helmholtz resonators were fabricated, as shown in Fig. 4.7:

1. Rigid 3D printed resonators: first, to preliminary test, as well as to better understand the influence of the origami-shaped cavity on the acoustic performance of the device; three rigid origami-based Helmholtz resonators were 3D printed, each with a different state of folding: folded, half-folded and unfolded. The three prototypes were printed from PLA, using an *Ultimaker 2*[1] 3D printer.

2. Quasi-rigid resonators: in order to study the effect of tunability on the acoustic properties of origami-based Helmholtz resonators, a quasi-rigid resonator was fabricated. The fabrication starts with a patterned, thick sheet of paper. The pattern is obtained by either using laser machining or a regular printing, which is used to generate the pattern before gluing it on top of the thick sheet. The sheet is then manually folded and dipped in a quasi-rigid glue. Finally, the neck of the resonator is then 3D printed and glued into its appropriate location. A quasi-rigid glue is used to add more stiffness to the device, as well as to ensure that the resonator cavity is correctly closed. As for the thick sheet of paper, it is used as a skeleton to give the device its origami shape; also, the thick sheet absorbs the glue better, resulting in an interestingly stiff device. The produced origami resonator is a quasi-rigid device that requires reasonably high tuning (folding) forces.

[1] https://ultimaker.com/en/resources/manuals/ultimaker-3d-printers/ultimaker-2

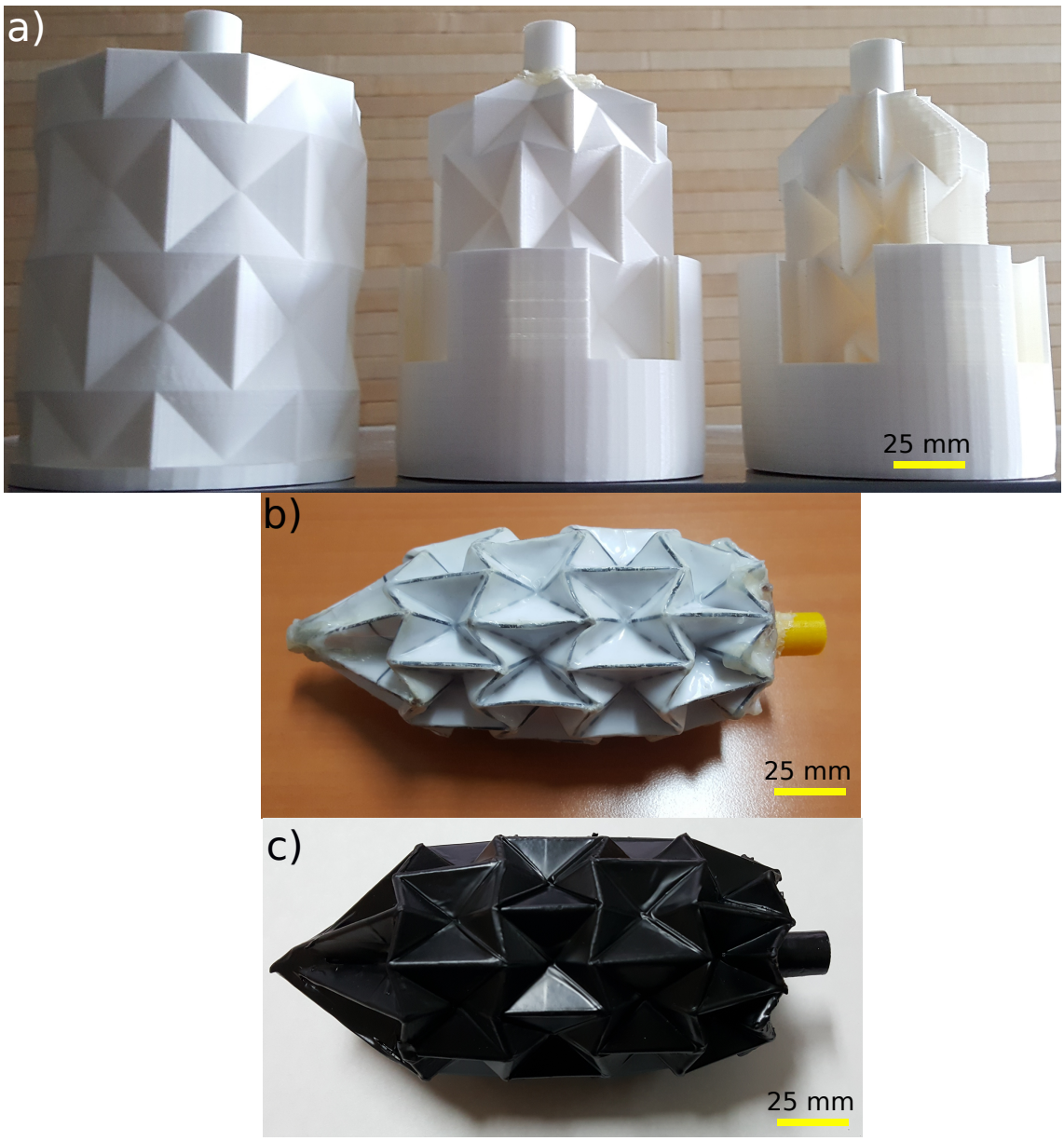

FIGURE 4.7: Different types of fabricated origami Helmholtz resonators: a)3D printed rigid origami resonators, unfolded, half-folded, and folded form left to right, respectively, b) quasi-rigid origami resonator, and c) flexible origami resonator.

3. Flexible resonators: to investigate the influence of flexibility on the origami-based Helmholtz resonators, more flexible resonators (compared to the quasi-rigid resonators) were fabricated. The fabrication process starts with the laser machining of a fatigue-resistant PETg polymer sheet, commercially known as *Axpet*[2]. The PETg sheet is utilized to create the facets, which make up 80% of the origami pattern, and the remaining 20% represents the folding lines (mountains and valleys). These ratios were chosen in order to generate a flexible device, compared to the quasi-rigid resonator, while also maintaining a certain rigidity, as it is necessary for Helmholtz resonators to self support. The laser-cut facets are connected with each other via small bridges of material left by the laser cutter. These bridges are used to temporarily hold the pattern (most of them will snap during folding). A clear thin film is glued on both sides of the 2D pattern before manually folding it. The clear film facilitates the folding and acts as folding lines. Then, both edges of the origami pattern are glued together. Once the origami structure is folded and glued properly, using a flexible glue from *Henkel AG Company*[3], a 3D printed rigid neck is added to the structure using the same glue. The use of ordinary epoxy glue may also work; however, it can make the glued parts very stiff, which defeats the purpose of fabricating a flexible device in the first place. Finally, a few layers of rubber coating is deposited on the origami-based structure in order to add some stiffness (especially to the folding lines), as well as, to help firmly close the cavity.

The study, characterization, and modeling of these origami-based structures can help us better understand and quantify their acoustic properties, in particular, as well as improve the process of designing high-performance origami-based acoustic devices, in general.

4.7 Experimental validation

Once the origami Helmholtz resonators are made, it is time to quantify their performances and characterize their properties. To that end, a series of experimental validation were conducted using a one-load two-microphone technique [E1050-10, 2012]. The latter is utilized to assess the acoustic absorption of the origami resonators. We settled on the acoustic absorption as our primary method for quantifying the performances of the resonators (as shown in Fig. 4.8), since unlike the acoustic transmission loss method, it can evaluate the acoustic energy absorbed by our systems, which we find to be a more significant factor for such systems at this stage. The experimental results were used in order to validate the proposed models for such acoustic devices, FE models, and analytical models (the natural frequency model and the P-TMM model). These models can provide valuable insights into the designing and control procedures of such origami-based tunable acoustic systems.
This section discusses the experimental quantification of the acoustic performances of the different types of origami-based Helmholtz resonators: rigid, quasi-rigid, and flexible.

[2] https://www.exolongroup.com/82/Axpet.htm
[3] https://www.henkel.com/company

Lastly, it provides a comparison between traditional Helmholtz resonators and the three studied origami-based resonators.

4.7.1 Rigid origami Helmholtz resonator

One of the concerns related to the use of origami devices is the identification and understanding of the extent of the impact of these shapes and structures in the desired field of application, in our case vibro-acoustics. For Helmholtz resonators with cylindrical neck and an origami-based cavity, some of these concerns can be expressed as such:

1. Does the origami shape of the resonator cavity has an influence on the acoustic properties of the devices?

2. In addition, does this influence or lack of, remain present after the activation of the device (folding/unfolding of the resonator cavity)?

In order to address these concerns, experimental testing on origami-based rigid Helmholtz resonators was conducted. Three rigid resonators with different states of folding (unfolded, half-folded, and folded) were 3D printed. The size and the folding states of the origami Helmholtz resonator were arbitrarily chosen. Compared to the volume of the unfolded state (100%), the half-folded and the folded states have relative volumes of 51% and 18%, respectively. Using an acoustic transmission tube, a one-load two-microphone technique [E1050-10, 2012] was used to evaluate the acoustic absorption of three resonators. The latter were inserted in a forward position (in the AB position as shown in Fig. 3.14) without leaving any space between the back of the resonators and the end wall of the tube. No foam was added with the resonators; instead, supports were printed to keep the resonators well centered inside the transmission tube, especially for the half-folded and the folded resonators.
The experimental results of the three rigid origami resonators generated curves similar to that of a traditional Helmholtz resonator with a cylindrical neck and cavity: a very high acoustic absorption in the low-frequency range (50-500 Hz) with a narrow (very selective) bandwidth, as shown in Fig. 4.8.a and Tab. 4.1. The relationship between the different absorption peaks also seems to be consistent with that of traditional Helmholtz resonators. In other terms, the bigger the volume of the resonator cavity is, the low its resonant frequency; however, this is only true for resonators with a cylindrical neck. These results are in accordance with the FE model introduced in Sec. 3.4.3.1 (see Fig. 4.9.a). The latter uses a Johnson-Champoux-Allard model to simulate the thermo-viscous losses produced by neck. The model also considers all the walls of the cavity and the neck to be acoustically rigid.
Furthermore, these results are also in a good agreement with the analytical models of the P-TMM (see Sec. 3.4.2) and the resonant frequency (see Sec. 3.2.2), as shown in Fig. 4.9.a. As a result, since the analytical models do not take into account the shape of the cavity into consideration, it is safe to consider that the shape of the cavity (origami shape) has no influence on the resonators acoustic performance, at least when it comes to the resonant frequency. Moreover, according to the experimental results here, it is

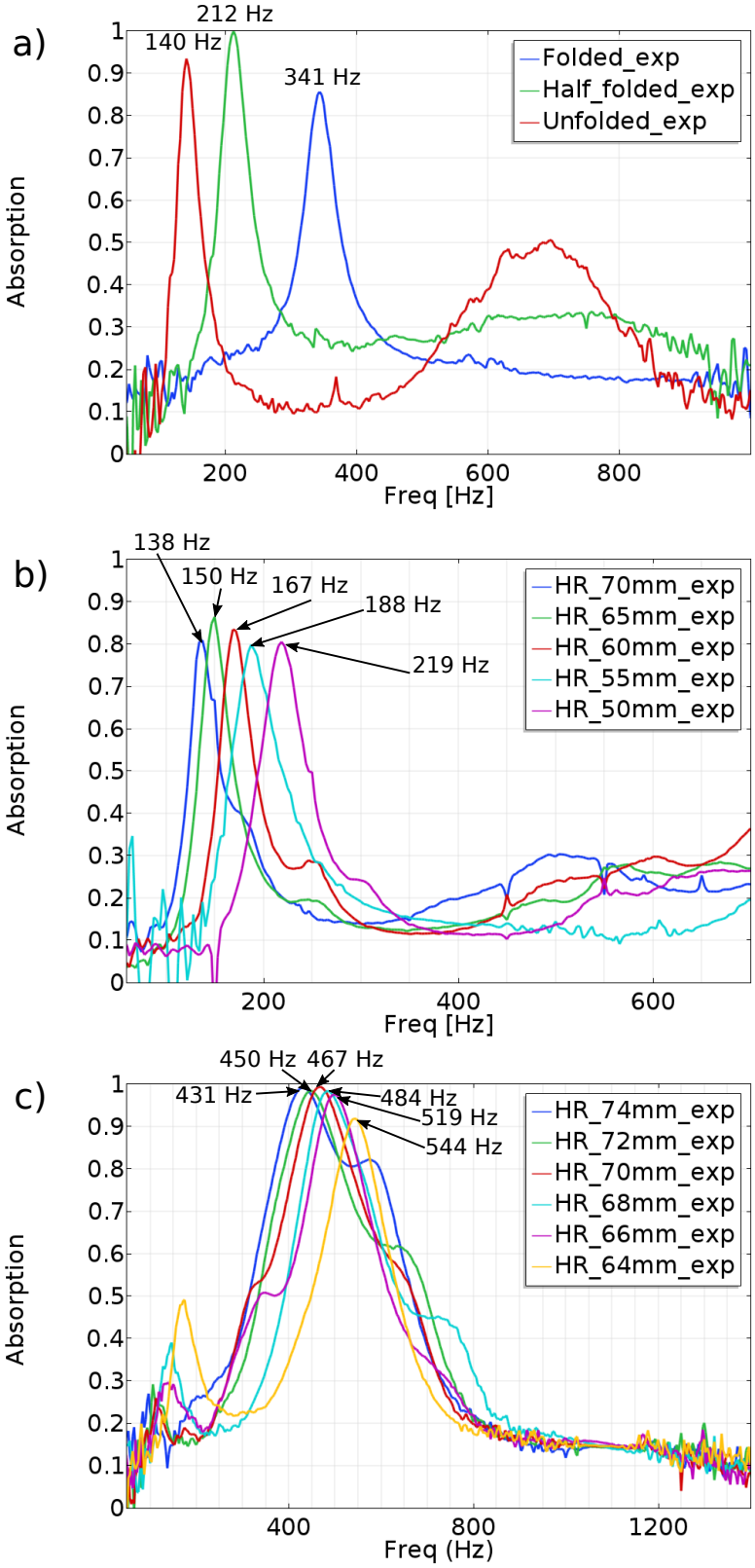

FIGURE 4.8: Experimental results of the acoustic performances (acoustic absorption) of the three different origami Helmholtz resonators: a) 3D printed rigid resonators, b) quasi-rigid resonator for different diameters of the cavity (70, 65, 60, 55, 50mm), and c) flexible resonator, also for different diameters of the cavity (74, 72, 70, 68, 66, 64mm).

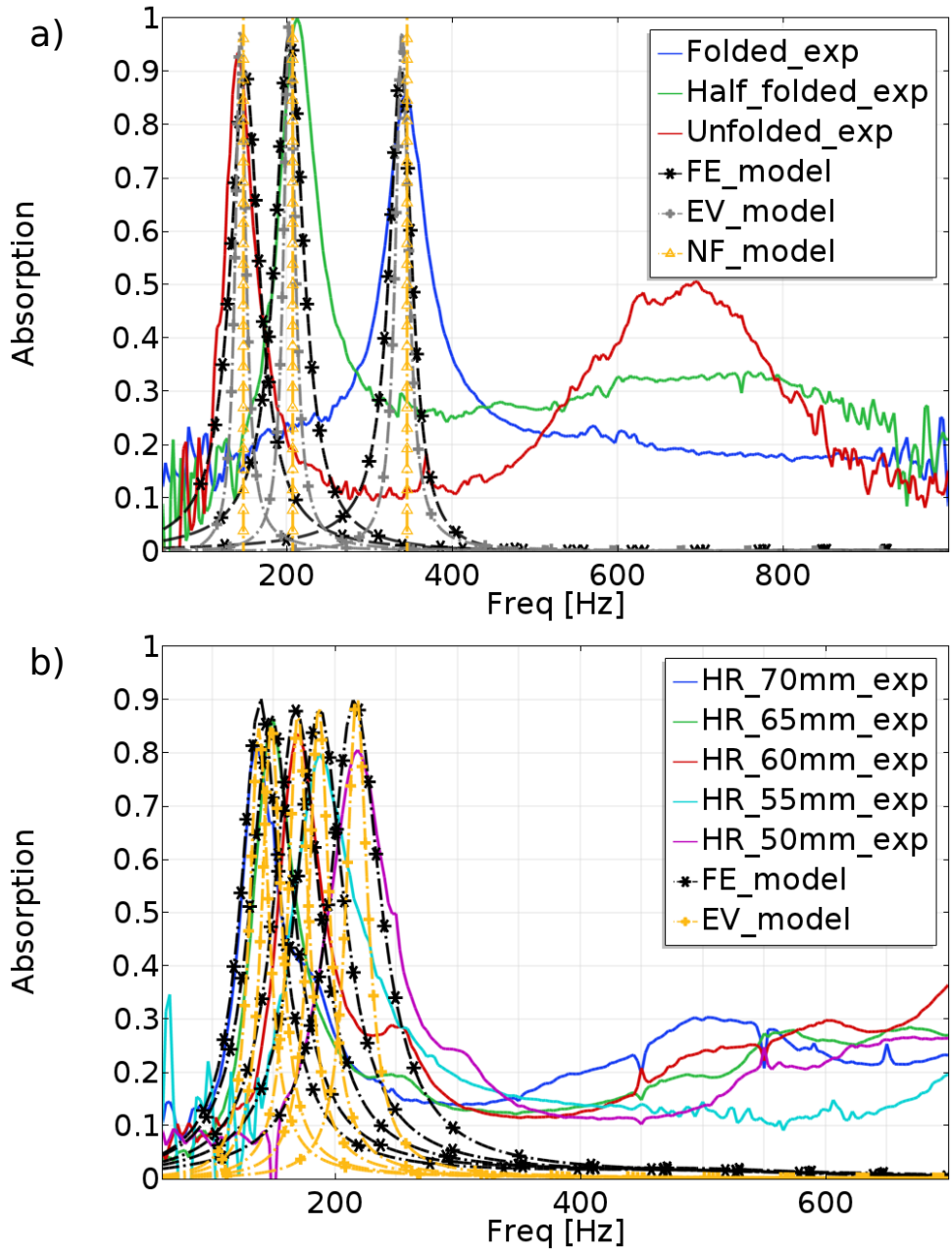

FIGURE 4.9: Comparison between the experimental results of the acoustic performance (acoustic absorption) of origami Helmholtz resonators and FE model, the equivalent volume (EV) model , and the natural frequency (NF) model: a) 3D printed rigid resonators and, b) quasi-rigid resonator.

not only valid when it comes to cavities with simple shapes, such as spheres, cubes, and cylinders as already known in the literature, but it is also true for far more complex shapes such as origami shapes and for different states of folding as well.
To summarize, the NF model is able to estimate the resonance frequency of the origami-based Helmholtz resonator. Additionally, the EV model, which was validated by an FE model, is a fast analytical tool for the design of origami-based Helmholtz resonators, as it is able to provide the frequency evolution of the acoustic performances around the resonance frequency. Lastly, all the developed models are not able to predict the increase in the absorption rate (α) measured in the higher frequency range (see Fig. 4.9), which may be due to structural behavior or losses in the vicinity of the origami walls.

Table 4.1: Experimental absorption of the rigid origami Helmholtz resonators for different states of folding.

State of folding	***Unfolded***	***Half-folded***	***Folded***
Freq. at the peak (Hz)	140	212	340
Absorp. At the peak (%)	93	100	86
Average absorption (%)	93		

4.7.2 Quasi-rigid origami Helmholtz resonator

As observed in the previous section, rigid origami-based Helmholtz resonators act as traditional Helmholtz resonators (for the case of cylindrical necks only). The objective of this section is to study the influence of the addition of foldability on acoustic performances. Such property will allow for the acoustic tunability of the resonators, which is the main purpose of using origami design in the first place. To that end, a quasi-rigid origami resonator was fabricated. A quasi-rigid configuration is a name we chosen for a resonator that is sufficiently rigid to prevent any leakage but also can be folded. For the purpose of obtaining such characteristics, the folding lines of the origami cavity need to be almost as rigid as the cavity facets. This gives the resonator acoustic properties comparable to those of a rigid resonator but also makes it harder to fold. However, due to the shape of the folding lines (V-shaped), when forces are applied on the origami cavity, they tend to attract a high concentration of stress, resulting in their deformation; thus, the folding/unfolding is achieved.
Once the quasi-rigid resonator was fabricated, a series of acoustic characterization tests were conducted using an acoustic transmission tube. Similar to the rigid resonators, here also a one-load two-microphone technique [E1050-10, 2012] was utilized to evaluate the acoustic absorption of the resonator. However, in this case, the resonator was inserted in a backward position (in the BA position as shown in Fig. 3.14) with a 10 mm space between the resonator and the end wall of the tube. This configuration seems to generate a little bit better performance in terms of the acoustic absorption rate. The volume of the resonator was modified by adjusting its diameter and then it was tested each time. Rings with diameters ranging from 70 to 50 mm, were utilized in order to adjust the middle section of the origami cavity to the desired folding state. The experimental results

were as expected, high acoustic absorption peaks in the low-frequency range (50-500 Hz) with a narrow (very selective) bandwidth, where the bigger the cavity volume is, the lower is the corresponding resonant frequency (as shown in Fig. 4.8.b). Acoustic properties exhibited by the quasi-rigid origami resonator are very consistent with those of a rigid origami resonator, which makes them also consistent with a traditional Helmholtz resonator as well. One thing to state, however, even though the absorption rate of the quasi-rigid resonator is high, with an averaging above the 80% for the five tested folding states, it is still a tiny bit lower than the rate of a rigid Helmholtz resonator (origami or otherwise). Nonetheless, we believe that the absorption rate of the quasi-rigid resonator can be improved by using high-performance materials and manufacturing machines. The quasi-rigid resonator was also able to generate a frequency shift of 81 Hz in the low end of the low-frequency domain. Starting from 138 Hz with a diameter of 70 mm to 219 Hz with a diameter of 50 mm. More details are available in Tab. 4.2. This shows that the quasi-rigid origami resonator has an impressive ratio of frequency shift to geometrical variation, which averages for more than 4 Hz for each 1 mm variation in the diameter of the origami cavity.

For the quasi-rigid origami Helmholtz resonator, comparing the experimental results to the analytical resonant frequency to confirm its acoustic behavior is not possible, since the added boundary conditions: the backward insertion of the resonator and the 10 mm space between the latter and the end wall of the tube, cannot be taken into account in a somewhat simple model. Therefore, the same FE model (see Sec. 3.4.3.1) and P-TMM model (see Sec. 3.4.2) used above for the rigid resonators were used here as well, with the appropriate boundary conditions, of course, and the results are presented in Fig. 4.9.b. The good agreement displayed between the experimental results and the models (natural frequency model, P-TMM model, and FE model) proves that the quasi-rigid origami has an acoustic behavior similar to that of the rigid origami as well as a traditional Helmholtz resonator, while at the same time it has tunability properties.

Finally, the results highlighted here validate the capabilities of our proposed origami methodology as well as our origami design for a tunable Helmholtz resonator. We were able to achieve using the same origami device a wide frequency shift 81 Hz (59% compared to the lower frequency), from 138 Hz to 219 Hz, with a relatively low geometrical variation, corresponding to a 20 mm variation in the diameter. Compared to the examples of the literature (see Sec.3.3), we were able to more than triple the value of the relative frequency shift of 59%, which is at 14% and 17.5% for the work of [Yu et al., 2017] and [Abbad et al., 2018], respectively. However, this value is still significantly lower to that of [De Bedout, 1996], which is at 158%; nonetheless, that is the price to pay for a small-scale, lightweight, monoblock concept with an optimal geometrical variation.

TABLE 4.2: Experimental absorption of the quasi-rigid origami Helmholtz resonator for folding different diameters.

Diameter of the origami HR (mm)	***70***	***65***	***60***	***55***	***50***
Freq. at the peak (Hz)	138	150	167	188	219
Absorp. At the peak (%)	81	80	83	76	81
Total bandwidth (Hz)	81(59%)*				
Average absorption (%)	80.2				

*Relative bandwidth compared to its low frequency (138 Hz)

4.7.3 Flexible origami Helmholtz resonator

Our final acoustic investigation here evolves, adding flexibility. In the previous section, we were able to validate our proposed origami concept: a tunable Helmholtz resonator, using an adaptive origami cavity, which can achieve a high acoustic absorption and a broad frequency shift for relatively low geometrical variation. Nonetheless, since this a fairly novel concept, it still holds many unknown and hard to predict factors and aspects. One of these unknown factors is the effect of adding flexibility to the folding lines of the origami structure. Also, what kind of exotic acoustic properties can such a process produce? Therefore, a previously manufactured flexible origami Helmholtz resonator is tested. It is important to note that the quasi-rigid and the flexible resonators have the same geometrical properties for both the neck and the cavity.
After the fabrication of the device, a series of acoustic tests are conducted to characterize its acoustic performance (acoustic absorption). A transmission acoustic tube and a one-load two-microphone technique [E1050-10, 2012] are utilized here as well. Furthermore, the resonator was also inserted in a backward position here (in the BA position as shown in Fig. 3.14) with a 10 mm space between the resonator and the end wall of the tube, without adding any foam. This configuration seems to generate better performance in terms acoustic absorption rate, especially in this case where the difference is noticeable. Furthermore, the resonator was folded into different diameters and tested each time. Rings with diameters ranging from 74 to 64 mm, were utilized in order to adjust the middle section of the origami cavity to the desired folding state. The experimental results, in this case, were very different from what is expected from a traditional Helmholtz resonator. The flexible resonator produced very high acoustic absorption peaks in the low-frequency range with a very wide (less selective) bandwidth (see Fig. 4.8.c). Moreover, the bigger the cavity volume is, the lower is the corresponding resonant frequency. Another thing to mention, besides the extensive bandwidth, is even though, the quasi-rigid and the flexible resonators have the same geometrical properties for the neck and cavity both, while the quasi-rigid tend to occupy the low end of the low-frequency domain (same as the rigid resonator) the flexible appear to occupy the high end of the low-frequency domain. In other words, the expected peaks of the resonator are lowered (have lost their high amplitude), but still visible in the lower-left corner of Fig. 4.8.c, and new peaks at higher frequencies and wider bandwidth have appeared (see also Fig. 4.8.c).

The flexible resonator was able to generate a frequency shift of its peak absorption of 113 Hz, from 431 to 544 Hz, which is a shift of 26% compared to the low point (431 Hz). The resonator was also able to generate a shift of 116, 169, and 213 Hz with an average bandwidth of 47, 63, and 124 Hz for the 95%, 90%, and 80% absorption rate, respectively (see Tab. 4.3).

In order to understand the physical reasons of this change in behavior, a multi-physics FE model (see Sec. 3.4.3.2) was utilized for modeling the flexible origami resonator. The model couples two different physics of the device: the acoustic behavior, which is basically, the behavior we modeled above for the rigid and quasi-rigid resonators, and the mechanical behavior, which cannot be ignored in this case since it plays a significant role in the overall behavior of the flexible origami resonator. For the acoustic behavior, it was similar to the two cases above, a one-load two-microphone technique [E1050-10, 2012] was implemented with the appropriate boundary conditions and a Johnson-Champoux-Allard model for the thermo-viscous losses in the neck, as well as, the cavity. As for the mechanical behavior, instead of supposing that the cavity and the neck walls to be acoustically rigid, we consider them to be a shell structure (a thin mechanical structure). Our origami design, described above in the 3D design step, allows us to separate the folding lines from the facets, which mean that we can assign a flexible material for the folding lines and rigid material for the facets. Finally, the FE model was coupled with ***Matlab*** and a genetic algorithm in order to identify the model parameters, such as airflow resistivity for such structure. The model proves to be in good agreement with experimental results, as shown in Fig. 4.10. This model can be an exciting tool for better understanding and mastering the properties of the flexible origami resonator.

The main limitation of using Helmholtz resonators, except its many advantages (simple concept, passive acoustic device, very effective at low frequencies, reasonably small geometrical properties . . .), is its narrow bandwidth. As a result, many scientists and researchers (including us) are always exploring different strategies, methodologies, and technologies for tunable (adaptive) Helmholtz resonators. Keeping that in mind, the results displayed by the flexible resonator shows that overcoming such limitation is entirely possible, which gives this resonator a whole new perspective. In addition to the fact that the flexible origami resonators can provide very high acoustic absorption with extensive bandwidth, it also provides tunability (adaptability) of the absorption bandwidth, and with relatively small geometrical variation, 20 mm of diameter variation for 113 Hz frequency shift of the absorption peak (from 431 to 544 Hz). In other words, it can generate a tunability (adaptability) with an average of 5.6 Hz per mm. In addition to these interesting and exotic acoustic properties, the origami-based Helmholtz resonators are also passive, lightweight, monoblock, relatively small, and cost-effective acoustic devices.

The flexible origami resonator can be a game-changer when it comes to low frequency, truly passive, and high-performance acoustic control devices.

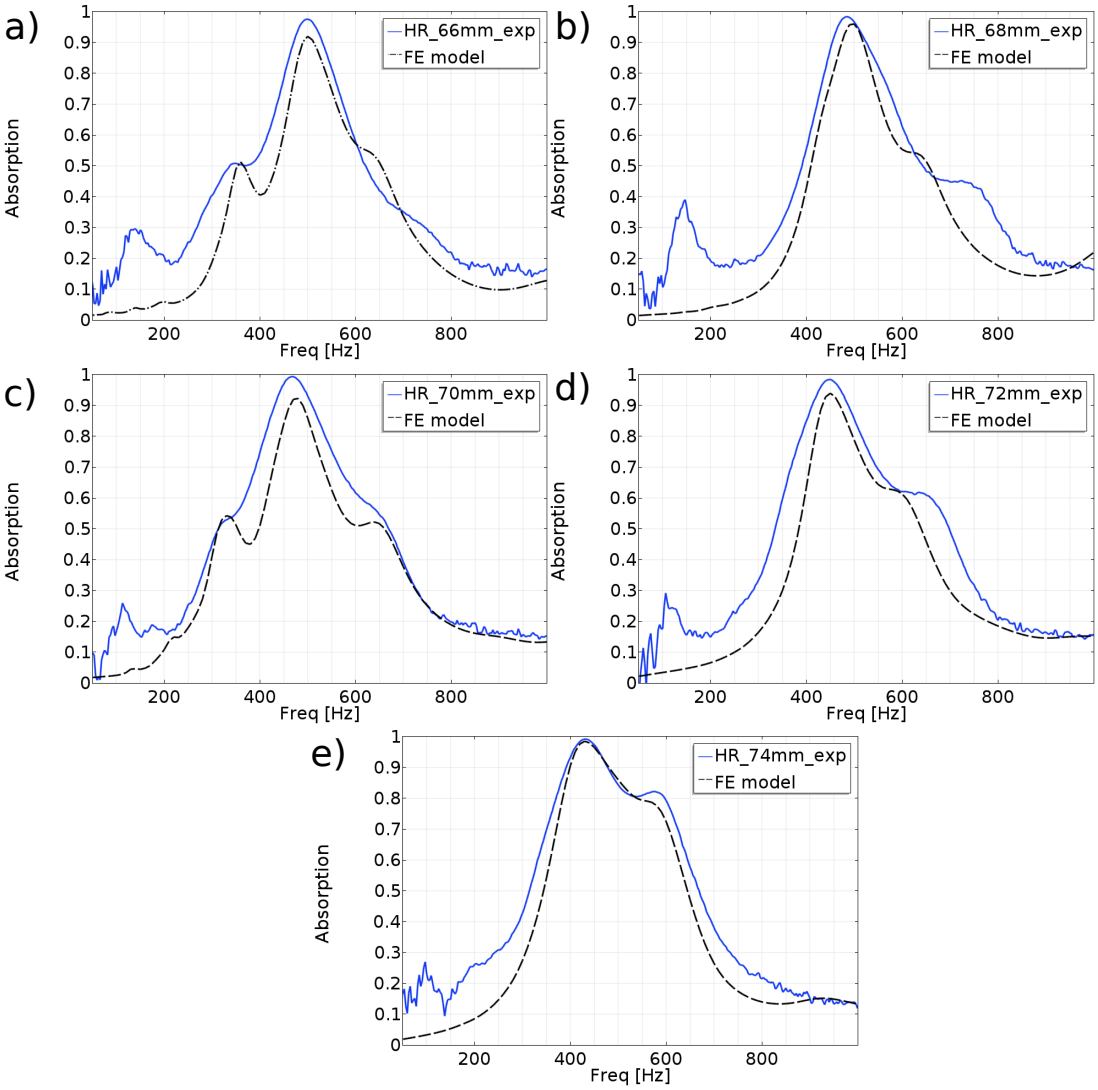

FIGURE 4.10: Comparison between the experimental results of the acoustic performance (acoustic absorption) of a flexible origami Helmholtz resonator and the corresponding FE model, for different values of the cavity diameter: a) 66mm, b) 68mm, c) 70mm, d) 72mm, and e) 74mm.

TABLE 4.3: Experimental absorption of the flexible origami Helmholtz resonator for different folding diameters.

Diameter of the origami HR (mm)		***74***	***72***	***70***	***68***	***66***	***65***	***64***	***Ave.***
Freq. at the peak (Hz)	peak	431	450	467	484	500	519	544	
	bandwidth	113(26%)*							
Freq. for 95% absorp. (Hz)	min-max	403-460	425-471	444-494	466-510	481-519	-	-	47
	indiv. bandwidth	57(14%)*	46(11%)*	50(11%)*	44(9%)*	38(8%)*	-	-	
	total bandwidth	116(29%)*							
Freq. for 90% absorp. (Hz)	min-max	391-478	413-488	431-509	453-525	472-531	497-541	531-560	63.4
	indiv. bandwidth	87(22%)*	75(18%)*	78(18%)*	72(16%)*	59(13%)*	44(9%)*	29(6%)*	
	total bandwidth	169(43%)*							
Freq. for 80% absorp.(Hz)	min-max	368-600	387-516	409-536	437-560	453-553	475-559	509-581	123.9
	indiv. bandwidth	232(63%)*	129(33%)*	127(31%)*	123(28%)*	100(22%)*	84(18%)*	72(14%)*	
	Total bandwidth	213(58%)*							

*Relative bandwidth compared to its low frequency

4.7.4 Comparison of the origami-based Helmholtz resonators

This section presents a comparison between tradition Helmholtz resonators and origami-based Helmholtz resonators(see Tab. 4.4). The comparison can be summarized in the following:

- All three Helmholtz resonators, the traditional, the rigid, and the quasi-rigid, exhibit the same acoustic behavior classified as a narrow (selective) bandwidth with a high absorption rate. This behavior is entirely independent of the mechanical behavior of the resonators, which is an apparent fact made clear by all the models (FE models and analytical models) used to describe it. In contrast, the origami-based flexible Helmholtz resonator displayed a rather unusual acoustic behavior, classified as a broad, thus less selective bandwidth with a high absorption rate. This behavior was the result of the tradition neck effect caused by the opening of the resonator combined with the resonance of the cavity walls, which hold a unique shape and mechanical properties compared to traditional resonators.

- Despite the high tunability of the quasi-rigid origami-based Helmholtz resonator, the flexible resonator still demonstrates an even greater tunability, which another benefit of using a flexible resonator in addition to its broad bandwidth effect. That said, these benefits come at a cost, as for resonators with the same geometrical properties, which is the case here, the flexible resonator seems to cover slightly higher frequencies (always in the low-frequency domain) compared to the quasi-rigid resonator.

Even though origami-based acoustic devices, in general, and Helmholtz resonators, in particular, remain a new concept which yet to revealed all its challenges or potential, these results provide a comprehensive example of the usefulness of origami-based Helmholtz resonators. This usefulness is not represented by the displayed high performance only, but also by the unprecedented and added options, qualities, and features as well.

Table 4.4: Comparison of the three different origami-based Helmholtz resonators.

Helmholtz resonator	***Traditional***	***Rigid***	***Quasi-rigid***	***Flexible***
Absorp. at the peak	Very high	Very high	High	Very high
Bandwidth at the peak	Narrow	Narrow	Narrow	Very wide
Selectivity	High	High	High	Low
Effect of the cavity's shape on the performance	Inconsequential	Inconsequential	Inconsequential	High
Modeling using equivalent volume supposition	Possible	Possible	Possible	Not possible
Region treated of the low frequency domain	Low end	Low end	Low end	High end
Tunability	Impossible	Impossible	High	Very high
Forces needed for the folding/unfoding	-	-	High	Medium

4.8 Actuation system integration and control

During the experimental validation, only the acoustic performances of the proposed structure were considered. It was confirmed that the origami Helmholtz resonators hold great potential for noise control applications specifically and vibro-acoustics in general. The next step is to move on to the actuation and control of such devices. Therefore, this section discusses the proposed actuation system, its integration, and the control of the origami resonators. In order to find an appropriate actuation system for the origami structures, a study composed of three different steps is conducted:

1. Kinetostatic analysis: this first step is required for the identification of the mechanical behavior of the proposed origami resonators.

2. Actuation system: the second step is needed for the determination of an appropriate actuation system and its different parameters. This is usually done by using the results generated from the kinetostatic analysis (first step) as a starting point (or input).

3. Control: the final step, which involves an experimental validation of the proposed actuation system.

This study is a crucial and essential step. It requires the exploitation of the 3D origami design (design of the origami structure in its active/deployed state) and the 3D multiphysics origami model, which, as mentioned before, are novel and critical steps of our proposed origami design methodology. Origami structures are extremely capable and proficient in terms of size reduction, they exhibit a lightweight concept, and they provide high adaptability and reconfigurability, especially in the case of shape-shifting origami devices. Therefore, conducting a full study in order to determine the appropriate actuation system, which can convey and conserve such characteristics and properties, is necessary.

4.8.1 Kinetostatic analysis

One of the main limitations of most origami methodologies available today is the concept of zero thickness. In other words, they consider and handle origami structures as systems with no thicknesses. As a result, only origami tools and models that simulate the kinematical behavior of origami structures can be developed (see Sec. 1.4). This represents a significant restriction for the design, modeling, and exploitation of origami structures in the engineering field, especially since the performance of such structures in real-life engineering applications depends heavily on their mechanical behavior. To that end, a 3D FE model based on the 3D origami design of the Helmholtz resonator was developed. The main purpose of this model is to simulate the mechanical behavior of the origami resonator during the folding phases. It was used here to perform a kinetostatic analysis (with a large deformation), which will identify the different parameters of the actuation system required for the studied origami structure.
Moreover, the two parts of the origami structure can be assigned two different materials:

a soft material for the folding lines and a more rigid material for the facets. This is very important for the modeling of the mechanical behavior of origami structures; otherwise if both parts of the geometry were assigned the same material, instead of simulating the folding of an origami structure, we would be simulating the deformation of a traditional mechanical structure. Furthermore, during the study we consider the origami structure to be a shell-like structure (a thin mechanical structure).
In order to validate the kinetostatic analysis conducted using the FE model, two experimental setups were considered. The first setup is for the validation of the folding/unfolding process of an origami base waterbomb, the basic unit for our resonator's origami design. The second setup is for the validation of the folding/unfolding motion of the full origami Helmholtz resonator. For the waterbomb experimental validation, four bases were used, each with a different rigid facets to flexible folding lines ratio, 80%, 70%, 60% and 50%, as shown in Fig. 4.11.a. Supports were fabricated to maintain the bases during the testing. The former contains two axes, which allow a uni-direction motion, thus permitting the folding/unfolding motion of the origami base. The tested origami base is taped form one side to the fixed part of the support and from the other side to its mobile part. The latter is then attached to one end of a load cell (sensor) using a stainless steel wire. The other end of the load cell is screwed to a linear stage, as shown in Fig. 4.11.b. The high precision stage is controlled using ***Matlab/Simulink*** software. Its linear motion, in its turn, controls the motion of the mobile part of the support; thus, it also controls the folding rate of the tested origami base. Simply put, when the linear stage generates a linear motion, it is translated to an equivalent folding rate. The force required to generate such folding is then determined by the load cell. For the model, the same boundary conditions were implemented. It is visible that there is a good agreement between the model and the experimental results for all origami bases with different ratios, as shown in Fig. 4.12. Consequently, it proves the efficiency of the model in the prediction of the kinetostatic behavior for relatively simple origami structures, mainly, origami bases.

As proof of concept for the validation of more complex origami geometries, a flexible origami Helmholtz resonator was fabricated and mounted into the experimental setup. It was fixed from one end (the neck) and attached the load cell using a stainless steel wire. Similarly as above, the load is screwed to a linear stage (see Fig. 4.11.c). When the linear stage moves, the origami resonators unfolds (deploys), which is initially in a folded state, and the corresponding required forces can be determined using the load cell. The same boundary conditions were duplicated in the model and tested, using the parameters displayed in Tab. 4.5. When the experimental results for five different tests of the origami Helmholtz resonator were compared to the model, it is evident that there

Table 4.5: Properties of the origami-based Helmholtz resonator.

Part of the resonator	Thickness (mm)	Young's modulus (MPa)	Density ($Kg.m^{-3}$)
Folding lines	0.2	62.5	1206
Facets	0.5	2500	1330

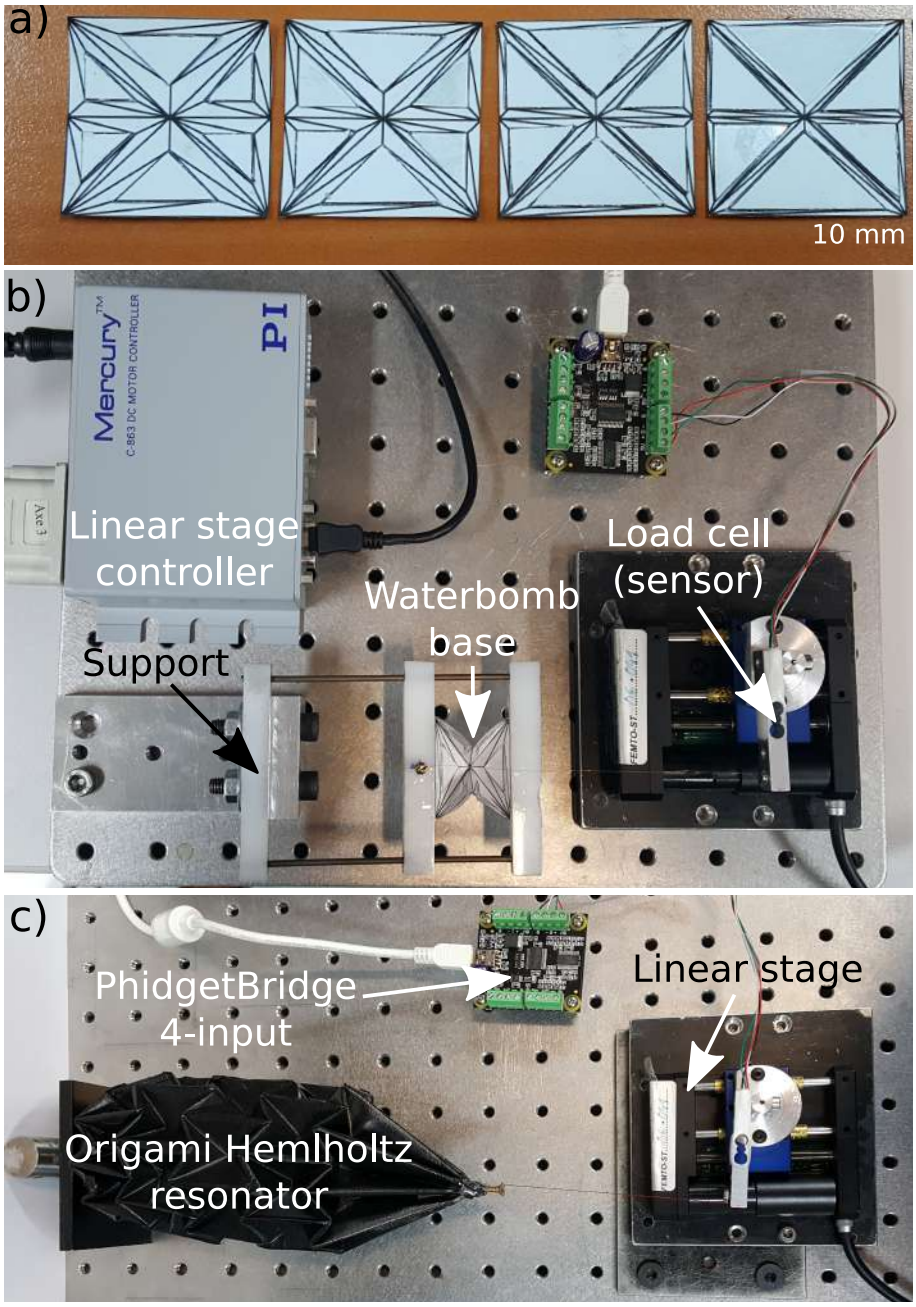

FIGURE 4.11: Experimental setup of the kinetostatic characterization of origami Helmholtz resonators: a) fabricated waterbomb origami bases containing different ratios of rigid (based on Axpet material) facets 50%, 60%, 70% and 80%, from left to right respectively, b) experimental setup for the characterization the waterbomb base and c) a similar setup for the characterization of an origami Helmholtz resonator.

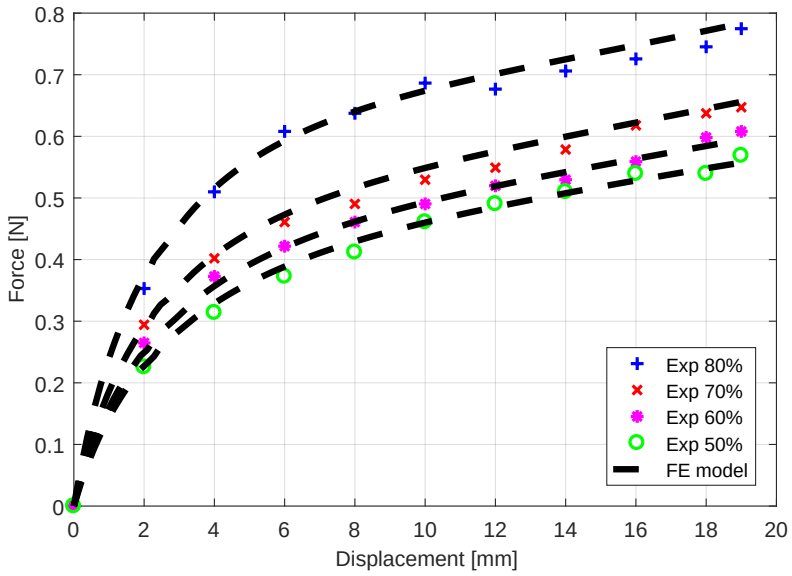

FIGURE 4.12: Comparison between the experimental results and the FE model during the folding of different waterbomb origami bases containing different ratios of rigid facets (80%, 70%, 60% and 50%).

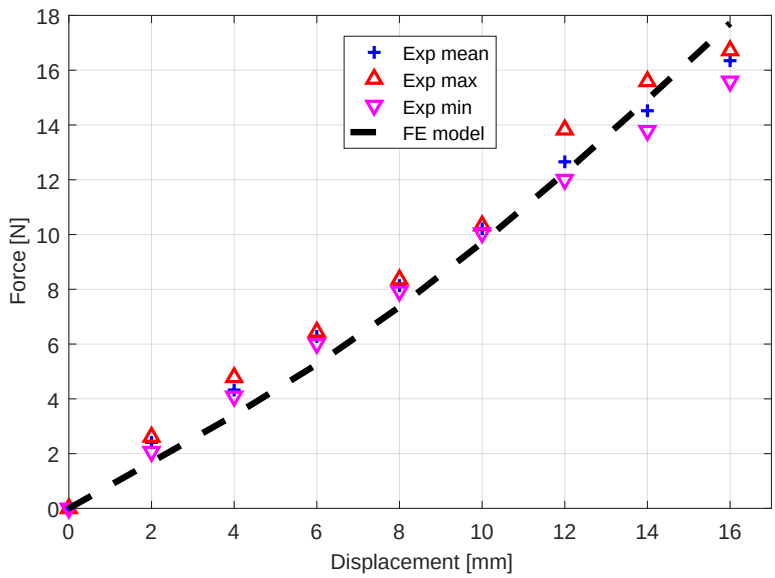

FIGURE 4.13: Comparison between the experimental results and the FE model during the unfolding of a flexible origami Helmholtz resonator: the mean, the maximum and the minimum of five different tests displaying the applied longitudinal force on the structure's length expansion, also known as the structure's unfolding or deployment.

is a good agreement between both of them, which proves the effectiveness of the model in this case as well, as shown in Fig. 4.13.
The modeling concept proposed and validated here of non-zero-thickness origami structures can be considered as a key tool as well as a game-changer for the design, modeling, fabrication, and exploitation of engineering-oriented origami devices in a wide range of applications.

4.8.2 Actuation system investigation

Now that we have an efficient model for conducting kinetostatic analyses on origami Helmholtz resonators, it is time to investigate actuation mechanisms which are the most appropriate for such an acoustic device. In order for the proposed actuation system to stay true to the interesting properties and the characteristics granted to the Helmholtz resonator from its origami design, it needs to respect a few terms:

1. Ability to generate very large deformations, or in this case high volume variation, which can be translated to a frequency shift in the studied vibro-acoustic application.

2. Simple system concept with a low number of actuators as possible, as it allows for more compactness and easier control.

3. Lightweight concept, which is essential in the case of noise control in aeronautics, for example, one of the targeted application fields.

4. Low required forces by generated deformation/volume variation (frequency shift) ratio, for more efficient folding/unfolding.

Now, let us suppose that we have an ideal origami Helmholtz resonator, a zero-thickness origami resonator that can be perfectly folded/unfolded without any external constraints. Meaning that it only respects origami kinematic principles, and each folding line contains its own folding actuator. Let us also suppose that such a resonator acts as a traditional Helmholtz resonator, acoustically speaking. Simply put, a paper-based origami Helmholtz resonator (from a foldability point of view) that performs like a rigid Helmholtz resonator, once it is put inside an acoustic transmission tube (the prefect case scenario), and let us call such resonator a reference resonator. When assessing the performance of origami Helmholtz resonators with different actuation systems, it is not enough to compare them to one another, but they should also be compared to the perfect case scenario (assuming that we can fabricate the perfect origami Helmholtz resonator), hence the need for a reference resonator.
To quantify the acoustic performance of the reference resonator, ***Freeform*** software was utilized in order to generate the extreme states of folding, the perfectly folded state (minimum volume possible), and the perfectly unfolded state (maximum volume possible). Then, both states of folding were used in the FE model of rigid Helmholtz resonators as well as the resonant frequency analytical model to obtain the acoustic performance of the reference resonator. As expected (established fact during the study of origami rigid

Helmholtz resonators), both models produced similar results, a frequency shift of 130 Hz, from 155 Hz to 285 Hz, as shown in Fig. 4.14.
As for the investigation of finding the appropriate actuation system for the origami Helmholtz resonator, three different actuation mechanisms were proposed and evaluated: the one-actuator technique, the four-actuator technique, and the eight-actuator technique, as shown in Fig. 4.15. The FE model validated experimentally during the kinetostatic analysis study was used to generate the folded/unfolded states for each proposed technique after applying the forces. The one-actuator and eight-actuator techniques apply longitudinal forces, while the four-actuator technique employs transversal forces. Furthermore, the four-actuator and eight-actuator techniques were tested for a folding action. Meaning, they start in a perfectly unfolded state, and after the actuators are activated, the resonator folds. As for the one-actuator technique, it is the other way around; the resonator is tested for an unfolding action. This choice was made for technical reasons. Since most origami structures use actuators made from smart materials, such as shape memory alloys, thanks to their compactness and the ability to produce large deformations and high applied forces, most of them require a recall mechanism. The recall mechanism, which can be made from passive springs, have the ability (or we assume they do) to resume the initial state of the resonator. For those reasons, there is no need to test both folding/unfolding actions for each technique, and only test one action, the most appropriate and convenient one from implementation and feasibility point of view.
After the folding/unfolding of the origami structure using the FE model made for the kinetostatic analyses, the newly generated structures were utilized to quantify their acoustic performances. The volume of the new produced structures was injected in the resonant frequency model in order to generate the new frequencies. The folded geometry generated from the four-actuator technique was also tested using the FE model of the rigid Helmholtz resonators, and not surprisingly, produced similar results as the resonant frequency model.
From looking at the results, we can say that in terms of generated volume variation/produced frequency shift, as well as high efficiency regarding maximum applied force per actuator for such variation, the four-actuator technique produced the best results. A frequency shift of 102 Hz for a 4.4 N maximum applied force per actuator (more details are shown in Tab. 4.6). That said, in terms of simplicity, compactness, and the more convenient to implement, the one-actuator technique has the best record. Therefore, we decided to combine the best two techniques and propose a new mechanism that highlights the best qualities of both tested techniques. The proposed mechanism uses one actuator but applies transversal forces in four different locations of the origami structure.

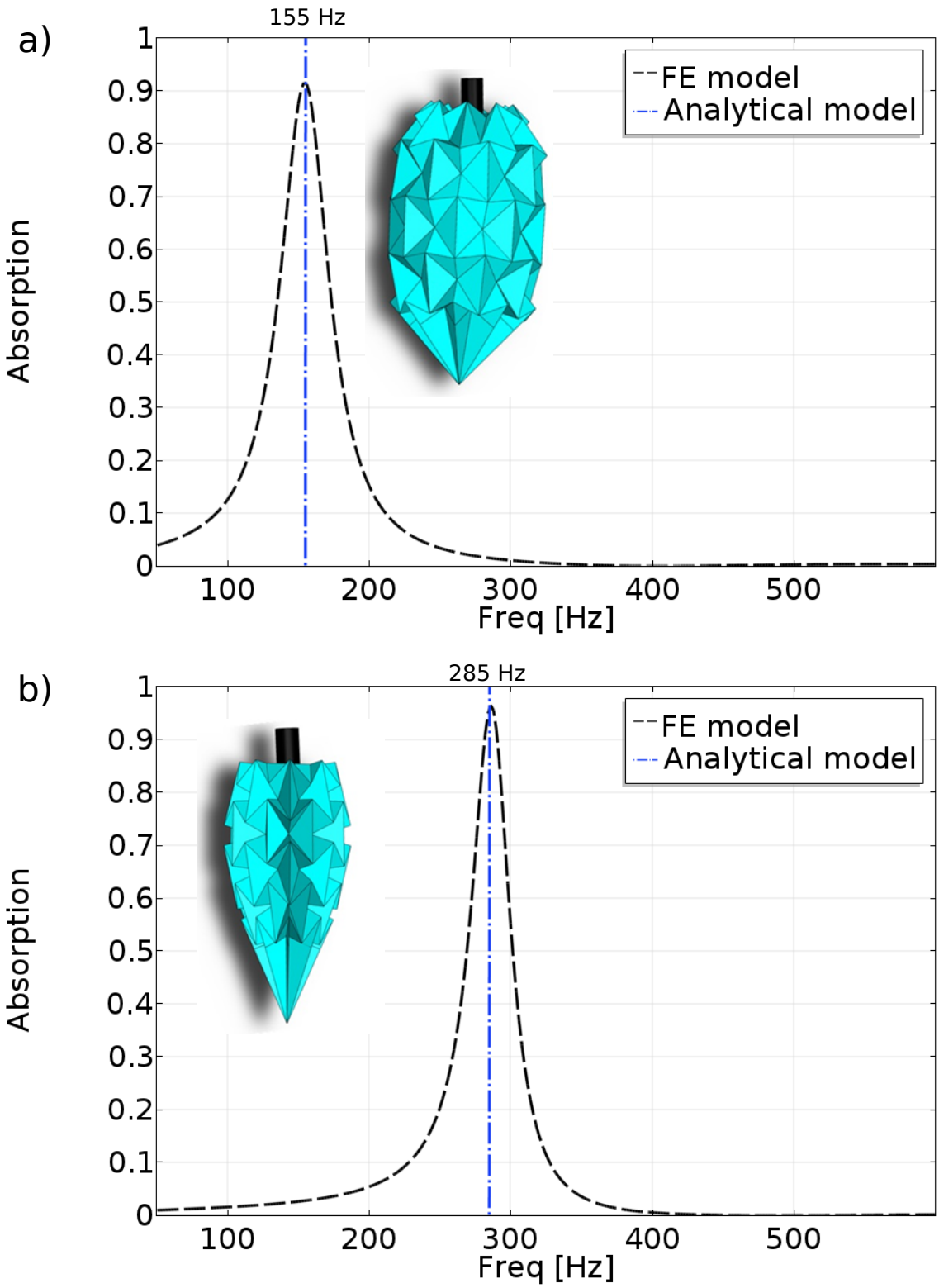

FIGURE 4.14: The theoretical acoustic performance (acoustic absorption) of an origami tunable Helmholtz resonator given by FE model as well as the resonant frequency model.

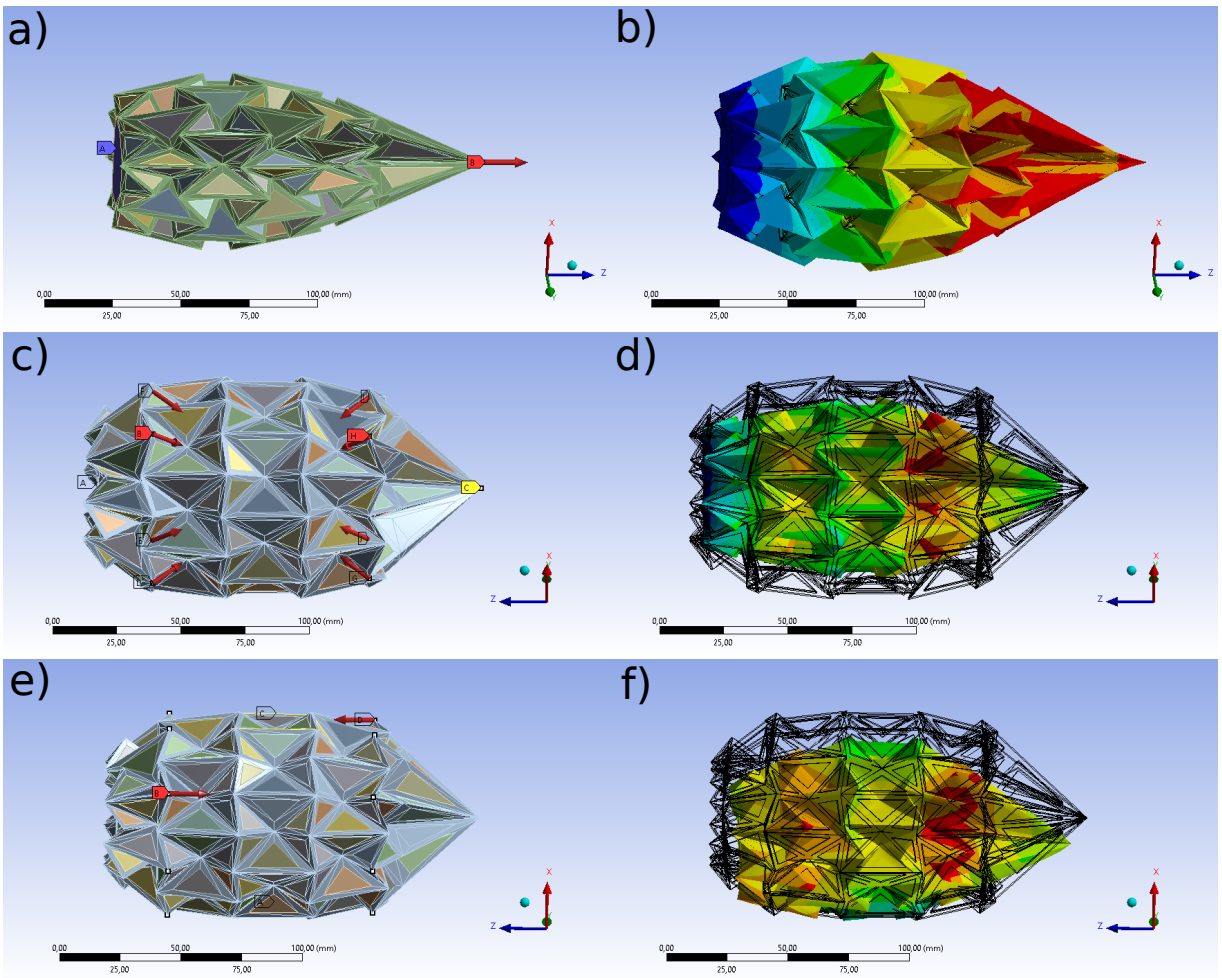

FIGURE 4.15: Different proposed techniques for the actuation of the origami Helmholtz resonators: a) one-actuator technique (applying longitudinal forces), c) four-actuator technique (applying transversal forces), and e) eight-actuator technique (applying longitudinal forces). b-d-f) the resulted deformation after the activation of the actuators for the one-actuator, the four-actuator and the eight-actuator techniques, respectively.

Table 4.6: Comparison between the different proposed actuation techniques for origami Helmholtz resonators, the one-actuator, the four-actuator and the eight-actuator techniques, as well as, a reference resonator, which represents the case of folding/unfolding a paper based origami resonator.

Actuation technique	***Reference resonator***	***One-actuator technique***	***Four-actuator technique***	***Eight-actuator technique***
Type of the Applied forces	-	Longitudinal forces	Transversal forces	Longitudinal forces
Number of actuators	-	1	4	8
Maximum applied force per actuator (N)	-	18	4.4	20
volume (cm^3) max-min	485.9-144	308.6-144	485.9-175.8	485.9-215.5
volume variation (cm^3)	341.9	154.6	300.1	260.4
Frequency (Hz) max-min	285-155	285-195	258-155	233-155
Frequency variation (Hz)	130	90(69%)*	102(79%)*	78(60%)*

*Relative frequency variation compared to the reference resonator (130 Hz)

4.8.3 Control

This subsection addresses the implementation of the proposed actuation mechanism and the closed-loop control of the origami Helmholtz resonator using such a mechanism. The latter was inspired by the umbrella mechanism. Since the bottom end of the origami-based structure was also inspired by the umbrella design, using an actuation mechanism of an umbrella as well, is a valid option. This fact was confirmed during the actuation system investigation, as the proposed umbrella mechanism was actually the combination of the two actuation techniques with the best performance, the one-actuator, and the four-actuator techniques. In order to stay coherent with the full study, the same origami Helmholtz resonator with a 60% rigid facets ratio, utilized during the kinetostatic analysis, was also used here. A square-shaped long bar containing four hinges in one end was 3D printed. Four thick steel wires were screwed to the bar from one end and glued to their designated locations in the origami structure, using the neck of the resonator as an access point. The bar and the steel wires make up the actuation mechanism. A support used to fix the origami structure from its neck was also 3D printed. Then, the actuation mechanism was attached to a linear stage, as shown in Fig. 4.17. The latter controls the linear motion of the mechanism. When the mechanism, or rather the square-shaped bar, is pushed, the origami structure unfolds, and when it is drawn, the structure folds. The experimental setup, in addition to the linear stage, includes a monochrome camera. The IEEE 1394 Guppy FireWire camera (Allied Vision Technologies, Stadtroda, Germany) is used for visual feedback. The operation is monitored by a ***Matlab/Simulink*** program using the Visual Servoing platform (ViSP) through a dedicated and opensource blockset CVLink. As for the utilized linear stage, it is a M111.1DG translation stage (Physik Instrumente GmbH Co. KG, Karlsruhe Germany) that has a travel range of 25 mm, a minimum incremental motion of 0.05 μm, and a velocity of 1.5 mm/s. The stage is controlled via a Mercury C-863 single-axis controller (Physik Instrumente).

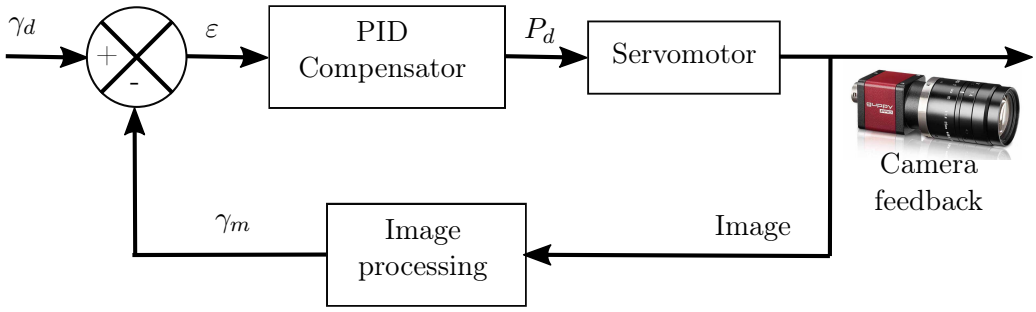

FIGURE 4.16: Block diagram for the origami-based Helmholtz resonator diameter control.

Considering that, during the experimental characterization of the acoustic behavior of the origami Helmholtz resonators, the performance was dependent and tracked by the diameter variation, we decided to select it as the main parameter for the control. The visual tracking of diameter was done using two attached physical markers, one for each side of the structure. The feedback program detects the physical markers by means of suitable thresholding. Additional evaluation of the shape factor of the detected area was conducted through the isoperimetric quotient (circularity). This operation allows for robust tracking of the physical markers even during luminosity variation. Once the markers are detected, the program determines the barycenter of each one of them and then uses it to evaluate the diameter (in pixels). During experimental testing and following the calibration of the camera, the variation of the origami device's diameter γ is detected, recorded and converted to millimeters.

A PID closed-loop control scheme for the origami device that uses a sampling time of 0.2 s was implemented (as shown in Fig. 4.16). It is actually the minimum rate permitted by a ***Matlab/Simulink*** program with the running processor. The experimental testing of the closed-loop control system was conducted as a response to two different reference signals, a stairstep signal (see Fig. 4.18) and sawtooth signal (see Fig. 4.19). The performance of the system was quantified in several calculated values, which include the root mean square error (RMS), its standard deviation (STD), and the maximum/minimum errors (MAX/MIN). For both reference signals, a 6 mm maximum diameter variation was arbitrarily chosen.

In the case of the stairstep control signal, despite the presence of a considerable overshoot, the system reaches the steady-state in 17 s. The overshoot can be significantly reduced at the expense of the time required for convergence, which will be expended considerably. However, since there is no risk of damaging the system even in the presence of such overshoot, we decided to prioritize the convergence time. Once in the steady-state, the system fulfills the control requirements with an RMS static error of 28 μm, an STD of 28 μm, and a MAX/MIN static error of 207/0 μm. These errors have relative, values compared to the maximum diameter variation, of 0.5 %, 0.5 %, 3.5 %/0 %, respectively (more details are presented in Tab. 4.7). As for the sawtooth control signal, the system fulfills the control requirements wi h an RMS error of 98 μm, an STD of 97 μm, and a

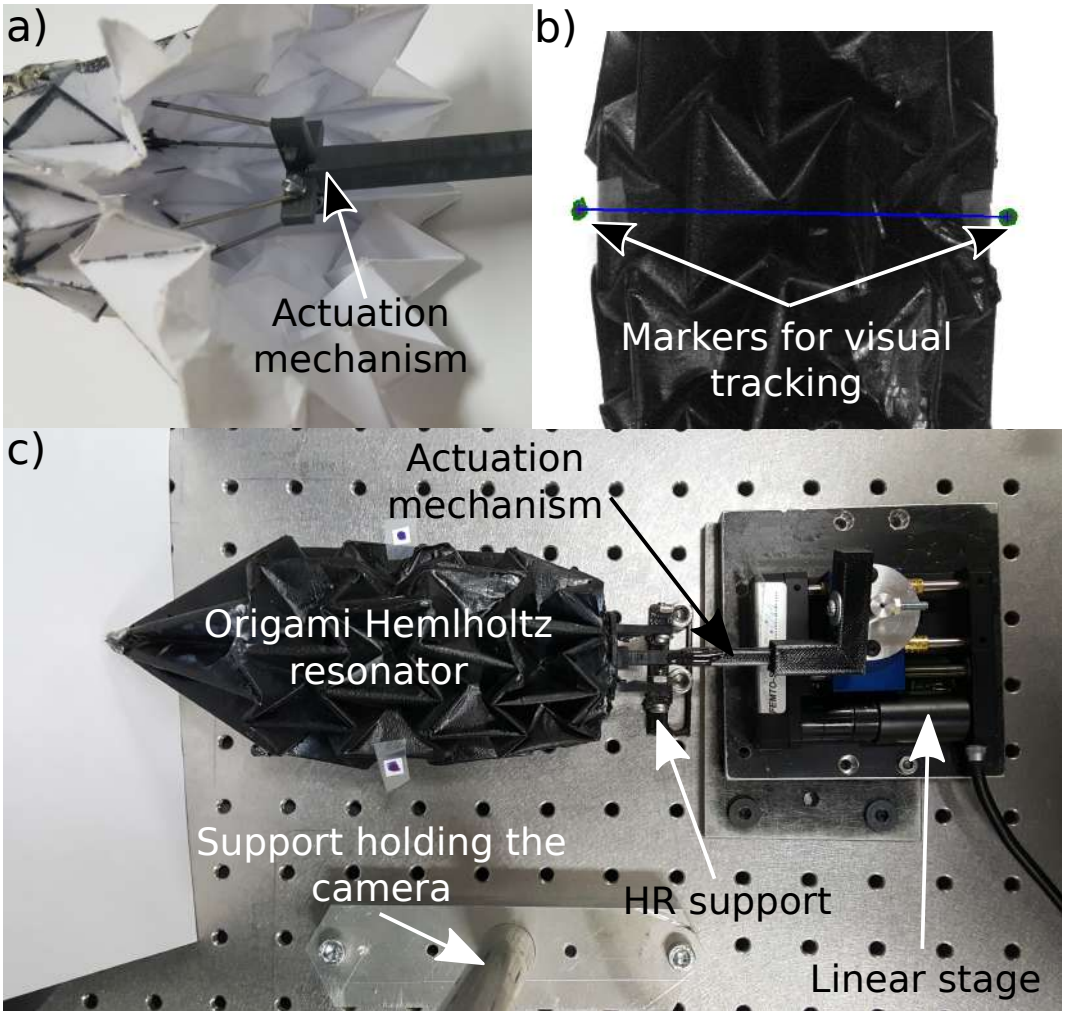

FIGURE 4.17: Experimental setup of the closed-loop control of the origami Helmholtz resonator: a) A cut paper based prototype of the origami resonator displaying the chosen actuation mechanism integration, b) the visual tracking concept and c) the fully assembled setup, using a camera for feedback and a linear stage for actuation.

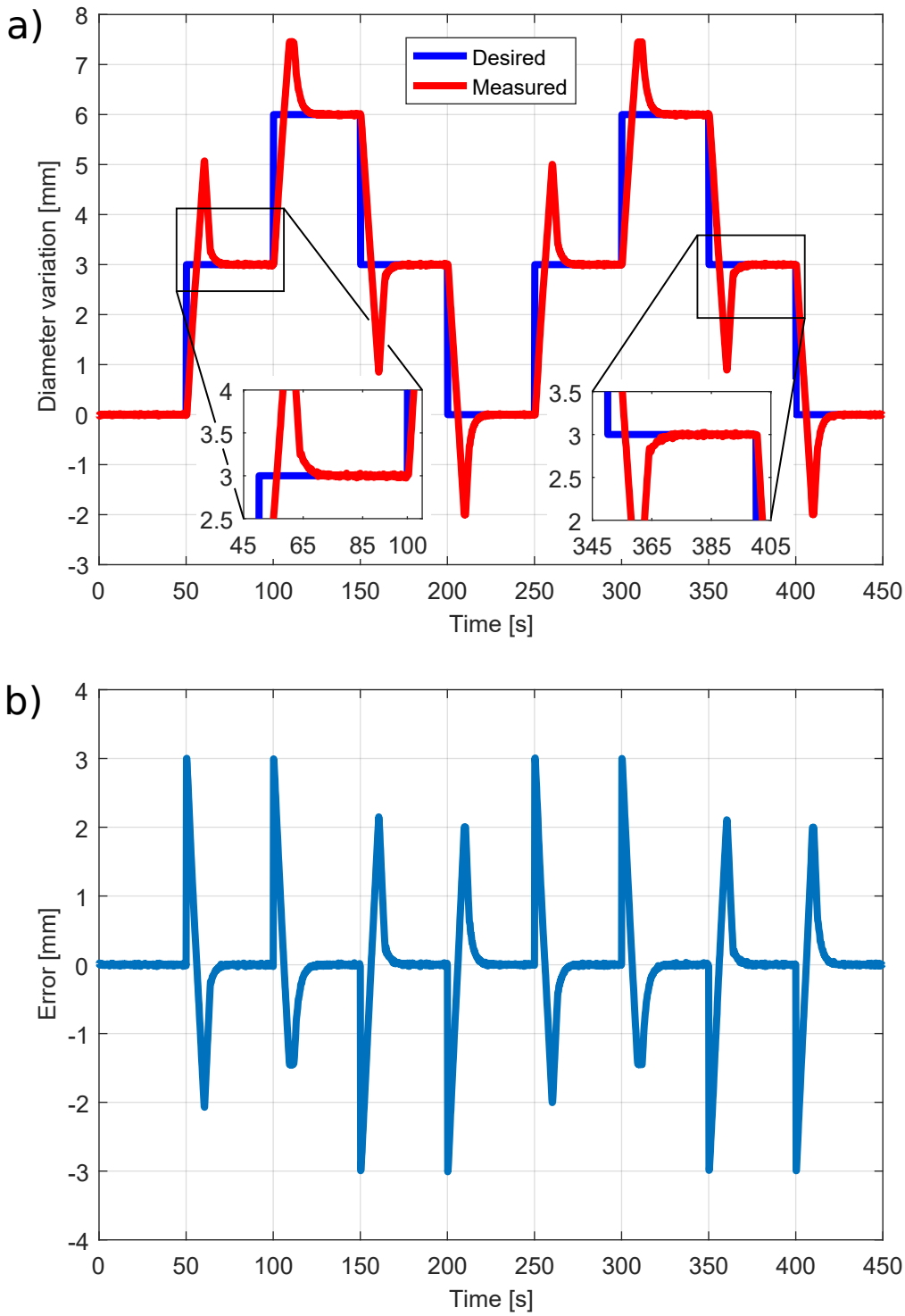

FIGURE 4.18: Diameter variation response of the origami Helmholtz resonator to a stairstep reference signal and (b) the corresponding error.

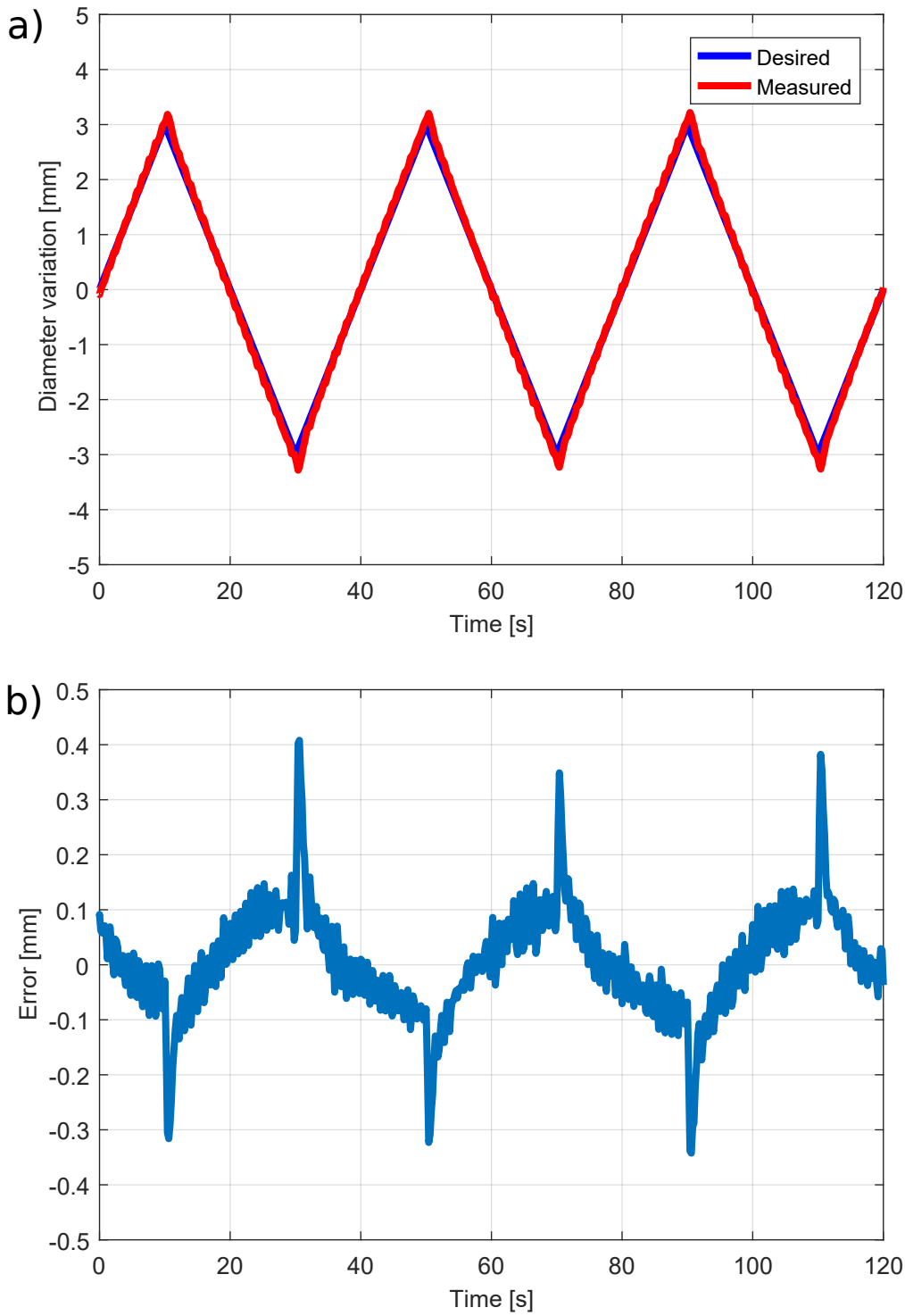

FIGURE 4.19: Diameter variation response of the origami Helmholtz resonator to a sawtooth reference signal and (b) the corresponding error.

MAX/MIN static error of 408/0 μm. Moreover, the relative values of these errors are as such, 2 %, 2 %, 7 %/ 0%, respectively (more details are presented in Tab. 4.8).

Table 4.7: Quantitative evaluation of folding/unfolding of a flexible origami Helmholtz resonator: static error for a stairstep input signal.

RMS (μm)	STD (μm)	MAX (μm)	MIN (μm)	Diameter variation (mm)	Response time to 5% (s)
28(0.5%)*	28(0.5%)*	207(3.5%)*	0(0%)*	6	17

*Relative static error compared to the diameter variation

Table 4.8: Quantitative evaluation of folding/unfolding of a flexible origami Helmholtz resonator: error for a sawtooth input signal.

RMS (μm)	STD (μm)	MAX (μm)	MIN (μm)	Diameter variation (mm)
98(2%)*	97(2%)*	408(7%)*	0(0%)*	6

*Relative error compared to the diameter variation

4.8.4 Partial conclusion

During the following study, we were able to develop a FE model that can simulate the mechanical behavior of our proposed origami vibro-acoustic device (Helmholtz resonator). The developed model was experimentally validated using different waterbomb origami bases. The model was also validated using an origami Helmholtz resonator with a rigid facets ratio of 60 %. After the model was developed and validated, it was utilized in order to launch an investigation into finding the appropriated actuation system for such origami devices. Once the actuation techniques tested and evaluated, the resulted were used to propose an adequate actuation system. Finally, The proposed actuation system was implemented, integrated, and tested. A closed-loop control with visual feedback was utilized to manipulate the diameter variation of the acoustic device.

4.9 Conclusion

For many years now, Helmholtz resonators have been used in adaptive-passive noise control. The resonance frequency is controlled by altering the geometrical properties of the Helmholtz resonator, being those of the neck, the cavity, or both, which makes dampening noise over a frequency domain of interest, just a matter of adjusting the parameters of the neck and the cavity. To that end, various experiments have been carried

out to determine the most effective methods of using adaptive Helmholtz resonators to control sound and, thereby, attenuation [Han, 2008]. In this chapter, due to the need for adaptive-passive noise control, an origami tunable Helmholtz resonator was proposed, modeled, fabricated, and experimentally evaluated. Furthermore, as a proof of concept, The origami design methodology introduced in the previous chapter was implemented here. Three different origami Helmholtz resonators were evaluated, rigid, quasi-rigid, and flexible. These origami resonators were able to display fascinating acoustic properties, especially, the flexible resonator which has wide bandwidth characteristics.
During the experimental validation, we were able to demonstrate, based on the results, that rigid and quasi-rigid origami Helmholtz resonators behavior as tradition Helmholtz resonator with a cylindrical neck. Moreover, using the quasi-rigid origami resonator, we were able to display the capabilities and effectiveness of our auxetic origami design, and our origami design methodology overall. The resonator was able to perform a high frequency shift in the low frequencies of 81 Hz, form 138 to 219 Hz. The frequency shift, which has an average absorption of 80 %, was achieved with a diameter variation of only 20 mm. This proves that using the origami design, we were able to obtain a Helmholtz resonator with very high tunability, and for minimal geometrical variation. More to the point, the flexible origami resonator did not only exhibit the many advantages inquired by using such designs, which includes, adaptive-passive system, high frequency shift to geometrical variation ratio, lightweight, monoblock, and energy/cost efficiency, it is also able to display a broad bandwidth behavior. As a holder of the latter and rather highly exciting property, the flexible origami resonator is able to overcome the main limitation of the Helmholtz resonator, which is the narrow bandwidth. As a result, the flexible origami resonator is a game-changer when it comes to low frequency, truly passive (but still tunable if needed), and highly effective noise control devices, as well as acoustic devices, in general. Finally, always within the framework of applying our origami design methodology, we were able to conduct a study on none-zero-thickness origami structures (kinetostatic analysis), use the results to investigate the appropriate actuation system for our proposed origami design, and then finalize the study with a closed-loop control with visual feedback of the diameter variation of an origami flexible resonator.
Based on all the results obtained in this chapter, we can conclude that using origami designs and applying origami methodologies is nowhere near, and easily feasible as traditional designs and structures, due to many reasons including, the complexity of the used geometries and the lack of proper tools. That said, all the exotic and highly exciting, obtained properties and characteristics, which can never be achieved otherwise, do more than just make up for it.

Chapter 5

Development of electroactive polymer based origami actuation

"Study and, in general, the pursuit of truth and beauty is a sphere of activity in which we are permitted to remain children all our lives."
- Albert Einstein

Contents

This chapter discusses electroactive polymer actuators, especially conducting polymer actuators, and all the potential that they can give to millimeter-scale origami systems. Such actuators can be very compact and lightweight. Additionally, they only require low activation voltages with the abilty to produce very large and reversible deformations. Furthermore, small origami devices are ideal for spatially constrained applications, like human body navigation, for example.

5.1 Introduction

The fact that origami-based systems have the ability to be folded compactly into very small devices, which can be deployed at a later time into a larger structure, makes them of interest to the scientific and engineering communities. Several recent examples of origami-based devices include a space solar array [Zirbel et al., 2013], medical devices [Kuribayashi et al., 2006, Bassik et al., 2010, Edmondson et al., 2013, Miyashita et al., 2016] or vibro-acoustic devices [Babaee et al., 2016, Fang et al., 2018, Cambonie and Gourdon, 2018]. Of special interest in the rapidly growing field of origami, engineering is autonomous folding, also known as self-folding, and shape-shifting [Hawkes et al., 2010, Tolley et al., 2014].

In the previous chapters, we considered origami engineering and origami applications from the point of view of origami designs, structures, shapes, and their different capabilities and properties. Nonetheless, origami devices, especially self-folding and shape-shifting devices, are as capable and as versatile as their actuation systems. In other words, trying to find the ultimate origami design for a certain application without having an actuation system that can keep up with such design is, in some cases if not all, a futile job. Furthermore, compared to traditional engineering devices, origami devices can be highly capable and also highly demanding in terms of actuation. As a result, there is always a real need for high-performance and more efficient origami actuation. For instance, a key parameter of origami structures is the folding angles. The values and the orientation (mount or valley) of the latter determine the geometry of the desired origami state (a certain shape and size). Considering that these angles usually need to have extensive alterations in order to achieve large volume and size variations (one of the main goals of utilizing origami designs in the first place), relaying on actuation systems with modest displacement such as piezoelectric materials is not a valid option. In addition to being able to produce substantial displacements, an origami actuation system should be highly compact, as it allows for seamless and more efficient integration as well as to avoid self-collision.

Thanks to their interesting properties and ability to comply with most of the requirements, smart materials are attractive and adequate candidates for origami actuation.

In the literature, various actuators intended for the self-folding and shape-shifting of origami-based systems have been proposed. such as EAP, especially Dielectric Elastomers (DE) [Ahmed et al., 2014], Shape Memory Alloys (SMA) [Hawkes et al., 2010, Paik and Wood, 2012, Peraza-Hernandez et al., 2013, Kim et al., 2016] and Shape Memory Polymers (SMP), which are found in heat-trigged systems [Miyashita et al., 2013, Tolley et al., 2014, Na et al., 2015, Miyashita et al., 2015, Silverberg et al., 2015] and light-trigged systems [Liu et al., 2012, Liu et al., 2014, Liu et al., 2017b].
In this chapter, we propose to use EAPs, more specifically, Conductive Polymer (CP)-based micro-actuators for milli-origami-inspired systems. besides its ability to produce considerable angle variations while maintaining a small size for more seamless and efficient integration, This actuator also offers many other advantages. These advantages include energy efficiency, lightweight, flexibility, reversibility of folding motion, and a low activation voltage. This origami device is based on polypyrrole trilayer CP actuators, where certain regions are stiffened using structural layers (such as paper or copper tape). The remaining regions are kept free to enable the folding/unfolding of the origami structure. The selection of stiffened/free regions depends on the desired origami design. Instead of directly addressing the operation of origami-inspired devices, we begin by studying the behavior of polypyrrole trilayer micro-actuators. Then we move to more sophisticated systems, origami systems.
This chapter is divided into 4 sections, Sec. 5.2 discusses polypyrrole trilayer micro-actuators. It also introduces a multi-physics model describing the large displacement behavior of these actuators. The model was experimentally validated using 2D and 3D polypyrrole-based milli-continuum soft robots. Sec. 5.3 presents a hybrid model for milli-origami devices. This model is based on the previously mentioned multi-physics model of the actuators and a kinematic model of the origami systems. For each applied voltage, the multi-physics model estimates the curvature of each free region of the origami device, while the kinematic model helps to reconstruct the origami shape. The proposed hybrid model was experimentally validated using a three-segment design and an origami cube. Finally, the last section concludes the chapter and also discusses the intended applications as well as future work.

5.2 Polypyrrole electroactive polymer actuators

The electromechanical proprieties of the electroactive polymers (EAPs) have been widely utilized for actuation in various applications. Furthermore, they are being increasingly investigated for sensing chemical and mechanical stimuli. EAPs are a special class of materials, with low-moduli high-strain capabilities and the ability to conform to surfaces of different shapes. These features make them very appealing for applications such as wearable sensors and interfacing with soft tissues.

5.2.1 Types of electroactive polymer actuators

EAPs have the ability to respond to an electrical stimulation by a change in shape or size, and are often considered as precursors of “artificial muscles”. In 2002, Y. Bar-

Cohen [Bar-Cohen, 2002] developed a classification of these polymers according to their activation systems. These materials are divided into two main classes: electronic EAPs and ionic EAPs.
Electronic EAPs: The actuation is caused by an electric field and more precisely by the coulombic forces. This class of actuators includes ferroelectric polymers, electrostrictive polymers, and dielectric elastomers (as shown in Tab. 5.1). Very well described in the literature, these materials have the advantage of consuming very little current, generating relatively large forces for a response time of the order of one millisecond. However, they require the application of very high electric fields ($\approx 100\ kV/mm$) making their use delicate, even dangerous.
Ionic EAPs: The deformation of the polymer is due here to the movements of ions coming from an electrolyte, in response to an applied electric field ($\approx 100\ V/mm$). This family includes actuators based on conducting polymers (CP), ionic polymer / metal composites (IPMC), carbon nanotube-based actuators, and ionic polymer gels (IPG). Although, more recent research in the field of ionic EAP-based actuators is continually advancing their capabilities, the low activation voltage is still one of their main advantages, justifying their use in many applications [Maziz, 2014].

Table 5.1: List of leading EAPs materials [Kim and Tadokoro, 2007].

Electronic EAPs	***Ionic EAPs***
Dielectric EAPs	Ionic polymer gels (IPG)
Electrostrictive graft elastomers	Ionic polymer metal composite (IPMC)
Electrostrictive paper	Conducting polymers (CP)
Electro-viscoelastic elastomers	Carbon nanotubes (CNT)
Ferroelectric polymers	
Liquid crystal elastomers (LCE)	

5.2.2 State of the art of PPy conducting polymer micro-actuators

In 2003, the group of Professor G. G. Wallace [Zhou et al., 2003b] (University of Wollongong, Australia) described a trilayer actuator composed of a porous PVDF membrane on which a layer of polypyrrole is electrochemically deposited on each of the faces after the metallization of PVDF. The major advantage of this type of device lies in the porosity of the membrane, which allows anchoring of the CP in its thickness (see Fig. 5.1), thus limiting the delamination. As a result, the actuators, impregnated with lithium salts in propylene carbonate, are capable of deforming up to 180° angular amplitudes.
In 2007 J. Madden et al. [Madden et al., 2007, Madden et al., 2000] develop PPy-based trilayer actuators capable of operating over very long periods, for 120,000 and 32,000 cycles at frequencies of 3 Hz and 1 Hz, respectively, but with a linear loss of the deformation over time due to the evaporation of the solvent. Therefore, the use of organic electrolytic solutions does not allow operation of electrochemical devices in the open air over a wide range of temperatures and times due to the evaporation of solvents.
In order to remedy the situation, research laboratories have moved towards the use of

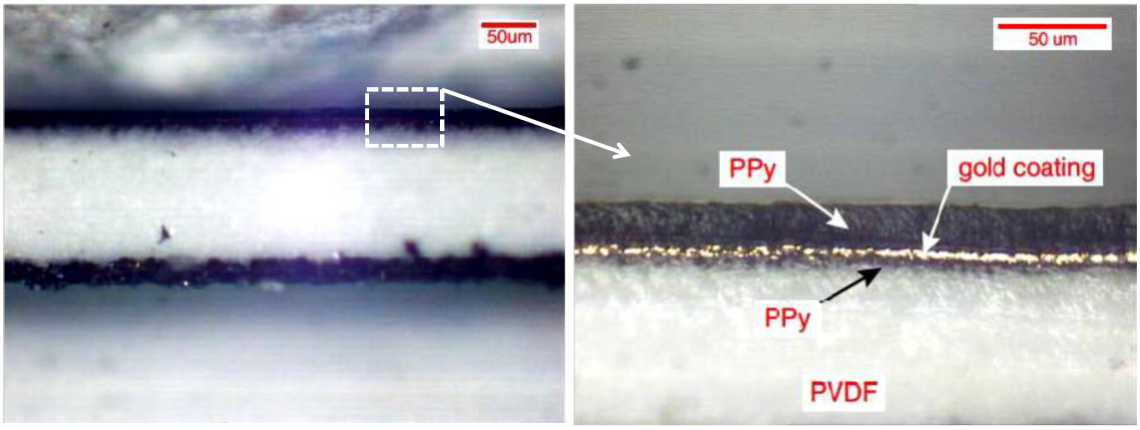

FIGURE 5.1: Image obtained by optical microscopy of the cross-section of a trilayer PPy/PVDF/PPy micro-actuator [Maziz, 2014].

TABLE 5.2: Some numbers about the trilayer PPy microactuator [Wu et al., 2006].

Definition	Value	Unit
Length	40	mm
Width	2	mm
Thickness	~ 100	μm
Applied voltage	1	V
Current	~ 10	mA
Tip displacement	60	mm
Frequency	4	Hz
Generated force	> 1	mN

ionic liquids (LI) in CP-based devices. These liquids are salts having the particularity of being in liquid form at low temperatures and especially at room temperature. In 2003, G.G Wallace's group carried out the first comparative studies between trilayer open-air actuators using either ionic liquids or electrolytes based on organic solvents [Ding et al., 2003, Zhou et al., 2003a]. These studies have clearly demonstrated the significant improvement in the performance of the actuators (deformation, lifetime, thermal stability) by using an ionic liquid as the electrolyte. Later in 2004, Spinks et al. [Spinks et al., 2004] demonstrate that a PPy-PVDF actuator can undergo a hundred cycles without degradation of performance. Some values regarding such miroactuators can be found in Tab. 5.2.

5.2.3 Working principle of trilayer polypyrrole micro-actuator

The group of Professor G. G. Wallace [Zhou et al., 2003b] (University of Wollongong, Australia) proposed an interesting architecture for open-air EAP actuators. The latter

have a carrier substrate of the electrolyte and two ionic EAP electrodes. Although ionic EAPs are conductive, a metal layer can also be interposed between the EAP and the substrate to promote electrical conduction, as shown in Fig. 5.1. For this configuration, the application of a potential difference to the two EAP electrodes leads to a chemical reaction between the EAP ions and the electrolyte in contact with it (see Fig. 5.2). In fact, an oxidation reaction takes place on the side of the cathode, which absorbs cations and sees its volume increase, while the anions are attracted to the anode because of the reduction reaction, and therefore its volume decreases. With a planar structure and opposite electrode positions, the volume change on both sides of the actuator causes a flexing moment at its end.
If we take the example of a micro-actuator consisting of PPy electrodes activated by an electrolyte solution of lithium bis (trifluoromethylsulfonyl) imide (LiTFSI) consisting of Li^+ and $TFSI^-$ the following oxidation-reduction reaction occurs:

$$\mathrm{PPy}^0 + \mathrm{TFSI}^- \underset{oxidation}{\overset{reduction}{\rightleftharpoons}} \mathrm{PPy}^+\mathrm{TFSI}^- + \mathrm{e}^- \tag{5.1}$$

Thus, the lift-to-right direction of Eqn. (5.1) corresponds to the reduction that occurs at the positively activated electrode, and the opposite direction equals the oxidation reaction at the negatively charged electrode, as schematized in Fig. 5.2.
The micro-actuators based on ionic EAP provide significant deformations (of the order 30%), very low activation voltage (less than 2V), and reversibility of the generated motion. Nevertheless, these materials require operation in a wet environment (i.e., the presence of an electrolyte solution), which in this case is stored insides the porous substrate.

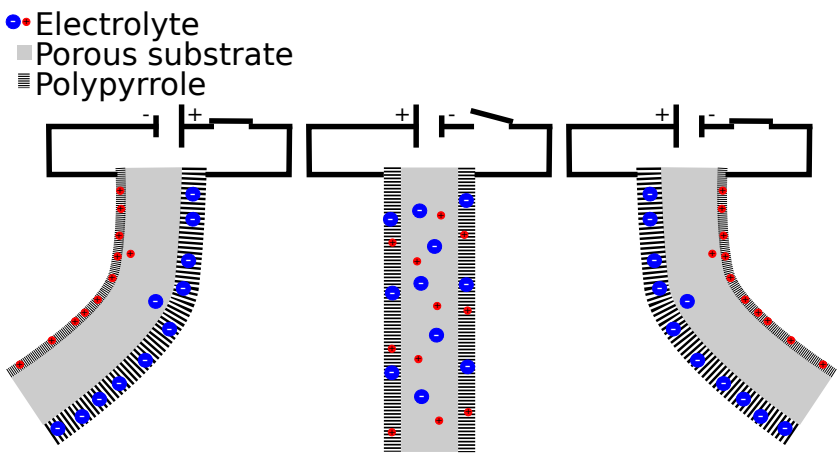

FIGURE 5.2: Working principle of trilayer polypyrrole micro-actuator.

5.2.4 Synthesis of trilayer polypyrrole micro-actuator

There are several processes for the polymerization of monomers [Nalwa, 2001]. Two most common methods in the literature will be presented in the following and include chemical polymerizations [Diaz et al., 1979, Kanazawa et al., 1979] and electrochemical polymerizations [Bowen et al., 1989, Kim et al., 1993]:

- the chemical polymerization - also known as chemical oxidative polymerization- is the effect of the chemical reaction between a monomer and an oxidizing agent. Among the oxides employed [Castillo-Ortega et al., 1989, Mohammadi et al., 1987], we can cite in particular iron (III) chloride [Kanazawa et al., 1979];
- the electrochemical polymerization (the process used in this work) makes it possible to control the kinetics of the reaction, the morphology (roughness, compactness, etc.) of the polymer as well as its thickness [Le Floch et al., 2009]. Several types can be used: chronoamperometry performed at a constant potential, galvanostatic polymerization or chronopotentiometry performed at a constant current, and cyclic voltammetry [Waltman et al., 1983].

5.2.5 Modeling

Table 5.3: List of variables.

Variables	Definition	Value	Unit
E_1/E_3	Young's modulus of the first/third layers of PPy	80×10^6	Pa
E_2	Young's modulus of the second layer of PVDF	440×10^6	Pa
t_1/t_3	Thicknesses of the first/third layers of PPy	7.5×10^{-6}	m
t_2	Thickness of the second layer of PVDF	55×10^{-6}	m
b	Width of the multilayer cantilever	1×10^{-3}	m
L	Length of the multilayer cantilever	27×10^{-3}	m
α	Corrective factor	1.226×10^{-1}	$(F/m^2)/(C/m^3)$
C	Volumetric capacitance	4×10^8	F/m^3
DV	Input voltage	$0.1 < DV < 0.7$	V

This subsection introduces a static large-deflection model of a multi-layer cantilever that represents the CP actuator. First, there are few assumptions to be considered:

- j represents the index for a layer;
- the material of each layer remains linearly elastic;
- two consecutive layers are perfectly bonded;
- the radius of the curvature ρ of the multi-layer cantilever caused by the combined effect of all stresses is much bigger than its thickness.

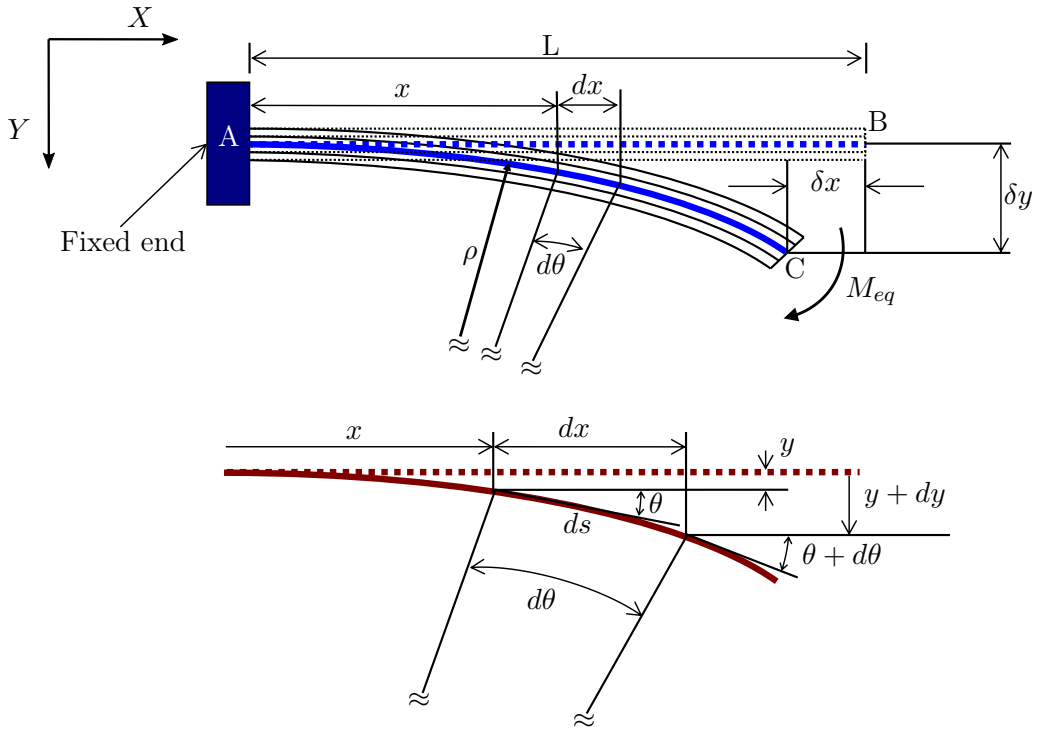

FIGURE 5.3: Description of large deflection of multi-layer cantilever adapted from [Kim, 2008].

The proposed model is derived from the non-linear beam equation. For x, a position between 0 and L the length of the multilayer cantilever (as shown in Fig. 5.3), the curvature writes:

$$\frac{1}{\rho} = \frac{M_{eq}}{(EI_{eq})} = \frac{\sum_{j=1}^{n} M_j}{\sum_{j=1}^{n} E_j I_j} = \frac{d\theta}{ds} = \frac{\frac{d^2y}{dx^2}}{(1+(\frac{dy}{dx})^2)^{\frac{3}{2}}} \tag{5.2}$$

where M_j is the individual bending moment and $E_j I_j$ is the flexural rigidity of layer j. An induced longitudinal strain at any level of the multilayer cantilever, causes a bending moment, which can be considered constant across $\overline{AC}$ (as shown in Fig. 5.3), since the cross-section of the cantilever is uniform along its length. An analytical solution of Eqn. 5.2 for a linear elastic material multilayer cantilever, was proposed by Kim [Kim, 2008]. It was given by direct integration and application of the boundary conditions, $y'(0) = 0$ and $y(0) = 0$, hence, the shape of the whole beam (solution of Eqn. (5.2)) is determined as follows :

$$\frac{x}{\rho} = \frac{\frac{dy}{dx}}{(1+(\frac{dy}{dx})^2)^{\frac{1}{2}}} \tag{5.3}$$

$$y = \rho \left(1 - \sqrt{(1 - \left(\frac{x}{\rho}\right)^2)} \right) \tag{5.4}$$

and since the length of the unbent multilayer cantilever $\overline{AB} = L$, is the same as the one of the bent cantilever $\overline{AC}$, the horizontal deflection can be determined with the arc length $ds = \sqrt{1 + (dy/dx)^2}$. In addition :

$$L = \int_0^{L-\delta x} \sqrt{1 + \left(\frac{dy}{dx}\right)^2} dx \tag{5.5}$$

and by using the trigonometric substitution, $x = \rho\, sin\theta$, the tip deflection of the multilayer cantilever can be obtained as:

$$\delta x = L - \rho\, sin\left(\frac{L}{\rho}\right) \tag{5.6}$$

$$\delta y = \rho \left(1 - cos\left(\frac{L}{\rho}\right) \right). \tag{5.7}$$

5.2.5.1 Single-segment system

Based on the general case introduced above (large-deflection model of a multilayer cantilever), this section presents a model able to describe the behavior of a trilayer electroactive micro-actuator, composed of two PPy active layers and a porous PolyVinylidene DiFluoride (PVDF) passive layer. When a voltage DV is applied, the longitudinal strain generated in the active layers, caused by the rushing of ions from one side to the other, induces the bending of the cantilever, thus transforming an electric field into a bending motion, as shown in Fig. 5.2. The generated longitudinal strain ϵ_j of a layer j, in this case, is approximated by $2\alpha\frac{C.DV_j}{t_j bLE_j}$. The variable list is given in Tab. 5.6. Furthermore, the radius of the curvature ρ is derived according to Kim [Kim, 2008]:

$$\rho = \frac{2RA^{-1}S}{2 + RA^{-1}B} \tag{5.8}$$

where:

$$R = \frac{-1}{E_1I_1 + E_2I_2 + E_3I_3} \begin{bmatrix} \frac{t_1}{2} & t_1 + \frac{t_2}{2} & t_1 + t_2 + \frac{t_3}{2} \end{bmatrix} \tag{5.9}$$

$$A = \begin{bmatrix} \frac{1}{E_1I_1} & \frac{-1}{E_2I_2} & 0 \\ 0 & \frac{1}{E_2I_2} & \frac{-1}{E_3I_3} \\ 1 & 1 & 1 \end{bmatrix} \tag{5.10}$$

$$B = \begin{bmatrix} t_1 + t_2 \\ t_2 + t_3 \\ 0 \end{bmatrix} \tag{5.11}$$

and

$$S = \begin{bmatrix} \epsilon_2 - \epsilon_1 \\ \epsilon_3 - \epsilon_2 \\ 0 \end{bmatrix} \tag{5.12}$$

In Eqn. (5.12) the strain ϵ_2 of the second layer is null, considering the fact that it is a passive layer. However, the strain for the first/third layers are: $\epsilon_1 = 2\alpha\frac{C.DV_1}{t_1bLE_1}$, and $\epsilon_3 = 2\alpha\frac{C.DV_3}{t_3bLE_3}$, respectively. Additionally, since $DV_1 = -DV_3$, which is essential to activate the trilayer micro-actuator, Eqn. (5.12) becomes:

$$S = \begin{bmatrix} 2\alpha\frac{C.DV}{t_1bLE_1} \\ 2\alpha\frac{C.DV}{t_3bLE_3} \\ 0 \end{bmatrix} \tag{5.13}$$

Furthermore, by using Eqns. (5.9) (5.10) (5.11) (5.13) and (5.8), the radius of the curvature of the trilayer micro-actuator, ρ is equal to:

$$\frac{(t_1+t_2)\left(\frac{E_1E_3I_1I_3\psi_2}{\psi_1} - \frac{\psi_3}{2\psi_1} + \frac{E_1E_2I_1I_2\left(t_1+\frac{t_2}{2}\right)}{\psi_1}\right) - (t_2+t_3)\left(\frac{\psi_5}{2\psi_1} - \frac{E_3I_3\psi_4\psi_2}{\psi_1} + \frac{E_2E_3I_2I_3\left(t_1+\frac{t_2}{2}\right)}{\psi_1}\right) + 2}{\frac{C.DV\alpha\left(\frac{E_1E_3I_1I_3\psi_2 2}{\psi_1} - \frac{\psi_3}{2\psi_1} + \frac{E_1E_2I_1I_2\left(t_1+\frac{t_2}{2}\right)2}{\psi_1}\right)}{E_1Lbt_1} - \frac{C.DV\alpha\left(\frac{\psi_5}{2\psi_1} - \frac{E_3I_3\psi_4\psi_2 2}{\psi_1} + \frac{E_2E_3I_2I_3\left(t_1+\frac{t_2}{2}\right)2}{\psi_1}\right)2}{E_3Lbt_3}} \tag{5.14}$$

Where:
$\psi_1 = (E_1I_1 + E_2I_2 + E_3I_3)^2$
$\psi_2 = t_1 + t_2 + \frac{t_3}{2}$
$\psi_3 = E_1I_1t_1(E_2I_2 + E_3I_3)$
$\psi_4 = E_1I_1 + E_2I_2$
$\psi_5 = E_1E_3I_1I_3t_1$

Eqn. (5.14) provides us with the radius of the curvature ρ which allows the computation of the tip deflection of the trilayer micro-actuator, along the x and y axis, according to Eqns. (5.6) and (5.7).

5.2.5.2 Two-segment system

The two-segment system is a serial type soft robot, with two micro-actuators attached serially. It can have more than two serially linked segments (the case of Sec.5.3); however, for the sake of simplicity, this section will only discuss the two-segment continuum soft robot. Furthermore, for the model, each segment will be modeled separately, then, the base of the second segment will be attached to the end of the first one, using a small transition part (a few mm long). The latter is a straight part tangent to the first segment

at its tip. Its main role is to ensure that the second segment is correctly attached and that it has a suitable orientation. Lastly, the curvature of the second segment is computed in a similar manner as the first segment.

5.2.6 Fabrication

The main objective of the subsection is to discuss the fabrication process of different types of EAPs systems used during this study, starting by the trilayer EAPs micro-actuator. The fabrication of the trilayer micro-actuator was done using an electropolymerization process. First, a PVDF membrane Immobilion P from Millipore (product specifications: pore size 0.45 μm, porosity 70%, and thickness of 100 μm), was previously covered by a layer of chromium/platinum with a thickness of 10/50 nm on both sides, using a cathodic sputtering process. This step is crucial, since the conductive properties of PVDF membrane, are necessary for the electropolymerization process. However, the added layers can also generate unwanted residual stresses that can have a very negative effect on the final micro-actuator. Then, the PVDF membrane was mounted on a standard three-electrode system (as shown in Fig. 5.4.a), as a working electrode, for the electropolymerization process. The three-electrode system was also composed of Ag/AgCl reference electrode and a platinum grid counter electrode. The former system was linked to a potentiostat, OrigaFlex-OGF500 (from OrigaLys ElectroChem SAS), which was controlled by OrigaMaster5[1] software. The process is similar to the one proposed in the work of Cot et al [Cot et al., 2016], but the electropolymerization setup is based on a more accurate potentiostat. After the electropolymerization process, the final product was cleaned using acetone, then cut by a very sharp scalpel to a 1 mm wide strips, to be used in the experimental setup afterward.

5.2.7 Experimental validation

5.2.7.1 Experimental setup

In order to characterize the designed and fabricated actuators, a test bench is developed based on ***Matlab/Simulink*** software using Visual Servoing Platform (ViSP) with a dedicated blockset cvlink[2]. The system is held at its base by a small gripper made conductive with copper tape (Fig. 5.4.b). Voltage is provided via a National Instruments multifunction data acquisition module (USB-6211), which can manage a voltage between $\pm$ 10 V with a resolution of 3.5 mV. The camera (IEE 1394 Guppy Firewire) is positioned in front of the actuation platform (as shown in Fig. 5.4.b) in order to visualize the side of the actuator in its thickness. The dimensions of the considered two-segment system are about 16×1 mm^2 for the first segment and 20×1 mm^2 for the second segment.

[1] http://www.origalys.com/origasoft-logiciel-pc-\origamaster-c2x19668303
[2] https://sourcesup.renater.fr/cvlink/

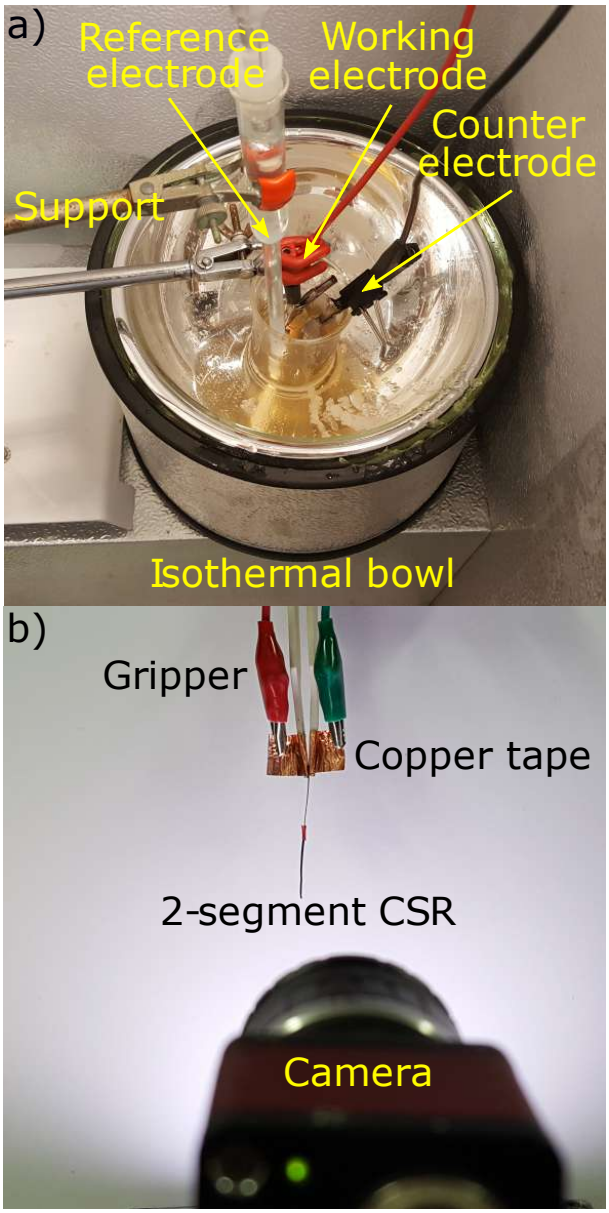

FIGURE 5.4: a) Electropolymerization system with three electrodes put inside a freezer during PPy growing, and b) the experimental setup for characterization of the proposed systems.

5.2.7.2 Single-segment system

This section describes the experimental validation of the model for the PPy micro-actuator, and in order to do so, a series of experimental tests were conducted. The process starts by cutting a 27 mm long and 1 mm wide trilayer PPy micro-actuator, and

hang it from one end in front of the camera, as mentioned above. Then, for each test, a voltage is applied, for 25 s, while the camera is recording. The 25 s duration is required to ensure that the PPy micro-actuator has reached the steady-state and its maximum deformation under the applied voltage. The latter varies from 0.1 to 0.7 V (higher voltages can damage the PPy micro-actuator). Afterward, the PPy micro-actuator gets a 30 s rest time, in order to go back to its former state (zero deformation). In the next step, the videos were decomposed into frames, and then, the frames corresponding to the maximum deformation were used to determine the curvature of the PPy micro-actuator for each applied voltage. The information was initially given in pixels; therefore, it was converted to mm and then compared to the results of the model, as shown in Fig. 5.5. The model is compared to experimental results, and the systematic error is presented in Tab. 5.4. The root-mean-square Error is less than 1 mm, which corresponds to 3.7% of the segment length, which is considered to be satisfactory.

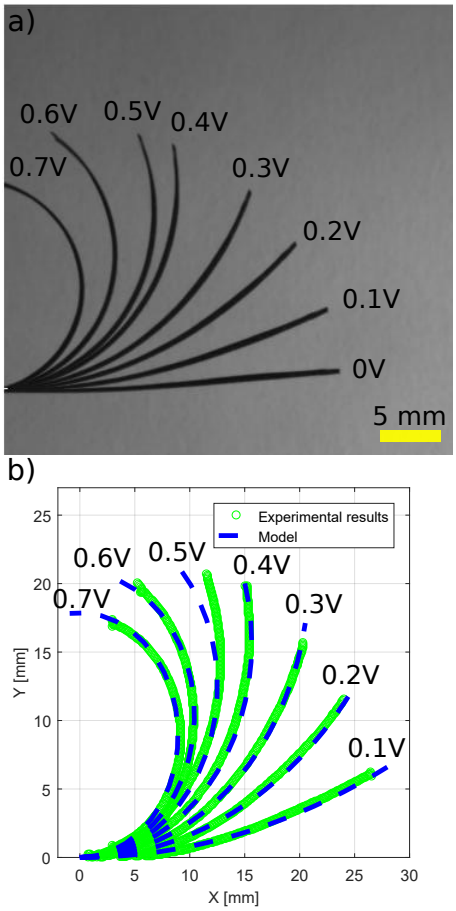

FIGURE 5.5: Single-segment system experimental validation: a) the responses for an applied voltage varying from 0.1 to 0.7 V obtained through the overlay of images, and b) comparison of the experimental results to the model.

TABLE 5.4: Error of the single-segment model.

RMS (μm)	STD (μm)	MAX (μm)	MIN (μm)
840	555	1677	2

5.2.7.3 Two-segment system

In order to characterize the two-segment system, a strip of trilayer PPy actuator was cut to a width of 2 mm. Then, in approximately its middle, its width was narrowed down by cutting off small rectangular pieces of it from each side. As a result, the concerned zone became very flexible, therefore twisting the actuator by 180° at this area was feasible.

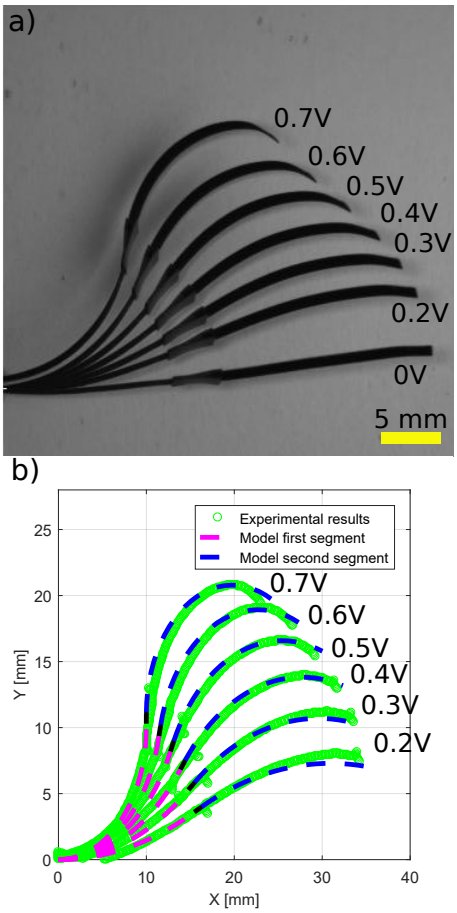

FIGURE 5.6: Two-segment system experimental validation: a) the responses for an applied voltage varying from 0.1 to 0.7 V obtained through The overlay of images, and b) comparison of the experimental results to the model (dashed line, red for the first segment and blue for the second segment).

The actuator was held in the twisted state by a tiny strip of duct tape. The final product was a two-segment system, 16 mm long first segment, 1 mm rigid link, and a 20 mm long second segment. The rigid link is essential for a two-segment system because it ensures the electric connection to the second segment; that way, the latter can achieve high deformations as well as the first segment. As for the characterization of the two-segment system, the latter was mounted on the experimental setup, and a series of experimental tests similar to those discussed above were conducted. Finally, the deformation of the two-segment system for the different applied voltages is compared to the model, as shown in Fig. 5.6. The proposed two-segment model is able to simulate the large deformation generated by the two-segment system. The RMS error for the different actuation voltages is about 356 μm, and the STD error is 209 μm (as shown in Tab. 5.5). One can conclude that the model works well, then it can be used for later developments.

Table 5.5: Error of the two-segment model.

RMS (μm)	STD (μm)	MAX (μm)	MIN (μm)
356	209	864	21

5.2.7.4 Proof of concept of 3D system

In this section, a three-segment system was fabricated by cutting three strips of the tri-layer micro-actuator; each one is 8 mm long and 1 mm wide. The strips were then placed in the top of the 3D printed model of the three-segment system, in order to ensure that all of the three segments are oriented at 120° form one another. Next, using a small piece of adhesive copper tape, the three-segment were fixed at their proximal ends. Finally, the excess copper tape was carefully cut. For this demonstration, the three-segment system was side-viewed by a camera and held by two long copper parts. One was used to press on the copper tape and the second to press against all of the three-segment at the same time, from the other side (as shown in Fig. 5.15).
It was demonstrated that the fabricated three-segment system is functioning, and consequently, the fabrication process is validated. In addition, this result opens the possibility to design multi-arm collaborative robots at small scales.

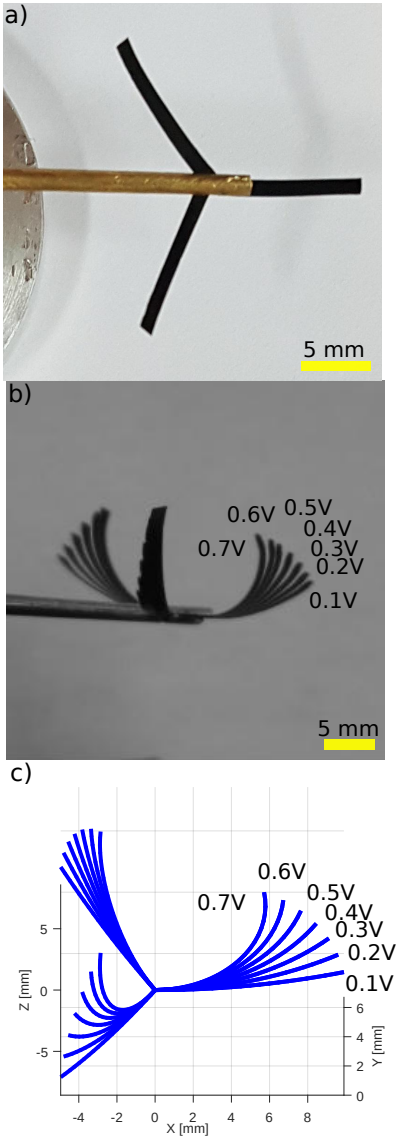

FIGURE 5.7: a) Top view of the three segment system, b) the overlay of images for an applied voltage varying from 0.1 to 0.7 V, and c) the corresponding model results.

5.3 Milli-origami based on electoactive polymers

Our search for better milli-origami actuators led us to polypyrrole based CP actuators. Based on the results obtained during the previous study (see Sec. 5.2), the latter seems to represent an attractive fit for the required job. This fact was consolidated by the many advantages that such actuators can offer:

- **Large deformations:** origami designs are able to achieve large shape and size variations; therefore, it is highly important to utilize actuators that can preserve such property, which is the case for CP actuators.
- **Compactness:** the polypyrrole based CP actuators used here, have a thickness of only 100 μm. Such thickness provides far more seamless and efficient integration.
- **Reversibility:** an interesting property to have, especially for origami devices, as it allows for dynamic reconfigurability that comes with far more properties and functionalities.
- **Flexibility:** such property ensures a safe interaction with the environment, as it absorbs shocks in case of impacts. For instance, in biomedical applications causing damage to the surrounding area is considered to be a far more serious issue than failing to accomplish the task itself.
- **Lightweight:** compared to traditional structures, origami structures are usually very lightweight; thus, it is highly important to maintain such an advantage.
- **Low activation voltage:** polypyrrole based CP actuators require a very low activation voltage, usually less than 2V. As a result, applying these actuators to biomedical applications can be perfectly safe.

Thanks to such interesting properties and characteristics we propose in this section to study polypyrrole based CP actuators as a potential actuation system for milli-origami devices.

5.3.1 Modeling

This subsection aims to model CP-based origami-inspired milli-robots, as multi-segment millimeter scale soft continuum robots with a tree configurations, as shown in Fig. 5.8. Based on the standard approach detailed by [Webster III, 2007], a continuum robot can be divided down into n successive segments, which in our case include both active and passive segments. Each active segment is then equated with a constant curvature, which assimilates the folds in an origami system. The use of the Denavit-Hartenberg formalism has been validated by [Hannan and Walker, 2003] in the case of the description of an arc in space through 3 variables. The latter constitute the space of variables of the arc :

- the radius of the curvature ρ;
- the length of the arc L;
- and the angle ϕ, which represents the orientation angle of the segment.

The definitions of the 3 variables were modified in order to suit our systems adequately. We can also define the angle of curvature $\theta = L/\rho$. These arc variables can be visualized in Fig. 5.8, for the case of a segment i, where the different frames, which will be used later on, are introduced.

Nomenclature

m	Number of segments in the origami soft milli-robot.
i	Index of the segment
SR	Matrix of the origami soft milli-robot
C_P	Matrix used to express a passive segment
L	Length of a segment
C_A	Matrix used to express an active segment
n	Number of points used to define the active segment
j	Index of the points of the CP actuator curvature
x_n	Coordinate of the tip of the active segment along the X-axis
y_n	Coordinate of the tip of the active segment along the Y-axis
z_n	Coordinate of the tip of the active segment along the Z-axis
T	Homogeneous transformation matrix
θ	Rotation around Z-axis (folding angle)
ϕ	Rotation around X-axis (the segment's orientation angle)

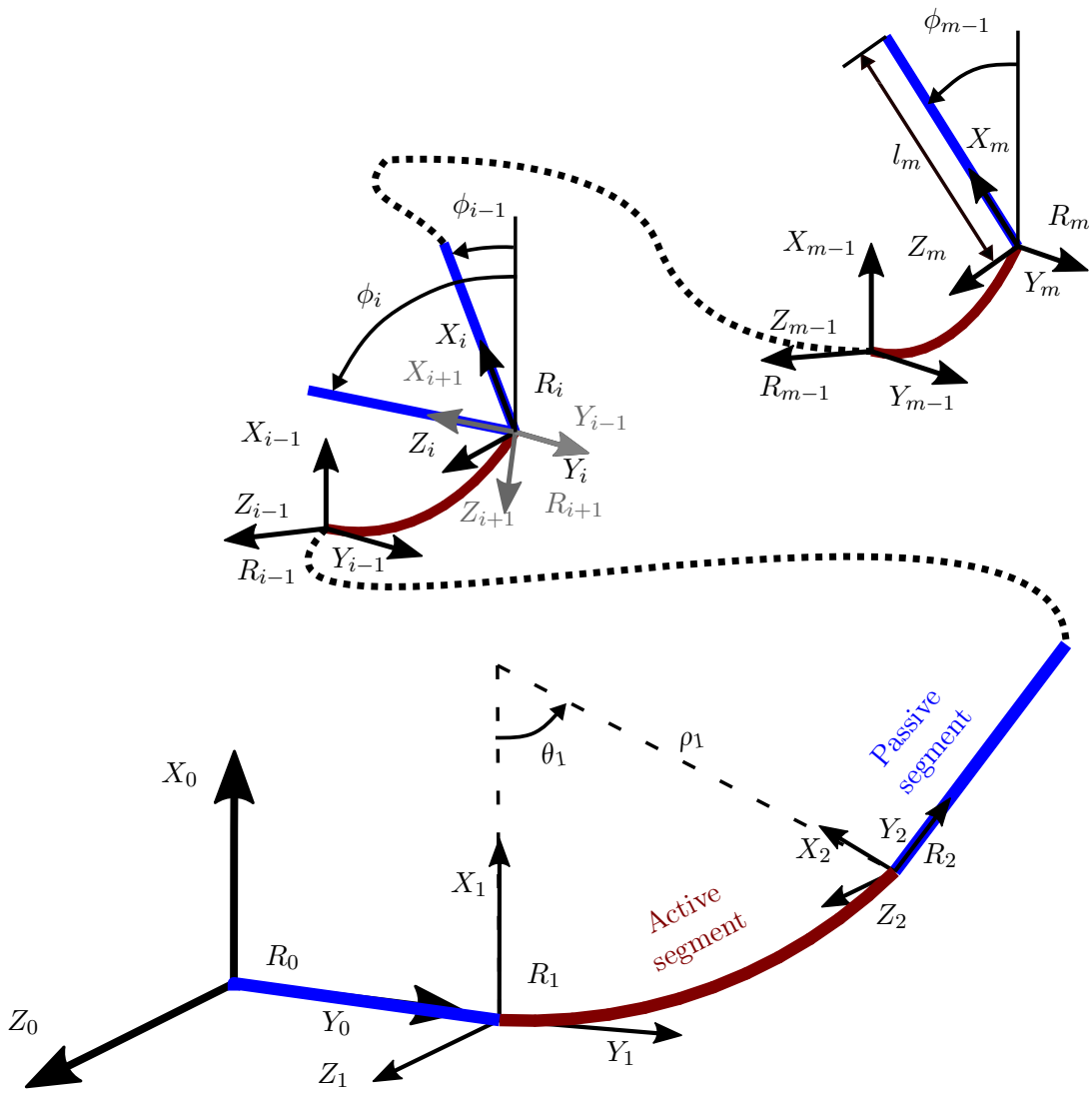

FIGURE 5.8: Coordinate system for the soft milli-robot.

Note: To allow the construction of a kinematic model by following the direct chain of the structures, it is necessary to introduce the orientation angle relative to each segment compared to the previous one. Thus: $\Delta\phi_i = \phi_i - \phi_{i-1}$ for all $i \in \{2..n\}$ and $\Delta\phi_1 = \phi_1$.

To ensure consistent modeling of continuum robots in general and our origami-inspired robot in particular, an intermediate space called configuration space was introduced by [Jones and Walker, 2005]. It was reused later on for different continuum robots, such as the case of concentric-tube continuum robots [Webster III and Jones, 2010]. Admittedly, so far, only the space of the actuators defined by $\mathbf{q} = [q_1 ... q_N]^T$ (where N is the total number of actuators, which depends on the number m of the segments used) and the task space defined by the pose $\mathbb{X}$ of the robot (where $\mathbb{X} \in SE(3)$) were introduced. The configuration space is defined by the variables of the arc noted $\chi = [\chi_1 ... \chi_i ... \chi_m]^T$, where $\chi \in \mathbb{R}^{3m}$ and $\chi_i = [\rho_i \ \Delta\phi_i \ L_i \ ]^T$. Two functions, as shown schematically in Fig. 5.9, were defined to describe the transition between the three spaces previously presented:

- a specific function (known here as the multi-physics model), which depends solely on the actuators used (EAP-based trilayer actuators in our case). This function allows the transition from the actuator variables $\mathbf{q}$ to the arc variables χ. In our case, Eqns. (5.6) (5.7) and (5.14) are sufficient to define this function.
- an independent function (known here as the kinematic model), which depends on the geometry of the robot and can be developed generically as long as the constant curvature assumption is satisfied. It then allows the transition from the arc variables χ to the pose of the robot $\mathbb{X}$.

In order to define the independent function, a transformation matrix is detailed in what follows. In accordance with the formalism of Denavit-Hartenberg modified by Khalil-Kleinfinger [Khalil and Kleinfinger, 1986], the transformation noted ${}^{i-1}T_i$, allows the transition from the base of the segment $i-1$ to that of the segment i. It contains the translation $P_i = [\rho_i(1 - cos\theta_i) \quad \rho_i sin\theta_i \quad 0]^T$ (expressed in the frame $\{X_i, Y_i, Z_i\}$), the center rotation $\rho_i = [0 \quad \rho_i \quad 0]^T$ (expressed in this same reference) and angle $\theta_i = l_i/\rho_i$ (angle of curvature) around the Z_i axis and the orientation angle ϕ_i around the X_i axis (see Fig. 5.9). Therefore, the transformation matrix is obtained by:

$$ {}^{i-1}T_i = \begin{bmatrix} R_x(\Delta\phi_i) & 0 \\ 0 & 1 \end{bmatrix} \begin{bmatrix} R_z(\theta_i) & P_i \\ 0 & 1 \end{bmatrix} = \begin{bmatrix} R_x(\Delta\phi_i)R_z(\theta_i) & R_x(\Delta\phi_i)P_i \\ 0 & 1 \end{bmatrix} \tag{5.15} $$

In the general case, the transition from the base of a m-segment robot to its terminal organ takes the following form:

$$ {}^0T_m = \prod_{i=1}^{m} {}^{i-1}T_i = \begin{bmatrix} {}^0R_m & {}^0t_m \\ 0 & 1 \end{bmatrix}, \tag{5.16} $$

Once we reach this point, the similarities between the modeling of multi-segment continuum robots and origami-inspired systems end here. Unlike continuum robots, the

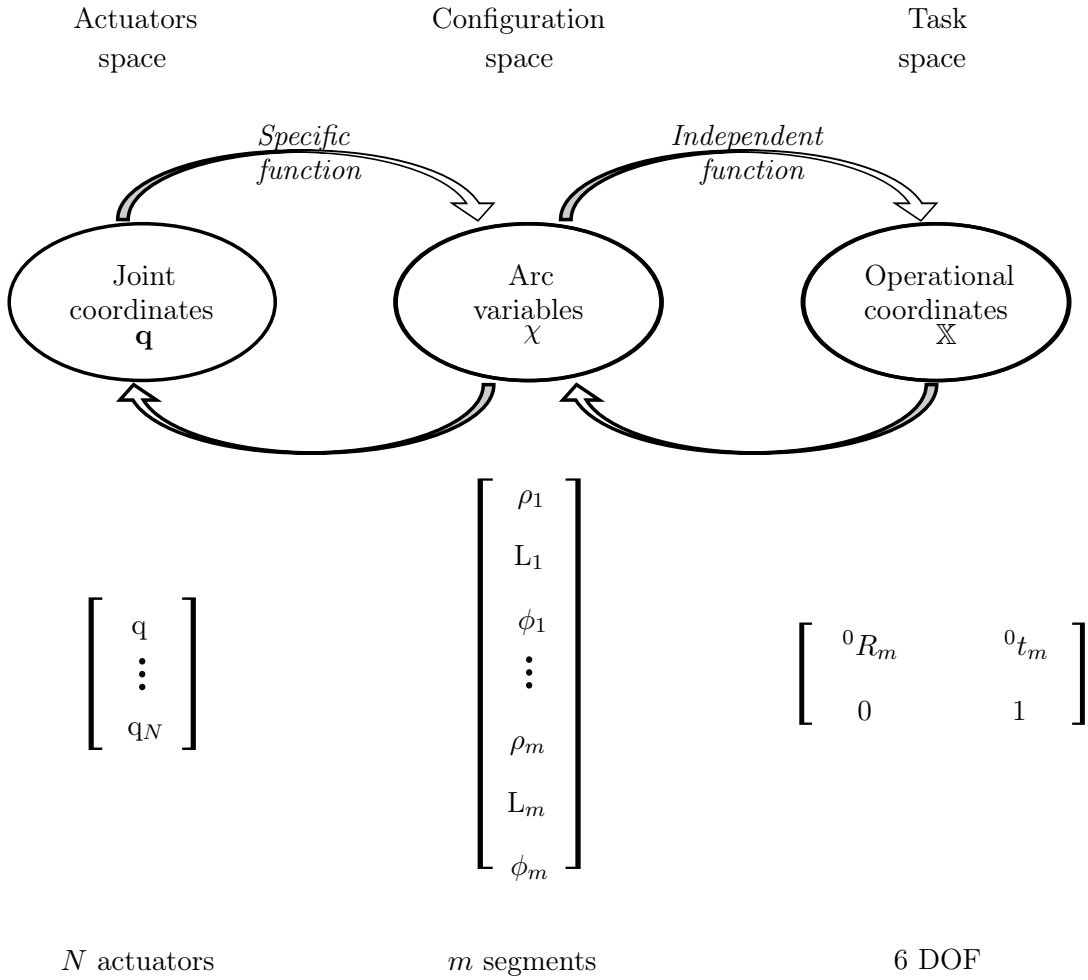

FIGURE 5.9: Definition of the transition functions between the different spaces used for modeling [Chikhaoui, 2016]

.

kinematic modeling of the origami-inspired systems does not end until a model for the geometry of the system is provided, as the shape of the origami system at a given state of folding is a representation of its functionality. Also, it is essential to know that the passive segments are usually made of arbitrary flat surfaces (such as squares and triangles, etc.). Furthermore, for each applied voltage, the deformation of all active segments can be estimated using the multi-physics model, the kinematic model is used in order to reconstruct the entire form of the origami design, using both a discrete representation of active segments (C_A^i) and passive segments (C_P^i). The curvature of the active segments is discretized into n points. The n coordinates for the curvature are obtained using the multi-physics model. The two types of segments can be represented in the global frame

R_0, as shown in Fig. 5.8 using their own frames by the following matrices, respectively:

$$C_A^i = \begin{bmatrix} 0 & x_{i,1} & ... & x_{i,n} \\ 0 & y_{i,1} & ... & y_{i,n} \\ 0 & z_{i,1} & ... & z_{i,n} \\ 1 & 1 & ... & 1 \end{bmatrix}, \tag{5.17}$$

$$C_P^i = \begin{bmatrix} 0 & x_i \\ 0 & y_i \\ 0 & z_i \\ 1 & 1 \end{bmatrix}, \tag{5.18}$$

where x_i, y_i and z_i are the coordinates of the passive segment i, and $x_{i,j}$, $y_{i,j}$ and $z_{i,j}$ are the coordinates of the point j from the curvature of the active segment i.

Finally, using equations (5.18)(5.17)(5.16), the geometry of the milli-origami robot can be obtained in the global frame R_0 using the concatenation of all the expressions of the m different segments, as such:

$$SR_m = \left[|{}^0T_1\, C_{Sgt}^1| \;, ..., \; |\prod_{j=1}^{i} {}^{j-1}T_j\, C_{Sgt}^i| \;, ..., \; |\prod_{j=1}^{m} {}^{j-1}T_j\, C_{Sgt}^m| \right]. \tag{5.19}$$

where Sgt is equal to A or C, depending of the type of the segment.

5.3.1.1 Three-segment system

In this subsection, a three-segment straight structure is modeled. The structure contains one active segment (CP actuator), linking two rigid segments moving in the (X_0,Y_0) plan. In this case, all the z coordinates, as well as the rotation angle ϕ, are null. The three segments are defined in their own frames R_1, R_2 and R_3, respectively, by the following matrices, for the first segment:

$$C_P^1 = \begin{bmatrix} 0 & L_1 \\ 0 & 0 \\ 0 & 0 \\ 1 & 1 \end{bmatrix}, \tag{5.20}$$

for the second segment:

$$C_A^2 = \begin{bmatrix} 0 & x_{2,1} & ... & x_{2,n} \\ 0 & y_{2,1} & ... & y_{2,n} \\ 0 & 0 & ... & 0 \\ 1 & 1 & ... & 1 \end{bmatrix}. \tag{5.21}$$

The coordinates of the points of the active segment, in expression (5.21), were determined using an electro-chemico-mechanical model, as discussed above. Finally, the matrix of

the third segment is:

$$C_P^3 = \begin{bmatrix} 0 & L_3 \\ 0 & 0 \\ 0 & 0 \\ 1 & 1 \end{bmatrix}. \tag{5.22}$$

Then, in order to express the three segments in the global frame R_0 using the method discussed above, the following transformation matrices are required:

$$\begin{gathered} {}^0T_1 = \begin{bmatrix} 1 & 0 & 0 & 0 \\ 0 & 1 & 0 & 0 \\ 0 & 0 & 1 & 0 \\ 0 & 0 & 0 & 1 \end{bmatrix}, {}^1T_2 = \begin{bmatrix} 1 & 0 & 0 & L_1 \\ 0 & 1 & 0 & 0 \\ 0 & 0 & 1 & 0 \\ 0 & 0 & 0 & 1 \end{bmatrix}, \\ {}^2T_3 = \begin{bmatrix} cos\theta_3 & -sin\theta_3 & 0 & x_{2,n} \\ sin\theta_3 & cos\theta_3 & 0 & y_{2,n} \\ 0 & 0 & 1 & 0 \\ 0 & 0 & 0 & 1 \end{bmatrix}. \end{gathered} \tag{5.23}$$

Where θ_3 is the angle between the tangent of the second segment (active segment) at its tip and the X_0-axis. Furthermore, by using expressions (5.20), (5.21), (5.22) and (5.23) the full three-segment structure can be given as:

$$\begin{gathered} SR_3 = \begin{bmatrix} {}^0T_1\, C_P^1 & {}^0T_1{}^1T_2\, C_A^2 & {}^0T_1{}^1T_2{}^2T_3\, C_P^3 \end{bmatrix} = \\ \begin{bmatrix} 0 & L_1 & L_1 & x_{2,1}+l_1 & .. & x_{2,n}+l_1 & x_{2,n}+L_1 & x_{2,n}+L_1+L_3\, cos\theta_3 \\ 0 & 0 & 0 & y_{2,1} & .. & y_{2,n} & y_{2,n} & y_{2,n}+L_3\, sin\theta_3 \\ 0 & 0 & 0 & 0 & .. & 0 & 0 & 0 \\ 1 & 1 & 1 & 1 & .. & 1 & 1 & 1 \end{bmatrix} \end{gathered} \tag{5.24}$$

The expression (5.24) is $[4 \times (n+5)]$ matrix, which is the concatenation of first segment matrix $[4 \times 2]$, second segment matrix $[4 \times (n+1)]$ and third segment matrix $[4 \times 2]$. It allows the modeling of the folding behavior of the three-segment structure. The angle θ_3, also known as the folding angle of the structure, depends on the curvature of the active segment (second segment), which is induced by the applied voltage.

5.3.1.2 Origami cube model

The model of the self-folding origami cube is a three-dimensional model, and it uses one applied voltage to control all active segments. The model contains 14 segments: 9 passive segments (1, 2, 4, 6, 8, 9, 11, 12 and 14) and 5 active segments (3, 5, 7, 10 and 13), as shown in Fig. 5.10. Contrarily to the serial model discussed above, some joints connect more than two segments. In this case, one joint connects four segments (1, 2, 9, and 12). Furthermore, segments from 1 to 8 are all in the plan (X,Y), which means that their orientation angle ϕ is equal to 0. As for segments 9 to 14 they are all in the plan (Y,Z). Nonetheless, the orientation angle ϕ for the segments 9 to 11 is $\frac{\pi}{2}$, and for

segments, 12 to 14 is $-\frac{\pi}{2}$, as shown in Tab. 5.6. However, for the sake of brevity, the model will not be developed here.

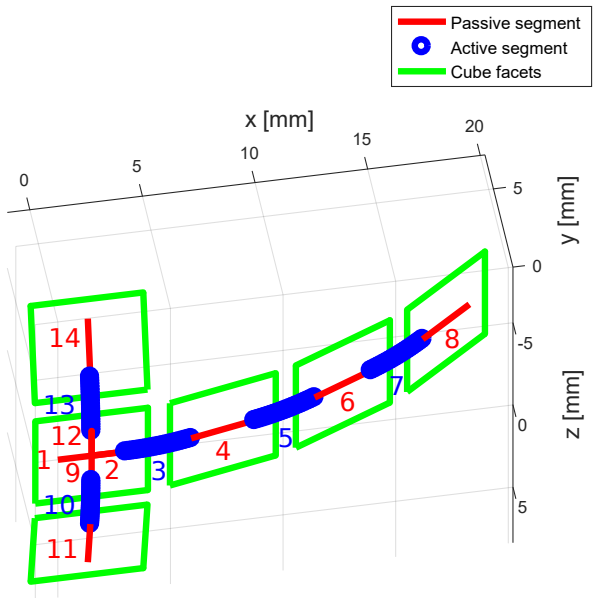

FIGURE 5.10: kinematic model of the self-folding origami cube for an applied voltage of 0.1 V.

TABLE 5.6: List of variable for the origami cube model.

Segment	Type	Length (mm)	width (mm)	Orientation angle ϕ (rad)
1	passive	3	5	0
2	passive	3	5	0
3	active	2	1	0
4	passive	3	5	0
5	active	2	1	0
6	passive	3	5	0
7	active	2	1	0
8	passive	3	5	0
9	passive	3	5	$\frac{\pi}{2}$
10	active	2	1	$\frac{\pi}{2}$
11	passive	3	5	$\frac{\pi}{2}$
12	passive	3	5	$-\frac{\pi}{2}$
13	active	2	1	$-\frac{\pi}{2}$
14	passive	3	5	$-\frac{\pi}{2}$

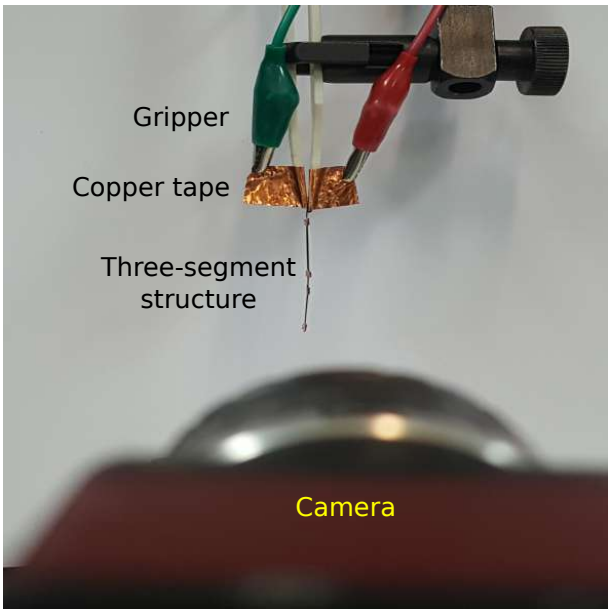

FIGURE 5.11: Experimental setup for the characterization of the CP actuator-based self-folding structures.

5.3.2 Experimental validation

A test bench was mounted in order to characterize the three-segment structure. It was based on ***Matlab/Simulink*** software using Visual Servoing Platform (ViSP) and a dedicated blockset cvlink[3]. The self-folding structures were hugged from a gripper covered by conductive copper tape from each side, to allow electrical stimulation of the structure, as shown in Fig. 5.11. The gripper was also used to constrain the first segment, in order to not move during the experimental testing. The applied voltage is provided via a National Instruments multifunction data acquisition module (USB-6211), which can generate a voltage between $\pm$ 10 V with a resolution of 3.5 mV. A camera (IEE 1394 Guppy Firewire) is placed in front of three-segment structure such that it allows the visualization of the structure thickness.
The aim of this section is to discuss the fabrication process of the trilayer CP actuators utilized in the proposed self-folding approach. Then, the experimental setup is presented. Next, the model of self-folding three-segment structure (passive/active/passive) is experimentally validated. Finally, a proof of concept of a more complex origami-based structure (origami cube) is presented.

[3]https://sourcesup.renater.fr/cvlink/

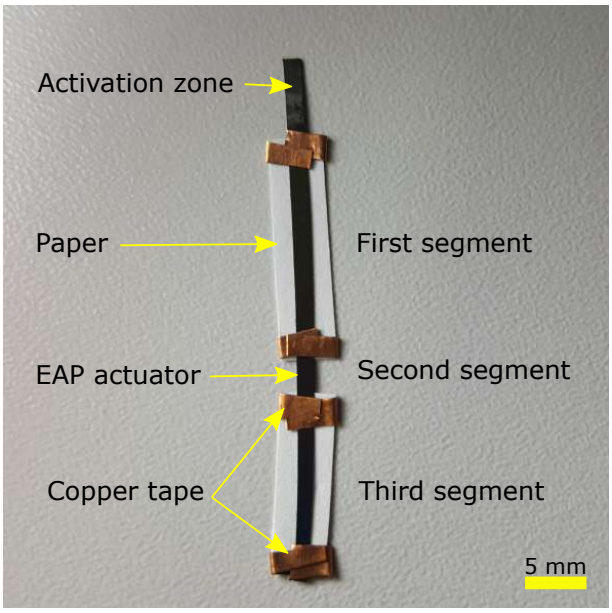

FIGURE 5.12: Top view of the three-segment self-folding straight structure.

5.3.2.1 Three-segment structure

The main objective of this subsection is to validate the model of the three-segment self-folding structure experimentally. First, a 41 mm long and 3 mm wide strip of the trilayer CP actuator was cut using a sharp scalpel. Then, two strips of paper (15×5 mm^2 and 20×5 mm^2) were glued to each end of the actuator: the two paper strips were put against each end of the CP actuator, then using small pieces of tape they were glued to the actuator (as shown in Fig. 5.12). The paper strips were utilized in order to rigidify certain regions of the actuator where bending is not needed (both ends) and to allow the design of the self-folding three-segment structure: two passive (rigid segments) linked by an active segment (bendable). The dimensions of the segments are 15×5 mm^2, 6×3 mm^2 and 20×5 mm^2, from the first to the third segment, respectively. The three-segment structure was mounted into the experimental setup, and series of experimental tests were conducted. For different applied voltages (from 0.2 to 0.7 V), the behavior of the studied structure was observed and compared to the model discussed above. The results are shown in Fig. 5.13. An applied voltage of 0.2 V induces a folding angle of about 38°. Then, for each additional 0.1 V to the applied voltage, the folding angles gain approximately 10°, until it reaches almost 90° for a voltage of 0.7 V as shown in Tab. 5.7. One can notice that even though the paper strips help maintain the passive segments rigid, their weight (less than 10 mg) has a negligible effect on the folding motion. However, if their weight exceeds 100 mg, it will have a very negative effect on the folding motion as well as the maximum folding angle.

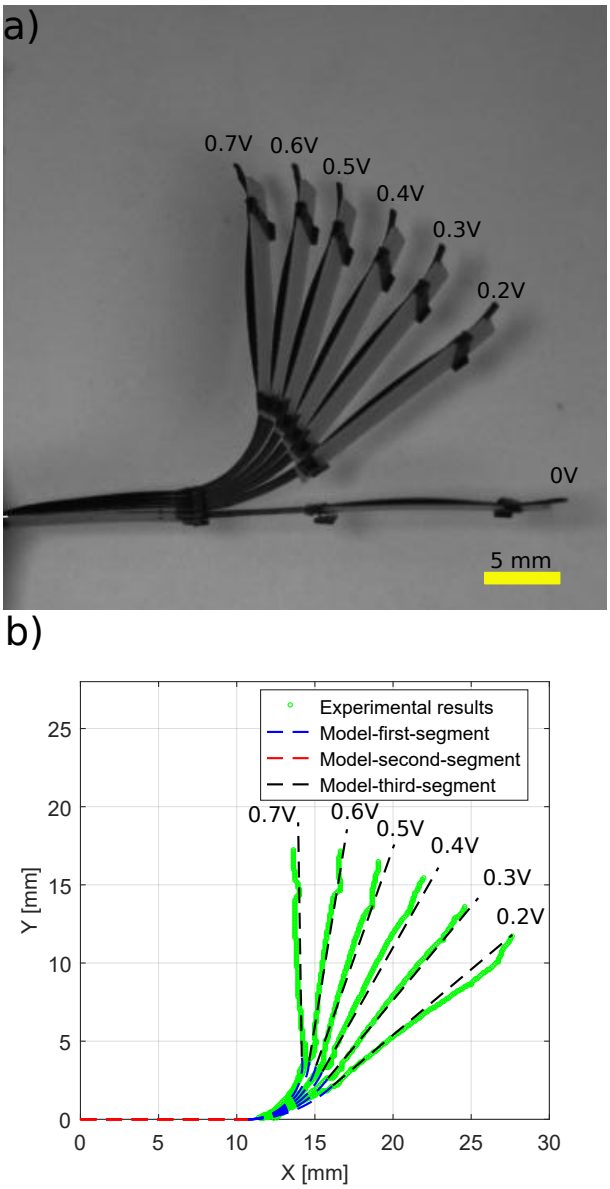

FIGURE 5.13: Three-segment self-folding structure: a) responses for an applied voltage varying from 0.2 to 0.7 V obtained through superimposition of images, and b) comparison of the experimental results to the model.

The proposed model is able to simulate the behavior of the three-segment structure (the folding) with an RMS error of 1.3° as shown in Tab. 5.8, which is less than 1.5 % of the maximum folding angle. It can be concluded that the model works well and can be utilized to simulate more complex self-folding structures and designs.

TABLE 5.7: Folding angles of the three-segment structure.

Applied voltage (V)	0.2	0.3	0.4	0.5	0.6	0.7
Folding angle (°)	37.8	51.4	61.7	71.7	81.1	89.6

TABLE 5.8: Error of the model for the three-segment structure.

RMS (°)	STD (°)	MAX (°)	MIN (°)
1.3	0.5	2.2	0.4

5.3.2.2 Origami cube

As proof of concept for more complex self-folding structures based on CP actuators, the folding of an origami cube was tested. The design of the origami cube contains three types of components: (i) a T-shaped CP actuator, which was cut using a sharp scalpel, (ii) a 3×3 mm^2 squares of double-sided copper tape and (iii) 5×5 mm^2 squares of paper (see Fig. 5.14). Five copper tape squares were used in the fabrication of the 2D design of the origami cube. They were glued to the T-shaped CP actuator to act as 3 mm passive segments. The reason behind using copper taper instead of regular tape is, to avoid the bending of the passive segments by the CP actuator. Each copper square (passive segment) was at a distance of 2 mm from the next ones. In other words, the length of the active segments is 2 mm, and they have a width of 1 mm. Finally, the 5×5 mm^2 paper squares were glued on top of the copper tape squares in order to compensate for the some-what long active segment and to ensure a closed cube-shaped structure.

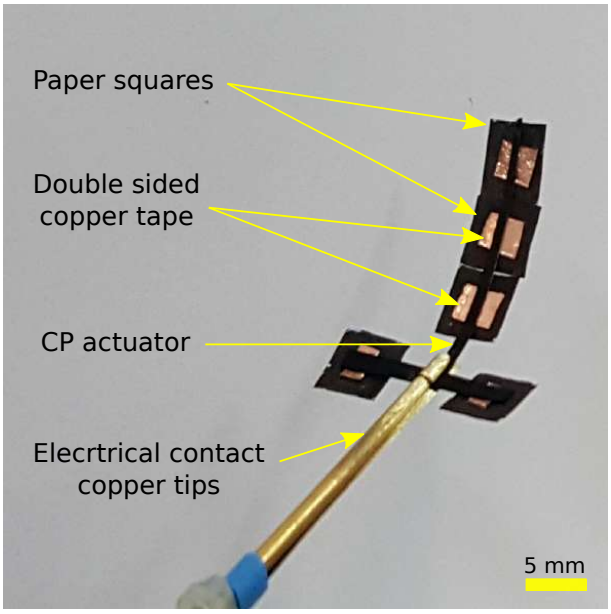

FIGURE 5.14: Top view of the 2D design of the self-folding origami cube.

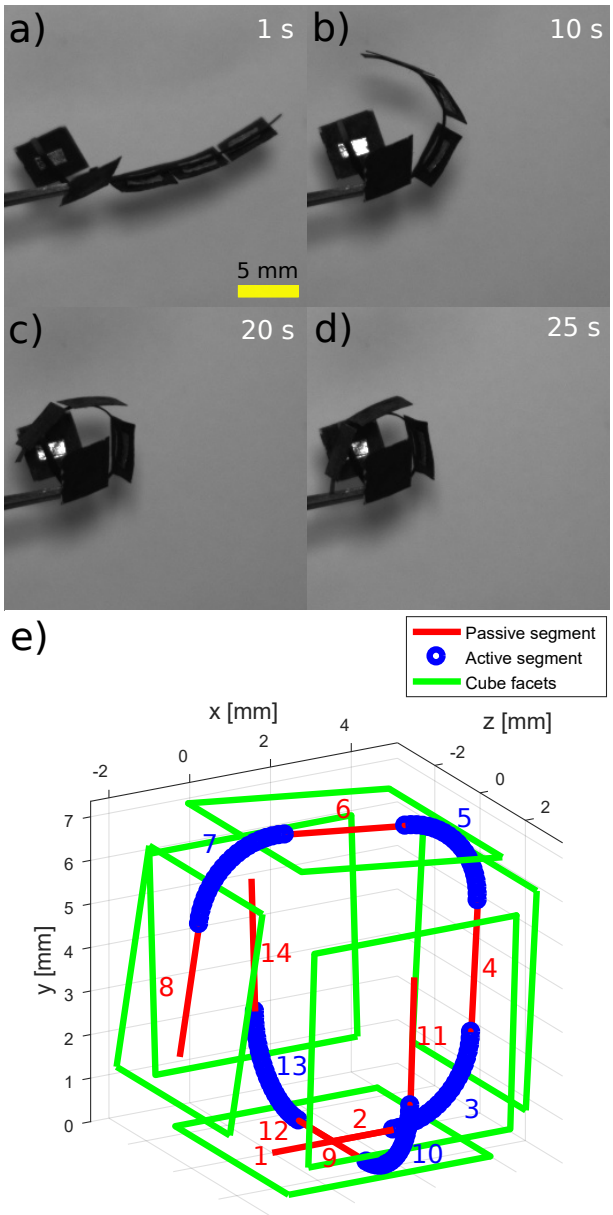

FIGURE 5.15: Folding of the origami cube for an applied voltage of 0.7 V: time laps of the experimental folding a) at 1 s b) at 10 s c) at 20 s d) at 25 s and e) self-folding simulation model.

A shorter active segment can be used; however, in this case, higher voltages (around 2 V) are needed to achieve the folding. Nonetheless, the high voltage can gradually damage the CP actuator and drastically lower its performance. The effect of the damage can be easily observed after a few cycles of activation. However, this not the case for an

applied voltage of 0.7 V or less. The CP actuator suffers zero damage, no matter how many activation cycles are performed.
An applied voltage of 0.7 V was used to activate the self-folding system of the origami cube. The results are shown in Fig. 5.15. The model was able to estimate the behavior of the self-folding origami cube. Nonetheless, even by exploiting the model, it will not be enough to achieve more precise folding, because the manual cutting really limits this approach, in terms of the complexity and the accuracy of the cut shapes. For example, it will be useful to have the same width across the entire cut shape in order to have a uniform behavior (i.e., the same folding angle from all active segments) for the self-folding structure. Furthermore, to overcome such limitations, laser machining has to be used during the fabrication process.

5.4 Conclusion

Among other properties, large volume and shape variation of origami robot designs pushes their dynamic reconfigurability to the extreme, to the point of giving not just new forms but also new functionalities. Such dynamic reconfigurability has been highly sought after in robotic applications as it allows for on-demand multifunctionality. Furthermore, in addition to the dynamic reconfigurability, the miniaturization of robots down to milli, micro, and even nano-metric scales has been equally if not more sought after in the hope of hugely widening the application scope. As a result, seeking a marriage between these two properties seems to be highly attractive, especially since the miniaturization of origami robots can be relatively easier to achieve. To that end and for the prospect of taking a step toward the scaling down of our proposed origami approach, we decided to investigate EAPs as potential high-performance actuators for milli-origami robots. EAPs have an electromechanical coupling with a very high strain, biocompatible characteristics, and the ability to conform to different surfaces and shapes, also known as Polymorphic Adaptability. Therefore, such smart materials are in very high demand for actuation and sensing in a vast range of applications, especially those concerning the biomedical field.
In this chapter, the investigation was divided into two studies. The first study was regarding CPs (sub-class of EAPs) based milli-soft robots. This study seemed inevitable in order to better understand the behavior of the CPs actuators/systems since they represent the folding parts of the milli-origami robots. Once the first study was conducted, a transition toward more complex milli-robots, origami milli-robots can be possible. In the first study, a multi-segment EAPs based soft systems are introduced. The fabrication process of such systems was discussed, as well. A large deformation analytical model of the single and two-segment systems was also introduced and experimentally validated with high accuracy. Moreover, more complex configurations of the multi-segment soft system were investigated, and details on the fabrication process and their functioning was demonstrated.
In the second study, an approach for self-folding origami systems based on CP actuators is discussed. A hybrid model for simulating the behavior of such systems is proposed: a

composition between the multi-physics model for of the model contains two types of segments: passive segments rigidified using paper or copper tape, and active segments made of CP actuators. Furthermore, since the maximum used voltage is 0.7 V, one can conclude that using CP actuators allows for an energy-efficient self-folding approach, without compromising the significant and reversible folding behavior. An origami cube was used as a proof of concept for more complex self-folding origami robots. The development of such systems can be very beneficial for many applications, especially applications where navigating through a constrained environment is a major concern, such as biomedical applications and manipulation at small scales. For instance, the multi-segment system can navigate in narrow spaces either by itself or by using its surroundings as a support when the deformation needed is significant even for it. Furthermore, inserting more than one multi-segment milli-soft robots should be possible, so collaboration between the robots can be planned.
The next step will be the study of milli-robots with more complex origami designs. This will enlarge their field of applications and improve their properties. In addition, controlling each part of the origami robots separately or simultaneously in order to achieve a particular task will be an interesting challenge. The complexity of the shape can be increased by using laser micromachining; this process is under development. The designed structures will be developed for biomedical applications in confined spaces such as the navigation of the human body and/or drug delivery.

Conclusion and perspectives

"Difficult roads often lead to beautiful destinations." - Unknown

Contents

Conclusion

The ultimate goal of this thesis is to contribute to the advancement and the progress of origami engineering in general and scalable origami-based active structures in particular. Origami, the ancient oriental art, enables the creation of complex 3D shapes from a single flat sheet of paper just by folding. Folding is also one of the primary fabrication tools of nature, as it can achieve elegant designs and sophisticated functionalities. Today, as one of the fast-growing research fields, origami engineering has redefined how to make and use structures, active devices, and robots. More personally, this thesis, which is a collaboration between two different departments, AS2M department and Applied Mechanics department, was a unique opportunity to learn, share, contribute, and push the limits of the state of the art of these topics related to origami engineering with a considerable margin of freedom and an exceptionally broad range of disciplines including acoustics, robotics, micro-fabrication and smart materials. The contributions proposed in our work, because of their multidisciplinarity, can be classified as theoretical and technological.

First, we have provided a synthesis of state of the art regarding the field of origami engineering both in a broad and precise manner. It included definitions, axioms and theorems, mathematical tools and algorithms, description of the used fabrication technologies and different applications, in addition to the adopted actuation systems. We also discussed the different challenges and difficulties surrounding such a field.

In an attempt to address these challenges, we proposed a novel and original origami design methodology for active structures by considering the application requirements. The

proposed methodology is composed of two different cycles. A numerical validation cycle which contains: (i) the identification of the application requirements, (ii) selection of an origami base that embodies such requirements, (iii) creation of a 2D and a 3D origami design, and (iv) multiphysics simulation of the behavior of the origami structure in the targeted application. A big experimental validation cycle which besides the numerical validation cycle includes: (v) the selection of materials and the fabrication technologies, (vi) the selection and integration of an actuation system, and (vii) the experimental validation and control (open-loop or closed-loop control) of the active origami structure. Furthermore, we also presented an origami-based Helmholtz resonator for low-frequency sound control. The resonator is a proof of concept of our proposed origami design methodology in the field of vibro-acoustics. Following the proposed methodology:

(i) the application requirements were identified, which include a lightweight, adaptative-passive, low-frequency noise control device;

(ii) the waterbomb origami base, which has the ability to produce auxetic structures (structures with negative Poisson coefficient) was selected for the design;

(iii) a 2D design with three different parts was created, a middle part containing the auxetic cylinder design with a top and bottom parts, one to facilitate the resonator's neck integration and the other to close the cylindrical cavity design from the bottom. The 2D design was followed by a 3D design;

(iv) a set of models, depending on the flexibility (rigid, quasi-rigid, flexible) of the tunable origami-based Helmholtz resonator, were developed to simulate their acoustic behavior. A dynamic/kinetostatic model was also developed to study the mechanical behavior of the resonator and determine the appropriate parameters for the required actuation system;

(v) using, 3D printing, laser machining, manual-folding, dipping, and rubber coating the three types of the origami Helmholtz resonator (rigid, quasi-rigid, flexible) were fabricated;

(vi) a dynamics/kinetostatics analysis were conducted to determine and propose an actuation system for the resonator, which was implemented and utilized for the closed-loop control of the origami device;

(vii) finally the acoustic performance of the three fabricated origami-based resonators were experimentally characterized. The experimental results were able to demonstrate the efficiency and effectiveness of our proposed origami design methodology. First, the results of the rigid origami resonator confirmed that the origami-based shape of the cavity does not have an influence on the acoustic performance, and only its volume does. Secondly, the quasi-rigid origami resonator was able to display an impressive frequency shift of 81 Hz (from 138 to 219 Hz) for a 20 mm cavity diameter variation only, from 70 to 50 mm. Lastly, the flexible origami-based resonator proved to be the most impressive of the bunch, as it was able to

overcome one of the intrinsic limitations of Helmholtz resonators. Despite the fact that Helmholtz resonators are passive and very efficient noise control devices in the low-frequency domain, they have a very narrow absorption bandwidth; therefore, a need for adaptive Helmholtz resonators immerged. That said, the flexible origami-based resonator was able to surpass such a limitation and exhibit a broad bandwidth effect. Additionally, what makes flexible more remarkable is that this effect can be controlled as well. It was able to achieve an impressive frequency shift of 131 Hz (from 431 to 544 Hz) for a 10 mm cavity diameter variation only, from 74 to 64 mm.

Moreover, we also investigated the actuation of small-scale origami-based structures using polypyrrole electroactive polymer. These actuators, which we make our selfed using microfabrication technology and electro-polymerization process, are able to display interesting properties for small-scale origami actuation. They are lightweight, compact, biocompatible with large reversible deformations, and low activation voltages. In addition, we also proposed a hybrid model for origami structures based on polypyrrole electroactive polymer. The model, which based on defining two different segments, is comprised of two models: (i) a static multiphysics model that can estimate the curvature of the active segments depending on the applied voltage, and (ii) a kinematic model for the reconstruction of the full soft continuum robots and origami-based milli-robots, containing both active and passive segments, depending on the applied voltage. The model was experimentally validated in a gradual fashion. First, the active segment model was validated using single-segment and two-segment structures. Then, with the exception of 3D origami robots, the complete hybrid model containing the two segments, active and passive, was validated.

Perspectives

The perspectives are divided into two parts, short and medium term, and long term.

Short and medium term

The multidisciplinary nature of this thesis work has, on the one hand, covered a wide range of topics and offers, on the other hand, several perspectives. We propose in this section to classify the perspectives according to the particularly concerned themes. Three different themes were chosen: (i) origami-based acoustic devices, more precisely tunable Helmholtz resonators; (ii) miniaturized origami-based active devices; and (iii) Polypyrrole origami/soft milli-robots. In addition to perspectives and future work, this section provides some preliminary results regarding each theme.

Origami-based Helmholtz resonator

First of all, with regard to origami-based Helmholtz resonators, some work still to need be done:

– The experimental investigation and validation of the acoustic behavior of origami-based Helmholtz resonators, coupled to porous/fibrous materials, for broad-spectrum sound control, which includes all low, medium, and high frequency ranges.

– The implementation of a more efficient actuation mechanism based on smart materials, such as the SMA, and validate the performances, in open and closed loop control, of the proposed Helmholtz resonator. A PhD thesis concerning the actuation of such a mechanism started within the framework of the ANR project, OrigaBot [ANR-18-CE33-0008, 2019].

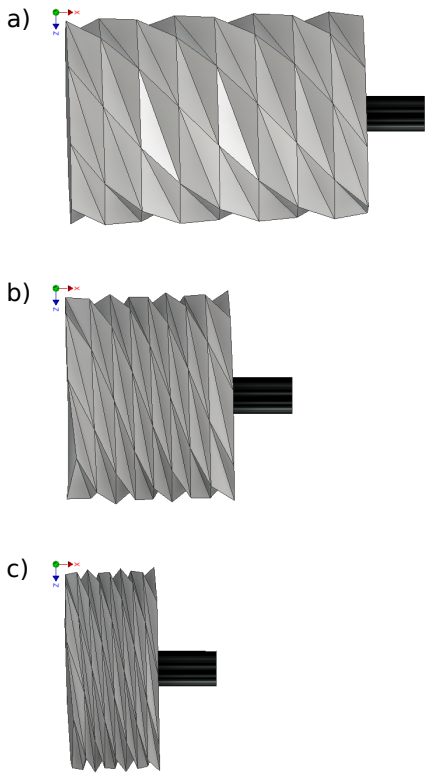

FIGURE A: Origami-based twisting tower design of Helmholtz resonator: a) unfolded state, b) half-folded state, and c) folded state.

Furthermore, even though by using our origami-based design of tunable Helmholtz resonators (introduced in chapter 4), we are well aware that there is no optimal design for a given acoustic device or any other device in general. Depending on the conditions and place of use, in addition to other aspects, the selection of the optimal design may vary considerably. From the beginning, our goal, therefore, was never to find the optimal origami design for tunable Helmholtz resonators but rather to offer an origami design methodology that, once applied, allows us to test and continuously improve the design.

These improvements can also be presented in the form of a brand new origami design. Bearing this in mind and considering that the origami design methodology has already been applied to tunable Helmholtz resonators, the primary purpose of this section is to test a new origami design. The new design is an origami twisting tower design, based on the Kresling origami base, as shown in Fig. A. It allows for a continuous change of the length of the origami-based cavity of the resonator. Although the new design is not as efficient as the old one, which has an auxetic effect and thus allows higher frequency/geometry variation ratios, it nevertheless has other advantages. Given its less complicated shape, the new design can be less troublesome in terms of fabrication and actuation. Besides, since it allows only longitudinal variations of the cavity, the coupling with foam can be performed more easily and efficiently. Furthermore, the origami design, similar to the old design, was able to achieve impressive frequency shifts in low frequencies, as shown in Fig. B. The values of these frequency shifts are available in Tab. A. The acoustic performance of the new design was quantified using the FE model developed for origami devices with rigid and motionless walls (see Sec. 3.4.3.1), which was experimentally validated using the old origami design (see Sec. 4.7.1 and Sec. 4.7.2). Lastly, based on the results of the simulations, it seems interesting to study the acoustic behavior of the twisting tower origami-Helmholtz resonators.

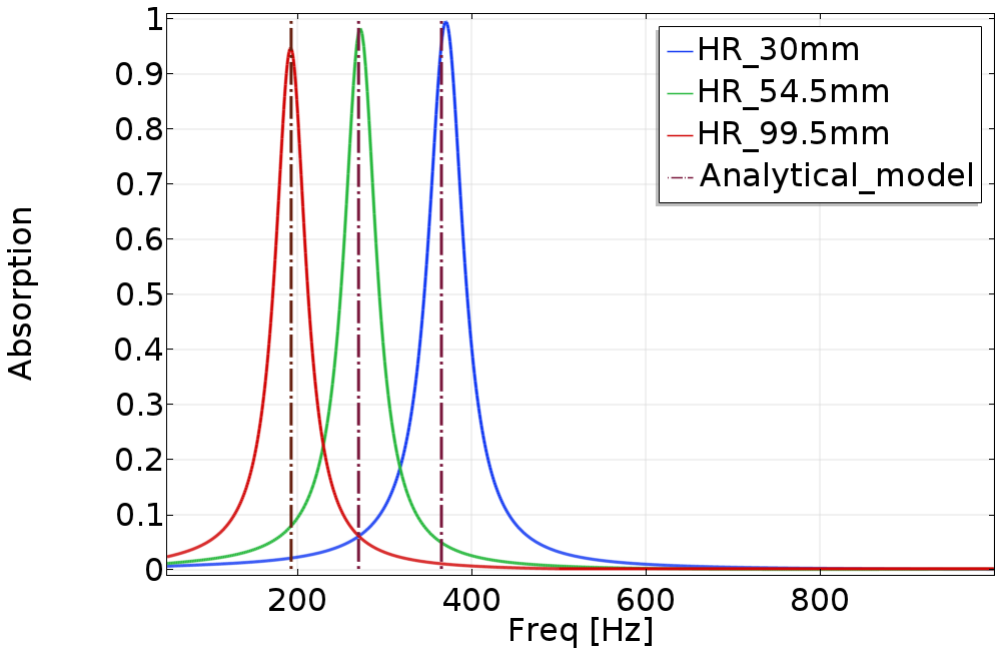

FIGURE B: Comparison between the FE model of the acoustic performance (acoustic absorption) of twisting tower Helmholtz resonator and the resonant frequency analytical model.

Table A: Acoustic absorption for different lengths of the twisting tower origami Helmholtz resonator, given by the FE model.

Length of the origami HR (mm)	***99.5***	***54.5***	***30***
Resonance frequency (Hz)	192	272	370
Total bandwidth (Hz)	178(93%)*		

*Relative bandwidth compared to its starting frequency (192.4 Hz)

Miniaturized origami-based active devices

Compared to traditional devices, origami-based devices support and facilitate miniaturization. As a result, it will be very interesting to apply our origami design methodology for miniaturized origami devices. An excellent example of such devices is the milli-origami deformable wheel discussed here. The wheel was made from thick paper. The 2D design, as well as the 3D design, were generated as discussed in the design steps of the methodology. Once the 3D design was created, the folding lines and the facets were separated, using our ***Matlab*** codes, and reassemble again inside CAD software. Also, two octagons, one for each side of the wheel design, were added as well. Next, the design was imported into FE software in order to create the FE model. Even though the folding lines and the facets are made from the same material (paper), they were assigned slightly different materials since we assume that the folded regions are a damaged material, hence, unlike the untouched regions they have slightly different properties. A load was applied on both octagonal faces in order to simulate the effect of a shape memory alloy actuator, and then simulations on the behavior of the milli-deformable origami wheel were conducted.

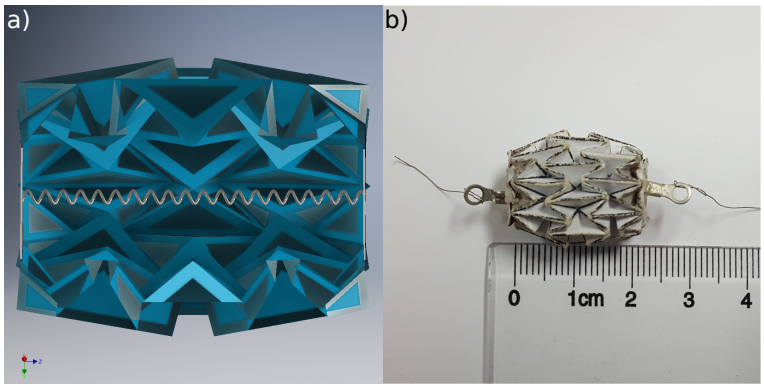

Figure C: Millimeter scale Prototype of a deformable origami ball fabricated using thick paper and utilizing a single shape memory alloy spring as an actuation system. (a) Longitudinal cut view of the milli-origami ball and (b) an image displaying the real size of the origami device. This kind of devices can be very interesting for highly space constrained applications such as the biomedical field.

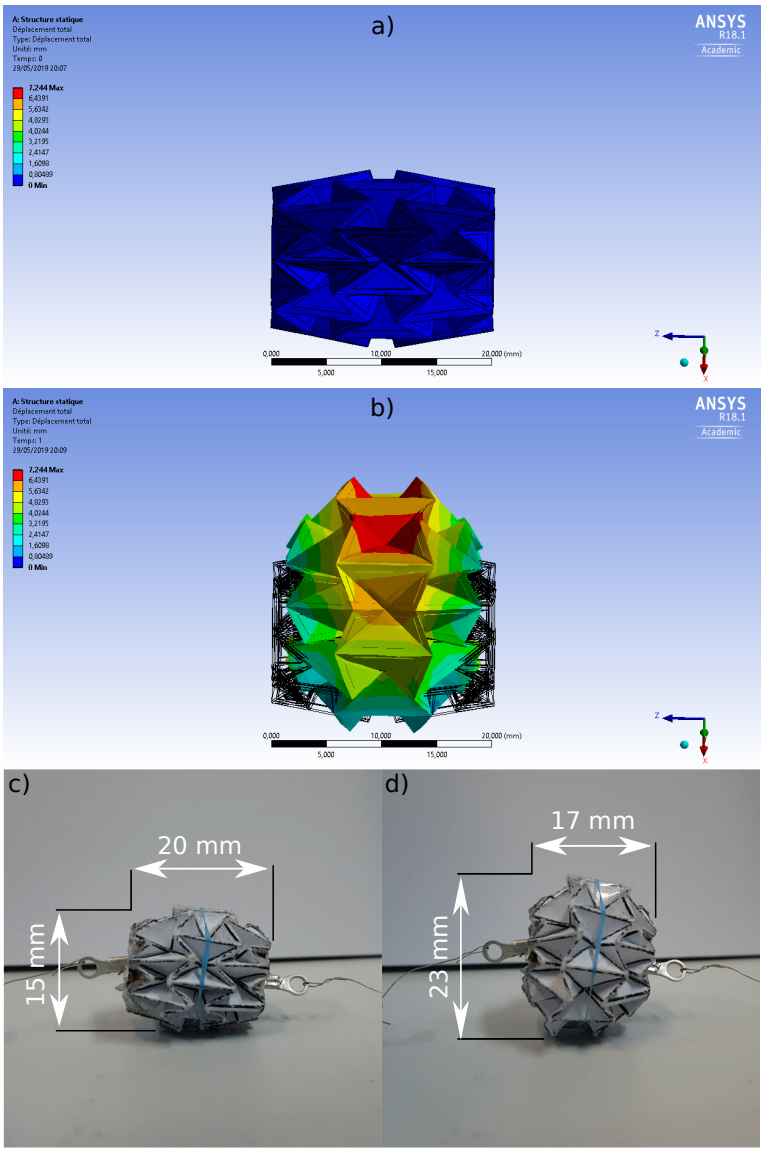

FIGURE D: Comparison between the experimental results of the milli-deformable origami ball and the FE model (developed using our origami approach). The results of the model (a) before applying any force and (b) after applying a force of 0.3 N, show that the device can generate a deformation along its diameter of 7.8 mm (a deformation of 52%). As for the experimental results, the diameter of the device has gone from 15 mm, (c) before applying any force, to 23 mm after applying a force of 0.3 N (by activating the shape memory alloy spring), which is actually an 8 mm (53%) deformation along the diameter.

On the other hand, the generated 2D design was printed with the appropriate size on a piece of paper; then, it was manually folded. The glue was used to add the two octagonal facets from both sides, as well as the shape memory alloy spring, which has

a 0.2 mm diameter (as shown in Fig. C). Finally, an external generator was utilized to apply an electric field on both ends of the actuator, which is able to generate a force of a 0.3 N. The produced results were then compared to those of the model.
As shown in Tab. B after activating the shape memory alloy actuator the origami wheel was able to generate a 8 mm (53%) increase in the diameter, which is comparable to the results generated by the model, which, for the same boundary conditions, was able to achieve a diameter increase of 7.8 mm (52%). This kind of origami devices at this size, fabricated with different materials (such as stainless steel as shown in Fig. D), can be highly beneficial for biomedical applications, such a capsule endoscopy for monitoring tasks in the gastrointestinal tract [Menciassi et al., 2005] as well as a stabilization support during gastrointestinal surgery, in addition to many other interesting applications.

Table B: Comparison between the experimental and model results of a milli-deformable origami wheel, for an applied force of 0.3 N.

Dimensions	***Initial values***	***Results after deformation***	
		experimental	***model***
Diameter (mm)	15	23 (+53%)	22.8 (+52%)
Length (mm)	20	17 (-15%)	17.3 (-13.5%)

Polypyrrole origami/soft milli-robots

This section discusses the potential of polypyrrole origami/soft milli-robots. Consequently, a polypyrrole S-shaped milli-robot is tested. The milli-robot was fabricated through the laser machining (a CO_2 laser machine was utilized) of trilayer polypyrrole-based electroactive sheets. The S-shaped configuration has a line width of 0.4 mm (the width of the active material), and it occupies a surface of $6.2 \times 2.4\ mm^2$. It also has two opposite locations for electric activation; each one has a top and bottom electrode. Technically speaking, both top electrodes and bottom electrodes, for each location are connected; however, applying an electric field in both locations helps improve the response of the soft milli-robot. The latter was then mounted into its 3D printed support, and maintained in place by stainless steel pieces, as shown in Fig. E. The stainless steel is also used to deliver the required electric field, without being affected by the system (reacting with the system), which may lead to negatively effecting its electric connections.
Once the system is appropriately mounted on the testing workbench, a series of experimental tests were conducted in order to characterize the performances of such systems. A voltage ranging from 0.2 to 1 v with a step of 0.2 v, was applied at both electrically connected locations. Each voltage was applied for a period of 25 s; then, a 30 s resting period was given to the system in order for it to regain its original form. The maximum deformation was then captured by the camera. A superimposition of the frames containing the maximum deformations can be shown in Fig. F.

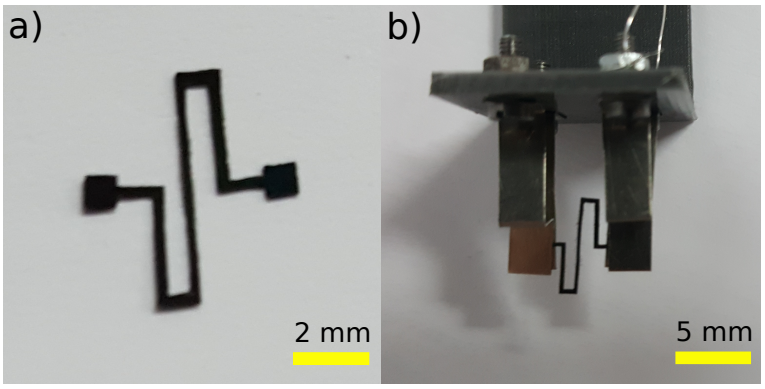

FIGURE E: Prototype of a Polypyrrole-based milli-system, fabricated using laser machining: (a) an S-shaped system which was (b) mounted into an experimental setup, using 3D printed support and machined strips of thin stainless steel sheets.

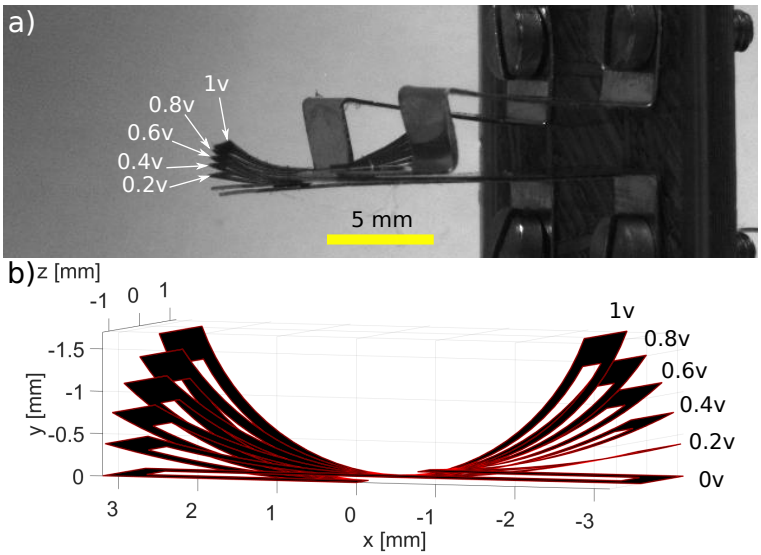

FIGURE F: Comparison of (a) the experiment behavior of the S-shaped Polypyrrole-based milli-robot to (b) the behavior of the multi-physics model. Different voltages were used during the experiment, ranging from 0.2 to 1 V with a step of 0.2 V .

The maximum tip displacements of the robot were then calculated from the frames provided by the camera, using pixels to *mm* conversion. The experimental results were then compared to the results of the complex model (multi-physics and kinematic model). A comparison between the behavior of the S-shaped soft system (the generated forms) and the model, for the different applied voltages, can also be seen in Fig. F. However, a more quantitative comparison, regarding the tip displacements of the milli-system, is

shown in Fig. G. The S-shaped soft milli-robot was able to generate a maximum vertical tip displacement of 1.5 mm, which is compared to the size of the deformed part of the system (the 3.1 mm active segments) is a very high displacement ratio of 48%. The root mean square error between the experimental results and the model is of 88 μm, which is 5.8% error compared to the maximum displacements of the tip. These values, as well as, the values of the standard, maximum and minimum errors are available in Tab. C.

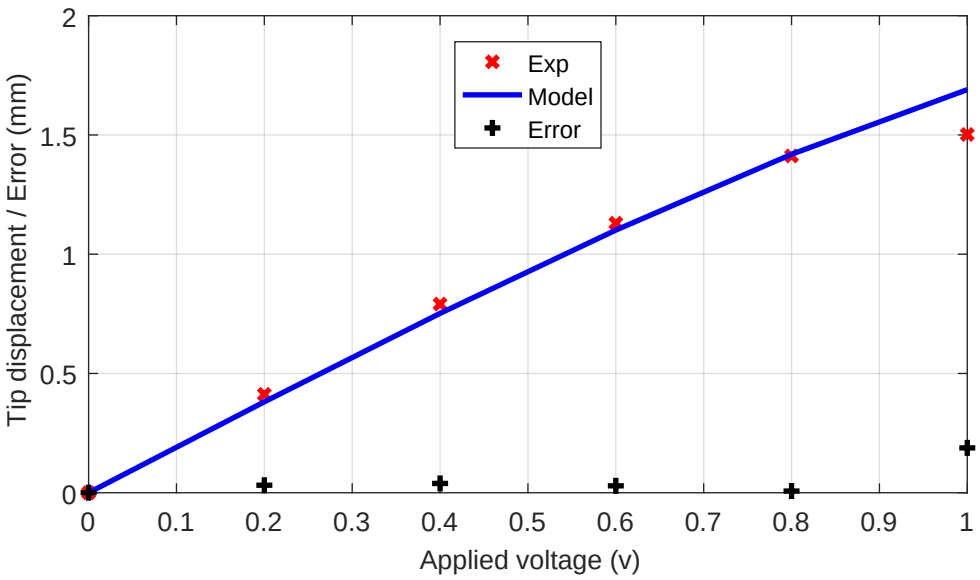

FIGURE G: Comparison between experimental results and the proposed model, of tip displacement of the S-shaped soft milli-robot, for applied voltages ranging from 0 to 1 v.

These results show that the model was able to predict with a high accuracy the behavior of the soft milli-robot for the applied voltages, ranging from 0.2 to 0.8 v, however, once 0.8 v is reached the robot's deformation is saturated (an increase in voltage will only result in a minimal deformation). Therefore, the model was not able to accurately predict the deformation after this point.
Finally, based on the previous results and the results provided here, polypyrrole based electro-active polymers show great potential for origami-based as well as soft milli-robots for a wide range of applications. Therefore, this is highly interesting to study, investigate, and develop such robots, especially for micro/nano-manipulation and biomedical applications.

Table C: Tip displacement's error of the S-shaped system model.

RMS (μm)	STD (μm)	MAX (μm)	MIN (μm)
88(5.8%)*	73(5.8%)*	187(12.4%)*	0.6(0.4%)*

*Relative error compared to the maximum tip displacement

Long term

Even though origami robotics and mechatronics are one of the rapidly growing fields of research, thanks to the continuously growing number of works, including this one, various technical challenges remain.
For the physical structures, we need tools to design, model, fabricate origami structures and evaluate their performances in a given field of interest. Self-contained structures made of a variety of different materials and are able to accommodate different environments and work conditions. We need structures with smarter materials in addition to embedded electronic components that are production-ready, self-powered, remotely-controlled, able to sense, compute, act, execute, communicate, and collaborate. Structures with programmable material properties that not only able to shape-shift but also are able to be locally soft or rigid if needed and have a dynamic origami pattern instead of a preset pattern.
As for control, origami robots come with their own set of challenges, and they drastically increase with the number of folds required. We need better computational algorithms based on more realistic physical models tailored for origami robots, not only to improve the design, performance evaluation, and fabrication processes but also to better guide and inform the control algorithms during task planning and execution.
Finally, a better understanding of the relationship between the algorithms and structures/materials, origami robots and surrounding environments, in addition to performances and requirements, will allow for the design and fabrication of cheap, customizable robots for a wide range of applications, and with exceptional properties, combining all; rigid, semi-rigid, and soft characteristics.

Personal profile

- **Journals**
  - **Benouhiba, A.**, Patrick, P., Andreff, N., Rabenorosoa, K., and Ouisse, M."Origami-based tunable Helmholtz resonator for noise control". Sound and Vibration, 2020, (under submission).
  - **Benouhiba, A.**, Patrick, P., Ouisse, M.,Clévy, C.,Andreff, N., and Rabenorosoa, K."Toward high performance conductive polymer-based soft milli-robots for vacuum applications". Frontiers in Robotics and AI, 2019, vol. 6, p. 122.
  - **Benouhiba, A.**, Belharet, A., Bienaimé, A., Chalvet, V., Rakotondrabe, M., and Clévy, C. "Development and characterization of thinned PZT bulk technology based actuators devoted to a 6-DOF micropositioning platform" Microelectronic Engineering, 2018, vol. 197, p. 53-60.
  - Chikhaoui, M. T., **Benouhiba, A.**, Patrick, P., Rabenorosoa, K., Ouisse, M., and Andreff, N. "Developments and Control of Biocompatible Conducting Polymer for Intracorporeal Continuum Robots" The Journal of the Biomedical Engineering Society, Annals of Biomedical Engineering, 2018,vol. 46, no 10, p. 1511-1521.
- **Conferences and proceedings**
  - **Benouhiba, A.**, Ouisse, M., and Rabenorosoa, K., Andreff, N. "Investigations on an Adaptive Helmholtz Resonator Concept", 17-19 February, MEDYNA2020, Napoli, Italy.
  - **Benouhiba, A.**, Rabenorosoa, K., Patrick, P., Ouisse, M., and Andreff, N. "A Multi-segment Electro-Active Polymer based milli-Continuum Soft Robots", 1-5 octobre, IROS2018, Madrid, Spain.
  - **Benouhiba, A.**, Rabenorosoa, K., Patrick, P., Ouisse, M., and Andreff, N. "Electro-active Polymer Based Self-folding Approach Devoted to Origami-inspired Structures", 10-12 septembre, SMASIS2018, San Antonio, TX.
  - **Benouhiba, A.**, Rabenorosoa, K., Ouisse, M., and Andreff, N."An Origami-Based Tunable Helmholtz Resonator for Noise Control: Introduction of the Concept and Preliminary Results", 18-20 septembre, SMASIS2017, Snowbird, UT.

Appendices

Appendix A

Kinematics of PPy-based multisegment continuum soft robots

The link and joint parameters in the classical convention as shown in Fig. A.a are as follows:

- Twist angle, α_{i-1} is the angle between Z_{i-1} to Z_i measured about X_{i-1}
- Link length, a_{i-1} a is the distance from Z_{i-1} to Z_i measured along X_{i-1}
- Offset length, d_i is the distance from X_{i-1} to X_i measured along Z_i
- Joint angle, θ_i is the angle between X_{i-1} to X_i measured about Z_i

The DHKK parameters are determined as per Tab. A.

Table A: Parameters of Denavit-Hartenberg modified by Khalil-Kleinfinger formalism.

Link, i	α_{i-1}	a_{i-1}	d_i	θ_i
1				
2				

The frame transformation ${}^{i-1}T_i$ describing the finite motion from link $i-1$ to link i may then be expressed as the following sequence of elementary transformations, starting from link $(i-1)$:

- A rotation α_{i-1} about the X_{i-1} axis;
- A translation a_{i-1} along the X_{i-1} axis;
- A translation d_i along the Z_i axis;
- A rotation θ_i around the Z_i axis.

The homogeneous transformation ${}^{i-1}T_i$ is represented as a product of four basic transformations as follows (see Fig. A.a):

$$
\begin{aligned}
{}^{i-1}T_i &= R(X_{i-1},\alpha_{i-1})T(X_{i-1},a_{i-1})R(Z_i,\theta_i)T(Z_i,d_i) \\
&= \begin{bmatrix} 1 & 0 & 0 & 0 \\ 0 & C\alpha_{i-1} & -S\alpha_{i-1} & 0 \\ 0 & S\alpha_{i-1} & C\alpha_{i-1} & 0 \\ 0 & 0 & 0 & 1 \end{bmatrix} \begin{bmatrix} 1 & 0 & 0 & a_{i-1} \\ 0 & 1 & 0 & 0 \\ 0 & 0 & 1 & 0 \\ 0 & 0 & 0 & 1 \end{bmatrix} \begin{bmatrix} C\theta_i & -S\theta_i & 0 & 0 \\ S\theta_i & C\theta_i & 0 & 0 \\ 0 & 0 & 0 & 0 \\ 0 & 0 & 0 & 1 \end{bmatrix} \begin{bmatrix} 1 & 0 & 0 & 0 \\ 0 & 1 & 0 & 0 \\ 0 & 0 & 1 & d_i \\ 0 & 0 & 0 & 1 \end{bmatrix} \\
&= \begin{bmatrix} C\theta_i & -S\theta_i & 0 & a_{i-1} \\ S\theta_i C\alpha_{i-1} & C\theta_i C\alpha_{i-1} & -S\alpha_{i-1} & -d_i S\alpha_{i-1} \\ S\theta_i S\alpha_{i-1} & C\theta_i S\alpha_{i-1} & C\alpha_{i-1} & d_i C\alpha_{i-1} \\ 0 & 0 & 0 & 1 \end{bmatrix}
\end{aligned}
\tag{A.1}
$$

However, in the case of a PPy-based multisegment continuum soft robot (see Fig. A.b), the transformation $R(Z_i,\theta_i)$ from Eqn. A.1 is replaced by $T_{curv}(u_i)$, which is written as

$$
T_{cur}(u_i) = R_{curv}(Z_i,\theta_i(u_i))t_{curv}((u_i)) = \begin{bmatrix} C\theta_i(u_i) & -S\theta_i(u_i) & 0 & x_{in}(u_i) \\ S\theta_i(u_i) & C\theta_i(u_i) & 0 & y_{in}(u_i) \\ 0 & 0 & 0 & z_{in}(u_i) \\ 0 & 0 & 0 & 1 \end{bmatrix} \tag{A.2}
$$

where $\theta_i(u_i)$ and $(x_{in}(u_i),y_{in}(u_i),z_{in}(u_i))$ are the angle of the curvature and the tip coordinates of the active segment i, respectively. This parameters depend on the applied voltage u and they can be determined using the multiphysics model described in Sec. 5.2.5.

An alternative representation of ${}^{base}T_{end-effector}$ for a continuum robot with an m number of segments can be written as

$$
{}^{base}T_{end-effector} = {}^{0}T_m = \prod_{i=1}^{m} {}^{i-1}T_i = \begin{bmatrix} r_{11} & r_{12} & r_{13} & p_x \\ r_{21} & r_{22} & r_{23} & p_y \\ r_{31} & r_{32} & r_{33} & p_z \\ 0 & 0 & 0 & 1 \end{bmatrix} \tag{A.3}
$$

where $r_{kk'}$ represent the rotational elements of the global transformation matrix (k and $k' = 1$, 2 and 3); while, p_x, p_y, and p_z denote the elements of the position vector.

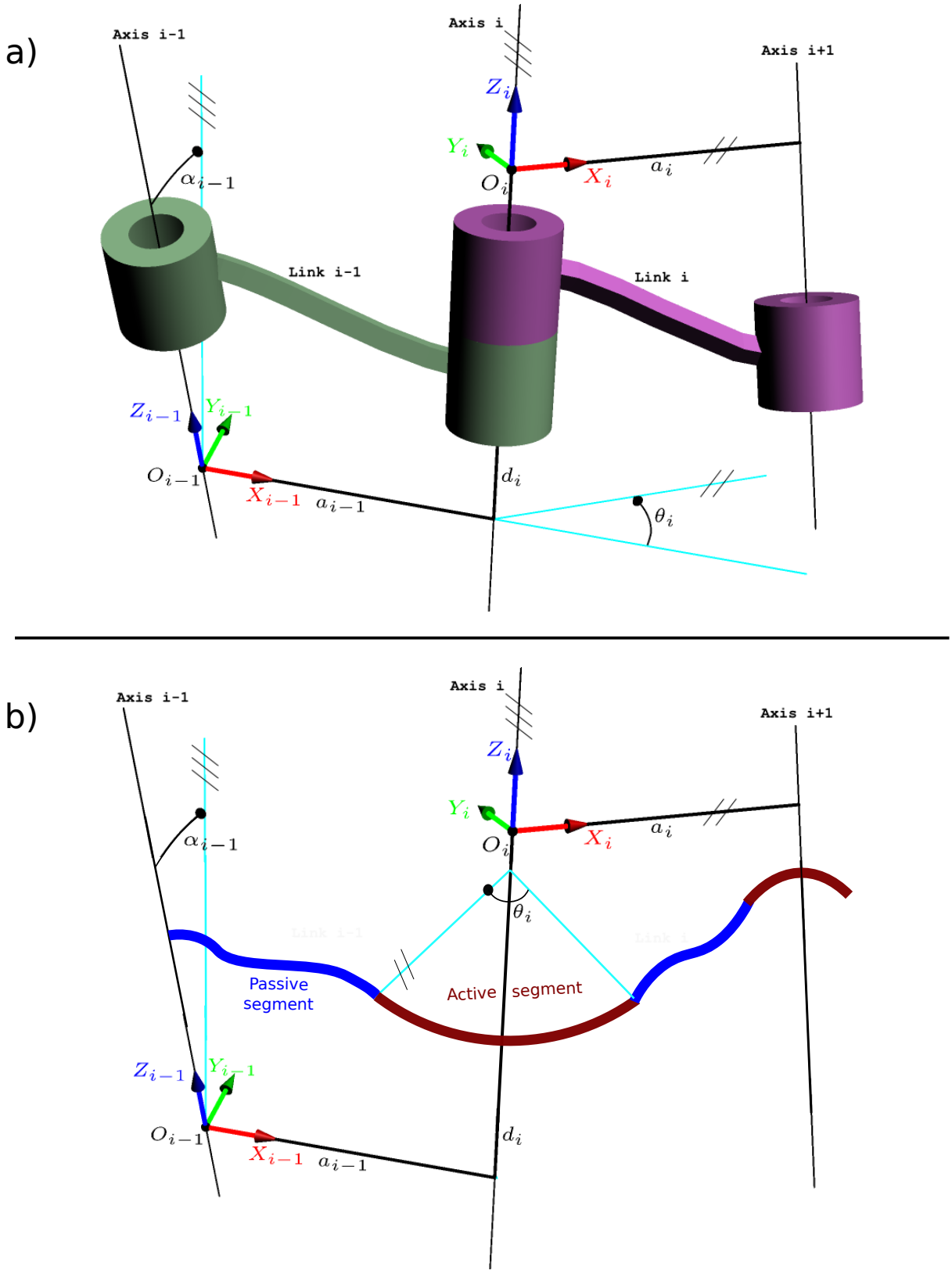

FIGURE A: Illustration of kinematics parameters of a serial robot according to Khalil-Kleinfinger-Denavit-Hartenberg formalism [Khalil and Kleinfinger, 1986]: a) a traditional serial robot, and b) a PPy-based multisegment continuum soft robot.

Bibliography

[Abbad, 2016] Abbad, A. (2016). Numerical investigations on a tunable helmholtz resonator: Integration of a passive polymer membrane in a helmholtz resonator. Technical report, SAE Technical Paper. 70

[Abbad, 2017] Abbad, A. (2017). *Développement d'un traitement acoustique basses-fréquences à base de résonateurs d'Helmholtz intégrés à membrane électroactive*. PhD thesis, Université de Sherbrooke. xiii, 73

[Abbad et al., 2019] Abbad, A., Atalla, N., Ouisse, M., and Doutres, O. (2019). Numerical and experimental investigations on the acoustic performances of membraned helmholtz resonators embedded in a porous matrix. *Journal of Sound and Vibration*, page 114873. 67, 70

[Abbad et al., 2017] Abbad, A., Rabenorosoa, K., Ouisse, M., and Atalla, N. (2017). Investigations on an electroactive polymer based tunable helmholtz resonator. In *SPIE Smart Structures and Materials+ Nondestructive Evaluation and Health Monitoring*, pages 101640P–101640P. International Society for Optics and Photonics. 70

[Abbad et al., 2018] Abbad, A., Rabenorosoa, K., Ouisse, M., and Atalla, N. (2018). Adaptive helmholtz resonator based on electroactive polymers: modeling, characterization, and control. *Smart Materials and Structures*, 27(10):105029. xiii, 70, 71, 100

[Ahmed et al., 2014] Ahmed, S., Lauff, C., Crivaro, A., McGough, K., Sheridan, R., Frecker, M., von Lockette, P., Ounaies, Z., Simpson, T., Lien, J.-M., et al. (2014). Multi-field responsive origami structures: Preliminary modeling and experiments. In *ASME 2013 international design engineering technical conferences and computers and information in engineering conference*. American Society of Mechanical Engineers Digital Collection. 36, 123

[Allard and Atalla, 2009] Allard, J. and Atalla, N. (2009). *Propagation of sound in porous media: modelling sound absorbing materials 2e*. John Wiley & Sons. 67, 71, 73, 76, 77, 78

[Alster, 1972] Alster, M. (1972). Improved calculation of resonant frequencies of helmholtz resonators. *Journal of Sound and Vibration*, 24(1):63–85. 64

[Anderson and Bratos-Anderson, 1993] Anderson, J. S. and Bratos-Anderson, M. (1993). *Noise: Its measurement, analysis, rating and control*. Gower Technical. 62

[ANR-18-CE33-0008, 2019] ANR-18-CE33-0008 (2019). Origami-based structures for multi-modal robots – origabot. https://anr.fr/Project-ANR-18-CE33-0008. (Accessed: Jan. 09, 2020). 154

[Babaee et al., 2016] Babaee, S., Overvelde, J. T., Chen, E. R., Tournat, V., and Bertoldi, K. (2016). Reconfigurable origami-inspired acoustic waveguides. *Science Advances*, 2(11):e1601019. 122

[Bar-Cohen, 2002] Bar-Cohen, Y. (2002). Electroactive polymers as artificial muscles: a review. *Journal of Spacecraft and Rockets*, 39(6):822–827. 124

[Barile, 2019] Barile, M. (2019). Kawasaki's theorem. from mathworld–a wolfram web resource, created by eric w. weisstein. http://mathworld.wolfram.com/KawasakisTheorem.html. (Accessed: Feb 17, 2019). 8

[Bassik et al., 2010] Bassik, N., Brafman, A., Zarafshar, A. M., Jamal, M., Luvsanjav, D., Selaru, F. M., and Gracias, D. H. (2010). Enzymatically triggered actuation of miniaturized tools. *Journal of the American Chemical Society*, 132(46):16314–16317. 16, 36, 122

[Bowen et al., 1989] Bowen, W. R., Kingdon, R. S., and Sabuni, H. A. (1989). Electrically enhanced separation processes: the basis of in situ intermittent electrolytic membrane cleaning (iiemc) and in situ electrolytic membrane restoration (iemr). *Journal of Membrane Science*, 40(2):219–229. 127

[Bunget and Seelecke, 2008] Bunget, G. and Seelecke, S. (2008). Batmav: a biologically inspired micro air vehicle for flapping flight: kinematic modeling. In *Active and Passive Smart Structures and Integrated Systems 2008*, volume 6928, page 69282F. International Society for Optics and Photonics. 6

[Bunget and Seelecke, 2010] Bunget, G. and Seelecke, S. (2010). Batmav: a 2-dof bio-inspired flapping flight platform. In *Active and Passive Smart Structures and Integrated Systems 2010*, volume 7643, page 76433B. International Society for Optics and Photonics. 6

[Cambonie and Gourdon, 2018] Cambonie, T. and Gourdon, E. (2018). Innovative origami-based solutions for enhanced quarter-wavelength resonators. *Journal of Sound and Vibration*, 434:379–403. ix, 13, 14, 36, 122

[Castillo-Ortega et al., 1989] Castillo-Ortega, M., Inoue, M., and Inoue, M. (1989). Chemical synthesis of highly conducting polypyrrole by the use of copper (ii) perchlorate as an oxidant. *Synthetic metals*, 28(1-2):65–70. 127

[Chai and Tan, 2019] Chai, T. and Tan, C. (2019). Review on deployable structure. In *IOP Conference Series: Earth and Environmental Science*, volume 220, page 012034. IOP Publishing. 6

[Champoux and Allard, 1991] Champoux, Y. and Allard, J.-F. (1991). Dynamic tortuosity and bulk modulus in air-saturated porous media. *Journal of applied physics*, 70(4):1975–1979. 71

[Chanaud, 1994] Chanaud, R. (1994). Effects of geometry on the resonance frequency of helmholtz resonators. *Journal of Sound and Vibration*, 178(3):337–348. 64, 67

[Chen et al., 1998] Chen, K., Chen, Y., Lin, K., and Weng, C. (1998). The improvement on the transmission loss of a duct by adding helmholtz resonators. *Applied Acoustics*, 54(1):71–82. 67

[Chen et al., 2015] Chen, Y., Zion, T. T., Wang, W., Kwong, R. Y., Stevenson, W. G., and Schmidt, E. J. (2015). Intra-cardiac mr imaging & mr-tracking catheter for improved mr-guided ep. *Journal of Cardiovascular Magnetic Resonance*, 17(1):P237. x, 18

[Chikhaoui, 2016] Chikhaoui, M. T. (2016). *Nouveau concept de robots à tubes concentriques à micro-actionneurs à base de polymères électro-actifs*. PhD thesis, Université de Franche-Comté. xv, 140

[Collet et al., 2014] Collet, M., Ouisse, M., and Tateo, F. (2014). Adaptive metacomposites for vibroacoustic control applications. *IEEE Sensors Journal*, 14(7):2145–2152. 66

[Cot et al., 2016] Cot, A., Chikhaoui, M. T., Rabenorosoa, K., Rougeot, P., and Andreff, N. (2016). Synthesis, encapsulation, and performance analysis of large deformation tri-layer polypyrrole actuator. In *2016 IEEE International Conference on Advanced Intelligent Mechatronics (AIM)*, pages 436–441. IEEE. 131

[Cromvik and Eriksson, 2006] Cromvik, C. and Eriksson, K. (2006). Airbag folding based on origami mathematics. *Origami*, 4:129–139. 6

[Cybulski et al., 2014] Cybulski, J. S., Clements, J., and Prakash, M. (2014). Foldscope: origami-based paper microscope. *PloS one*, 9(6):e98781. x, 17

[De Bedout, 1996] De Bedout, J. M. (1996). *Adaptive-passive noise control with self-tuning Helmholtz resonators*. PhD thesis, Purdue University. xiii, 67, 68, 100

[de Bedout et al., 1997] de Bedout, J. M., Franchek, M. A., Bernhard, R. J., and Mongeau, L. (1997). Adaptive-passive noise control with self-tuning helmholtz resonators. *Journal of Sound and Vibration*, 202(1):109–123. 67

[Debnath and Fei, 2013] Debnath, S. and Fei, L. (2013). Origami theory and its applications: A literature review. *World Academy of Science, Engineering and Technology*, pages 1131–1135. ix, 6, 7, 9

[Demaine and Demaine, 2002] Demaine, E. D. and Demaine, M. L. (2002). Recent results in computational origami. In *Origami3: Third International Meeting of Origami Science, Mathematics and Education*, pages 3–16. 25

[Demaine et al., 2000] Demaine, E. D., Demaine, M. L., and Mitchell, J. S. (2000). Folding flat silhouettes and wrapping polyhedral packages: New results in computational origami. *Computational Geometry*, 16(1):3–21. 25

[Demaine and O'Rourke, 2008] Demaine, E. D. and O'Rourke, J. (2008). *Geometric folding algorithms: linkages, origami, polyhedra*. Cambridge university press. 7

[Diaz et al., 1979] Diaz, A., Kanazawa, K. K., and Gardini, G. P. (1979). Electrochemical polymerization of pyrrole. *Journal of the Chemical Society, Chemical Communications*, (14):635–636. 127

[Dickey and Selamet, 1996] Dickey, N. and Selamet, A. (1996). Helmholtz resonators: one-dimensional limit for small cavity length-to-diameter ratios. *Journal of Sound and Vibration*, 3(195):512–517. 67

[Ding et al., 2003] Ding, J., Zhou, D., Spinks, G., Wallace, G., Forsyth, S., Forsyth, M., and MacFarlane, D. (2003). Use of ionic liquids as electrolytes in electromechanical actuator systems based on inherently conducting polymers. *Chemistry of materials*, 15(12):2392–2398. 125

[Doutres et al., 2015] Doutres, O., Atalla, N., and Osman, H. (2015). Transfer matrix modeling and experimental validation of cellular porous material with resonant inclusions. *The Journal of the Acoustical Society of America*, 137(6):3502–3513. xiii, 73, 75, 76

[du Plessis d'Argentré et al., 2018] du Plessis d'Argentré, A., Perry, S., Iwata, Y., Iwasaki, H., Iwase, E., Fabozzo, A., Will, I., Rus, D., Damian, D. D., and Miyashita, S. (2018). Programmable medicine: Autonomous, ingestible, deployable hydrogel patch and plug for stomach ulcer therapy. In *2018 IEEE International Conference on Robotics and Automation (ICRA)*, pages 1511–1518. IEEE. 6

[E1050-10, 2012] E1050-10, A. (2012). Standard test method for impedance and absorption of acoustical materials using a tube, two microphones and a digital frequency analysis system. xiii, 78, 79, 80, 93, 95, 96, 99, 101, 102

[E2611-09, 2009] E2611-09, A. (2009). Astm e2611-09 standard test method for measurement of normal incidence sound transmission of acoustical materials based on the transfer matrix method. ASTM. 77

[Early et al., 2004] Early, J. T., Hyde, R., and Baron, R. L. (2004). Twenty-meter space telescope based on diffractive fresnel lens. In *UV/Optical/IR Space Telescopes: Innovative Technologies and Concepts*, volume 5166, pages 148–157. International Society for Optics and Photonics. 6

[Edmondson et al., 2013] Edmondson, B. J., Bowen, L. A., Grames, C. L., Magleby, S. P., Howell, L. L., and Bateman, T. C. (2013). Oriceps: Origami-inspired forceps. In *ASME 2013 conference on smart materials, adaptive structures and intelligent systems*, pages V001T01A027–V001T01A027. American Society of Mechanical Engineers. 6, 122

[Efimtsov and Lazarev, 2001] Efimtsov, B. and Lazarev, L. (2001). Sound transmission loss of panels with resonant elements. *Acoustical Physics*, 47(3):291–296. 76

[Engelhardt et al., 2019] Engelhardt, F. A., Praetorius, F., Wachauf, C. H., Bruggenthies, G., Kohler, F., Kick, B., Kadletz, K. L., Pham, P. N., Behler, K. L., Gerling, T., et al. (2019). Custom-size, functional, and durable dna origami with design-specific scaffolds. *ACS nano*. 6

[Fang et al., 2018] Fang, H., Yu, X., and Cheng, L. (2018). Reconfigurable origami silencers for tunable and programmable sound attenuation. *Smart Materials and Structures*, 27(9):095007. ix, 13, 14, 36, 122

[Felton et al., 2013a] Felton, S. M., Tolley, M. T., Onal, C. D., Rus, D., and Wood, R. J. (2013a). Robot self-assembly by folding: A printed inchworm robot. In *2013 IEEE International Conference on Robotics and Automation*, pages 277–282. IEEE. 30

[Felton et al., 2013b] Felton, S. M., Tolley, M. T., Shin, B., Onal, C. D., Demaine, E. D., Rus, D., and Wood, R. J. (2013b). Self-folding with shape memory composites. *Soft Matter*, 9(32):7688–7694. xi, 30

[Fuchi and Diaz, 2013] Fuchi, K. and Diaz, A. R. (2013). Origami design by topology optimization. *Journal of Mechanical Design*, 135(11):111003. 27

[Fuchi et al., 2012] Fuchi, K., Diaz, A. R., Rothwell, E. J., Ouedraogo, R. O., and Tang, J. (2012). An origami tunable metamaterial. *Journal of Applied Physics*, 111(8):084905. 6

[Gao et al., 2018] Gao, C., Gao, J., Shao, C., Xiao, Y., Zhao, Y., and Qu, L. (2018). Versatile origami micro-supercapacitors array as a wind energy harvester. *Journal of Materials Chemistry A*, 6(40):19750–19756. 6

[Garcia, 2016] Garcia, M. (2016). Beam expanded to full size. `https://blogs.nasa.gov/spacestation/2016/05/28/beam-expanded-to-full-size/`. (Accessed: May 24, 2019). 6

[Gattas and You, 2013] Gattas, J. M. and You, Z. (2013). Quasi-static impact response of alternative origami-core sandwich panels. In *ASME 2013 International Design Engineering Technical Conferences and Computers and Information in Engineering Conference*, pages V06BT07A032–V06BT07A032. American Society of Mechanical Engineers. 6

[Goshi et al., 2018] Goshi, N., Castagnola, E., Vomero, M., Gueli, C., Cea, C., Zucchini, E., Bjanes, D., Maggiolini, E., Moritz, C., Kassegne, S., et al. (2018). Glassy carbon mems for novel origami-styled 3d integrated intracortical and epicortical neural probes. *Journal of Micromechanics and Microengineering*, 28(6):065009. 6

[Grzeschik, 2013] Grzeschik, M. (2013). Performance of foldcores mechanical properties and testing. In *ASME 2013 International Design Engineering Technical Conferences and Computers and Information in Engineering Conference*, pages V06BT07A042–V06BT07A042. American Society of Mechanical Engineers. 6

[Guibas and Stolfi, 1985] Guibas, L. and Stolfi, J. (1985). Primitives for the manipulation of general subdivisions and the computation of voronoi. *ACM transactions on graphics (TOG)*, 4(2):74–123. 27

[Han, 2008] Han, M. (2008). Sound reduction by a helmholtz resonateur. Master's thesis, Lehigh University. 65, 120

[Hanna et al., 2014] Hanna, B. H., Lund, J. M., Lang, R. J., Magleby, S. P., and Howell, L. L. (2014). Waterbomb base: a symmetric single-vertex bistable origami mechanism. *Smart Materials and Structures*, 23(9):094009. 87

[Hannan and Walker, 2003] Hannan, M. W. and Walker, I. D. (2003). Kinematics and the implementation of an elephant's trunk manipulator and other continuum style robots. *Journal of robotic systems*, 20(2):45–63. 137

[Hawkes et al., 2010] Hawkes, E., An, B., Benbernou, N. M., Tanaka, H., Kim, S., Demaine, E., Rus, D., and Wood, R. J. (2010). Programmable matter by folding. *Proceedings of the National Academy of Sciences*, 107(28):12441–12445. xi, 32, 33, 36, 122, 123

[Hernandez et al., 2013] Hernandez, E. A. P., Hu, S., Kung, H. W., Hartl, D., and Akleman, E. (2013). Towards building smart self-folding structures. *Computers & Graphics*, 37(6):730–742. 27

[Hoffmann, 2001] Hoffmann, R. (2001). Airbag folding: Origami design applied to an engineering problem. In *3rd International Meeting of Origami Science, Math, and Education, Asilomar, CA, Mar*, pages 9–11. 6

[Hoover and Fearing, 2008] Hoover, A. M. and Fearing, R. S. (2008). Fast scale prototyping for folded millirobots. In *2008 IEEE International Conference on Robotics and Automation*, pages 886–892. IEEE. 6

[Huzita, 1989] Huzita, H. (1989). Axiomatic development of origami geometry. In *Proceedings of the First International Meeting of Origami Science and Technology, 1989*, pages 143–158. 27

[Huzita-Hatori, 2009] Huzita-Hatori (2009). Axioms. https://en.wikipedia.org/wiki/Huzita-Hatori_axioms. (Accessed: Feb 10, 2019). 7

[Ida et al., 2007] Ida, T., Takahashi, H., Marin, M., and Ghourabi, F. (2007). Modeling origami for computational construction and beyond. In *International Conference on Computational Science and Its Applications*, pages 653–665. Springer. 27, 36

[Ida et al., 2009] Ida, T., Takahashi, H., Marin, M., Kasem, A., and Ghourabi, F. (2009). Computational origami system eos. In *Proc. 4th International Conference of Origami Science, Mathematics and Education (4OSME)*, pages 285–293. 27, 36

[Ingard, 1953] Ingard, U. (1953). On the theory and design of acoustic resonators. *The Journal of the acoustical society of America*, 25(6):1037–1061. 64

[Johnson et al., 1987] Johnson, D. L., Koplik, J., and Dashen, R. (1987). Theory of dynamic permeability and tortuosity in fluid-saturated porous media. *Journal of fluid mechanics*, 176:379–402. 71

[Johnson et al., 2017] Johnson, M., Chen, Y., Hovet, S., Xu, S., Wood, B., Ren, H., Tokuda, J., and Tse, Z. T. H. (2017). Fabricating biomedical origami: a state-of-the-art review. *International journal of computer assisted radiology and surgery*, 12(11):2023–2032. 16

[Jones and Walker, 2005] Jones, B. A. and Walker, I. D. (2005). A new approach to jacobian formulation for a class of multi-section continuum robots. In *Proceedings of the 2005 IEEE International Conference on Robotics and Automation*, pages 3268–3273. IEEE. 139

[Kamrava et al., 2018] Kamrava, S., Mousanezhad, D., Felton, S. M., and Vaziri, A. (2018). Programmable structures: Programmable origami strings (adv. mater. technol. 3/2018). *Advanced Materials Technologies*, 3(3):1870012. 87

[Kanade, 1980] Kanade, T. (1980). A theory of origami world. *Artificial intelligence*, 13(3):279–311. 7

[Kanazawa et al., 1979] Kanazawa, K. K., Diaz, A., Geiss, R. H., Gill, W. D., Kwak, J. F., Logan, J. A., Rabolt, J. F., and Street, G. B. (1979). 'organic metals': polypyrrole, a stable synthetic 'metallic'polymer. *Journal of the Chemical Society, Chemical Communications*, (19):854–855. 127

[Kasem and Ida, 2008] Kasem, A. and Ida, T. (2008). Computational origami environment on the web. *Frontiers of computer science in China*, 2(1):39–54. 27, 36

[Kasem et al., 2006] Kasem, A., Ida, T., Takahashi, H., Marin, M., and Ghourabi, F. (2006). E-origami system eos. In *Proceedings of the Annual Symposium of Japan Society for Software Science and Technology, JSSST, Tokyo, Japan (September 2006)*. 27, 36

[Khalil and Kleinfinger, 1986] Khalil, W. and Kleinfinger, J. (1986). A new geometric notation for open and closed-loop robots. In *Proceedings. 1986 IEEE International Conference on Robotics and Automation*, volume 3, pages 1174–1179. IEEE. xvi, 139, 169

[Kim, 2008] Kim, J. I. (2008). *Compact multi-physics models for large-displacement multilayer cantilevers in RF MEMS circuits, antennas and sensors*. PhD thesis, Purdue University. xv, 128, 129

[Kim et al., 1993] Kim, K.-J., Sun, P., Chen, V., Wiley, D. E., and Fane, A. G. (1993). The cleaning of ultrafiltration membranes fouled by protein. *Journal of Membrane Science*, 80(1):241–249. 127

[Kim and Tadokoro, 2007] Kim, K. J. and Tadokoro, S. (2007). Electroactive polymers for robotic applications. *Artificial Muscles and Sensors*. xvii, 124

[Kim et al., 2016] Kim, S.-R., Lee, D.-Y., Koh, J.-S., and Cho, K.-J. (2016). Fast, compact, and lightweight shape-shifting system composed of distributed self-folding origami modules. In *2016 IEEE International Conference on Robotics and Automation (ICRA)*, pages 4969–4974. IEEE. xi, 34, 36, 44, 123

[Kosinski et al., 2019] Kosinski, R., Mukhortava, A., Pfeifer, W., Candelli, A., Rauch, P., and Saccà, B. (2019). Sites of high local frustration in dna origami. *Nature communications*, 10(1):1061. 6

[Kuo and Morgan, 1999] Kuo, S. M. and Morgan, D. R. (1999). Active noise control: a tutorial review. *Proceedings of the IEEE*, 87(6):943–973. 66

[Kuribayashi et al., 2006] Kuribayashi, K., Tsuchiya, K., You, Z., Tomus, D., Umemoto, M., Ito, T., and Sasaki, M. (2006). Self-deployable origami stent grafts as a biomedical application of ni-rich tini shape memory alloy foil. *Materials Science and Engineering: A*, 419(1):131–137. ix, xi, 15, 26, 36, 87, 122

[Kuribayashi-Shigetomi and Takeuchi, 2011] Kuribayashi-Shigetomi, K. and Takeuchi, S. (2011). Foldable parylene origami sheets covered with cells: Toward applications in bio-implantable devices. In *Origami 5: Fifth International Meeting of Origami Science, Mathematics, and Education*, page 385. CRC Press. 44

[Lagoudas, 2008] Lagoudas, D. C. (2008). *Shape memory alloys: modeling and engineering applications*. Springer. xii, 57

[Landau, 2014] Landau, E. (2014). Solar power, origami-style. `https://www.nasa.gov/jpl/news/origami-style-solar-power-20140814`. (Accessed: Feb 10, 2019). ix, 6, 9, 11, 44

[Lang, 2001] Lang, R. (2001). Trees and circles: an efficient algorithm for origami design. In *Proceedings of the 3rd International Meeting of Origami Science, Math, and Education*. xi, 25, 26

[Lang, 2005] Lang, R. (2005). Origami design secrets: Mathematical methods for an ancient art vol. 27. *Wellesley, MA: Springer: Springer*. 25

[Lang, 1996] Lang, R. J. (1996). A computational algorithm for origami design. In *Proceedings of the twelfth annual symposium on Computational geometry*, pages 98–105. ACM. 25

[Lang, 2004] Lang, R. J. (2004). Treemaker user manual. www.langorigami.com. (Accessed: Feb 27, 2019). 7, 36

[Lang, 2011] Lang, R. J. (2011). *Origami design secrets: mathematical methods for an ancient art*. AK Peters/CRC Press. 7

[Lang, 2015] Lang, R. J. (2015). Eyeglass telescope. http://www.langorigami.com/article/eyeglass-telescope/. (Accessed: Feb 10, 2019). ix, 9, 10, 36

[Lauriks et al., 1992] Lauriks, W., Mees, P., and Allard, J. F. (1992). The acoustic transmission through layered systems. *Journal of sound and vibration*, 155(1):125–132. 72

[Le Floch et al., 2009] Le Floch, F., Thuaire, A., Bidan, G., and Simonato, J.-P. (2009). The electrochemical signature of functionalized single-walled carbon nanotubes bearing electroactive groups. *Nanotechnology*, 20(14):145705. 127

[Lecocq, 2006] Lecocq, B. H. (2006). *Contribution à l'étude du comportement acoustique de matériaux présentant des cavites debouchantes*. PhD thesis, Ecole Nationale Supérieure d'Arts et Metiers. 62

[Lee et al., 2013] Lee, D.-Y., Kim, J.-S., Kim, S.-R., Koh, J.-S., and Cho, K.-J. (2013). The deformable wheel robot using magic-ball origami structure. In *ASME 2013 international design engineering technical conferences and computers and information in engineering conference*, pages V06BT07A040–V06BT07A040. American Society of Mechanical Engineers. xi, xii, 21, 26, 44, 53, 55, 87, 88

[Lee et al., 2014] Lee, D.-Y., Kim, J.-S., Park, J.-J., Kim, S.-R., and Cho, K.-J. (2014). Fabrication of origami wheel using pattern embedded fabric and its application to a deformable mobile robot. In *Robotics and Automation (ICRA), 2014 IEEE International Conference on*, pages 2565–2565. IEEE. x, 21, 22, 36, 44, 87

[Lee and Choi, 2015] Lee, H. and Choi, S. (2015). An origami paper-based bacteria-powered battery. *Nano Energy*, 15:549–557. 13

[Lee and Choi, 2013] Lee, H. Y. and Choi, B. (2013). A multilayer pvdf composite cantilever in the helmholtz resonator for energy harvesting from sound pressure. *Smart Materials and Structures*, 22(11):115025. xii, 64

[Leong et al., 2009] Leong, T. G., Randall, C. L., Benson, B. R., Bassik, N., Stern, G. M., and Gracias, D. H. (2009). Tetherless thermobiochemically actuated microgrippers. *Proceedings of the National Academy of Sciences*, pages pnas–0807698106. x, 15, 16, 36

[Li et al., 2015] Li, L., Wu, Z. P., Sun, H., Chen, D., Gao, J., Suresh, S., Chow, P., Singh, C. V., and Koratkar, N. (2015). A foldable lithium–sulfur battery. *ACS nano*, 9(11):11342–11350. ix, 13, 36

[Li et al., 2019] Li, S., Stampfli, J. J., Xu, H. J., Malkin, E., Diaz, E. V., Rus, D., and Wood, R. J. (2019). A vacuum-driven origami "magic-ball" soft gripper. x, 24, 36, 44

[Liu et al., 2018] Liu, R., Kuang, X., Deng, J., Wang, Y.-C., Wang, A. C., Ding, W., Lai, Y.-C., Chen, J., Wang, P., Lin, Z., et al. (2018). Shape memory polymers for body motion energy harvesting and self-powered mechanosensing. *Advanced Materials*, 30(8):1705195. 6

[Liu et al., 2017a] Liu, T., Wang, Y., and Lee, K. (2017a). Three-dimensional printable origami twisted tower: Design, fabrication, and robot embodiment. *IEEE Robotics and Automation Letters*, 3(1):116–123. 36

[Liu et al., 2018] Liu, T., Wang, Y., and Lee, K. (2018). Three-dimensional printable origami twisted tower: Design, fabrication, and robot embodiment. *IEEE Robotics and Automation Letters*, 3(1):116–123. 44

[Liu et al., 2012] Liu, Y., Boyles, J. K., Genzer, J., and Dickey, M. D. (2012). Self-folding of polymer sheets using local light absorption. *Soft matter*, 8(6):1764–1769. xi, 31, 123

[Liu et al., 2014] Liu, Y., Miskiewicz, M., Escuti, M. J., Genzer, J., and Dickey, M. D. (2014). Three-dimensional folding of pre-strained polymer sheets via absorption of laser light. *Journal of Applied Physics*, 115(20):204911. 31, 123

[Liu et al., 2017b] Liu, Y., Shaw, B., Dickey, M. D., and Genzer, J. (2017b). Sequential self-folding of polymer sheets. *Science Advances*, 3(3):e1602417. 31, 123

[Madden et al., 2000] Madden, J. D., Cush, R. A., Kanigan, T. S., and Hunter, I. W. (2000). Fast contracting polypyrrole actuators. *Synthetic Metals*, 113(1-2):185–192. 124

[Madden et al., 2007] Madden, J. D., Rinderknecht, D., Anquetil, P. A., and Hunter, I. W. (2007). Creep and cycle life in polypyrrole actuators. *Sensors and Actuators A: Physical*, 133(1):210–217. 124

[Mancewicz, 1992] Mancewicz, M. J. (1992). *Developable surfaces: properties, representations and methods of design*. PhD thesis, Kalamazoo College. 26

[Mao et al., 2019] Mao, X., Li, K., Liu, M., Wang, X., Zhao, T., An, B., Cui, M., Li, Y., Pu, J., Li, J., et al. (2019). Directing curli polymerization with dna origami nucleators. *Nature communications*, 10(1):1395. 6

[Martínez-Martín and Thrall, 2014] Martínez-Martín, F. and Thrall, A. (2014). Honeycomb core sandwich panels for origami-inspired deployable shelters: multi-objective

optimization for minimum weight and maximum energy efficiency. *Engineering Structures*, 69:158–167. 6

[Maziz, 2014] Maziz, A. (2014). *Microactionneurs à base de polymeres conducteurs électroniques : Vers l'intégration aux microsystèmes par de nouveaux procédés d'élaboration*. PhD thesis, université de cergy-pontoise. xv, 124, 125

[Menciassi et al., 2005] Menciassi, A., Moglia, A., Gorini, S., Pernorio, G., Stefanini, C., and Dario, P. (2005). Shape memory alloy clamping devices of a capsule for monitoring tasks in the gastrointestinal tract. *Journal of Micromechanics and Microengineering*, 15(11):2045. 158

[Miskin et al., 2018] Miskin, M. Z., Dorsey, K. J., Bircan, B., Han, Y., Muller, D. A., McEuen, P. L., and Cohen, I. (2018). Graphene-based bimorphs for micron-sized, autonomous origami machines. *Proceedings of the National Academy of Sciences*, 115(3):466–470. 6

[Mitani, 2005] Mitani, J. (2005). Oripa (origami pattern editor). available at: http://mitani. cs. tsukuba. ac. jp/floripa. 36, 46

[Miura, 1994] Miura, K. (1994). Map fold a la miura style, its physical characteristics and application to the space science. ix, 9, 10, 36, 44

[Miyashita et al., 2015] Miyashita, S., Guitron, S., Ludersdorfer, M., Sung, C. R., and Rus, D. (2015). An untethered miniature origami robot that self-folds, walks, swims, and degrades. In *Robotics and Automation (ICRA), 2015 IEEE International Conference on*, pages 1490–1496. IEEE. x, 22, 23, 36, 123

[Miyashita et al., 2016] Miyashita, S., Guitron, S., Yoshida, K., Li, S., Damian, D. D., and Rus, D. (2016). Ingestible, controllable, and degradable origami robot for patching stomach wounds. In *Proceedings-IEEE International Conference on Robotics and Automation*, volume 2016, pages 909–916. Sheffield. x, 18, 19, 36, 122

[Miyashita et al., 2014] Miyashita, S., Meeker, L., Tolley, M. T., Wood, R. J., and Rus, D. (2014). Self-folding miniature elastic electric devices. *Smart Materials and Structures*, 23(9):094005. 6, 29, 36, 44

[Miyashita et al., 2013] Miyashita, S., Onal, C. D., and Rus, D. (2013). Self-pop-up cylindrical structure by global heating. In *2013 IEEE/RSJ International Conference on Intelligent Robots and Systems*, pages 4065–4071. IEEE. 29, 36, 44, 123

[Mohammadi et al., 1987] Mohammadi, A., Lundström, I., Salaneck, W., and Inganäs, O. (1987). Polypyrrole prepared by chemical vapour deposition using hydrogen peroxide and hydrochloric acid. *Synthetic Metals*, 21(1-3):169–173. 127

[Morgan et al., 2016] Morgan, J., Magleby, S. P., and Howell, L. L. (2016). An approach to designing origami-adapted aerospace mechanisms. *Journal of Mechanical Design*, 138(5):052301. 44

[Munjal, 1987] Munjal, M. L. (1987). *Acoustics of ducts and mufflers with application to exhaust and ventilation system design*. John Wiley & Sons. 62

[Na et al., 2015] Na, J.-H., Evans, A. A., Bae, J., Chiappelli, M. C., Santangelo, C. D., Lang, R. J., Hull, T. C., and Hayward, R. C. (2015). Programming reversibly self-folding origami with micropatterned photo-crosslinkable polymer trilayers. *Advanced Materials*, 27(1):79–85. 123

[Nalwa, 2001] Nalwa, H. S. (2001). *Handbook of surfaces and interfaces of materials, five-volume set*. Elsevier. 127

[Norman and Arjomandi, 2017] Norman, M. and Arjomandi, K. (2017). Origami applications in structural engineering: A look at temporary shelters. In *Proceedings of the 2nd World Congress on Civil, Structural, and Environmental Engineering (CSEE'17), Barcelona, Spain*. 44

[Ocampo et al., 2004] Ocampo, J. M. Z., Vaccaro, P. O., Kubota, K., Fleischmann, T., Wang, T.-S., Aida, T., Ohnishi, T., Sugimura, A., Izumoto, R., Hosoda, M., et al. (2004). Characterization of gaas-based micro-origami mirrors by optical actuation. *Microelectronic engineering*, 73:429–434. 6

[Onal et al., 2011] Onal, C. D., Wood, R. J., and Rus, D. (2011). Towards printable robotics: Origami-inspired planar fabrication of three-dimensional mechanisms. In *Robotics and Automation (ICRA), 2011 IEEE International Conference on*, pages 4608–4613. IEEE. x, 20, 21, 22, 36

[Paik and Wood, 2012] Paik, J. K. and Wood, R. J. (2012). A bidirectional shape memory alloy folding actuator. *Smart materials and structures*, 21(6):065013. 123

[Panneton, 2009] Panneton, R. (2009). Normal incidence sound transmission loss evaluation by upstream surface impedance measurements. *The Journal of the Acoustical Society of America*, 125(3):1490–1497. 77

[Panton and Miller, 1975] Panton, R. L. and Miller, J. M. (1975). Resonant frequencies of cylindrical helmholtz resonators. *The Journal of the Acoustical Society of America*, 57(6):1533–1535. 67

[Pehrson et al., 2019] Pehrson, N. A., Smith, S. P., Ames, D. C., Magleby, S. P., and Arya, M. (2019). Self-deployable, self-stiffening, and retractable origami-based arrays for spacecraft. In *AIAA Scitech 2019 Forum*, page 0484. 6

[Pellicier and Trompette, 2007] Pellicier, A. and Trompette, N. (2007). A review of analytical methods, based on the wave approach, to compute partitions transmission loss. *Applied Acoustics*, 68(10):1192–1212. 73

[Peraza-Hernandez et al., 2013] Peraza-Hernandez, E., Hartl, D., Galvan, E., and Malak, R. (2013). Design and optimization of a shape memory alloy-based self-folding sheet. *Journal of Mechanical Design*, 135(11):111007. 123

[Peraza-Hernandez et al., 2014] Peraza-Hernandez, E. A., Hartl, D. J., Malak Jr, R. J., and Lagoudas, D. C. (2014). Origami-inspired active structures: a synthesis and review. *Smart Materials and Structures*, 23(9):094001. 6

[Pounds, 2012] Pounds, P. (2012). Paper plane: Towards disposable low-cost folded cellulose-substrate uavs. In *Australasian Conference on Robotics and Automation*. 6

[Quagli et al., 2014] Quagli, C., Ballard, Z., and Thrall, A. (2014). Parametric modelling of an air-liftable origami-inspired deployable shelter with a novel erection strategy. *Mobile and Rapidly Assembled Structures IV*, 136:23. 6

[Randlett, 1963] Randlett, S. (1963). *The Art of Origami: Paper Folding, Traditional and Modern*. Faber & Faber. 15

[Ranzani et al., 2017] Ranzani, T., Russo, S., Schwab, F., Walsh, C. J., and Wood, R. J. (2017). Deployable stabilization mechanisms for endoscopic procedures. In *Robotics and Automation (ICRA), 2017 IEEE International Conference on*, pages 1125–1131. IEEE. x, 18, 20, 36

[Rayleigh, 1945] Rayleigh, J. (1945). The theory of sound,(1945). 64

[Rayleigh, 1916] Rayleigh, L. (1916). The theory of the helmholtz resonator. *Proceedings of the Royal Society of London. Series A, Containing Papers of a Mathematical and Physical Character*, 92(638):265–275. 62

[Rodrigues et al., 2017] Rodrigues, G. V., Fonseca, L. M., Savi, M. A., and Paiva, A. (2017). Nonlinear dynamics of an adaptive origami-stent system. *International Journal of Mechanical Sciences*, 133:303–318. 15

[Rus and Tolley, 2018] Rus, D. and Tolley, M. T. (2018). Design, fabrication and control of origami robots. *Nature Reviews Materials*, page 1. 6

[Schenk and Guest, 2013] Schenk, M. and Guest, S. D. (2013). Geometry of miura-folded metamaterials. *Proceedings of the National Academy of Sciences*, 110(9):3276–3281. 6

[Schmidt et al., 2011] Schmidt, E., Qin, L., Santos, J., Michaud, G., Kwong, R., Butts-Pauly, K., Stevenson, W., and Dumoulin, C. (2011). Intra-cardiac mri catheter for ep ablation monitoring: preliminary studies. In *Proceedings of the 19th annual meeting of ISMRM, Montreal, Canada*, page 3741. x, 17, 18

[Selamet and Lee, 2003] Selamet, A. and Lee, I. (2003). Helmholtz resonator with extended neck. *The Journal of the Acoustical Society of America*, 113(4):1975–1985. 67

[Silverberg et al., 2015] Silverberg, J. L., Na, J.-H., Evans, A. A., Liu, B., Hull, T. C., Santangelo, C. D., Lang, R. J., Hayward, R. C., and Cohen, I. (2015). Origami structures with a critical transition to bistability arising from hidden degrees of freedom. *Nature materials*, 14(4):389. 123

[Song et al., 2014] Song, Z., Ma, T., Tang, R., Cheng, Q., Wang, X., Krishnaraju, D., Panat, R., Chan, C. K., Yu, H., and Jiang, H. (2014). Origami lithium-ion batteries. *Nature communications*, 5:3140. ix, 11, 12, 36

[Spinks et al., 2004] Spinks, G. M., Xi, B., Zhou, D., Truong, V.-T., and Wallace, G. G. (2004). Enhanced control and stability of polypyrrole electromechanical actuators. *Synthetic Metals*, 140(2-3):273–280. 125

[Stinson, 1991] Stinson, M. R. (1991). The propagation of plane sound waves in narrow and wide circular tubes, and generalization to uniform tubes of arbitrary cross-sectional shape. *The Journal of the Acoustical Society of America*, 89(2):550–558. 79

[Tachi, 2007] Tachi, T. (2007). Origamizing 3d surface by symmetry constraints. In *SIGGRAPH Posters*, page 25. 25, 36

[Tachi, 2009a] Tachi, T. (2009a). Generalization of rigid-foldable quadrilateral-mesh origami. *Journal of the International Association for Shell and Spatial Structures*, 50(3):173–179. 47

[Tachi, 2009b] Tachi, T. (2009b). Simulation of rigid origami. *Origami*, 4:175–187. 26

[Tachi, 2010a] Tachi, T. (2010a). Freeform rigid-foldable structure using bidirectionally flat-foldable planar quadrilateral mesh. *Advances in architectural geometry 2010*, pages 87–102. xi, 25, 26, 36, 47

[Tachi, 2010b] Tachi, T. (2010b). Freeform variations of origami. *J. Geom. Graph*, 14(2):203–215. 25, 36, 47

[Tachi, 2010] Tachi, T. (2010). Origamizing polyhedral surfaces. *IEEE Transactions on Visualization and Computer Graphics*, 16(2):298–311. 25, 36

[Tachi, 2013] Tachi, T. (2013). Designing freeform origami tessellations by generalizing resch's patterns. *Journal of mechanical design*, 135(11):111006. 25

[Tachi and Miura, 2012] Tachi, T. and Miura, K. (2012). Rigid-foldable cylinders and cells. *Journal of the international association for shell and spatial structures*, 53(4):217–226. 44

[Tang and Sirignano, 1973] Tang, P. and Sirignano, W. (1973). Theory of a generalized helmholtz resonator. *Journal of Sound and Vibration*, 26(2):247–262. 67

[Tang, 2005] Tang, S. (2005). On helmholtz resonators with tapered necks. *Journal of Sound and Vibration*, 279(3-5):1085–1096. 67

[Taylor et al., 2016] Taylor, A., Miller, M., Fok, M., Nilsson, K., and Tse, Z. T. H. (2016). Intracardiac magnetic resonance imaging catheter with origami deployable mechanisms. *Journal of Medical Devices*, 10(2):020957. x, 18, 44

[Taylor et al., 2019] Taylor, A. J., Slutzky, T., Feuerman, L., Ren, H., Tokuda, J., Nilsson, K., and Tse, Z. T. H. (2019). Mr conditional sma-based origami joint. *IEEE/ASME Transactions on Mechatronics*. 6

[Thrall and Quaglia, 2014] Thrall, A. and Quaglia, C. (2014). Accordion shelters: A historical review of origami-like deployable shelters developed by the us military. *Engineering structures*, 59:686–692. 44

[Tolley et al., 2014] Tolley, M. T., Felton, S. M., Miyashita, S., Aukes, D., Rus, D., and Wood, R. J. (2014). Self-folding origami: shape memory composites activated by uniform heating. *Smart Materials and Structures*, 23(9):094006. xi, 7, 28, 29, 122, 123

[Tolley et al., 2013] Tolley, M. T., Felton, S. M., Miyashita, S., Xu, L., Shin, B., Zhou, M., Rus, D., and Wood, R. J. (2013). Self-folding shape memory laminates for automated fabrication. In *2013 IEEE/RSJ International Conference on Intelligent Robots and Systems*, pages 4931–4936. IEEE. xvii, 32

[Varrasi, 2014] Varrasi, J. (2014). How the future of origami engineering is unfolding (op-ed). https://www.livescience.com/49121-origami-inspired-engineering-is-expanding.html. (Accessed: Oct 07, 2019). 44

[Verdière et al., 2013] Verdière, K., Panneton, R., Elkoun, S., Dupont, T., and Leclaire, P. (2013). Transfer matrix method applied to the parallel assembly of sound absorbing materials. *The Journal of the Acoustical Society of America*, 134(6):4648–4658. 72, 73, 74

[Verdière et al., 2014] Verdière, K., Panneton, R., Elkoun, S., Dupont, T., and Leclaire, P. (2014). Comparison between parallel transfer matrix method and admittance sum method. *The Journal of the Acoustical Society of America*, 136(2):EL90–EL95. 72, 73

[Von Helmholtz, 1912] Von Helmholtz, H. (1912). *On the Sensations of Tone as a Physiological Basis for the Theory of Music*. Longmans, Green. 63

[Waltman et al., 1983] Waltman, R. J., Bargon, J., and Diaz, A. (1983). Electrochemical studies of some conducting polythiophene films. *The Journal of Physical Chemistry*, 87(8):1459–1463. 127

[Wang and Choy, 2019] Wang, Z. and Choy, Y. (2019). Tunable parallel barriers using helmholtz resonator. *Journal of Sound and Vibration*, 443:109–123. 67

[Webster and Davies, 2010] Webster, E. S. and Davies, C. E. (2010). The use of helmholtz resonance for measuring the volume of liquids and solids. *Sensors*, 10(12):10663–10672. 63, 65

[Webster III, 2007] Webster III, R. J. (2007). *Design and mechanics of continuum robots for surgery*. PhD thesis, Johns Hopkins University. 137

[Webster III and Jones, 2010] Webster III, R. J. and Jones, B. A. (2010). Design and kinematic modeling of constant curvature continuum robots: A review. *The International Journal of Robotics Research*, 29(13):1661–1683. 139

[Weisstein, 2019] Weisstein, E. (2019). Spanning tree. http://mathworld.wolfram.com/SpanningTree.html. (Accessed: Spet 30, 2019). 27

[Wu et al., 2019] Wu, D., Zhang, N., Mak, C. M., and Cai, C. (2019). Hybrid noise control using multiple helmholtz resonator arrays. *Applied Acoustics*, 143:31–37. 67

[Wu et al., 2006] Wu, Y., Alici, G., Spinks, G. M., and Wallace, G. (2006). Fast trilayer polypyrrole bending actuators for high speed applications. *Synthetic Metals*, 156(16-17):1017–1022. xvii, 125

[Yang, 2018] Yang, K. (2018). Design optimization of energy absorption structures with origami patterns. 6

[Yao et al., 2014] Yao, S., Georgakopoulos, S. V., Cook, B., and Tentzeris, M. (2014). A novel reconfigurable origami accordion antenna. In *2014 IEEE MTT-S International Microwave Symposium (IMS2014)*, pages 1–4. IEEE. 44

[Yasu and Inami, 2012] Yasu, K. and Inami, M. (2012). Popapy: instant paper craft made up in a microwave oven. In *Advances in Computer Entertainment*, pages 406–420. Springer. 29, 36

[Yu et al., 2017] Yu, X., Lu, Z., Cui, F., Cheng, L., and Cui, Y. (2017). Tunable acoustic metamaterial with an array of resonators actuated by dielectric elastomer. *Extreme Mechanics Letters*, 12:37–40. xiii, 68, 69, 100

[Zeng et al., 2019] Zeng, F., Li, Z., Li, X., Wang, J., Kong, Z., Sun, Y., Liu, Z., and Feng, H. (2019). Almond-derived origami-like hierarchically porous and n/o co-functionalized carbon sheet for high-performance supercapacitor. *Applied Surface Science*, 467:229–235. 6

[Zhao et al., 2011] Zhao, Y., Nandra, M., and Tai, Y. (2011). A mems intraocular origami coil. In *2011 16th International Solid-State Sensors, Actuators and Microsystems Conference*, pages 2172–2175. IEEE. 6

[Zhou et al., 2017] Zhou, C., Jiang, L., Tian, K., Bi, X., and Wang, B. (2017). Origami crash boxes subjected to dynamic oblique loading. *Journal of Applied Mechanics*, 84(9):091006. 6

[Zhou et al., 2003a] Zhou, D., Spinks, G. M., Wallace, G. G., Tiyapiboonchaiya, C., MacFarlane, D. R., Forsyth, M., and Sun, J. (2003a). Solid state actuators based on polypyrrole and polymer-in-ionic liquid electrolytes. *Electrochimica acta*, 48(14-16):2355–2359. 125

[Zhou et al., 2003b] Zhou, D., Wallace, G., Spinks, G., Liu, L., Cowan, R., Saunders, E., and Newbold, C. (2003b). Actuators for the cochlear implant. *Synthetic Metals*, 135:39–40. 124, 125

[Zhu and Li, 2014] Zhu, S. and Li, T. (2014). Hydrogenation-assisted graphene origami and its application in programmable molecular mass uptake, storage, and release. *ACS nano*, 8(3):2864–2872. x, 16, 17

[Zirbel et al., 2013] Zirbel, S. A., Lang, R. J., Thomson, M. W., Sigel, D. A., Walkemeyer, P. E., Trease, B. P., Magleby, S. P., and Howell, L. L. (2013). Accommodating thickness in origami-based deployable arrays. *Journal of Mechanical Design*, 135(11):111005. 122

This document contains 192 references.

SPIM

Titre : Structures actives à base d'origami pour des résonateurs de Helmholtz adaptatifs et la robotique souple

Mots clés : *origami, conception mécatronique, structure active, résonateurs de Helmholtz adaptatif, auto-pliage, changement de forme.*

Résumé : Aujourd'hui, les découvertes les plus passionnantes et les réalisations les plus fascinantes se déroulent à la périphérie de différents domaines. Un domaine peu connu qui a récemment démontré des résultats spectaculaires est l'application des principes de l'origami à la science et les technologies modernes. Cette approche présente des avantages qui justifient que l'on s'y attarde. Ce travail de thèse se concentre sur le développement de structures actives à base d'origami à la fois reconfigurables et adaptatives. Nous avons proposé une méthode de synthèse de structures actives à base d'origami. Elle est composée de plusieurs étapes : définition du cahier des charges, création du motif origami en 2D après un choix préalable de la base, conversion en 3D, modélisation multi-physique, choix des technologies de fabrication, intégration de systèmes d'actionnement, validation expérimentale et contrôle. Elle a été suivie du choix des outils logiciels assurant une interopérabilité mutuelle. Elle a ensuite été appliquée et validée pour une application en acoustique. Nous avons alors proposé un concept de résonateurs de Helmholtz adaptatifs à base d'origami pour le contrôle adaptatif-passif du bruit, et nous avons pu obtenir des résultats remarquables en termes de plage de fréquence et de largeur de bande. Un ensemble de modèle a été proposé pour décrire le fonctionnement des résonateurs de Helmholtz adaptatifs à base d'origami suivant leur flexibilité. Nous avons également étudié des actionneurs à base de matériaux actifs pour des structures à base d'origami. Plus précisément les polymères conducteurs qui sont capable de réaliser de grandes déformations à faible tension d'activation pour l'auto-pliage réversible.

Title : Origami-based active structures for tunable Helmholtz resonators and soft robotics

Keywords : *origami, mechatronic designs, active structure, tunable Helmholtz resonators, self-folding, shape-shifting.*

Abstract : Today, the most exciting discoveries and fascinating accomplishments are performed on the peripheries of different areas. A not very well-known area which has recently demonstrated spectacular achievements is the application of origami principles in modern science and technology. This approach has advantages that justify the recent attention. This thesis work focuses on the development of origami-based active structures, both reconfigurable and adaptive. We proposed a new synthesis method of origami-based active structures. It is composed of several stages: definition of the application requirements, creation of the origami motif in 2D after a preliminary choice of the base, conversion in 3D, multi-physics modeling, selection of fabrication technologies, integration of the actuation system, experimental validation, and control. The method was followed by a choice of software tools that ensure mutual interoperability. It was then applied and validated for an acoustics application. A concept of tunable origami-based Helmholtz resonators for adaptive-passive noise control. The resonators were able to achieve remarkable results in terms of frequency range and bandwidth. A set of models has been proposed to describe the functioning of tunable origami-based Helmholtz resonators according to their flexibility. We also studied actuators based on active materials for origami-based structures. More specifically, conductive polymers which are capable of producing large deformations with a low activation voltage, and a reversible self-folding.

UBFC UNIVERSITE BOURGOGNE FRANCHE-COMTE

Université Bourgogne Franche-Comté
32, avenue de l'Observatoire
25000 Besançon